



LANGLEY GRANT  
1N-32-CR  
123894  
2288

**A NEW APPROACH FOR SHAPING  
OF DUAL-REFLECTOR ANTENNAS**

**Teh-Hong Lee  
W.D. Burnside  
Roger C. Rudduck**

**The Ohio State University  
ElectroScience Laboratory**

**Department of Electrical Engineering  
Columbus, Ohio 43212**

**Technical Report No. 716148-26  
Grant No. NSG 1613  
December 1987**

**National Aeronautics and Space Administration  
Langley Research Center  
Hampton, Virginia 23665**

**(NASA-CR-182581) A NEW APPROACH FOR SHAPING  
OF DUAL-REFLECTOR ANTENNAS (Ohio State  
Univ.) 228 p CSCI 20N**

**N88-18806**

**Unclas  
G3/32 0128894**

## NOTICES

When Government drawings, specifications, or other data are used for any purpose other than in connection with a definitely related Government procurement operation, the United States Government thereby incurs no responsibility nor any obligation whatsoever, and the fact that the Government may have formulated, furnished, or in any way supplied the said drawings, specifications, or other data, is not to be regarded by implication or otherwise as in any manner licensing the holder or any other person or corporation, or conveying any rights or permission to manufacture, use, or sell any patented invention that may in any way be related thereto.

|  |   |                                |  |
|--|---|--------------------------------|--|
| <b>REPORT DOCUMENTATION PAGE</b>   | <b>1. REPORT NO.</b>                                    | <b>2.</b>                      | <b>3. Recipient's Accession No.</b>                          |
| <b>4. Title and Subtitle</b><br>A New Approach for Shaping of Dual-Reflector Antennas  |   |                                | <b>5. Report Date</b><br>December 1987                       |
| <b>7. Author(s)</b><br>Teh-Hong Lee, W.D. Burnside, Roger C. Rudduck   |   |                                | <b>6.</b>  |
| <b>9. Performing Organization Name and Address</b><br>The Ohio State University ElectroScience Laboratory<br>1320 Kinnear Road<br>Columbus, Ohio 43212   |   |                                | <b>8. Performing Organization Rept. No.</b><br>716148-26     |
|  |   |                                | <b>10. Project/Task/Work Unit No.</b>                        |
|  |   |                                | <b>11. Contract(C) or Grant(G) No</b><br>(C)<br>(G) NSG 1613 |
| <b>12. Sponsoring Organization Name and Address</b><br>NASA - Langley Research Center<br>Hampton, Virginia 23665   |   |                                | <b>13. Type of Report &amp; Period Covered</b><br>Technical  |
| <b>15. Supplementary Notes</b>   |   |                                | <b>14.</b>   |
| <b>16. Abstract (Limit: 200 words)</b><br><p>A new approach is studied for the shaping of two-dimensional dual-reflector antenna systems to generate a prescribed distribution with uniform phase at the aperture of the second reflector. This method is based on the geometrical nature of Cassegrain and Gregorian dual-reflector antennas. The method of synthesis satisfies the principles of geometrical optics which are the foundations of dual-reflector designs. Instead of setting up differential equations or heuristically designing the subreflector, a set of algebraic equations are formulated and solved numerically to obtain the desired surfaces. The caustics of the reflected rays from the subreflector can be obtained and examined. Several examples of two-dimensional dual-reflector shaping are shown to validate this study. Geometrical optics and physical optics are used to calculate the scattered fields from the reflectors.</p> <p>A blended rolled edge attachment to the shaped main reflector for compact range applications is also investigated. The addition of rolled edges to the main reflector reduces the edge diffracted field which causes ripple in the aperture field. A method for correcting false end-point contributions which result from the use of physical optics are reviewed. Several examples are given to illustrate the improvement achieved in the aperture field by adding the blended rolled edge terminations. Corrections for the end-point contributions are included in these examples in order to obtain the true scattered fields from the reflectors. The same method of synthesis is also used for shaping of a three-dimensional circularly symmetric dual-reflector antenna. This case is also verified by examples.</p> |   |                                |  |
| <b>17. Document Analysis a. Descriptors</b>  |   |                                |  |
| <b>b. Identifiers/Open-Ended Terms</b>   |   |                                |  |
| <b>c. COSATI Field/Group</b>   |   |                                |  |
| <b>18. Availability Statement</b>  | <b>19. Security Class (This Report)</b><br>Unclassified | <b>21. No. of Pages</b><br>231 |  |
|  | <b>20. Security Class (This Page)</b><br>Unclassified   | <b>22. Price</b>               |  |

## TABLE OF CONTENTS

|   |    |
|---|----|
| List of Figures   | v  |
| I. INTRODUCTION   | 1  |
| II. THEORETICAL TECHNIQUES  | 6  |
| 2.1 Geometrical Optics  | 7  |
| 2.2 Geometrical Optics Reflected Field  | 10 |
| 2.3 Physical Optics   | 13 |
| 2.4 Conventional Cassegrain Reflector Antenna   | 21 |
| 2.5 Conventional Gregorian Reflector Antenna  | 25 |
| III. SYNTHESIS OF TWO-DIMENSIONAL DUAL REFLECTOR ANTENNAS   | 29 |
| 3.1 Introduction  | 29 |
| 3.2 Method of Synthesis   | 31 |
| 3.2.1 Formulation   | 35 |
| A. Subreflector   | 35 |
| B. Main Reflector   | 41 |
| C. Snell's Law of Reflection  | 44 |
| D. Conservation of Power  | 46 |
| 3.2.2 Solution for the Surface Equations  | 51 |
| IV. EXAMPLES OR SHAPING OF TWO-DIMENSIONAL DUAL REFLECTOR ANTENNA   | 54 |
| 4.1. Shaping of a Center-Fed Gregorian Reflector Antenna for a Uniform Aperture Distribution                          | 56 |
| 4.1.1 Example G1  | 61 |
| 4.1.2 Example G2  | 70 |
| 4.2. Shaping of an Offset Reflector Antenna (Example G3)  | 75 |
| 4.3. Shaping of a Center-Fed Cassegrain Reflector Antenna for Uniform Aperture Distribution (Example C1)              | 79 |
| 4.4. Shaping of a Center-Fed Gregorian Reflector Antenna for Non-Uniform Aperture Amplitude Distribution (Example G4) | 90 |
| V. ROLLED EDGE MODIFICATION FOR THE SHAPED MAIN REFLECTOR   | 99 |
| 5.1. Introduction   | 99 |

|   |     |
|---|-----|
| 5.2. Rolled Edge Attachment to Main Reflector   | 104 |
| 5.2.1 Elliptic Rolled Edge  | 106 |
| 5.2.2 Blended Rolled Edge   | 109 |
| 5.3. End Point Correction of Physical Optics  | 114 |
| 5.4. Examples of Shaped Dual-Reflector with Blended<br>Rolled Edge Terminations on the Main Reflector | 124 |
| 5.4.1 Example BL1   | 124 |
| 5.4.2 Example BL2   | 128 |
| 5.4.3 Example BL3   | 138 |
| VI. SHAPING OF THREE-DIMENSIONAL CIRCULARLY SYMMETRIC DUAL-<br>REFLECTOR ANTENNAS                     | 147 |
| 6.1. Method of Shaping  | 147 |
| 6.2. Examples of Shaping of Three-Dimensional Dual-<br>Reflector Antennas                             | 152 |
| 6.2.1 Example 3D1   | 152 |
| 6.2.2 Example 3D2   | 155 |
| 6.2.3 Example 3D3   | 155 |
| VII. SUMMARY AND CONCLUSIONS  | 165 |
| APPENDICES  |     |
| A. DIRECT APPLICATION OF PRINCIPLES OF GEOMETRICAL OPTICS<br>TO DUAL-REFLECTOR ANTENNA SHAPING        | 167 |
| B. NUMERICAL METHOD FOR SOLVING THE SURFACE EQUATIONS   | 178 |
| C. GEOMETRICAL OPTICS REFLECTED FIELDS FOR CASSEGRAIN AND<br>GREGORIAN REFLECTOR ANTENNAS             | 191 |
| REFERENCES  | 209 |

## LIST OF FIGURES

|         |   |    |
|---------|---|----|
| 2.1     | Astigmatic tube of rays.  | 9  |
| 2.2     | Geometry associated with the reflection by a surface S.   | 11 |
| 2.3     | Induced surface current in the physical optics approximation.                                     | 11 |
| 2.4     | TE incidence in two-dimensional case.   | 17 |
| 2.5     | TM incidence in two-dimensional case.   | 19 |
| 2.6     | Geometry of the Cassegrain antenna system.  | 22 |
| 2.7     | Ray geometry of the Cassegrain antenna system.  | 24 |
| 2.8     | Geometry of the Gregorian antenna system.   | 27 |
| 2.9     | Ray geometry of the Gregorian antenna system.   | 28 |
| 3.1(a). | Shaped dual-reflector with convex subreflector.   | 33 |
| 3.1(b). | Shaped dual-reflector with concave subreflector.  | 34 |
| 3.2     | Canonic form of hyperbola and ellipse.  | 36 |
| 3.3     | Geometry of shaped subreflector section.  | 38 |
| 3.4     | Canonic form of parabola.   | 42 |
| 3.5     | Geometry of shaped main reflector.  | 43 |
| 3.6     | Geometry for describing the relations of various points.  | 45 |
| 3.7     | Geometry of describing conservation of power.   | 49 |
| 4.1     | A conventional Gregorian reflector antenna.   | 57 |
| 4.2     | Far-zone scattered field of the subreflector for the conventional Gregorian reflector. 20 GHz.    | 59 |
| 4.3     | Near-zone scattered field of the main reflector for the conventional Gregorian reflector. 20 GHz. | 60 |
| 4.4     | Shaped dual-reflector with inappropriate initial  |    |

|      |   |    |
|------|---|----|
|      | points of Example G1.   | 63 |
| 4.5  | Subreflector and caustics for the shaped dual-reflector with inappropriate initial points of Example G1.  | 64 |
| 4.6  | Improved shaped dual-reflector of Example G1.   | 65 |
| 4.7  | Subreflector and caustics of the improved shaped dual-reflector of Example G1.  | 66 |
| 4.8  | Far-zone scattered field of the shaped subreflector for Example G1. 20 GHz.   | 68 |
| 4.9  | Near-zone scattered field of the shaped main reflector for the Example G1. 20 GHz.  | 69 |
| 4.10 | Shaped dual-reflector of Example G2.  | 71 |
| 4.11 | Subreflector and caustics for the shaped dual-reflector of Example G2.  | 72 |
| 4.12 | Far-zone scattered field of the shaped subreflector of Example G2. 20 GHz.  | 73 |
| 4.13 | Near-zone scattered fields of the shaped main reflector of Example G2. 20 GHz.  | 74 |
| 4.14 | Geometry of an offset Gregorian reflector.  | 76 |
| 4.15 | Far-zone scattered fields from subreflector of the offset Gregorian reflector with a $\cos^{200} \phi$ magnetic line source illumination. 3 GHz.          | 77 |
| 4.16 | Near-zone scattered fields from subreflector of the offset Gregorian reflector with a $\cos^{200} \phi$ magnetic line source illumination. 3 GHz.         | 78 |
| 4.17 | Geometry of the shaped offset dual-reflector.   | 80 |
| 4.18 | Caustics and subreflector of the shaped offset dual-reflector.  | 81 |
| 4.19 | Far-zone scattered fields from subreflector of the shaped offset Gregorian reflector with a $\cos^{200} \phi$ magnetic line source illumination. 3 GHz.   | 82 |
| 4.20 | Near-zone scattered fields from the main reflector of the shaped offset dual-reflector with a $\cos^{200} \phi$ magnetic line source illumination. 3 GHz. | 83 |

|      |   |     |
|------|---|-----|
| 4.21 | A conventional Cassegrain antenna.  | 84  |
| 4.22 | Shaped dual-reflector with convex subreflector of the Example C1.   | 86  |
| 4.23 | Subreflector with the convex surface of the shaped dual-reflector Example C1.                             | 87  |
| 4.24 | Far-zone scattered fields from the subreflector of the conventional Cassegrain antenna. 10 GHz.           | 88  |
| 4.25 | Near-zone scattered field from the main reflector of the conventional Cassegrain reflector. 20 GHz.       | 89  |
| 4.26 | Far-zone scattered field from the convex subreflector of the shaped dual-reflector of Example C1. 20 GHz. | 92  |
| 4.27 | Near-zone scattered field from the main reflector of the shaped dual-reflector of Example C1. 20 GHz.     | 93  |
| 4.28 | Desired near-zone distribution of Example G4.   | 94  |
| 4.29 | Shaped dual-reflector of Example G4.  | 95  |
| 4.30 | Shaped subreflector and caustic of Example G4.  | 96  |
| 4.31 | Far-zone scattered fields from shaped subreflector of example G4. 20 GHz.                                 | 97  |
| 4.32 | Near-zone scattered fields from shaped main reflector of Example G4. 20 GHz.                              | 98  |
| 5.1  | Aperture edge taper due to feed-horn pattern and space attenuation.                                       | 100 |
| 5.2  | Variations of aperture field due to the interference between reflected and diffracted fields.             | 102 |
| 5.3  | Rolled edge modification of main reflector.   | 103 |
| 5.4  | Induced currents on main reflector with rolled edge modification.   | 105 |
| 5.5  | An elliptic rolled edge attached to the shaped main reflector.  | 107 |
| 5.6  | A blended rolled edge attached to the shaped main reflector.  | 110 |
| 5.7  | Definition of parameters for blending.  | 112 |



|      |   |     |
|------|---|-----|
| 5.8  | Illustration of three contributions from the physical optics integration.   | 116 |
| 5.9  | Surface current calculation for the case of shaped dual-reflector with concave subreflectors.                                     | 119 |
| 5.10 | Surface current calculation for the case of shaped dual reflector with convex subreflector.                                       | 123 |
| 5.11 | Shaped dual reflectors with blended rolled edge terminations for Example BL-1.  | 126 |
| 5.12 | Section of subreflector from which the reflected fields illuminate the blended main reflector in example BL-1.                    | 127 |
| 5.13 | Near-zone scattered fields from the blended main reflector of Example BL-1. 20 GHz, PO.   | 129 |
| 5.14 | Near-zone scattered fields from the blended main reflector of Example BL-1. PO with first order end point corrections.            | 130 |
| 5.15 | Near-zone scattered fields from blended main reflector of Example BL-1. PO fir first and second order end point corrections.      | 131 |
| 5.16 | Shaped dual reflectors with blended rolled edge terminations for Example BL-2.  | 133 |
| 5.17 | Section of subreflector from which the reflected fields illuminate the blended main reflector in Example BL-2.                    | 134 |
| 5.18 | Near-zone scattered fields from blended main reflector of Example BL-2. PO.   | 135 |
| 5.19 | Near-zone scattered fields from the blended main reflector of Example BL-2. PO with first order end point corrections.            | 136 |
| 5.20 | Near-zone scattered fields from the blended main reflector of Example BL-2. PO with first and second order end point corrections. | 137 |
| 5.21 | Shaped offset dual reflectors with blended rolled edges of Example BL-3.  | 140 |
| 5.22 | Near-zone scattered fields from the blended main reflector of Example BL-3 at 3 GHz. PO.  | 141 |

|      |   |     |
|------|---|-----|
| 5.23 | Near-zone scattered fields from the blended main reflector of Example BL-3 at 3 GHz. PO with first order end point corrections.             | 142 |
| 5.24 | Near-zone scattered fields from the blended main reflector of Example BL-3 at 3 GHz. PO with first and second order end point corrections.  | 143 |
| 5.25 | Near-zone scattered fields from blended main reflector of example BL-3 at 10 GHz. PO.   | 144 |
| 5.26 | Near-zone scattered fields from blended main reflector of Example BL=3 at 10 GHz. PO with first order end point corrections.                | 145 |
| 5.27 | Near-zone scattered fields from the blended main reflector of Example BL-3 at 10 GHz. PO with first and second order end point corrections. | 146 |
| 6.1  | Generating curve and axis of symmetry for surface of revolution.  | 148 |
| 6.2  | Geometry for defining parameters associated with a three-dimensional circular dual-reflector.   | 150 |
| 6.3  | Shaped dual-reflector of Example 3D1.   | 153 |
| 6.4  | Shaped dual-reflector of Example 3D1 obtained by the method of Narasimhan [20] and Ekelman [21].  | 154 |
| 6.5  | Shaped dual-reflector of Example 3D2.   | 156 |
| 6.6  | Shaped dual-reflector of Example 3D2 obtained by the method of Narasimham [20] and Ekelman [21].  | 157 |
| 6.7  | Shaped 3-dimensional circular symmetric dual-reflector from [11].   | 160 |
| 6.8  | Shaped dual-reflector of Example 3D3 obtained by the method of Narasimhan [23] and Ekelman [24].  | 161 |
| 6.9  | Shaped subreflector of Example 3D3 obtained by the method of Narasimhan [23] and Ekelman [24].  | 162 |
| 6.10 | Shaped dual-reflector of Example 3D3 obtained by the new approach.  | 163 |
| 6.11 | Shaped subreflector of Example 3D3 obtained by the new approach.  | 164 |
| A.1  | Geometry for direct application of principals of  |     |

|     |  |     |
|-----|--|-----|
|     | geometrical optics to dual-reflector shaping.                                  | 168 |
| A.2 | Snell's law on the subreflector.   | 170 |
| A.3 | Snell's law on the main reflector.   | 172 |
| B.1 | Geometry for analysis of $4a^2$ .  | 183 |
| C.1 | Geometrical optics reflected field from a hyperbolic subreflector.             | 193 |
| C.2 | Ray geometry of a Cassegrain reflector for calculation of reflected fields.    | 195 |
| C.3 | Geometrical optics reflected fields from an elliptic subreflector.             | 197 |
| C.4 | Ray geometry of Gregorian reflector for calculation of reflected fields.       | 199 |
| C.5 | Relation of initial points of shaped dual reflector with convex subreflector.  | 202 |
| C.6 | Relation of initial points of shaped dual reflector with concave subreflector. | 202 |

## CHAPTER I

### INTRODUCTION

The parabolic reflector antenna is the most useful and widely used antenna type for communications purposes at microwave frequencies. A parabolic reflector illuminated by a feed horn located at the focus of the parabola radiates a so-called "pencil beam" pattern which is a requirement for point-to-point communication. The other application of reflector antennas is in the field of radio astronomy. Normally, high gain and low noise temperature are required of the antenna for this application. The focus-fed parabolic reflector has limitations for large  $D/\lambda$  since the spillover from the feed is usually pointed toward ground which is a high noise temperature source. Consequently, dual-reflector antennas derived from the Cassegrain telescope have been used for high gain and low noise temperature purposes.

The parabolic reflector antenna with a feed at the focus preserves a fixed aperture distribution and thus, has a fixed radiation pattern when the feed pattern and the geometry of the reflector are given. The introduction of a second reflector in a dual-reflector system such as the Cassegrain antenna which consists of a hyperbolic subreflector and a parabolic main reflector or the Gregorian antenna which consists of an elliptic subreflector and a parabolic main reflector allows for more control over the aperture distribution of the main reflector. Although there is an extra degree of freedom provided by the addition of the

second reflector, the aperture distribution still possesses a certain amplitude taper which limits the performance of the antennas.

Recent developments in the technology of space communications require that the antenna gain be optimized; or that the power radiation pattern of the antenna illuminates an irregularly shaped target area, the so called "contour beam" antenna. For an antenna to have optimal gain, the illumination on the main reflector must be such that the resulting aperture distribution makes maximum use of the entire reflector surface. For an antenna to have a power radiation pattern that follows a prescribed function in the contour beam application, the aperture distribution must be specially designed. None of these are provided by the conventional prime focus fed parabolic reflector or dual-reflector such as the Cassegrain or Gregorian antennas.

Most recently, the reflector antenna is being used as a way to generate a plane wave which illuminates a target or antenna for measurement applications in indoor facilities. Electromagnetic measurements require that the antenna or scatterer under test be illuminated by a plane wave with a uniform amplitude distribution. In a compact range this is achieved approximately by a focused parabola. The non-uniform amplitude distribution caused by the taper of the feed-horn and the space attenuation limits the size of antenna or scatterer that can be measured.

In the past 20 years, considerable research has been conducted in the area of dual-reflector antenna shaping to provide the capabilities

that the conventional reflector antennas are not able to achieve. These capabilities include:

1. Maximize the illumination efficiency over the reflector aperture so that the antenna gain is optimized.
2. Maximize the spillover efficiency so that most of the microwave power radiates in the desired direction and the power radiated to the other directions are minimized in order to reduce the interference between adjacent antennas and antenna noise temperature.
3. Generate particular aperture distributions so that the radiation patterns of the antenna follow prescribed functions.
4. Generate a plane wave which has uniform amplitude and phase distributions over most of the aperture of a compact range reflector so that the size of antenna and scatterer under test can be increased.

A new approach of dual-reflector shaping is proposed and studied in this research. The main effort is limited to two-dimensional reflectors although the approach is demonstrated for three-dimensional shaping of a dual-reflector with circularly symmetric surfaces. This new approach is based on the geometrical properties of Cassegrain and Gregorian antennas. The shaped surface equations are formulated and solved numerically.

Most reflector analyses and designs are based on the principles of geometrical optics. The method of physical optics is also widely used to calculate the scattered fields from reflector surfaces. These

techniques are briefly reviewed in Chapter II. Also, the geometrical properties of conventional Cassegrain and Gregorian reflectors are addressed in this chapter.

Chapter III discusses the formulation for shaping of dual-reflector antennas when the primary source and required aperture distribution are given. This is the basis of this research. A set of algebraic equations are obtained. These equations have to be solved numerically. A numerical approximation for solving these equations is presented in the same chapter.

Several examples are presented in Chapter IV to validate the formulation and solution of the surface equations. A conventional Cassegrain or Gregorian reflector and feed pattern are assumed as a starting point, and then the reflectors are shaped to obtain a prescribed aperture distribution. The scattered fields of the subreflector and main reflector for both conventional and shaped dual-reflector antennas are calculated and presented for comparison.

One problem associated with compact range reflectors is the edge diffraction from the sharp terminations of the main reflector surface. This diffracted field enters the area where the antenna or scatterer are under test and interferes with the plane wave reflected from the reflector surface. This interference causes variations on both the amplitude and phase of the plane wave illuminating the target under test and reduces the accuracy of the measurements. The edge diffracted fields can be reduced by adding rolled edges [1,2] to the main reflector surface. This modification to the edges of the shaped main reflector is

discussed in Chapter V. Examples are also shown to illustrate the improvement of adding rolled edges. The scattered fields from the reflectors are calculated by the method of physical optics which results in false end-point contributions to the scattered fields. The method of correcting the end-point contributions [3,4] is also reviewed in the same chapter.

Chapter VI demonstrates the application of the shaping processes to three-dimensional circularly symmetric dual-reflectors that are illuminated by a primary source with a circularly symmetric power radiation pattern and thus the secondary aperture distribution of the reflector is also circularly symmetric.

A summary and conclusion of the study are given in Chapter VII. Suggestions for further studies are also addressed. Three appendices are included. Appendix A presents a direct application of the principles of geometrical optics to dual-reflector shaping. Appendix B provides the details of solving the surface equations which are formulated in Chapter III. Finally, Appendix C shows the calculation of the geometrical optics reflected fields for the conventional Cassegrain and Gregorian reflector antennas.



## CHAPTER II

### THEORETICAL TECHNIQUES

This chapter briefly reviews the techniques which are used in the analysis and synthesis of shaped dual-reflector antennas. The designs of microwave reflector antennas are basically based on the principles of geometrical optics. As to the pattern analysis of reflector antennas, there are many methods available such as Geometrical Theory of Diffraction (GTD) and Physical Optics (PO). In this study, the method of Geometrical Optics (GO) is used to calculate the incident fields and the induced surface currents on the reflector surfaces, and then, the method of Physical Optics is used to calculate the scattered fields from the reflector. These methods are briefly described in this chapter.

The method of synthesis of shaped dual-reflector antennas used in this research is based on the ray geometries of conventional Cassegrain and Gregorian dual-reflector antenna systems. The characteristics of the geometrical optics reflected rays of these antennas are reviewed.

Throughout this research, the electromagnetic field is assumed time harmonic, and the  $e^{j\omega t}$  time dependence is understood and suppressed. All the reflector surfaces are perfectly conducting and exist in free space.

## 2.1 Geometrical Optics

The electromagnetic field associated with the propagation of visible light is characterized by a very high frequency of the field or very small wavelength. A good first order approximation to the propagation of electromagnetic waves at very high frequencies may be obtained by neglecting the finiteness of the wavelength. The branch of optics which is characterized by the neglect of the wavelength is known as Geometrical Optics. Mathematically, Geometrical Optics is the leading term in the asymptotic high frequency solution of Maxwell's equations and is subjected to certain geometrical laws. An excellent reference to geometrical optics is the work by Born and Wolf [5]. Some basic properties of the geometrical optics field are

1. The time-averaged electric and magnetic energy densities are equal, and they are each equal to one half of the total stored energy density.
2. The average Poynting vector is in the direction of the normal to the geometrical wavefront, and its magnitude is equal to the product of the average energy density and the velocity  $v=c/n$  where  $c$  is the speed of light in free space, and  $n$  is the refractive index of the medium. In free space,  $n=1$  so that  $v=c$ .
3. Geometrical optics is a ray tracing technique in which geometrical rays are the family of directed curves perpendicular to the geometrical wavefront. Geometrical rays

also represent the direction of energy flow at every point. In a homogeneous medium, the geometrical rays are straight lines.

4. The geometrical optics field is a transverse electromagnetic field (TEM), i.e., the electric and magnetic field vectors at each point are orthogonal to each other and to the ray.
5. In a homogeneous medium the polarization of the geometrical optics field remains constant along a ray.
6. A ray optical field can be described in terms of an astigmatic ray tube as shown in Figure 2.1. The electric field at  $s$  associated with ray tube is given by

$$\vec{E}(s) = \vec{E}(0) A(\rho_1, \rho_2, s) e^{-jks} \quad (2.1)$$

in which  $\vec{E}(0)$  is the field at the reference 0,  $A(\rho_1, \rho_2, s)$  is the spread factor, and  $\rho_1, \rho_2$  are the radii of curvature of the geometrical wave front. The spread factor is given by

$$A(\rho_1, \rho_2, s) = \sqrt{\frac{\rho_1 \rho_2}{(\rho_1 + s)(\rho_2 + s)}} \quad (2.2)$$

which results from the conservation of energy along the ray. Equation (2.1) expresses the intensity law of geometrical optics. Since the geometrical optics field is TEM, the magnetic field must also follow these laws. If one of the radii of curvature is infinity as in the two-dimensional case, the spread factor reduces to

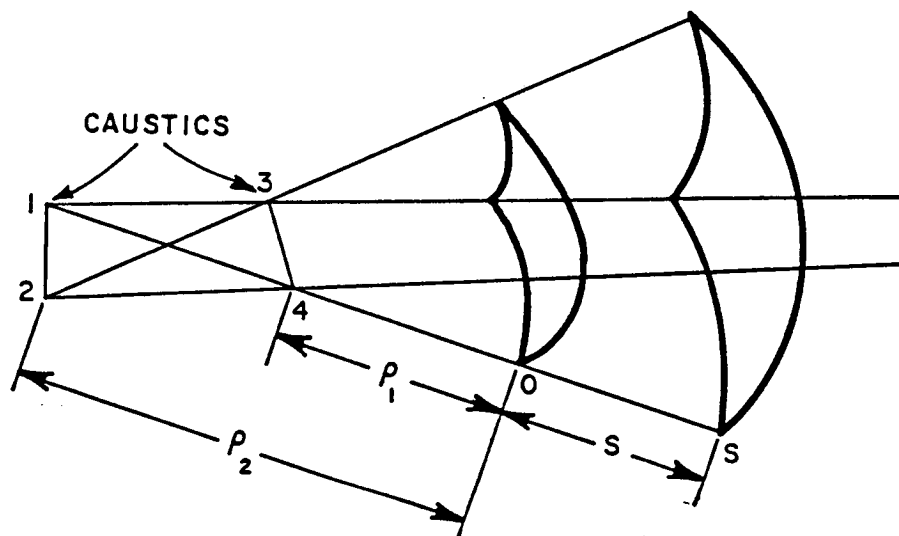


Figure 2.1. Astigmatic tube of rays.

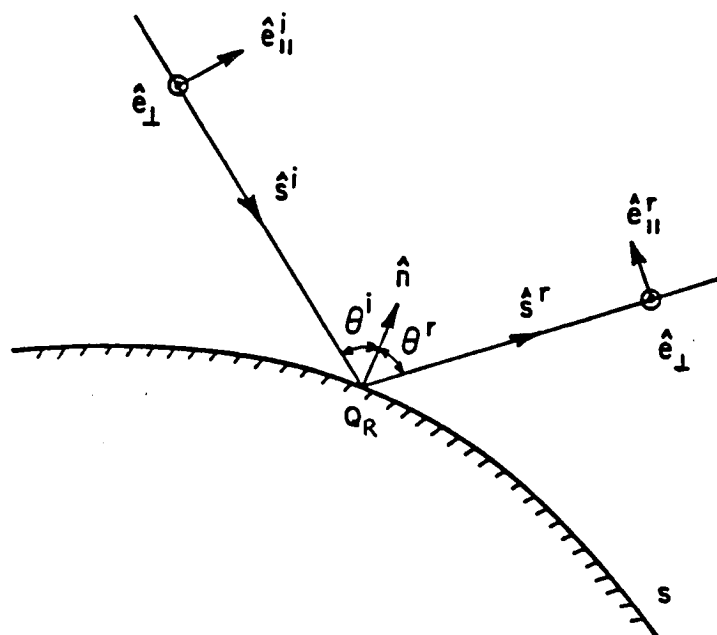


Figure 2.2. Geometry associated with the reflection by a surface S.

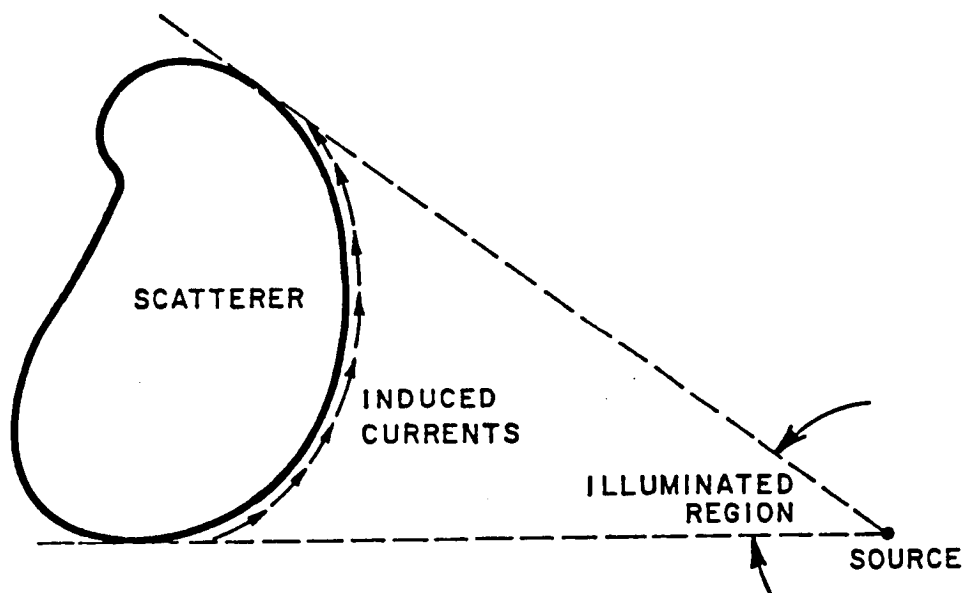


Figure 2.3. Induced surface current in the physical optics approximation.

$s$  = distance from reflection point to observation point and  $\rho_1^r, \rho_2^r$  are the principal radii of curvature of the reflected wavefront at the point of reflection  $Q_R$ . The unit vectors associated with the dyadic reflection coefficient are defined as

$\hat{e}_{||}^i$  = unit incident vector parallel to the plane of incidence and perpendicular to the incident ray

$\hat{e}_{||}^r$  = unit reflected vector parallel to the plane of incidence and perpendicular to the reflected ray

$\hat{e}_\perp$  = unit vector perpendicular to the plane of incidence where the plane of incidence is defined as the plane formed by the unit vectors  $\hat{s}^i$  and  $\hat{n}$  as shown in Figure 2.2.

The general expressions for  $\rho_1^r$  and  $\rho_2^r$  can be found in [6].

However, for some special surface geometries,  $\rho_1^r$  and  $\rho_2^r$  can be obtained numerically or directly from the properties of the surfaces. When one of the radii of curvature goes to infinity, as in the two-dimensional case, the reflected electric field becomes

$$\vec{E}^r(s) = \vec{E}^i(Q_R) \cdot \vec{R} \sqrt{\frac{\rho_1^r}{\rho_1^r + s}} e^{-jks} \quad (2.5)$$

For a two-dimensional surface which is infinitely long along the  $z$ -axis, the reflected electric field for a TE polarized incident wave (generated by a  $z$ -directed electric line source) is given by

$$\vec{E}^r(s) = E^r(s)\hat{z} = -\hat{z}E^i(Q_R) \sqrt{\frac{\rho_1^r}{\rho_1^r+s}} e^{-jks} \quad (2.6)$$

and the reflected magnetic field for a TM polarized incident wave (generated by a z-directed magnetic line source) is given by

$$\vec{H}^r(s) = H^r(s)\hat{z} = \hat{z}H^i(Q_R) \sqrt{\frac{\rho_1^r}{\rho_1^r+s}} e^{-jks} \quad (2.7)$$

One final note for the geometrical optics reflected field is that the law of reflection is satisfied; i.e., the angle of incident  $\theta^i$  and the angle of reflection  $\theta^r$  are equal, and the incident vector  $\hat{s}^i$ , the reflected vector  $\hat{s}^r$  and the surface normal  $\hat{n}$  are co-planar.

### 2.3 Physical Optics

Physical optics (PO) is also a high frequency method which uses the integral equation representation, along with the physically reasonable high frequency assumption that the scattered field from one point on a body to any other point is insignificant compared to the incident field strength. This method is based on the approximation of Stratton-Chu Equations for the scattered field [7] and states that for scattering from a perfectly conducting body in free space, the scattered fields are given by

$$\vec{E}^s = -jk_0 Z_0 \int_S \left[ \vec{J}_s \psi + \frac{1}{k^2} (\vec{J}_s \cdot \nabla) \nabla \psi \right] ds \quad (2.8)$$

and

$$\vec{H}^s = \int_S (\vec{J}_s \times \nabla \psi) ds. \quad (2.9)$$

Note that  $\psi$  is the free space Green's function, and  $\vec{J}_s$  is the induced surface current on the scatterer surface as shown in Figure 2.3. In general, the induced surface current  $\vec{J}_s$  is given by

$$\vec{J}_s = \hat{n} \times \vec{H}^{TOTAL} = \hat{n} \times (\vec{H}^i + \vec{H}^s) \quad (2.10)$$

in which  $\vec{H}^{TOTAL}$  is the total magnetic field on the surface of the scatterer,  $\vec{H}^i$  is the incident magnetic field on the surface, and  $\hat{n}$  is the surface normal. Substituting Equation (2.10) into Equations (2.8) and (2.9), it is apparent that the unknown field  $\vec{H}^s$  appears on both sides of the equation so that a coupled set of integral equations is obtained. Although one can solve  $\vec{H}^s$  by the Method of Moments, it is very tedious and inefficient since the size of the scatterers is usually very large in terms of a wavelength in the high frequency region. Consequently, from the boundary conditions at the perfectly conducting surface, one obtains that

$$\hat{n} \times \vec{H}^i = \hat{n} \times \vec{H}^s \text{ on surface } S.$$

The induced surface currents are approximated by



$$\vec{J}_s = \begin{cases} 2 \hat{n} \times \vec{H}^i & \text{on the lit side} \\ 0 & \text{on the shadow side} \end{cases} \quad (2.11)$$

and the scattered fields  $\vec{E}^s$  and  $\vec{H}^s$  can be calculated by Equations (2.8) and (2.9). This is the so-called "physical optics" approximation. The approximation to the induced surface currents are valid when the transverse dimensions of the surface, the radii of curvature of the surface, and the radii of curvature of the incident wave front are all much larger than a wavelength.

For the three-dimensional case, the free space Green's function is  $\frac{e^{-jkr}}{4\pi r}$  where  $r$  is the distance from the source point to the field point and when  $r \gg \lambda$ , Equations (2.8) and (2.9) become

$$\vec{E}^s = - \frac{j k_0 Z_0}{4\pi} \int_S \left[ \vec{J}_s - (\vec{J}_s \cdot \hat{r}) \hat{r} \right] \frac{e^{-jkr}}{r} ds \quad (2.12)$$

and

$$\vec{H}^s = \frac{1}{4\pi} \int_S \vec{J}_s \times \nabla \left( \frac{e^{-jkr}}{r} \right) ds. \quad (2.13)$$

For the two-dimensional case, the free space Green's function is  $\frac{1}{4j} H_0^{(2)}(k\rho)$  where  $H_0^{(2)}(k\rho)$  is the zero<sup>th</sup> order Hankel function of the 2<sup>nd</sup> kind, and the surface integral in Equations (2.8) and (2.9) should be replaced by a line integral. There are two polarizations in the two-dimensional problem, one is the Transverse Electric (TE) case, and the other is the Transverse Magnetic (TM) case. In the TE case, the

incident fields are generated by an electric line source along the z-axis; while in the TM case, the incident field is generated by a magnetic line source along the z-axis.

For an electric line source, the incident electric field is  $\vec{E}^i = \hat{z} E_z^i$  and the incident magnetic field is  $\vec{H}^i = \hat{\phi} H_\phi^i$  as shown in Figure 2.4. The physical optics induced surface current  $\vec{J}_s$  is given by

$$\vec{J}_s = 2 \hat{n} \times \vec{H}^i = 2 \hat{n} \times \hat{\phi} H_\phi^i = \hat{z} C H_\phi^i = \hat{z} J_z. \quad (2.14)$$

Thus, from Equation (2.8) with the surface integral replaced by a line integral, one finds that

$$\vec{E}^s = \hat{z} E_z^s = -jk_o Z_o \int_{\text{over illuminated region}} \hat{z} J_z \psi + \frac{1}{k^2} (J_z \hat{z} \cdot \nabla) \nabla \psi dl \quad (2.15)$$

But  $\frac{1}{k^2} (J_z \hat{z} \cdot \nabla) \nabla \psi = 0$  since there is no variation along z-axis, i.e.,

$$\frac{\partial}{\partial z} = 0, \text{ thus}$$

$$E_z^s = -jk_o Z_o \int J_z \cdot \frac{1}{4j} H_o^{(2)}(k\rho) dl = -\frac{k_o Z_o}{4} \int J_z H_o^{(2)}(k\rho) dl \quad (2.16)$$

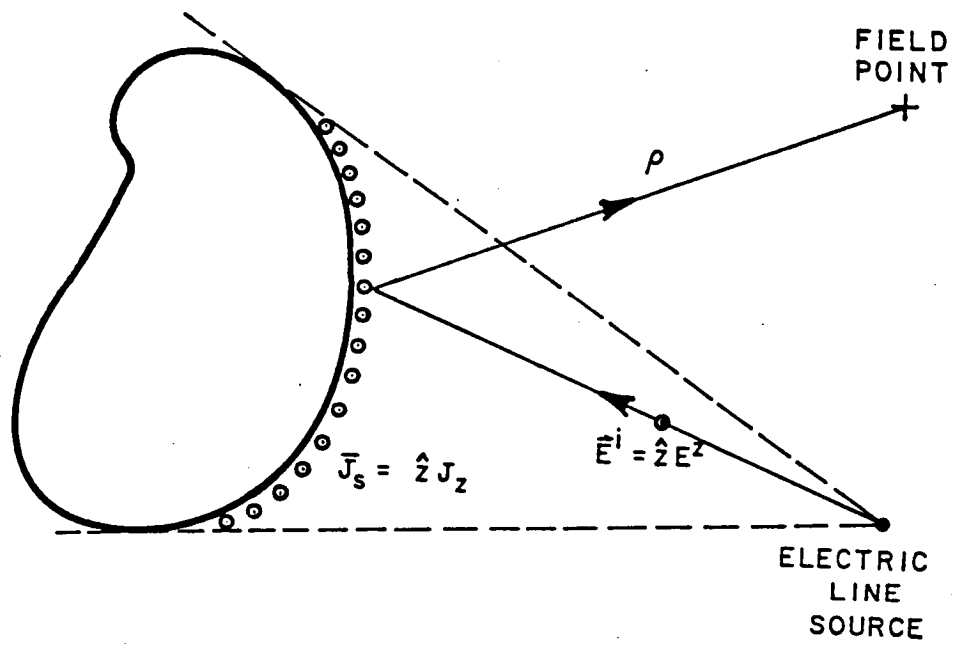


Figure 2.4. TE incidence in two-dimensional case.

For a magnetic line source, the incident magnetic field is  $\vec{H}^i = \hat{z} H_z$ ; thus, the induced surface current on the lit side is given as

$$\vec{J}_s = 2(\hat{n} \times \vec{H}^i)$$

$$\vec{J}_s = 2(\hat{n} \times \hat{z} H_z) = \hat{l} C H_z$$

or

$$\vec{J}_s = \hat{l} J_1 \quad (2.17)$$

where  $\hat{l}$  is the unit tangent vector along the surface of the scatterer as shown in Figure 2.5. The scattered magnetic field is then given by

$$\vec{H}^s = \int_l \hat{l} J_1 \times \nabla \psi \, dl \quad (2.18)$$

in which

$$\nabla \psi = \left( \hat{\rho} \frac{\partial}{\partial \rho} + \hat{\phi} \frac{1}{\rho} \frac{\partial}{\partial \phi} \right) \frac{1}{4j} H_0^{(2)}(k\rho)$$

$$\nabla \psi = + \frac{k}{4j} \hat{\rho} \frac{d}{d(k\rho)} H_0^{(2)}(k\rho)$$

$$\nabla \psi = + \frac{k}{4j} \hat{\rho} \left( -H_1^{(2)}(k\rho) \right)$$

or

$$\nabla \psi = - \frac{k}{4j} \hat{\rho} H_1^{(2)}(k\rho)$$

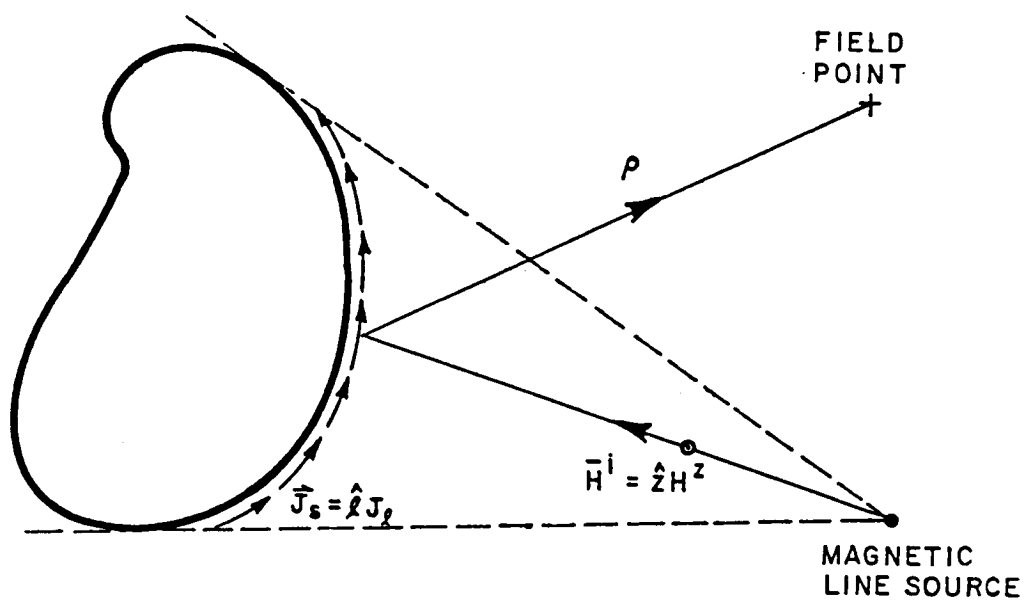


Figure 2.5. TM incidence in two-dimensional case.

Consequently, one obtains

$$\vec{H}^S = - \int_l J_l \hat{l} \times \left( + \frac{k}{4j} \hat{\rho} H_1^{(2)}(k\rho) \right) dl$$

or

$$\vec{H}^S = - \frac{k}{4j} \int (\hat{l} \times \hat{\rho}) J_l H_1^{(2)}(k\rho) dl \quad (2.19)$$

and the scattered magnetic field is given by

$$\vec{H}^S = \hat{z} H_z^S = - \frac{k}{4j} \hat{z} \int \hat{z} \cdot (\hat{l} \times \hat{\rho}) J_l H_1^{(2)}(k\rho) dl. \quad (2.20)$$

When the observation point is in the far-zone of the induced current the large argument approximation of the Hankel function can be used and Equations (2.16) and (2.20) become

$$E_z^S = - Z_o \sqrt{\frac{k_o}{8\pi}} e^{j\pi/4} \int_{lit} J_z \frac{e^{-jk\rho}}{\sqrt{\rho}} dl \quad (2.21)$$

$$H_z^S = - \sqrt{\frac{k_o}{8\pi}} e^{j\pi/4} \int_{lit} \hat{z} \cdot (\hat{l} \times \hat{\rho}) J_l \frac{e^{-jk\rho}}{\sqrt{\rho}} dl \quad (2.22)$$

These two equations are used in this research to calculate the scattered fields from the shaped reflector antennas.

#### 2.4 Conventional Cassegrain Reflector Antenna

The conventional Cassegrain reflector antenna is a two-reflector antenna which is designed in the form of a hyperbolic subreflector and a parabolic main reflector based on the principle of the Cassegrain optical telescope [8]. The geometry of the Cassegrain system is shown in Figure 2.6. The feed of the antenna is usually located at the real focal point of the hyperbolic surface while the focus of the main reflector is matched with the virtual focal point of the hyperbolic surface in a focused system. The surface of the subreflector can be described by

$$x = a \sqrt{1 + \left(\frac{y}{b}\right)^2} + \frac{F_c}{2} \quad (2.23)$$

and the surface of the parabolic main reflector by

$$x = \frac{y^2}{4F_m} - (F_m - F_c). \quad (2.24)$$

The various parameters associated with the reflector surface are defined below:

$F_c$  = distance between the two focii of the hyperbolic surface

$F$  = distance between the real focus and the vertex of the  
hyperbolic reflector

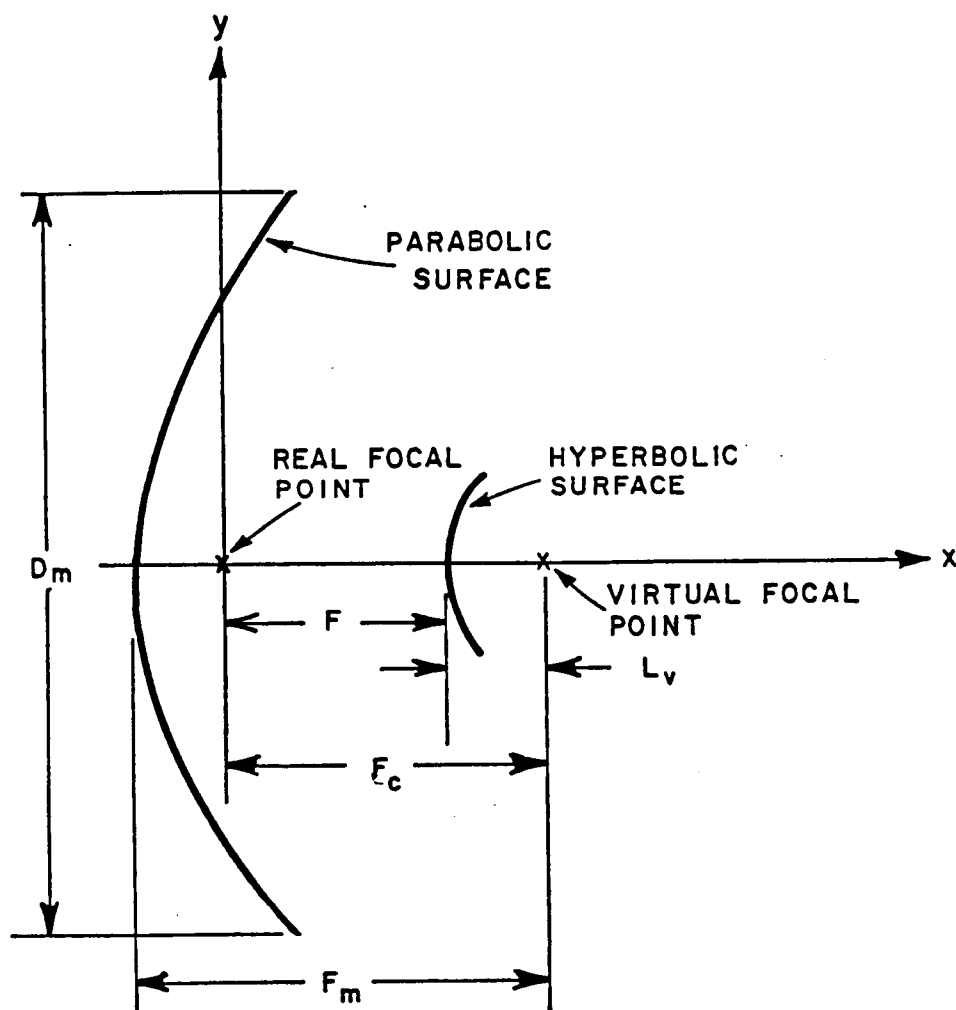


Figure 2.6. Geometry of the Cassegrain antenna system.



$L_v = F_c - F$  = distance between the virtual focus and the vertex of the hyperbolic surface

$e$  = eccentricity of the hyperbolic surface =  $\frac{F_c}{F_c - 2L_v}$

$2a$  = length of the transverse axis of the hyperbolic surface =  $F_c/e$

$2b$  = length of the conjugate axis of the hyperbolic surface

$$= a \sqrt{e^2 - 1}$$

Pattern analyses of the Cassegrain antenna have been well established such as the one in [9]. One can refer to this reference for more detail. However, the behavior of the reflected rays from the subreflector and main reflector will be summarized here. For a focused hyperbolic surface illuminated by a source located at the real focus, the reflected rays from the surface appear to emanate from the virtual focus. Thus, the reflected field caustic distance is equal to the distance between the virtual focus and the point of reflection on the subreflector. The reflected rays from the main reflector are then parallel to the reflector axis since the incident rays radiate from the virtual focus of the subreflector; i.e., the focus of the parabola. The ray geometry is given in Figure 2.7. This phenomenon is the basis for the dual-reflector shaping of this research.

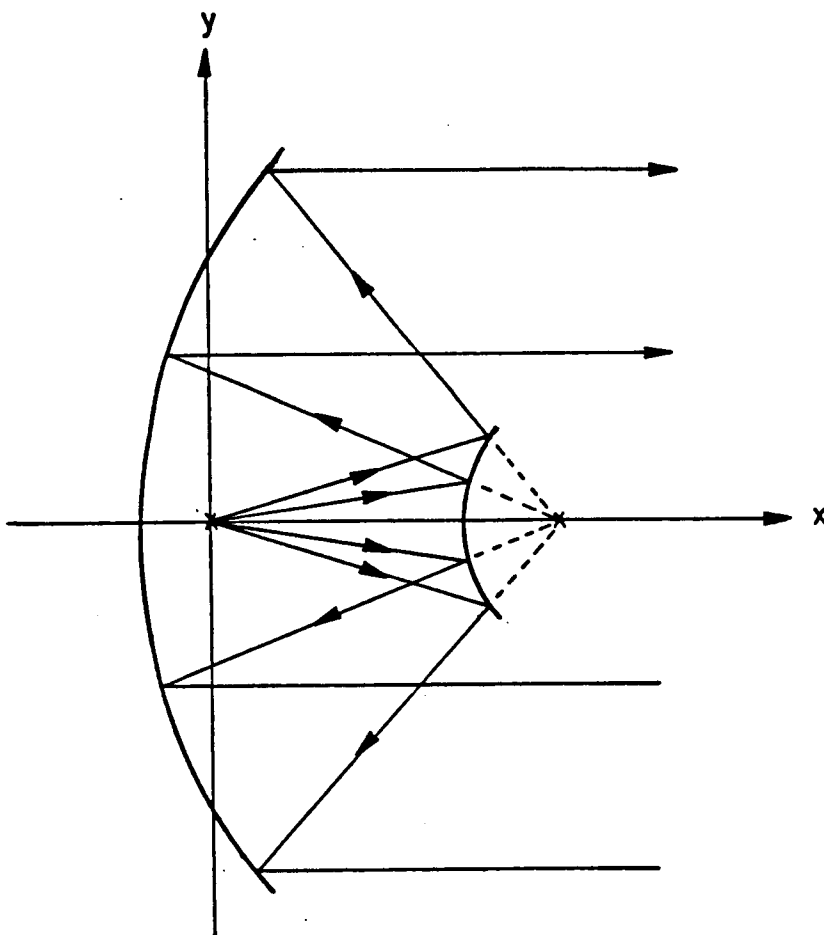


Figure 2.7. Ray geometry of the Cassegrain antenna system.

## 2.5 Conventional Gregorian Reflector Antenna

Similar to the Cassegrain reflector antenna, the Gregorian antenna is also a two-reflector system but, instead of the hyperbolic subreflector, the subreflector is an elliptical two-dimensional surface and the focus of the main reflector lies between the two reflectors as shown in Figure 2.8. The elliptic surface has two focii and the focus of the main reflector is usually matched with focal point #2 while the primary feed is located at focal point #1 in the focused case. The surface of the elliptic subreflector can be described by

$$x = a \sqrt{1 - \frac{y^2}{b^2}} + \frac{F_c}{2} \quad (2.25)$$

and the equation for the surface of the main reflector is the same as Equation (2.24). The parameters of the antenna are

$F_c$  = distance between the two focii of the elliptic surface

$F$  = distance between focal point #1 and the vertex of the elliptic reflector

$$L_v = F_c - F$$

$$e = \text{eccentricity} = \frac{F_c}{F_c - 2L_v}$$

$$2a = \text{length of the major axis of the elliptic surface} = F_c / e$$

$$2b = \text{length of the minor axis of the elliptic surface} = a \sqrt{1 - e^2}.$$

Note that  $F_c < F$  so that  $L_v$  is negative and  $e < 1$ .

The ray geometry of the Gregorian antenna is shown in Figure 2.9. When illuminated by a source located at focal point #1, the reflected rays from the elliptic subreflector pass through focal point #2 and the reflected rays from the main reflector are again parallel to the reflector axis since the incident rays emanate from focal point #2. The caustic distance of the reflected ray from the subreflector is the distance between focal point #2 and the point of reflection on the subreflector surface. However, this caustic distance is negative since the reflected rays pass through it.

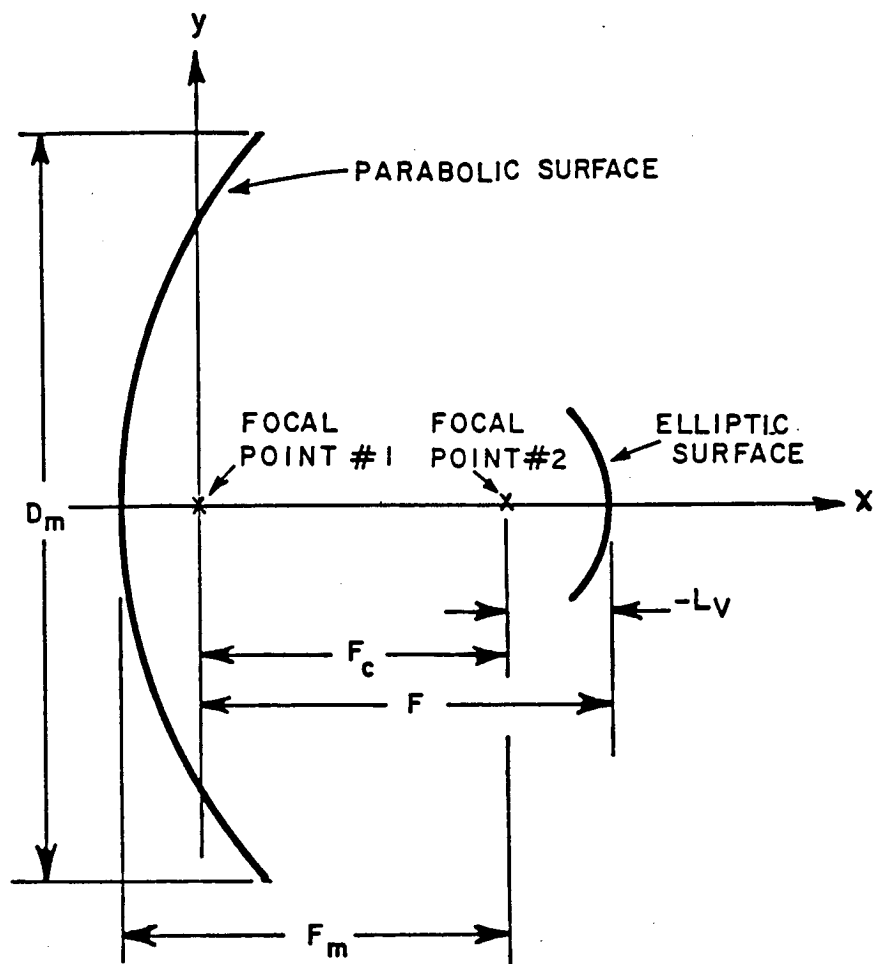


Figure 2.8. Geometry of the Gregorian antenna system.

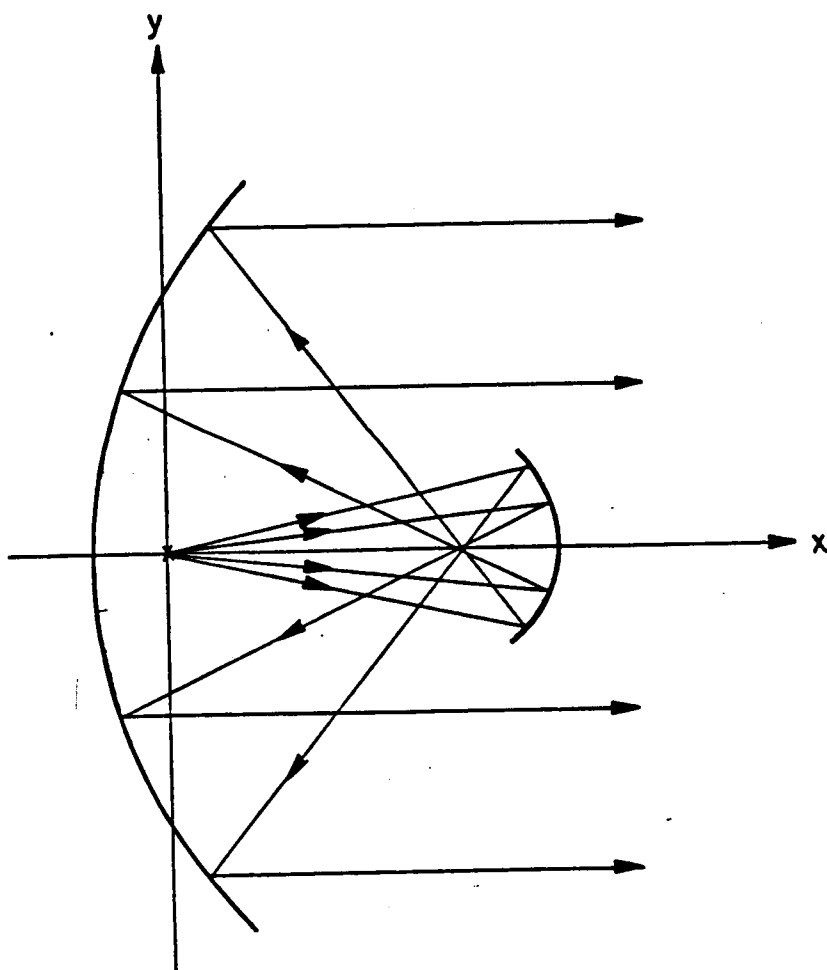


Figure 2.9. Ray geometry of the Gregorian antenna system.

## CHAPTER III

### SYNTHESIS OF TWO-DIMENSIONAL DUAL-REFLECTOR ANTENNAS

#### 3.1 Introduction

The design of dual-reflector antennas, including the conventional Cassegrain parabola-hyperbola and Gregorian parabola-ellipse antennas, are all based on the principles of geometrical optics. Since geometrical optics is a high frequency method, the reflectors must be large and have a large radius of curvature compared to the wavelength. The principles of geometrical optics state that:

1. Snell's law [10] must be satisfied at each reflector, that is, the incident ray, the reflected ray, and the surface normal at the reflection point on each reflector must be coplanar, and the angles of incidence and reflection are equal.
2. Power flow along each differential tube of rays remains constant, even when the tube undergoes a number of reflections (conservation of power [11]).
3. Ray directions are normal to the surface of constant phase, and this condition is maintained after a number of reflections (theorem of Malus [12]).

Conventional Cassegrain and Gregorian reflector antennas are two examples which satisfy the above principles. The geometries of these two antennas are shown in Figures 2.6 and 2.8 of the previous chapter. As discussed previously, with the source which has a spherical wavefront (or cylindrical wavefront for the two-dimensional case) and is located at focus #1, the reflected rays from the subreflector which satisfy Snell's law of reflection appear to emanate from the second focus and also have a spherical wavefront (or a cylindrical wavefront). Since the second focus is also the focus of the parabolic main reflector, the reflected rays from the parabola which also satisfy law of reflection form a uniform plane wave and are parallel to the axis of parabola. It can be shown that the power contained in the ray tubes before and after reflection are equal in order to satisfy the law of power conservation. Also, the incident and reflected rays from each reflector are normal to their corresponding wavefront.

In general, the geometrical optics designs of dual-reflector antennas must satisfy the above principles either mathematically or physically. Galindo [13] and Kinber [14] used these principles to set up two first-order ordinary differential equations which can be solved exactly, if possible, or numerically to obtain a couple of circularly symmetric reflectors for realizing a prespecified aperture amplitude distribution. Green [15] and Williams [16] also used these principles to design the subreflector and then correct the main reflector to achieve the desired uniform phase criterion at the aperture plane of main reflector. A direct application of principles of geometrical



optics in dual-reflector antenna shaping is given by [17] and is discussed in Appendix A. For offset dual-reflector antennas, these principles are again used to obtain partial differential equations which are then solved numerically to obtain the surfaces [18,19,20]. Westcott [21] used complex coordinates to set up a Monge-Ampère type partial differential equation, and solved this equation as a boundary value problem to synthesize a dual-reflector antenna. He also used the same approach to synthesize a single reflector for relating a given feed pattern to a prescribed far-zone pattern. In the following section, a new approach which is based on the knowledge of ray behavior of the conventional Cassegrain and Gregorian antennas is presented. Instead of setting up differential equations or heuristically designing the subreflectors, a set of nonlinear algebraic equations are obtained and solved numerically to obtain the surfaces. Also the caustics of the reflected rays from the subreflector can be obtained and examined.

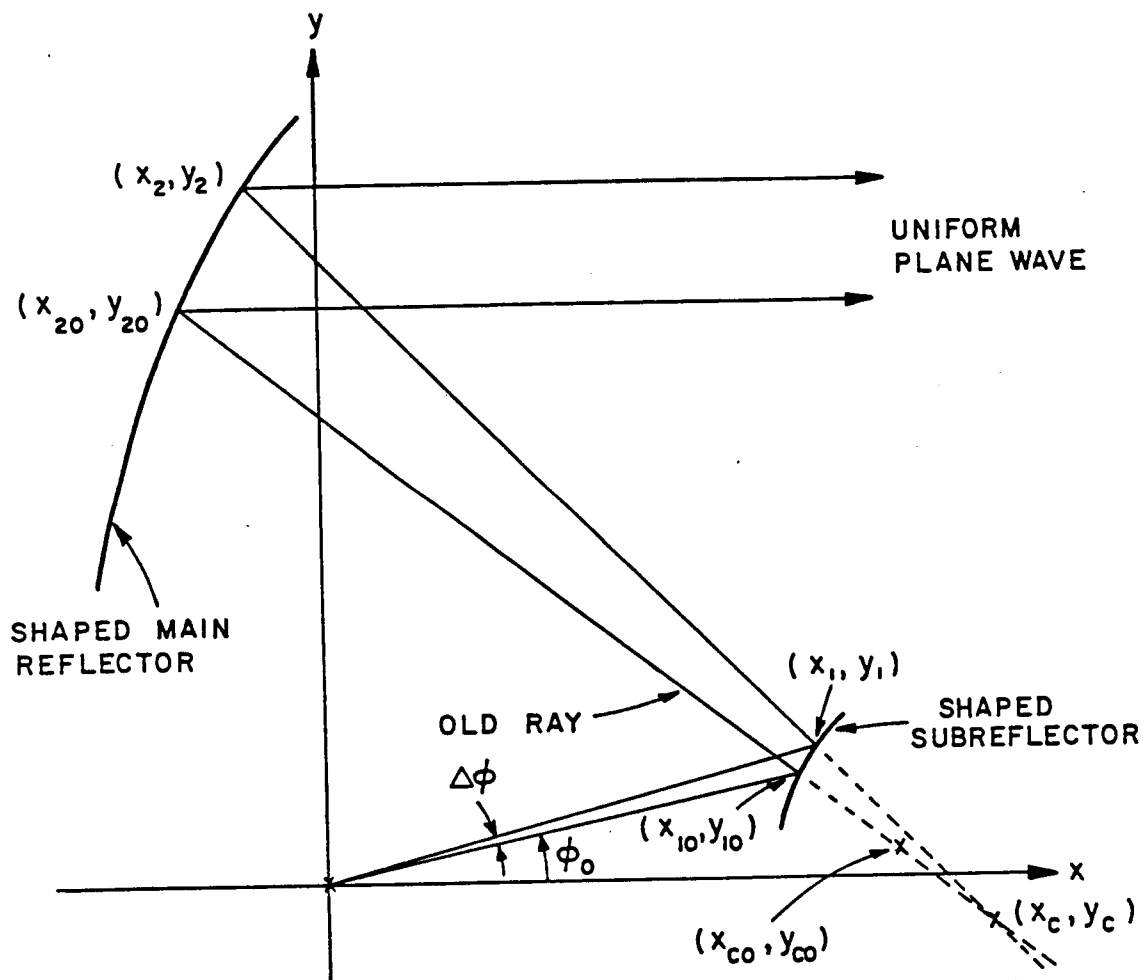
### 3.2 Method of Synthesis

As discussed in the previous section, a focus-fed Cassegrain or Gregorian reflector antenna will generate a uniform plane wave on the aperture plane of the main reflector. However, for a given primary source, the amplitude distribution of the aperture field preserves a certain amplitude taper which is fixed when the source and the parameters of the reflector surfaces are specified. From geometrical optics, it is known that the amplitude of the reflected field is dependent on the space spread factor or the location of the caustic of

the reflected wavefront. In order to realize a given aperture amplitude distribution for a given primary source, the incident rays on the main reflector which are also the reflected rays from the subreflector have to be different from those for the conventional Cassegrain and Gregorian reflectors. Also, in order to generate a uniform plane wave, the main reflector locally must have the properties of a pure parabola with its axis parallel to the ray direction of the desired plane wave. Since the caustic of the reflected ray from the subreflector is also the focus of the main reflector, this caustic will not be a fixed point as in the conventional Cassegrain and Gregorian antennas so that the amplitude distribution of the aperture field can be controlled by moving the caustic for each ray reflected from the subreflector. The formulation of this synthesis method will be discussed in detail in this section for two-dimensional reflectors. The general geometries are given in Figure 3.1 for both concave and convex subreflectors. The coordinate origin is assumed at the point where the primary source is located. Although these formulations are basically for two-dimensional geometries, they can be easily modified for shaping of three-dimensional dual-reflector antennas with circular symmetry.

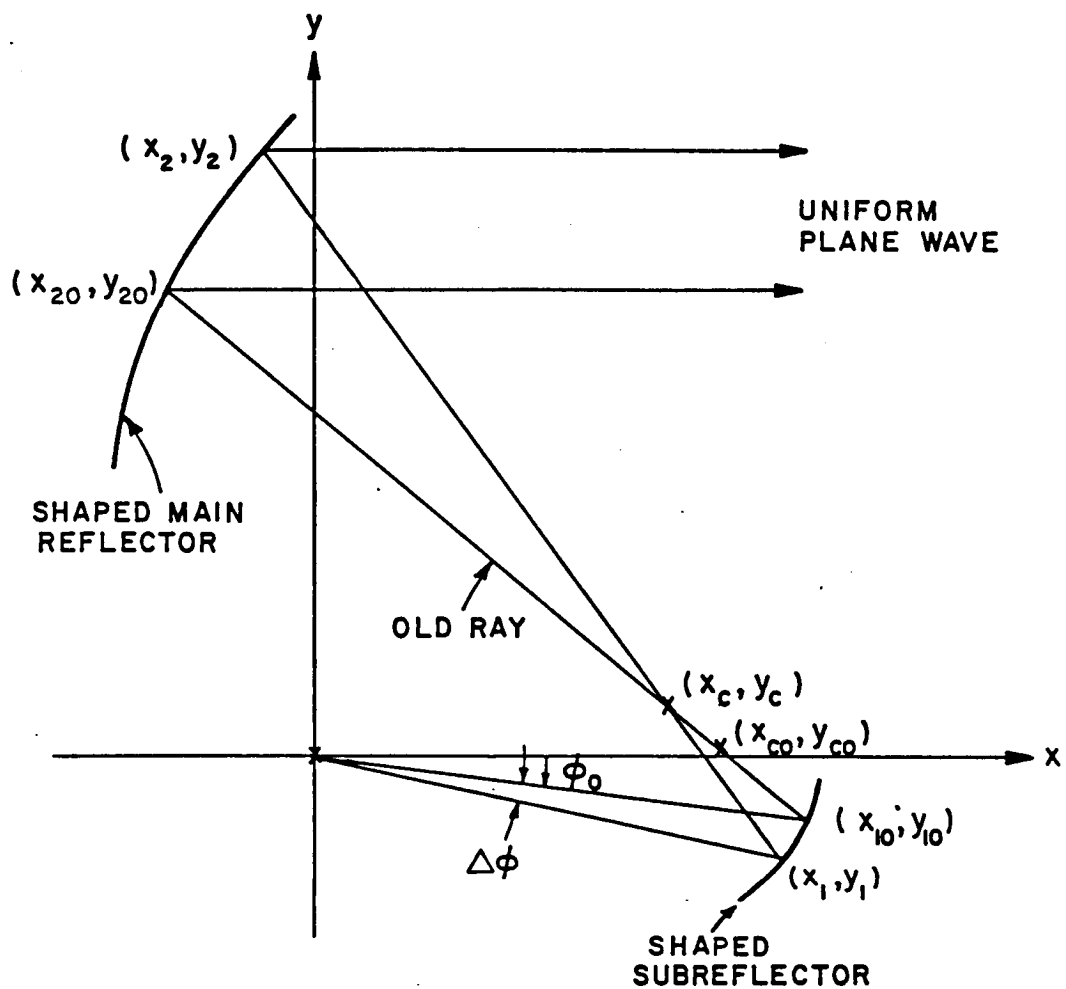
The basic idea is that for a differential tube of rays emanating from the primary source, the subreflector section between the intersection of the incident ray tube and the subreflector (i.e., the surface between  $(x_{10}, y_{10})$  and  $(x_1, y_1)$ ) is assumed to be either a hyperbola or an ellipse with the two foci at the coordinate origin and the caustic point  $(x_c, y_c)$ . The corresponding section on the main

reflector (i.e, the surface between  $(x_{20}, y_{20})$  and  $(x_2, y_2)$ ) is assumed to be a perfect parabola with focus at  $(x_c, y_c)$ . Also shown in Figure 3.1 is  $(x_{co}, y_{co})$  which is the caustic of the previous reflected ray tube. Based on these assumptions, one can set up a set of equations and solve these equations to obtain a solution of  $(x_c, y_c)$ ,  $(x_1, y_1)$  and  $(x_2, y_2)$ . These solutions will be accurate as long as the width of the incident ray tube from the primary source is small. The formulations for the surface are given below. Note that the "old" ray in Figure 3.1 is assumed to be known; i.e.,  $(x_{10}, y_{10})$ ,  $(x_{20}, y_{20})$  and  $(x_{co}, y_{co})$  are known.



(a) Convex subreflector

Figure 3.1. Geometry of shaped dual-reflector.



(b) Concave subreflector

Figure 3.1. Continued.

### 3.2.1. Formulation

#### A. Subreflector

The canonic form of a hyperbola as shown in Figure 3.2 can be written as

$$\frac{x^2}{a^2} - \frac{y^2}{b^2} = 1$$

where  $2a$  is the transverse axial length,  $2b$  is the conjugate axial length, and  $b$  is related to  $a$  by

$$b^2 = \frac{F_c^2 - 4a^2}{4} .$$

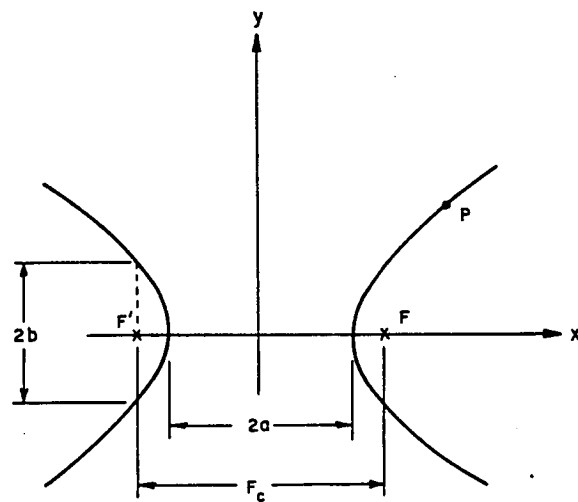
Note that  $F_c$  is the distance between the two foci  $F'$  and  $F$ , and

$$2a = \overline{F'P} - \overline{FP} .$$

The canonic form of an ellipse as shown in Figure 3.2 can be written as

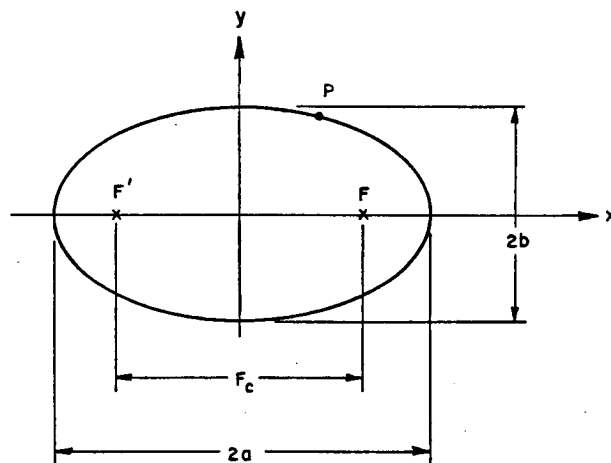
$$\frac{x^2}{a^2} + \frac{y^2}{b^2} = 1$$

where  $2a$  is the major axial length,  $2b$  is the minor axial length. The axial length can be related by



HYPERBOLA :  $\frac{x^2}{a^2} - \frac{y^2}{b^2} = 1$

(a) hyperbola



ELLIPSE :  $\frac{x^2}{a^2} + \frac{y^2}{b^2} = 1$

(b) ellipse

Figure 3.2. Canonic form of hyperbola and ellipse.

$$b^2 = \frac{4a^2 - F_c^2}{4} = - \frac{F_c^2 - 4a^2}{4} .$$

Also, one finds that

$$2a = \overline{F'P} + \overline{FP}$$

By observing that  $b^2$  in both the concave and convex cases has the same expression except for the sign, one can write, in general, the surface as

$$\frac{x^2}{a^2} - \frac{y^2}{b^2} = 1$$

where  $b^2 < 0$  for an ellipse

$b^2 > 0$  for a hyperbola

$2a = \overline{F'P} + \overline{FP}$  for an ellipse, and

$2a = \overline{F'P} - \overline{FP}$  for a hyperbola

From these canonic forms for the hyperbola and the ellipse, the shaped subreflector section between  $(x_{10}, y_{10})$  and  $(x_1, y_1)$  which is assumed to be a hyperbola or an ellipse can be formulated by proper rotation and translation of the corresponding canonic form. As shown in Figure 3.3, the distance  $F_c$  between the two focii for this section is





given by

$$F_c = (x_c^2 + y_c^2)^{1/2}.$$

The transverse axial length is given by

$$2a = \left\{ (x_{10}^2 + y_{10}^2)^{1/2} \pm \left[ (x_{10} - x_c)^2 + (y_{10} - y_c)^2 \right]^{1/2} \right\} \quad \begin{array}{l} +: \text{ ellipse} \\ -: \text{ hyperbola} \end{array}$$

where  $(x_{10}, y_{10})$  is assumed to be known a priori. The subreflector surface section is then defined by

$$\left( \frac{x''}{a} \right)^2 - \left( \frac{y''}{b} \right)^2 = 1$$

but  $x'' = x' \cos \theta + y' \sin \theta$  and  $y'' = -x' \sin \theta + y' \cos \theta$ .

Then,  $x'$  and  $y'$  are related to  $x$  and  $y$  as

$$x' = x - \frac{x_c}{2}$$

and

$$y' = y - \frac{y_c}{2}.$$

The surface in the  $x$ - $y$  coordinate is given by

$$\frac{1}{a^2} \left\{ \left( x - \frac{x_c}{2} \right) \cos\theta + \left( y - \frac{y_c}{2} \right) \sin\theta \right\}^2 - \frac{1}{b^2} \left\{ - \left( x - \frac{x_c}{2} \right) \sin\theta + \left( y - \frac{y_c}{2} \right) \cos\theta \right\}^2 = 1$$

which can be further simplified to

$$\frac{1}{a^2} \left\{ x \cos\theta + y \sin\theta - \frac{F_c}{2} \right\}^2 - \frac{4}{F_c^2 - 4a^2} \left\{ x \sin\theta - y \cos\theta \right\}^2 = 1$$

since  $F_c \cos\theta = x_c$  and  $F_c \sin\theta = y_c$ .

The unknown subreflector surface point  $(x_1, y_1)$  must thus satisfy the following equation:

$$\frac{1}{a^2} \left( x_1 \cos\theta + y_1 \sin\theta - \frac{F_c}{2} \right)^2 - \frac{4}{F_c^2 - 4a^2} \left( x_1 \sin\theta - y_1 \cos\theta \right)^2 = 1 \quad (3.1)$$

where

$$F_c^2 = (x_c^2 + y_c^2)$$

$$4a^2 = \left\{ (x_{10}^2 + y_{10}^2)^{\frac{1}{2}} \pm \left[ (x_{10} - x_c)^2 + (y_{10} - y_c)^2 \right]^{\frac{1}{2}} \right\}^2, \quad \begin{array}{l} +: \text{ ellipse} \\ -: \text{ hyperbola} \end{array}$$

and

$$\theta = \tan^{-1} \left( \frac{y_c}{x_c} \right).$$

## B. Main Reflector

The canonic form of a parabola, as shown in Figure 3.4 can be described as

$$x = \frac{y^2}{4F}$$

where  $F$  is the focal length of the parabola and can be expressed as

$$F = \frac{1}{2} (1 - \cos \alpha) \rho .$$

Now, by assuming that  $(x_{20}, y_{20})$  and  $(x_2, y_2)$  form a parabola with the focus at  $(x_c, y_c)$  as shown in Figure 3.5, the following expression is obtained to describe the main reflector surface:

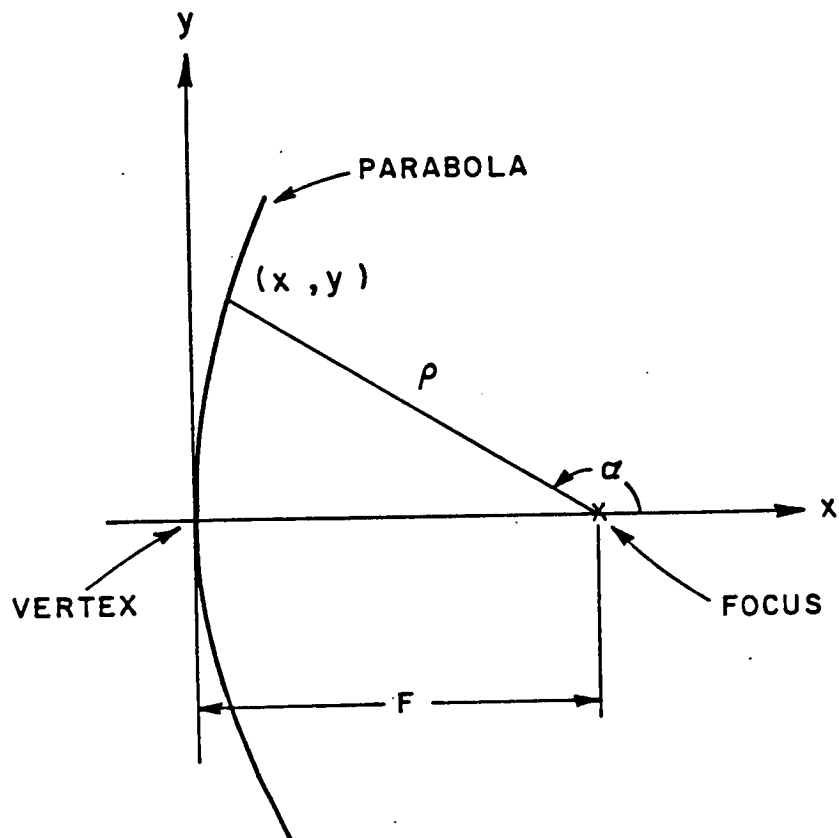
$$x - (x_c - F) = \frac{1}{4F} (y - y_c)^2$$

where

$$F = \frac{1}{2} (1 - \cos \alpha) \rho$$

or

$$F = \begin{cases} \frac{1}{2} (1 - \sec \alpha_o) (x_c - x_{20}) & \text{if } x_c \neq x_{20} \\ \frac{1}{2} \frac{1 - \cos \alpha_o}{\sin \alpha_o} (y_c - y_{20}) & \text{if } y_c \neq y_{20} \end{cases}$$



PARABOLA :  $x = \frac{y^2}{4F}$

Figure 3.4. Canonic form of parabola.

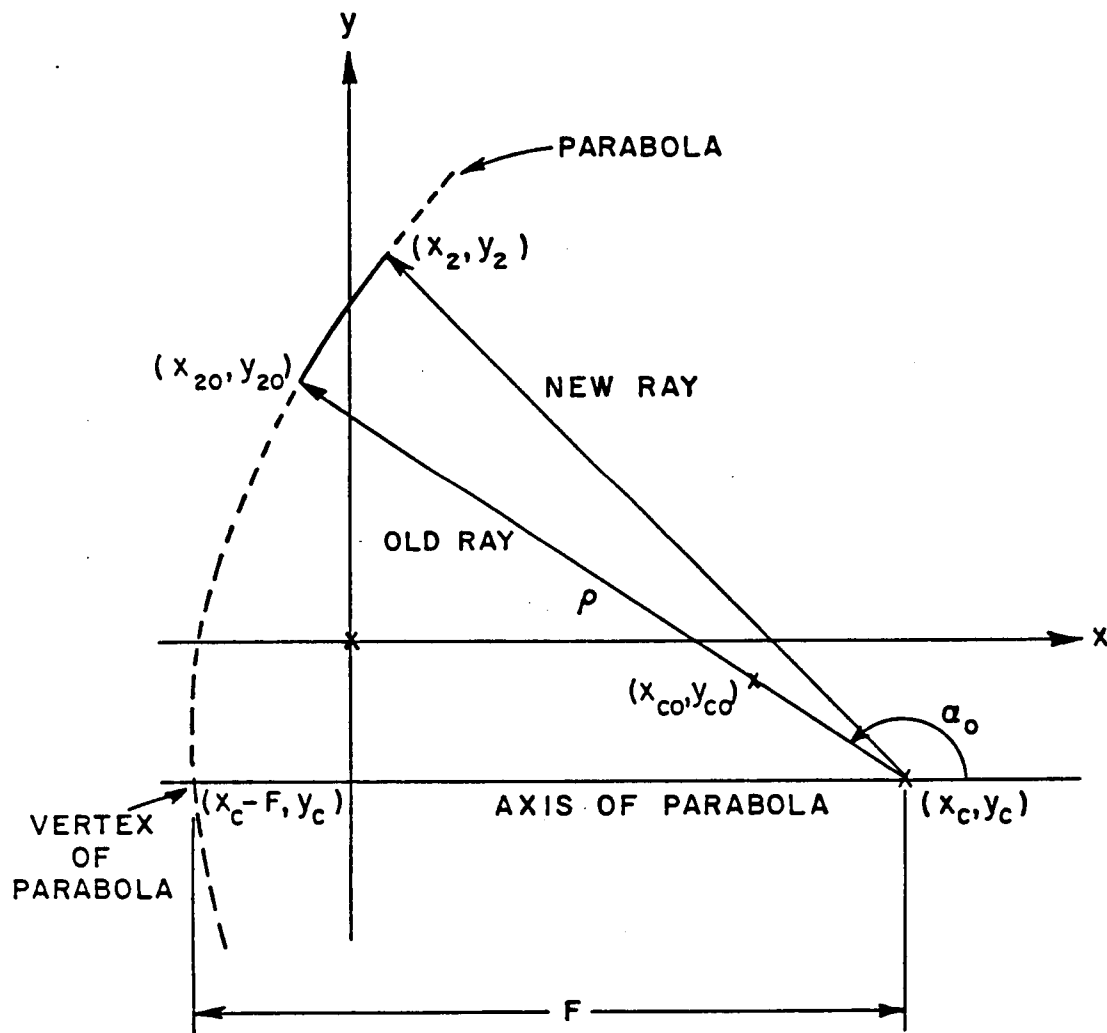


Figure 3.5. Geometry of shaped main reflector.

Therefore, the new main reflector surface point  $(x_2, y_2)$  must satisfy

$$x_2 - (x_c - F) = \frac{1}{4F} (y_2 - y_c)^2. \quad (3.2)$$

Equations (3.1) and (3.2) give two equations with 6 unknowns  $(x_1, y_1, x_2, y_2, x_c, y_c)$ . Four more equations are required to solve for all the unknowns. Basically equations (3.1) and (3.2) satisfy the theorem of Malus which has been discussed earlier. The other two conditions of geometrical optics will be used to obtain four more equations.

### C. Snell's Law of Reflection

At the point of reflection, the angles of incidence and reflection must be equal, and the incident ray, reflected ray, and surface normal must be coplanar. Since the antenna is assumed to be in a homogeneous medium, the incident and the reflected rays must be straight lines as shown in Figure 3.6. Consequently, one finds that

$$y_1 = (\tan \phi) x_1 = m_o x_1 \quad (3.3)$$

and

$$(x_2 - x_1)(y_c - y_1) = (y_2 - y_1)(x_c - x_1) \quad (3.4)$$

The angles of incidence and reflection will automatically be equal since the reflection point  $(x_1, y_1)$  is on either the hyperbolic or the elliptic subreflector. Snell's law of reflection will also be satisfied

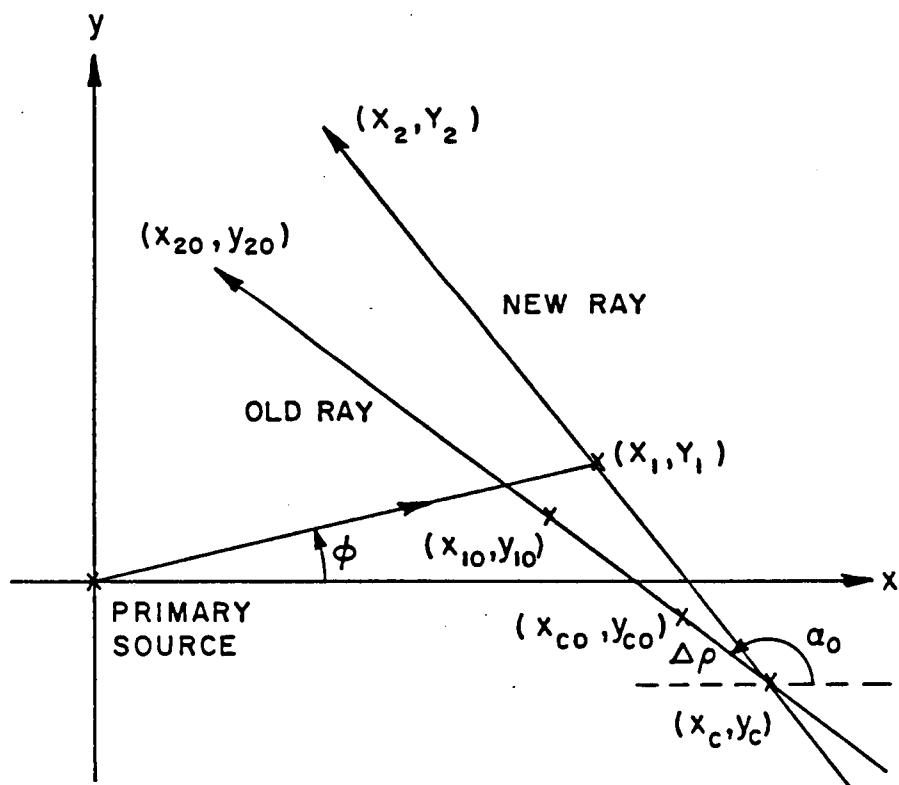


Figure 3.6. Geometry for describing the relations of various points.



automatically on the main reflector. One more equation can be obtained from Figure 3.6 by considering that the intersection point of the "old" ray with the "new" ray must be  $(x_c, y_c)$ ; i.e.,

$$\frac{x_c - x_{co}}{y_c - y_{co}} = \frac{x_{20} - x_{10}}{y_{20} - y_{10}} = \frac{1}{\tan \alpha_o} \quad (3.5)$$

which can be rewritten as

$$x_c = x_{co} + \Delta \rho \cos \alpha_o$$

and

$$y_c = y_{co} + \Delta \rho \sin \alpha_o$$

Note that  $\Delta \rho$  is the unknown distance between  $(x_c, y_c)$  and  $(x_{co}, y_{co})$  and can be positive or negative.

#### D. Conservation of Power

The major purpose of shaping the reflector is to redistribute a given primary source pattern into the prescribed secondary aperture distribution. Thus, conservation of power has to be satisfied.

Consider a primary source with a power density pattern  $F(\phi)$  and with its axis tilted  $\phi_o$  with respect to the positive x-axis. Note that the tilt angle  $\phi_o$  is zero for a symmetric reflector. The power between  $\phi = \phi_{\min}$  and  $\phi = \phi_{\max}$  of this primary source is to be distributed over a secondary aperture between  $y = y_{\min}$  and  $y = y_{\max}$  with an aperture distribution  $CI(y)$ . The angles  $\phi$ ,  $\phi_{\min}$  and  $\phi_{\max}$  are also measured with respect to the

positive x-axis. The constant C is determined from the conservation of power which states that

$$\int_{\phi_{\min}}^{\phi_{\max}} F(\phi) d\phi = \int_{y_{\min}}^{y_{\max}} C I(y) dy$$

or

$$C = \frac{\int_{\phi_{\min}}^{\phi_{\max}} F(\phi) d\phi}{\int_{y_{\min}}^{y_{\max}} I(y) dy}.$$

Note that in this study, the aperture blockage effects from the subreflector are not considered. It is assumed that the shaping process begins at the point where the incident ray from the primary source is along the feed axis  $\phi = \phi_0$  and the surfaces above and below this point are shaped separately. Thus, the conservation of power relates the feed angle  $\phi$  and the aperture point  $y$  as

$$\int_{\phi_0}^{\phi} F(\phi) d\phi = \int_{y_0}^y C I(y) dy \quad (3.6)$$

where  $y_0$  is the point at the aperture which corresponds to the ray which emanates along the feed axis. The geometry of describing conservation

of power is shown in Figure 3.7. For a given  $y$  (or  $\phi$ ), the corresponding  $\phi$  (or  $y$ ) can be solved from Equation (3.6).

The equations obtained thus far are summarized as follows:

$$\frac{1}{a^2} \left( x_1 \cos \theta + y_1 \sin \theta - \frac{F_c}{2} \right)^2 - \frac{4}{F_c^2 - 4a^2} \left( x_1 \sin \theta - y_1 \cos \theta \right)^2 = 1 \quad (3.1)$$

$$x_2 - (x_c - F) = \frac{1}{4F} (y_2 - y_c)^2 \quad (3.2)$$

$$y_1 = (\tan \phi) x_1 \quad (3.3)$$

$$(x_2 - x_1)(y_c - y_1) = (x_c - x_1)(y_2 - y_1) \quad (3.4)$$

$$\frac{x_c - x_{20}}{y_c - y_{20}} = \frac{x_{20} - x_{10}}{y_{20} - y_{10}} = \frac{1}{\tan \alpha_o} \quad (3.5)$$

and

$$\int_{\phi_o}^{\phi} F(\phi) d\phi = \frac{\int_{\phi_{\min}}^{\phi_{\max}} F(\phi) d\phi}{\int_{y_{\min}}^{y_{\max}} I(y) dy} \int_{y_o}^{y_2} I(y) dy \quad (3.6)$$

in which

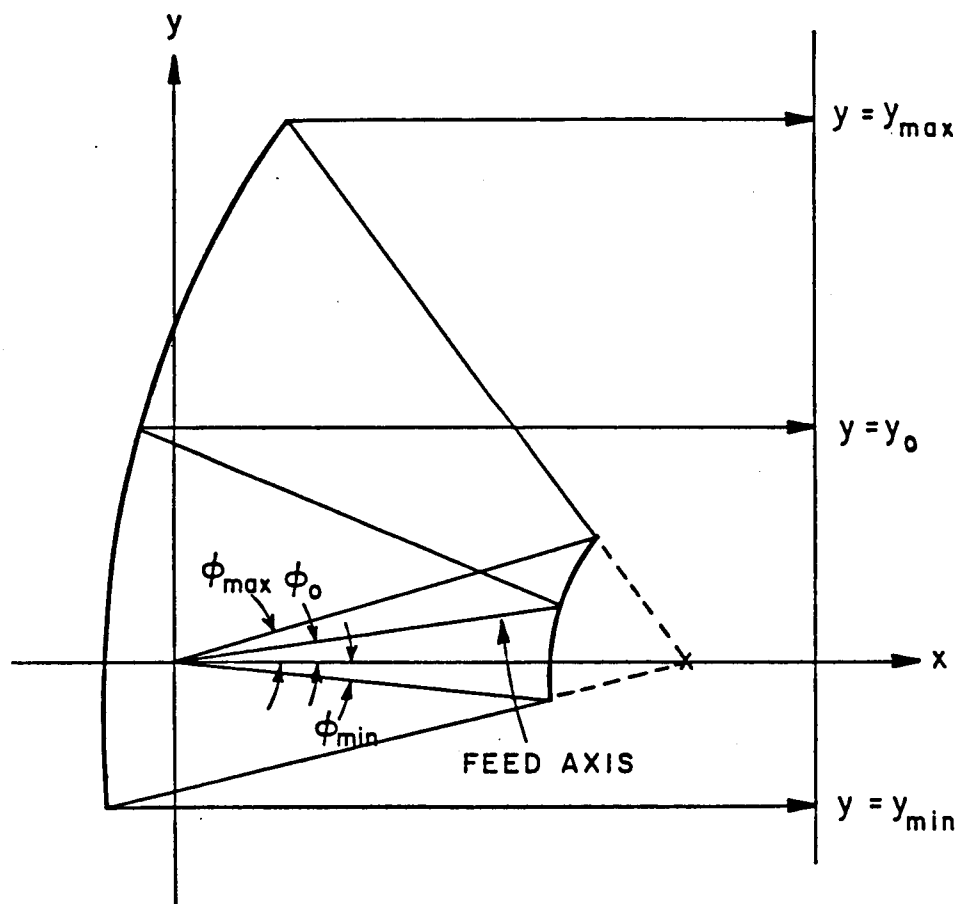


Figure 3.7. Geometry of describing conservation of power.

$$F_c = (x_c^2 + y_c^2)^{1/2} \quad (3.7)$$

$$4a^2 = \left\{ (x_{10}^2 + y_{10}^2)^{1/2} \pm \left[ (x_{10} - x_c)^2 + (y_{10} - y_c)^2 \right]^{1/2} \right\}^2$$

+: ellipse  
-: hyperbola

$$\theta = \tan^{-1} \left( \frac{y_c}{x_c} \right)$$

$$F_c \cos \theta = x_c, \quad F_c \sin \theta = y_c$$

and

$$F = \begin{cases} \frac{1}{2} (1 - \sec \alpha_o) (x_c - x_{20}) & , \text{ if } x_c \neq x_{20} \\ -\frac{1}{2} \frac{1 - \cos \alpha_o}{\sin \alpha_o} (y_c - y_{20}) & , \text{ if } y_c \neq y_{20} \end{cases}$$

Although there are 6 equations with 7 unknowns  $(x_1, y_1, x_2, y_2, x_c, y_c, \phi)$  one of these unknowns will be used as an independent variable so that the other 6 unknowns can be solved by the 6 nonlinear algebraic equations.

It is also noted that the method of shaping discussed above will generate uniform phase on the aperture when the primary source has a cylindrical wavefront since the path length from the primary source to

the aperture plane will be the same for two adjacent rays which are from the same section of a Cassegrain or Gregorian surface.

### 3.2.2. Solution for the Surface Equations

It is obvious that to solve the equations obtained in the previous section will not be easy even by numerical methods since they are nonlinear. In this section, an approach is proposed to solve these unknowns.

As mentioned earlier there are 6 equations with 7 unknowns; therefore, one of the unknowns must be chosen as an independent variable. The obvious choice will be either  $y_2$  or  $\phi$  since once one of these two variables is specified, the other one can be obtained from Equation (3.6). This reduces the set of equations to five equations with five unknowns. It is also noted that the above equations involve "old" and "new" rays and in the very first stage, the "old" ray is not defined unless one provides a set of initial points  $\{(x_{10}, y_{10}), (x_{20}, y_{20})$  and  $(x_{co}, y_{co})\}$ . Once these initial points are set, the method which will be discussed next can be used to solve for  $x_1, y_1, x_2, x_c, y_c$  and then, these newly generated points will be used as the "old" ray to solve the next "new" ray. This process is continued until the complete surfaces are generated.

The procedure of solving the above equations is discussed as follows:

- 1) From Equation (3.3),

$$y_1 = (\tan\phi)x_1 = m_o x_1 \quad (3.7)$$

2) Substituting (3.7) into (3.4), one obtains

$$x_1 = \frac{x_c y_2 - x_2 y_c}{y_2 - y_c - m_o (x_2 - x_c)} \quad (3.8)$$

3) Substituting Equation (3.2) into Equation (3.8), one obtains

$$x_1 = \frac{4F x_c y_2 - y_c [(y_2 - y_c)^2 + 4F x_c - 4F^2]}{4F(y_2 - y_c) - m_o \{[(y_c - y_c)^2 + 4F x_c - 4F^2] - 4F x_c\}} \quad (3.9)$$

4) Substituting Equations (3.7) and (3.9) into Equation (3.1), an equation which involves  $x_c, y_c, m_o, y_2$  is obtained. The resulting equation is

$$\begin{aligned} & \left[ (x_c + m_o y_c)^2 - 4a^2 (1 + m_o^2) \right] \left\{ 4F x_c y_c - y_c [(y_2 - y_c)^2 + 4F x_c - 4F^2] \right\}^2 \\ & - (x_c + m_o y_c) (F_c^2 - 4a^2) \left\{ 4F x_c y_2 - y_c [(y_2 - y_c)^2 + 4F x_c - 4F^2] \right\} \\ & \left\{ 4F (y_2 - y_c + m_o x_c) - m_o [(y_2 - y_c)^2 + 4F x_c - 4F^2] \right\} \\ & = - \frac{1}{4} (F_c^2 - 4a^2)^2 \left\{ 4F (y_2 - y_c + m_o x_c) - m_o [(y_2 - y_c)^2 + 4F x_c - 4F^2] \right\}^2 \end{aligned} \quad (3.10)$$

Although Equation (3.10) has  $m_0, y_2, F$  and  $F_c$  involved, it is noted that both  $m_0$  and  $y_2$  are known at this point and that  $F$  and  $F_c$  are functions of  $x_c$  and  $y_c$  only.

5) There are two equations, Equations (3.5) and (3.10), with two unknowns  $x_c$  and  $y_c$  which can be solved. However, Equation (3.10) is again a nonlinear equation so that it is still very difficult to solve for  $x_c$  and  $y_c$  exactly. Consequently, a numerical method has to be used to solve for  $x_c$  and  $y_c$ . One can directly solve these equations numerically, or by observing that Equation (3.5) can be written as

$$x_c = x_{co} + \Delta\rho \cos\alpha_0$$

and

$$y_c = y_{co} + \Delta\rho \sin\alpha_0 \quad (3.11)$$

in which  $\Delta\rho$  is the unknown distance between  $(x_{co}, y_{co})$  and  $(x_c, y_c)$ . After substituting Equation (3.11) into Equation (3.10), only one unknown  $\Delta\rho$  is involved. But this equation is still not easy to solve. However, it is expected that  $\Delta\rho$  will be very small when the angle  $\phi$  (or the aperture point  $y_2$ ) is changed gradually (i.e., the increment of  $\phi$  is very small) one can neglect the higher order terms of  $\Delta\rho$  such as  $(\Delta\rho)^2$ ,  $(\Delta\rho)^3$ , etc., in the newly obtained equation. After  $\Delta\rho$  is solved, all the unknowns can be solved. The detailed procedure of solving these unknowns is given in Appendix B.



## CHAPTER IV

### EXAMPLES FOR SHAPING OF TWO-DIMENSIONAL DUAL-REFLECTOR ANTENNA

The method of synthesis for dual-reflector antennas discussed in the previous chapter is actually quite general. For a given feed pattern, feed location, angular range of feed pattern which will illuminate the subreflector, and the desired aperture size and distribution, the reflector surfaces can be generated numerically provided that a set of appropriate initial points for the caustic, subreflector and main reflector is given. This set of initial points must satisfy a ray condition that the resulting aperture field obtained by connecting the rays through these points is equal to the desired aperture field. Two of the three initial points are chosen, the third one can be calculated. Generally, the initial points on the subreflector and main reflector are chosen and the initial point for the caustic is then calculated by the formula discussed in Appendix C. However, as it turns out, if the three initial points do not satisfy the above ray condition, the solution for the surface itself will try to correct the set of inappropriate initial points. This phenomenon can be seen from the examples given later in this chapter.

Several examples of two-dimensional dual-reflector shaping are presented in this chapter to illustrate the method of synthesis

discussed in the previous chapter. In these examples a conventional Gregorian or Cassegrain antenna is used as a starting point for the reflector surface; and a magnetic line source with power radiation intensity  $(\cos^q \phi)$  is used as the primary source. The goal of shaping is to modify the given reflector surfaces so that a prescribed aperture distribution with uniform phase is achieved at the aperture of the main reflector. The physical optics approximation is then used to calculate the scattered field from the shaped surfaces although the geometrical optics is used to compute the induced surface currents on the reflector surfaces.

In each example, the location of a "central ray" at the aperture is assumed known where the central ray is the reflected ray from main reflector which corresponds to the incident ray coming along the axis of primary feed. This central ray is used to determine the initial points of shaping. The reflector surfaces above and below the central ray are then shaped separately. The initial points on the reflector surface can be determined by the intersection of the central ray with the initial Cassegrain or Gregorian reflector surface; and the initial point for the caustic is determined by the condition given in Appendix C.

In addition, as mentioned earlier, there are six equations with seven unknowns related to these problems. Therefore, one of the unknowns has to be an independent variable. Consequently, the appropriate choice is either  $(y_2)$  or  $(\phi)$  since these two variables are related by the equation of conservation of power. Once one of these two

variables is fixed, the other variable is then found. The conservation of power principle implies that

$$\int_{\phi_0}^{\phi} F(\phi) d\phi = \int_{y_0}^y C I(y) dy \quad (4.1)$$

or

$$F(\phi) d\phi = C I(y) dy \quad (4.2)$$

for a differential ray tube in which  $y_0$  is the location of central ray at the aperture plane. This corresponds to the incident ray coming along  $\phi = \phi_0$  of the primary feed where  $\phi$  is measured from the positive x-axis. From Equation (4.2), one can determine the point by point relation between the aperture point  $y_2$  and feed angle  $\phi$  and thus, the rest of the equations for the reflector surfaces are solved by the method discussed in Chapter III and Appendix B.

#### 4.1 Shaping of a Center-Fed Gregorian Reflector Antenna for a Uniform Aperture Distribution

In this section, a center-fed two-dimensional Gregorian reflector antenna is used for a starting point of shaping. The geometry of this reflector is shown in Figure 4.1 with the following parameters:

$$F_m = 0.6667'$$

$$F_c = 0.1667'$$

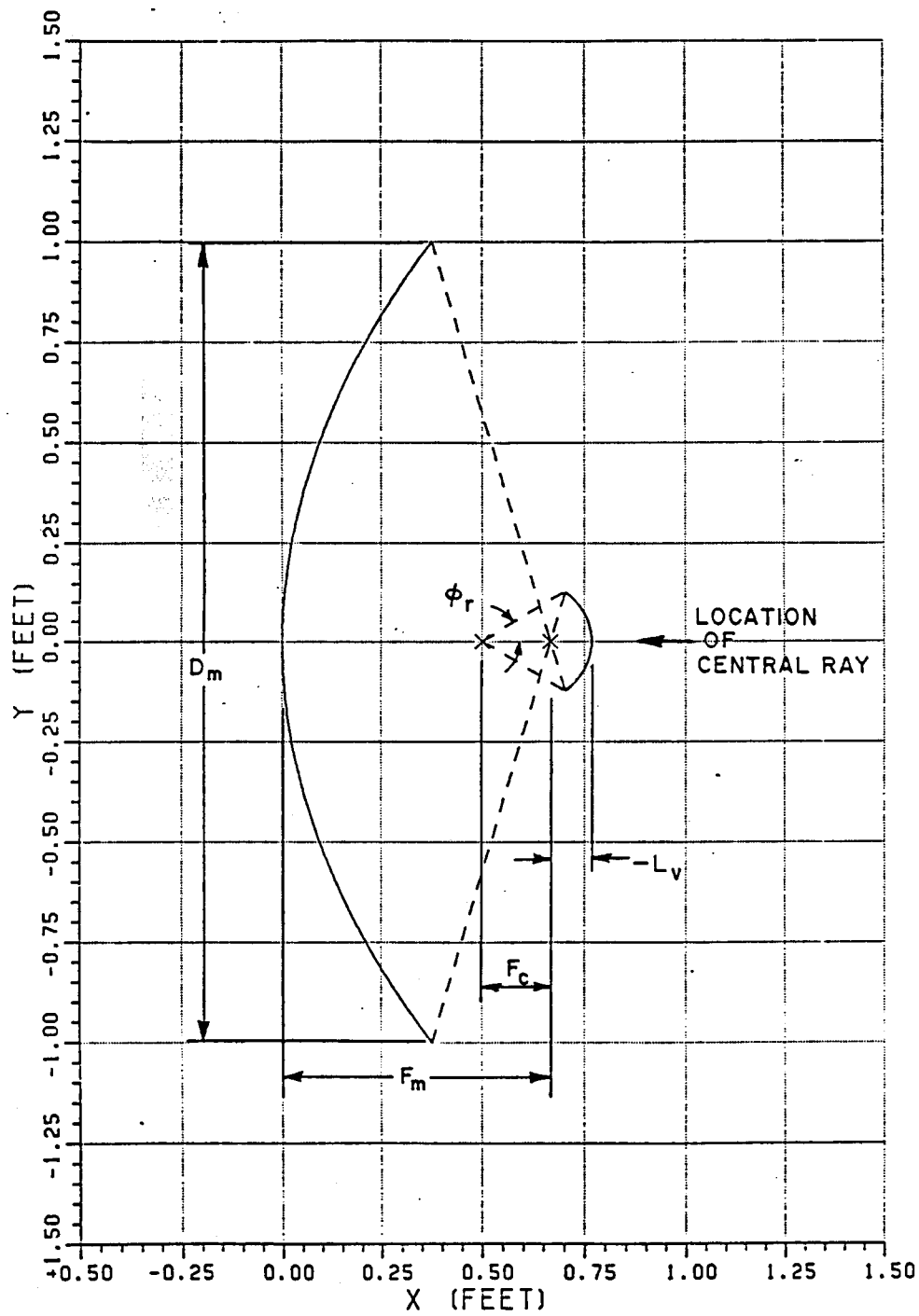


Figure 4.1. A conventional Gregorian reflector antenna.

$$L_v = -0.1'$$

$$D_m = 2.0'$$

$$\phi_r = 31.42^\circ.$$

These parameters are defined in Chapter II. The requirement for shaping in this example is to spread the power of the primary feed between  $-\phi_r$  and  $+\phi_r$  into a uniform aperture distribution between  $y=-1.0'$  and  $y=+1.0'$  with the central ray located at  $y=0.0'$ . A magnetic line source with radiation intensity  $\cos^{20} \phi$ , as shown in Figure 4.2, is used as the primary feed. The scattered field patterns are calculated for both the unshaped and shaped reflector for the purpose of checking the resulting scattered fields after the reflector surfaces are shaped.

The far-zone scattered fields from the subreflector of the original Gregorian reflector antenna calculated at 20 GHz are shown in Figure 4.3 and the near-zone scattered fields from the parabolic main reflector which were calculated at  $x=2.0'$  and 20 GHz are shown in Figure 4.4. In Figure 4.3,  $\theta$  is the angle measured from the negative x-axis and the phase center for the subreflector scattered fields is located at focal point #2 of the reflector. The dashed line in these figures shows the geometrical optics reflected field while the solid line shows the scattered fields calculated by the method of physical optics. The ripple in the physical optics results is caused by the interaction of the geometrical optics field with the edge diffracted field from the

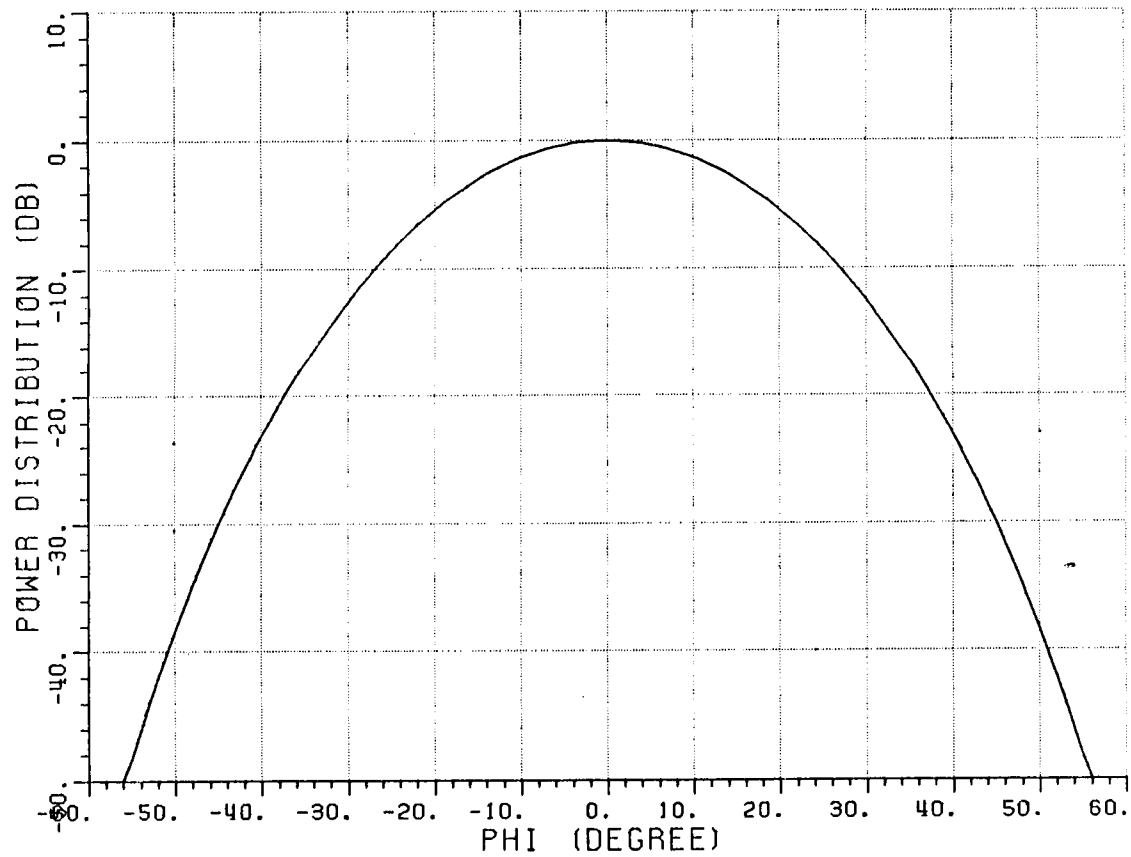


Figure 4.2. A  $\cos^2 \phi$  power distribution.

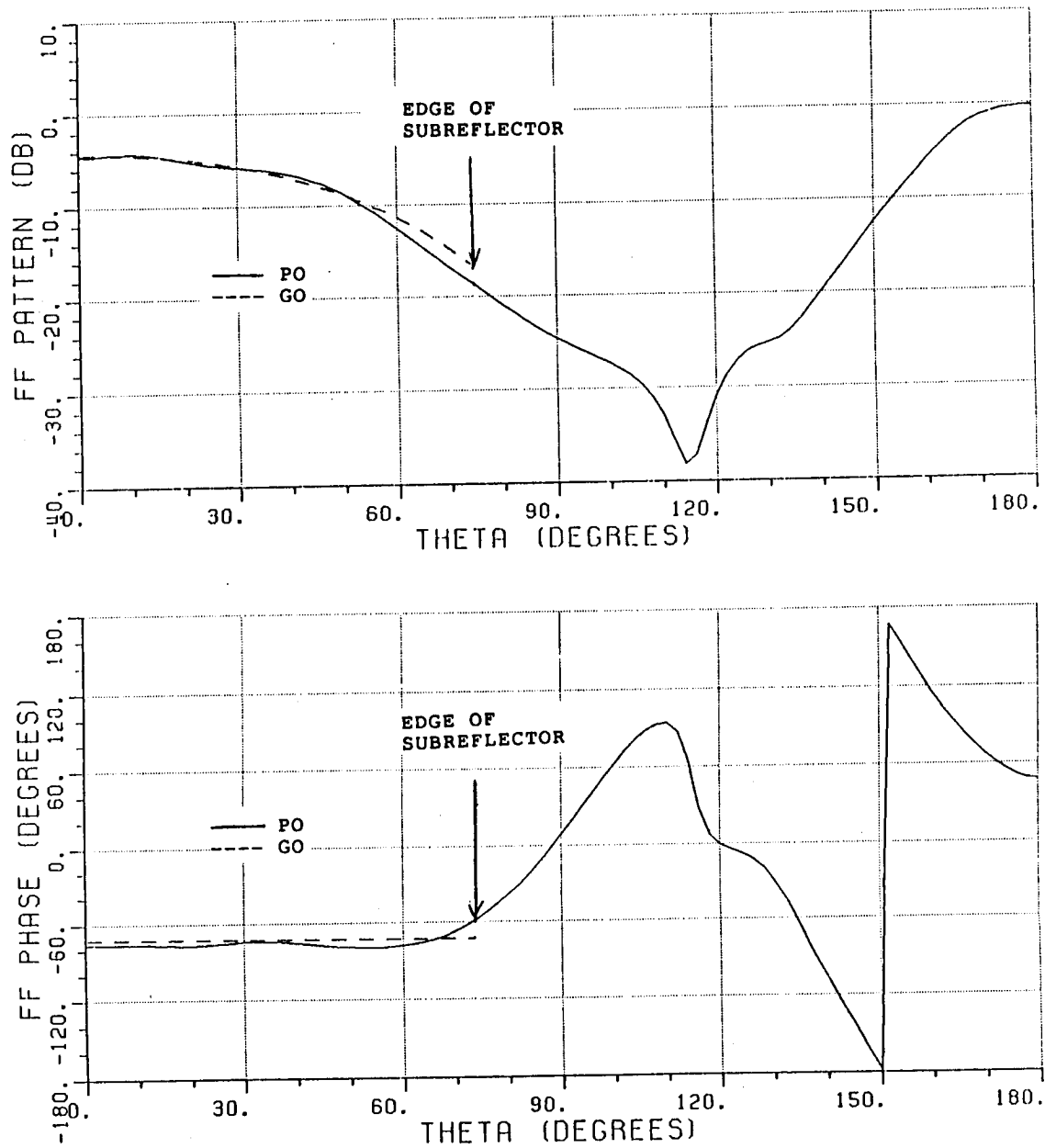


Figure 4.3. Far-zone scattered field of the subreflector for the conventional Gregorian reflector at 20 GHz.

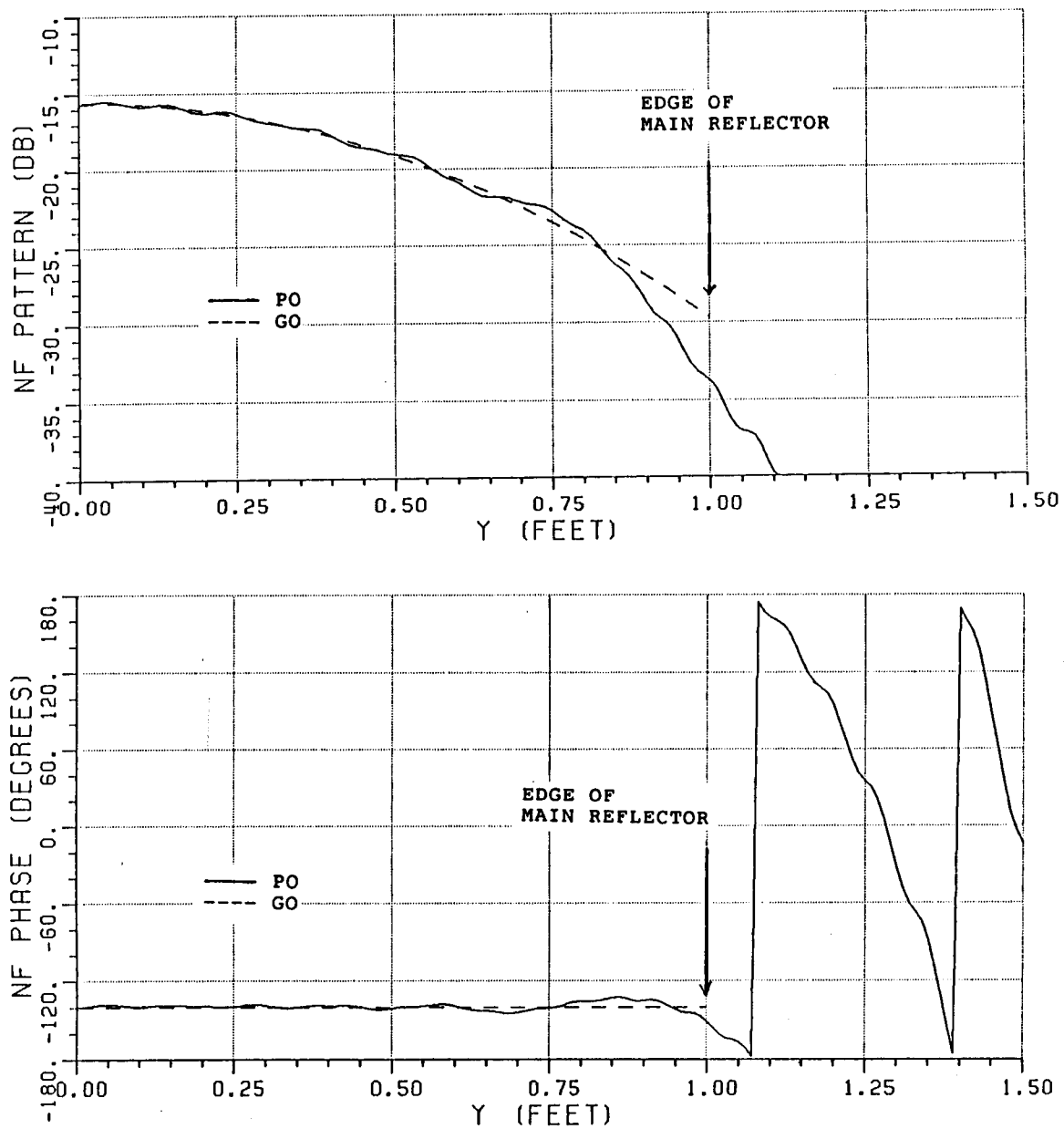


Figure 4.4. Near-zone scattered fields of the main reflector for the conventional Gregorian reflector at 20 GHz.



sharp terminations of the reflector surface. Consequently, the geometrical optics field passes through the average of the ripple. It can be seen from the optics field that the main reflector has an aperture edge taper of about -14dB. It is thus expected that the reflector surfaces have to be shaped significantly in order to achieve a uniform amplitude distribution. Also note that the G.O. phase pattern of the far-zone reflected fields from the subreflector is constant since the reflected field appears to emanate from focal point #2 which is the phase center. The phase pattern of the main reflector indicates that the aperture field is a plane wave.

It was mentioned earlier that in order to solve for the shaped reflector surfaces, one has to provide a set of appropriate initial points. However, if the initial points were not provided correctly, the resulting surfaces tend to adjust themselves in order to get the correct surfaces. Both of these cases are given next. Example G1 uses a set of initial points which do not satisfy the ray condition derived in Appendix C; whereas, Example G2 uses appropriate initial points which satisfy the ray condition.

#### 4.1.1 Example G1

The initial points for shaping are chosen as the intersection points of the central ray with the initial subreflector and main reflector surfaces, and the initial point on caustic is the second focus of the initial elliptic subreflector. The resulting reflector surfaces are shown in Figure 4.5. The subreflector surface is replotted in

Figure 4.6. The solid line shows the shaped reflectors whereas the dashed line shows the initial Gregorian reflector. The initial points for the shaping are indicated by small circles in these figures. Also shown in Figure 4.5 is the caustic curve for the reflected rays from the shaped subreflector. The upper half of the caustic curve corresponds to the lower half of the subreflector and the upper half of the main reflector; whereas, the lower half of the caustic curve corresponds to the remaining reflector surfaces. As is evident in Figure 4.6, the choice of the initial points are not quite correct. This happened because the power of the primary feed needs to be redistributed, and thus, the initially chosen points will not give the correct field at the aperture. However, the results of the analysis show where the appropriate initial points should be located since the solution tries to adjust the incorrect initial points to fit the right surfaces. Thus, one can choose the initial points indicated in these results and repeat the shaping process. The resulting surfaces which are designated as Example G1 are shown in Figures 4.7 and 4.8, and turn out to be identical to the previous results except for the initial points. This illustrates one of the characteristics of this method of synthesis; namely, that incorrect initial points on the reflector surfaces and caustic curve will be automatically corrected.

It can be seen from Figure 4.7 that the caustic of the reflected ray from the subreflector does not stay at a fixed point, instead, it moves gradually near the beginning of shaping but changes rather rapidly

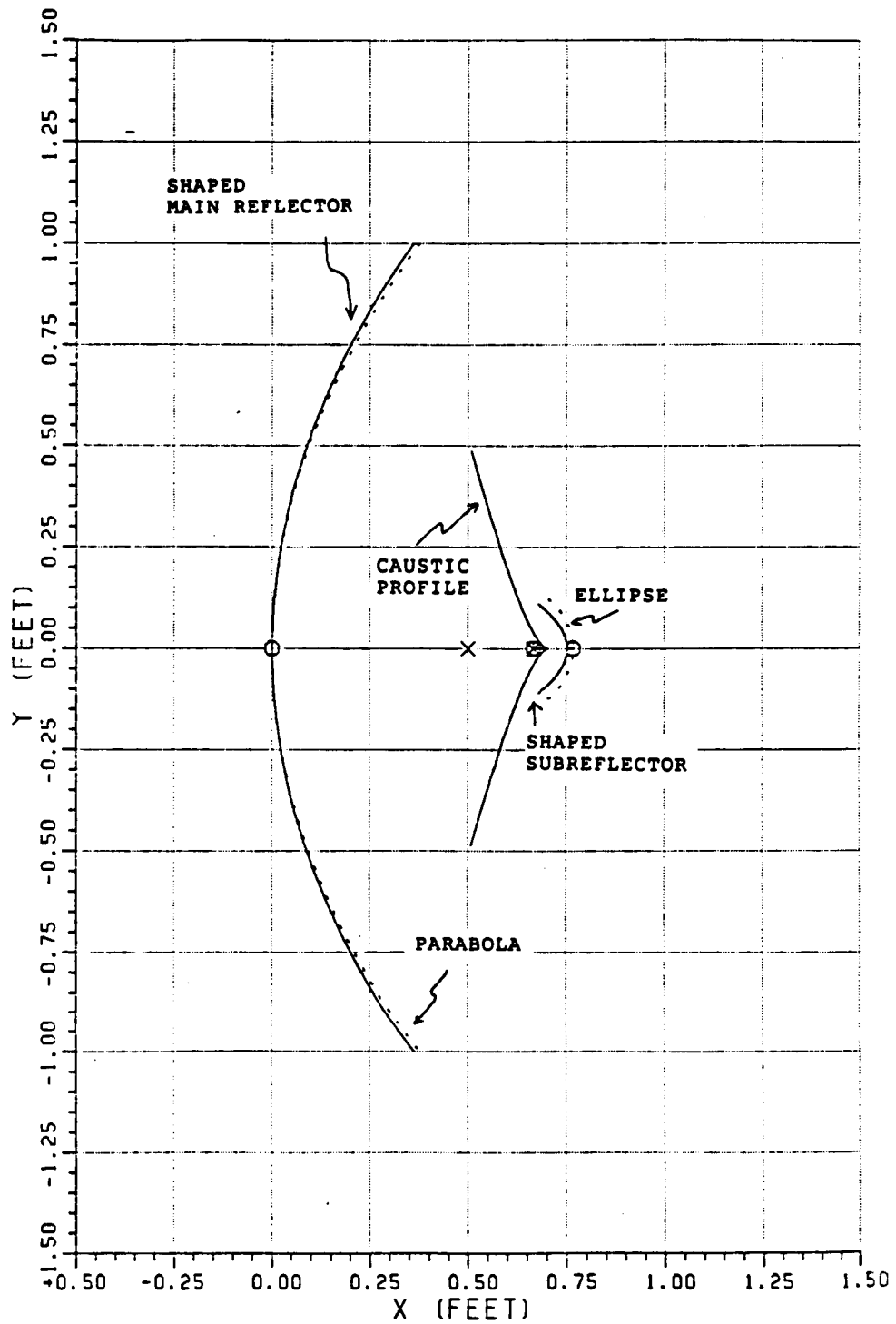


Figure 4.5. Shaped dual-reflector with inappropriate initial points of Example G1.

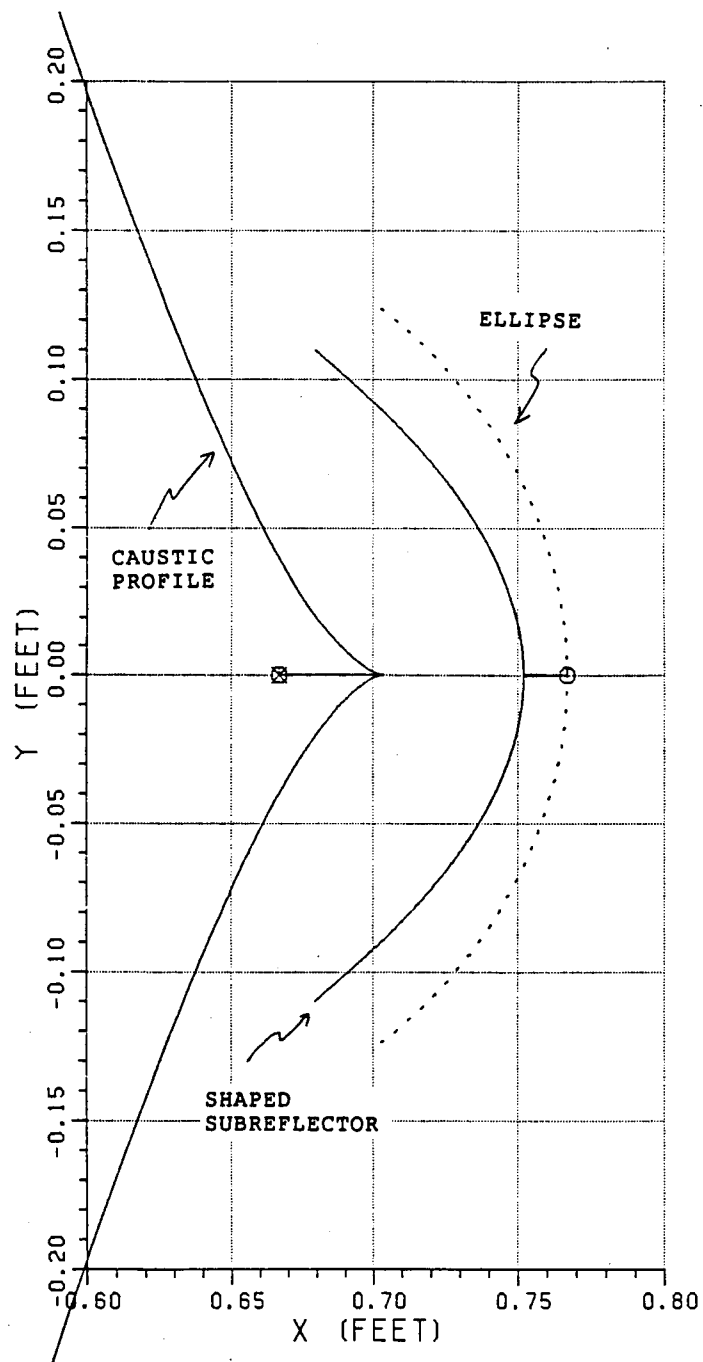


Figure 4.6. Subreflector and caustics for the shaped dual-reflector with inappropriate initial points of Example G1.

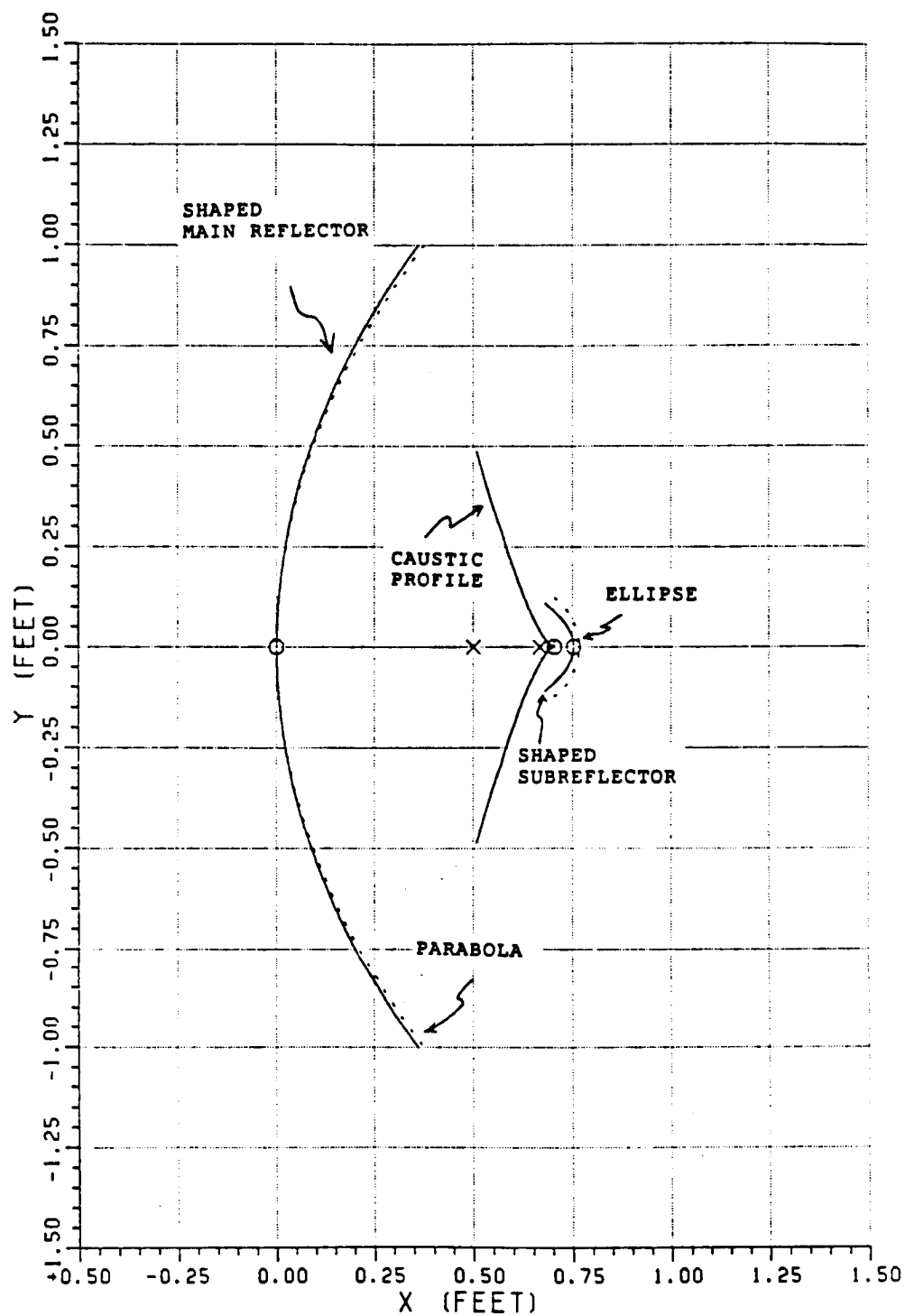


Figure 4.7. Improved shaped dual-reflector of Example G1.

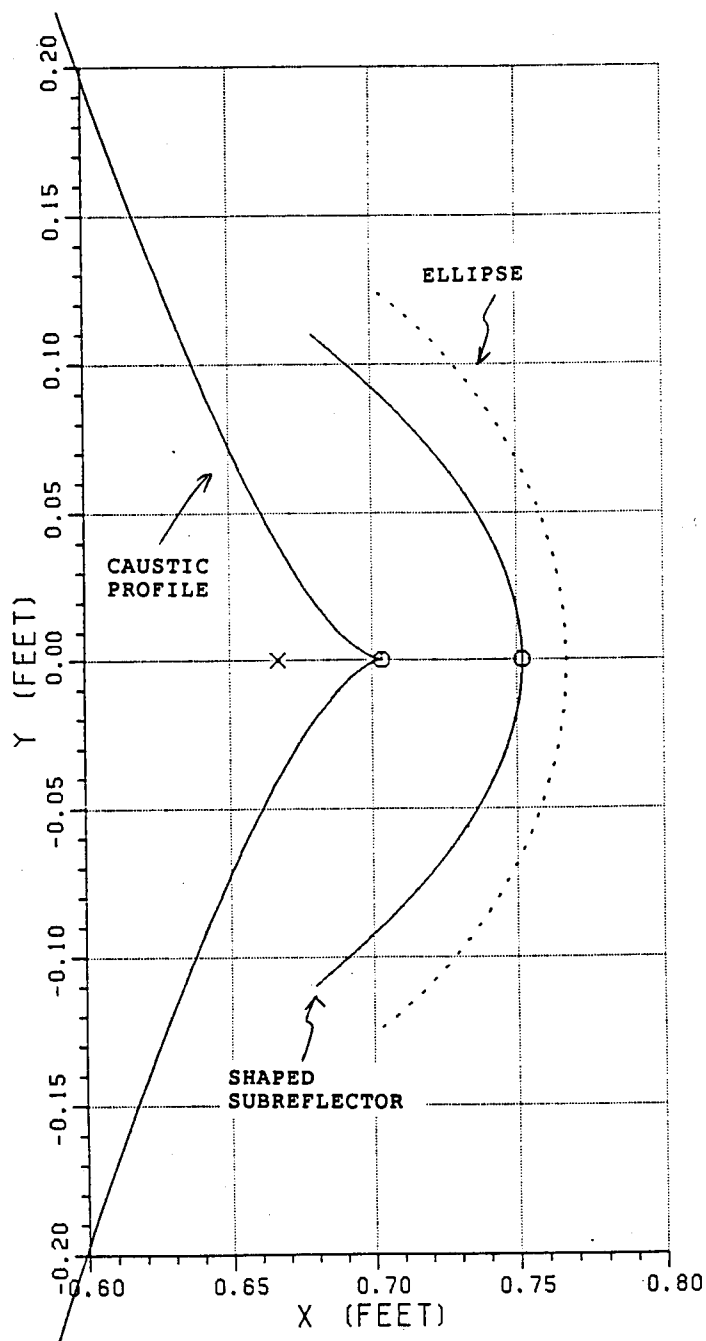


Figure 4.8. Subreflector and caustics of the improved shaped dual-reflector of Example G1.

toward the end of the shaping. The explanation for this behavior is that during the shaping process the incident field which emanates from the primary source tapers off, and thus, the reflected field from the subreflector must also decrease unless the spread factor of the reflected field increases. It is the magnitude of this subreflector reflected field which determines the magnitude of the aperture field since its magnitude does not change after reflection from the main reflector. The spread factor for this case is given by

$$\sqrt{\frac{-\rho_c}{(s_1 - \rho_c)}}$$

where  $\rho_c$  is positive and is the distance between the caustic and the reflection point on the subreflector; and  $s_1$  is the distance between the reflection points on the subreflector and main reflector. Thus, in order to increase the spread factor the magnitude of  $\rho_c$  has to be increased. Consequently, the caustic curve moves away from the subreflector surface. Figure 4.9 shows two rays for this reflector.

The scattered fields for Example G1 which are calculated at 20 GHz are given in Figures 4.10 and 4.11 for the far-zone subreflector and near-zone main reflector patterns, respectively. Both of these patterns are different from the conventional Gregorian reflector as they should be. The resulting near-zone scattered fields from the main reflector indicate that a uniform plane wave with a uniform amplitude distribution is nearly obtained. Also notice that the phase pattern of the subreflector geometrical optics scattered fields is not a constant as in

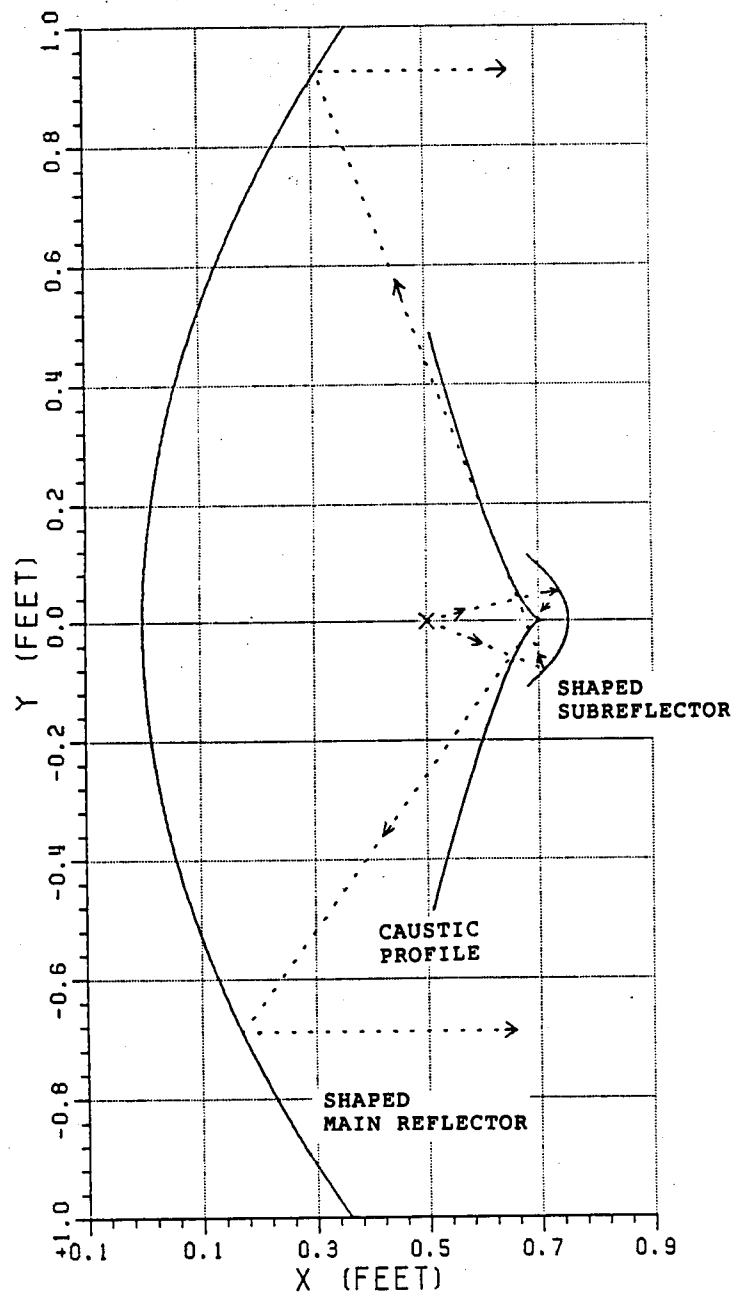


Figure 4.9. Ray geometries for the shaped reflectors of Example G1.



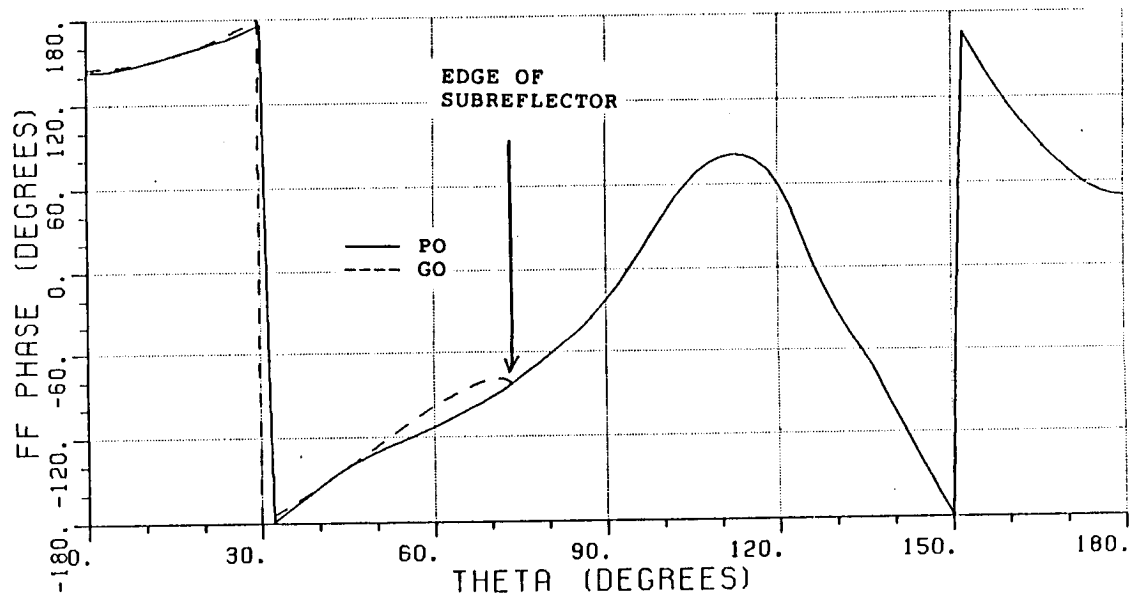
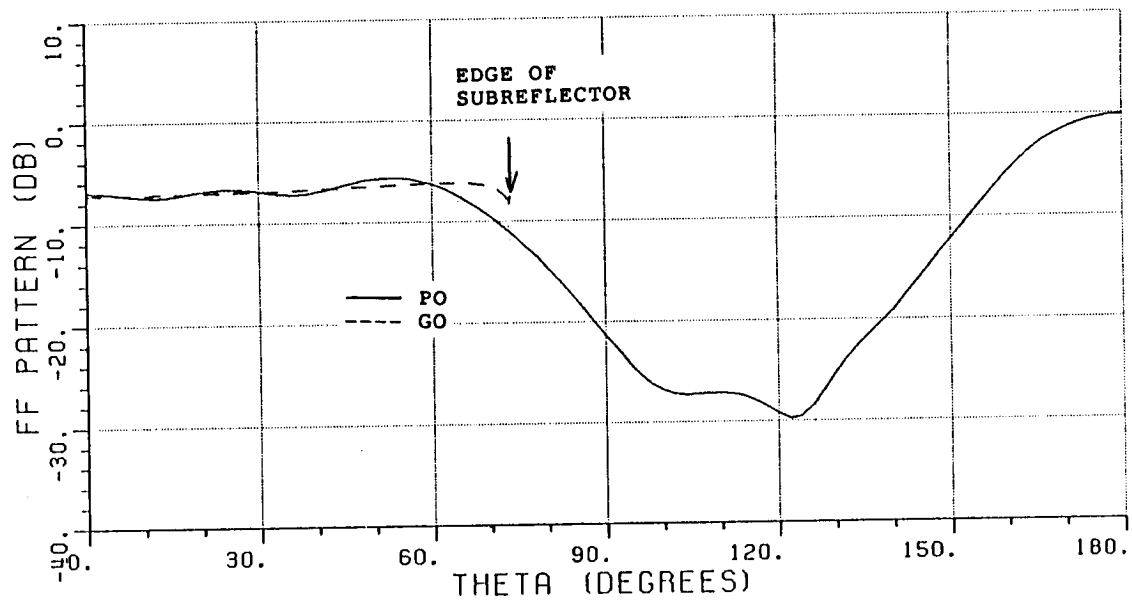


Figure 4.10. Far-zone scattered field of the shaped subreflector for Example G1 at 20 GHz.

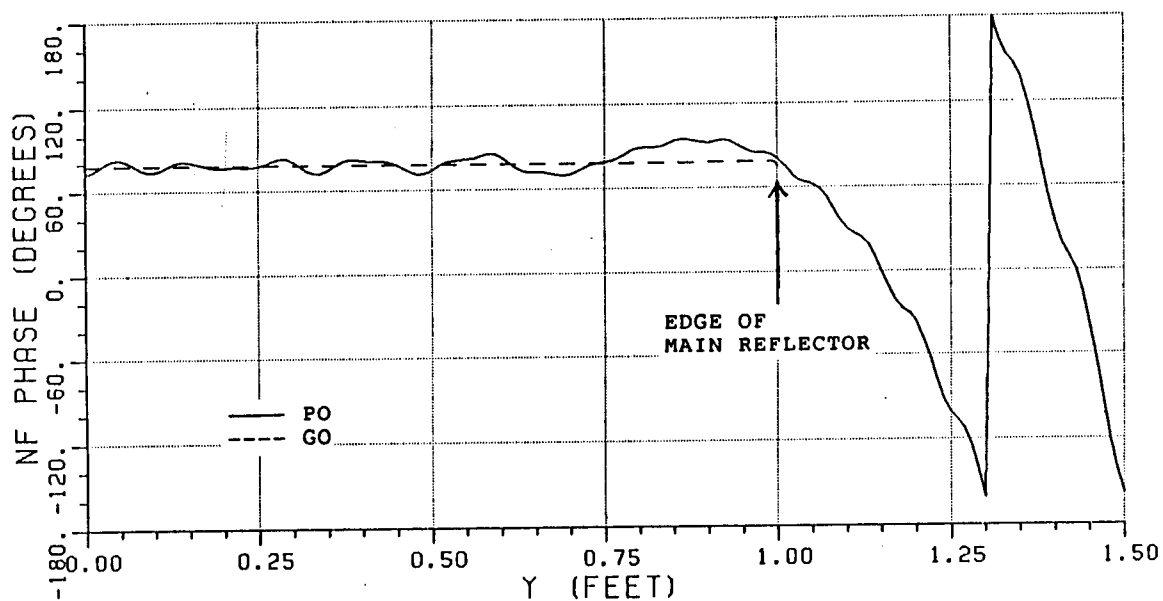
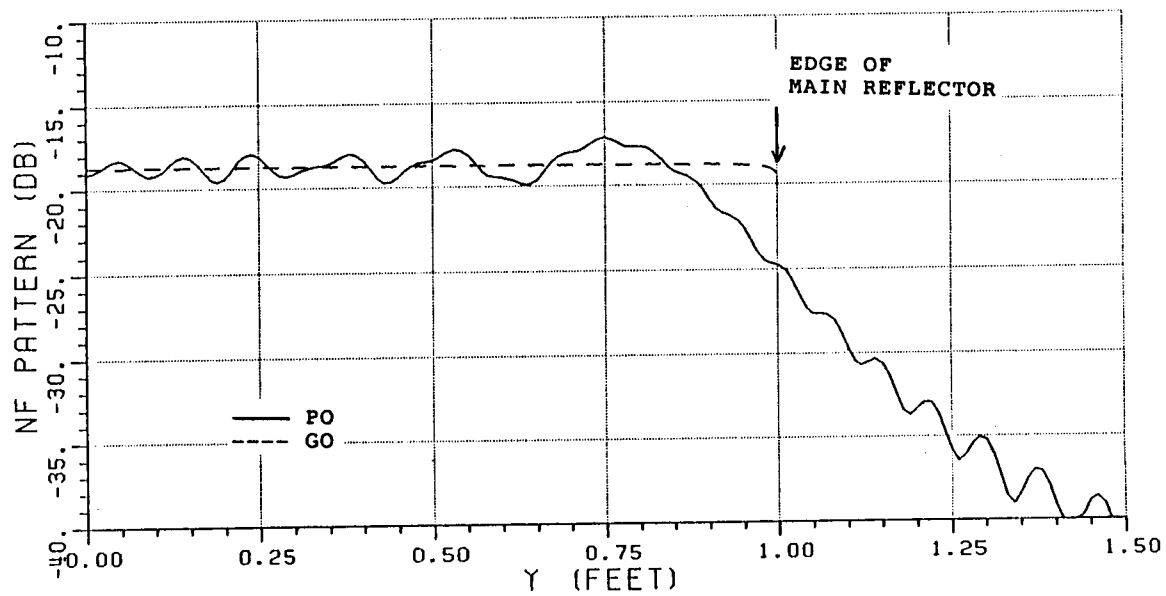


Figure 4.11. Near-zone scattered field of the shaped main reflector for the Example G1 at 20 GHz.

the conventional Gregorian reflector case since the caustic of the shaped subreflector reflected field is not a fixed point.

#### 4.1.2 Example G2

The initial points on the subreflector and main reflector are determined by the intersection of the central ray with the original subreflector and main reflector of the Gregorian antenna in this example. However, instead of using the second focus of the elliptic subreflector as the initial point for the caustic curve, the ray condition discussed in Appendix C is used to determine the initial point for the caustic. The resulting surfaces which are designated as Example G2 are given in Figures 4.12 and 4.13 for the overall system and the subreflector, respectively. Figure 4.14 shows two rays for the shaped reflectors. The far-zone scattered fields of the shaped subreflector and the near-zone scattered fields of the shaped main reflector calculated at 20 GHz are shown in Figures 4.15 and 4.16. Comparing these results with the ones of example G1, it is found that the subreflector scattered patterns are not quite the same, but the scattered patterns of the main reflector are identical in magnitude. This shows the non-uniqueness of the shaping solution when the initial points for shaping are different. The major difference in the reflector surfaces between Examples G1 and G2 is that the subreflector surface and the caustic curve are shifted although the overall surfaces are only slightly different.

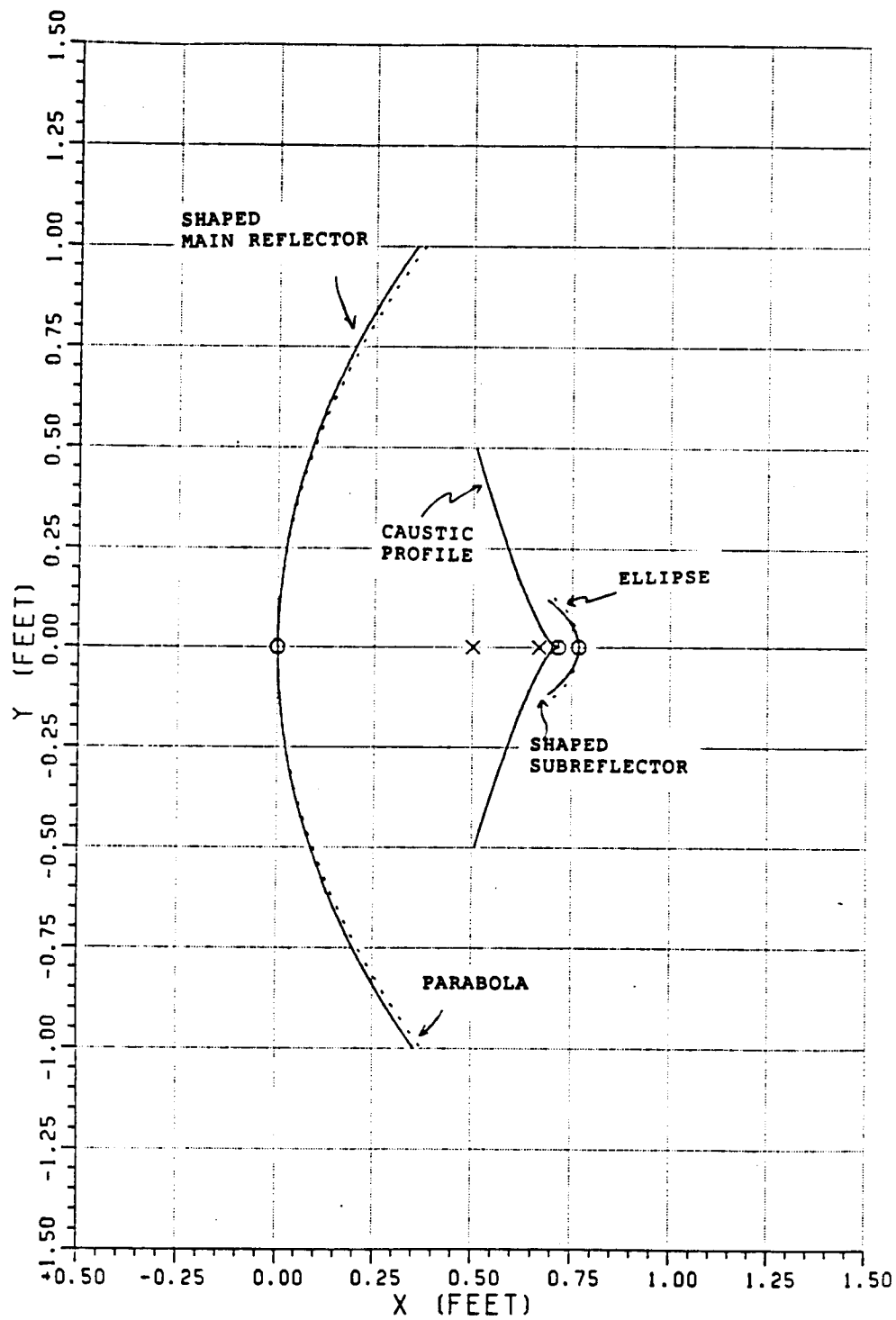


Figure 4.12. Shaped dual-reflector of Example G2.

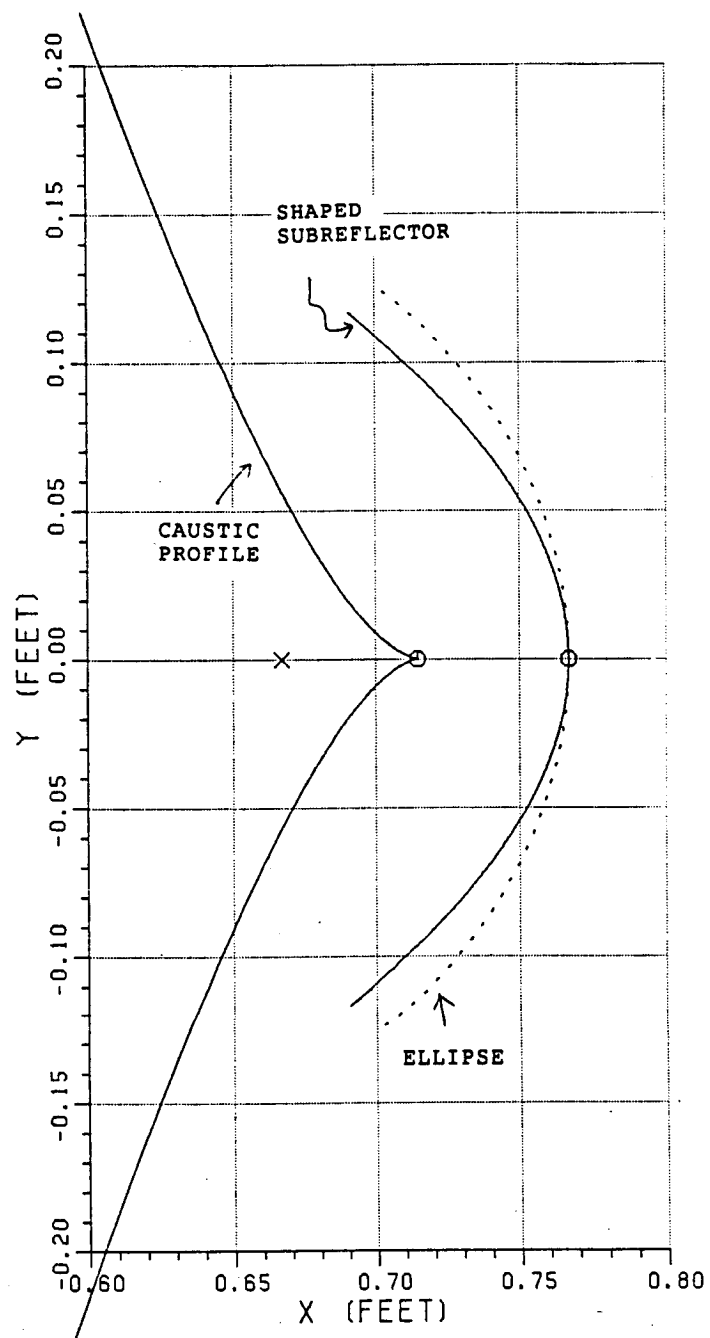


Figure 4.13. Subreflector and caustics for the shaped dual-reflector of Example G2.

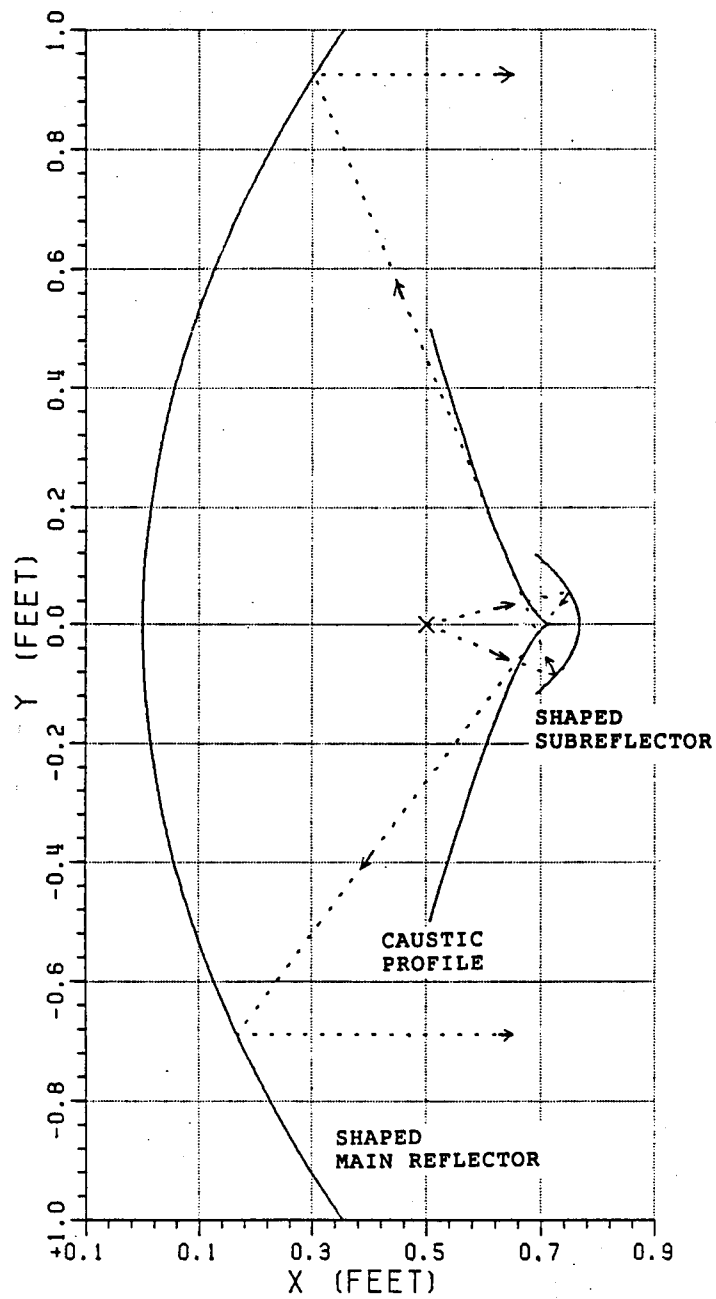


Figure 4.14. Ray geometries for the shaped reflectors of Example G2.

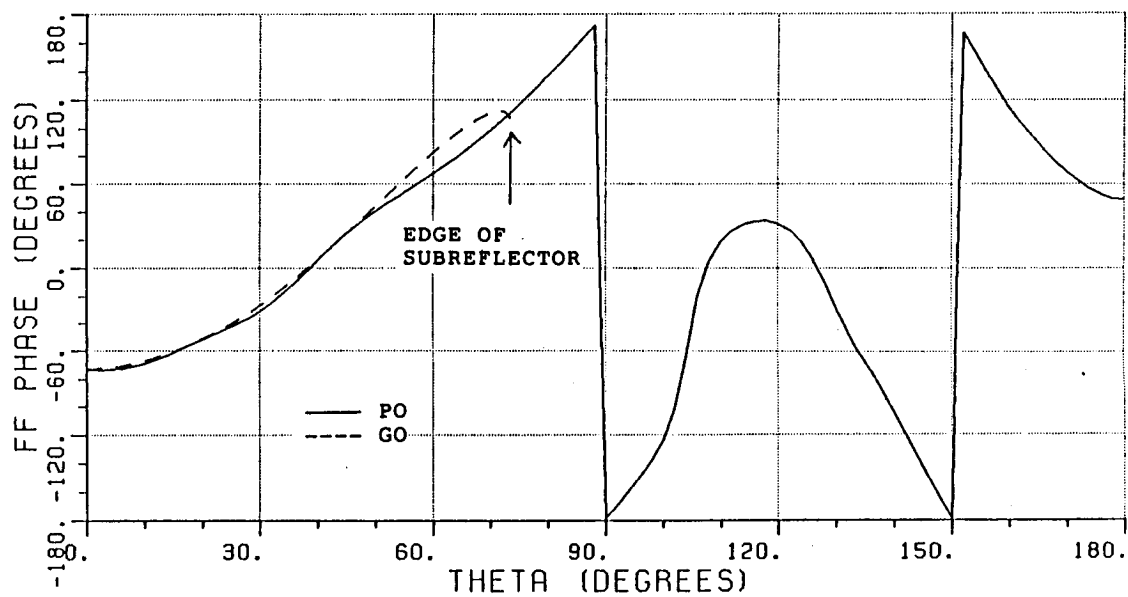
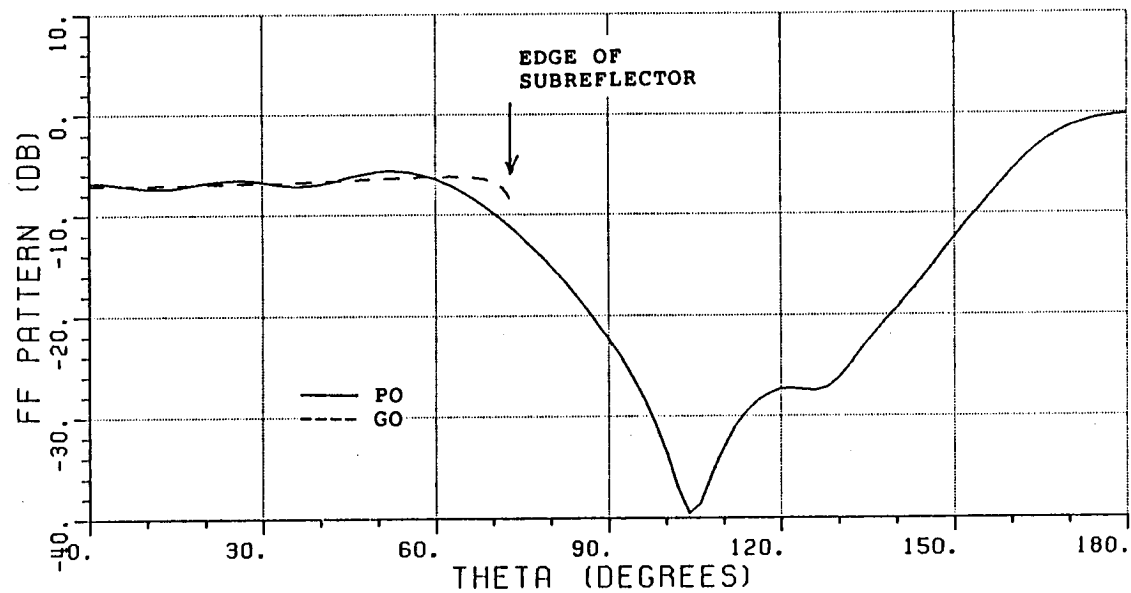


Figure 4.15. Far-zone scattered field of the shaped subreflector of Example G2 at 20 GHz.

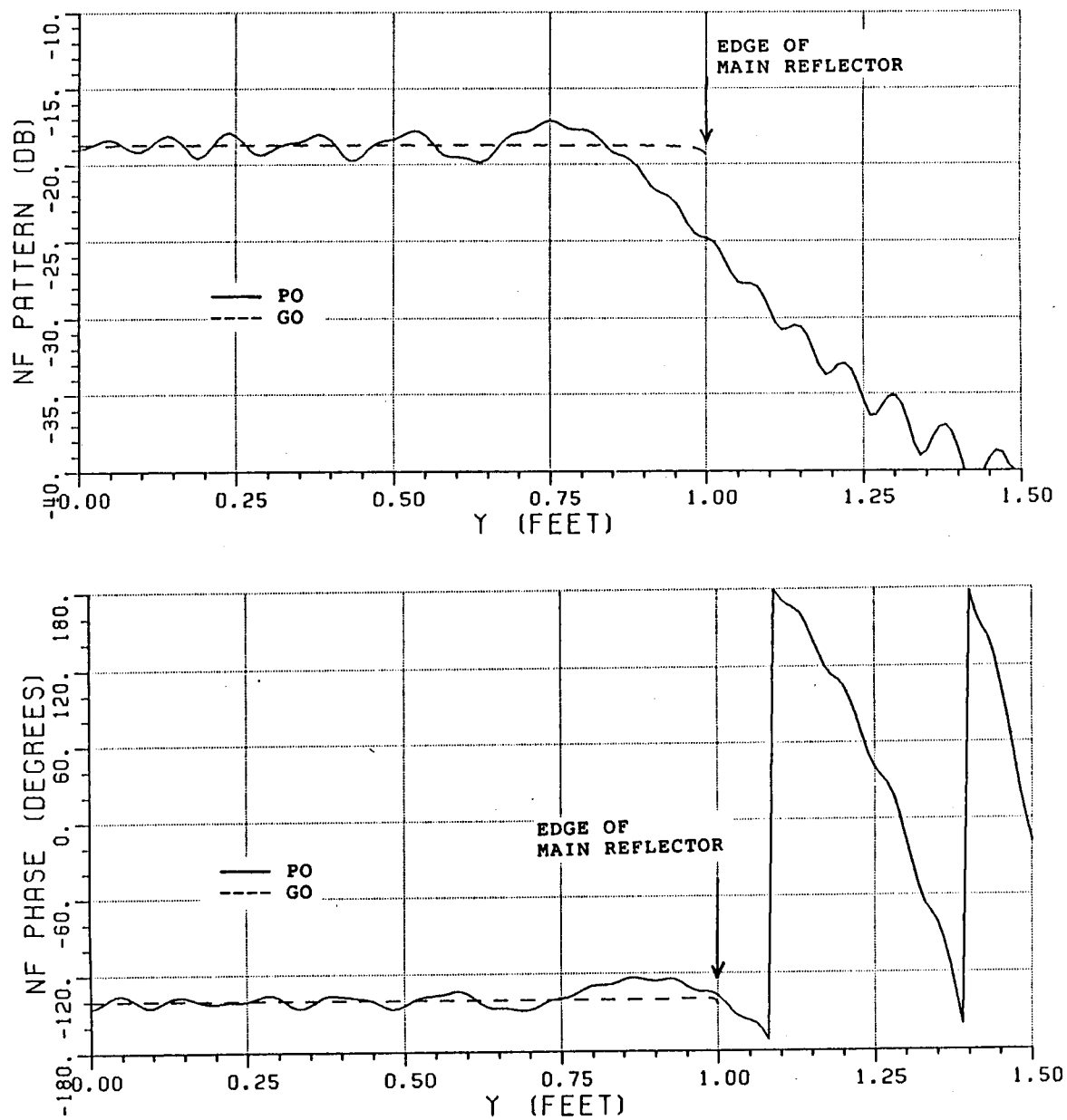


Figure 4.16. Near-zone scattered fields of the shaped main reflector of Example G2 at 20 GHz.



#### 4.2. Shaping of an Offset Reflector Antenna (Example G3)

In the previous section, a center-fed symmetric Gregorian antenna was shaped to generate a uniform plane wave with a uniform aperture distribution in which the aperture was designated between  $y=-1'$  to  $y=+1'$ . In this section, an offset fed Gregorian reflector is used as another example to illustrate that the same shaping process can be applied to an offset dual-reflector system. This example is designated as Example G3. The geometry of the initial offset Gregorian reflector is as follows:  $F_m=9.5'$ ,  $F_c=8.5'$ ,  $L_v=-1.5'$  and is shown in Figure 4.17. The central ray of the main reflector is designated at  $y=8.5'$ . The initial points on the subreflector and main reflector surfaces are chosen as the intersection points between this central ray and the initial Gregorian antenna. Consequently, the primary feed axis must be tilted by an angle of  $-7.68^\circ$ . The primary source is a magnetic line source with a radiation intensity  $\cos^{200} \phi$  with respect to the feed axis. The feed pattern is shown in Figure 4.18. A plane wave with a uniform amplitude distribution is to be obtained between  $y=-1.0'$  and  $y=18.0'$  by shaping the given offset Gregorian reflector antenna. This results in most of the power of the primary source being contained between  $\phi=-8.5^\circ$  and  $\phi=8.5^\circ$  with respect to the tilted feed axis which illuminates the subreflector. The feed pattern illuminates the edge of the subreflector at about 9.6 dB below the peak of the feed pattern.

The far-zone scattered field from the original subreflector calculated at 3 GHz is shown in Figure 4.19 for  $0^\circ \leq \theta \leq 180^\circ$  where  $\theta$  is

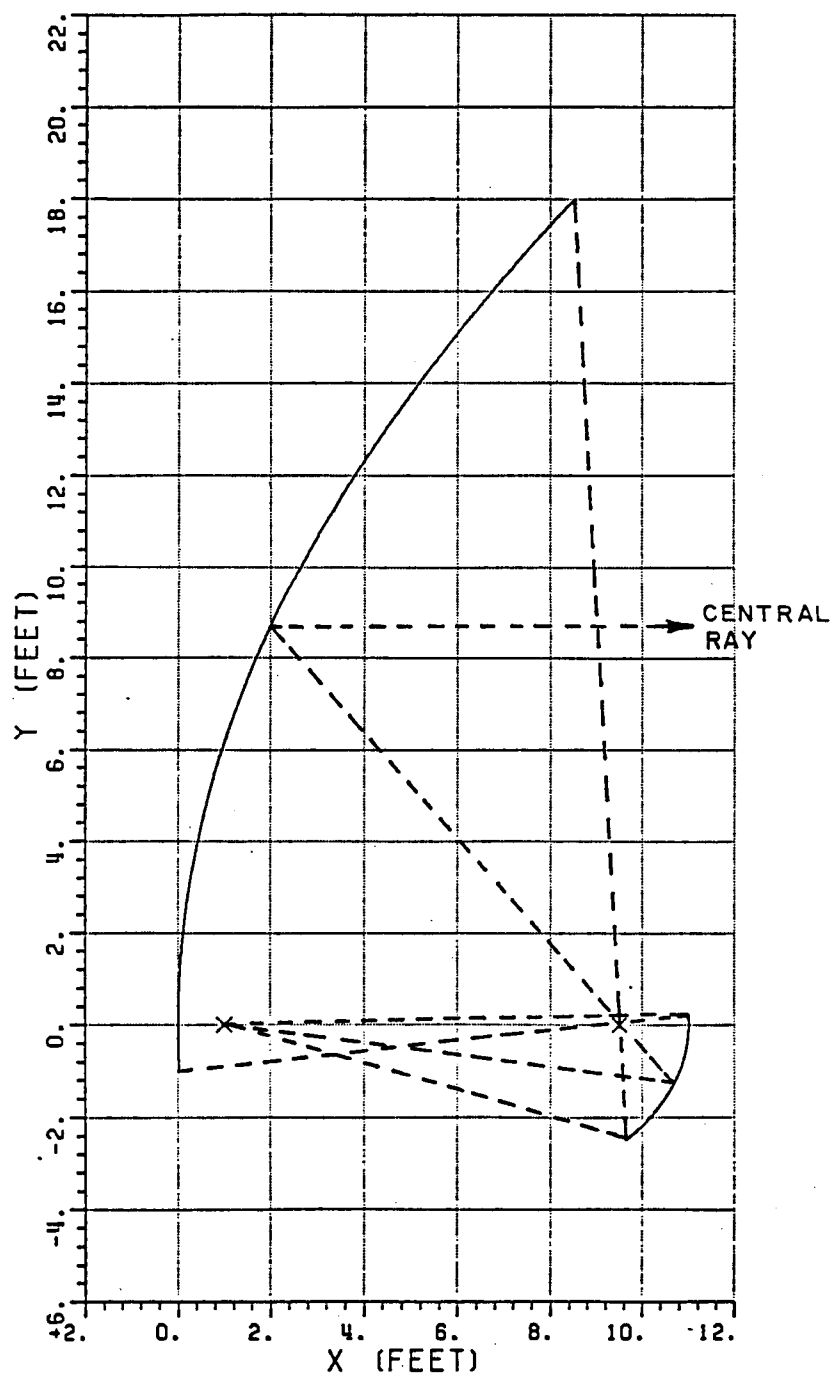


Figure 4.17. Geometry of an offset Gregorian reflector.

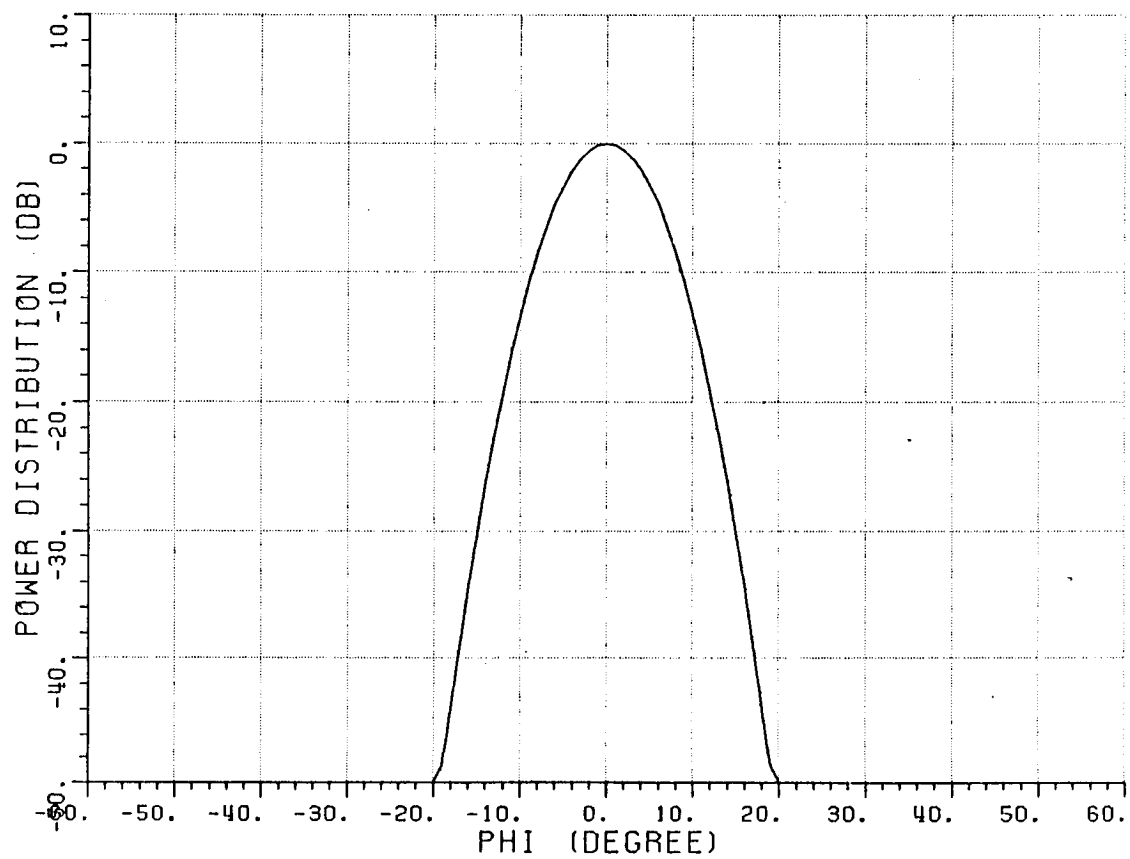


Figure 4.18. A  $\cos^{200} \phi$  power distribution.

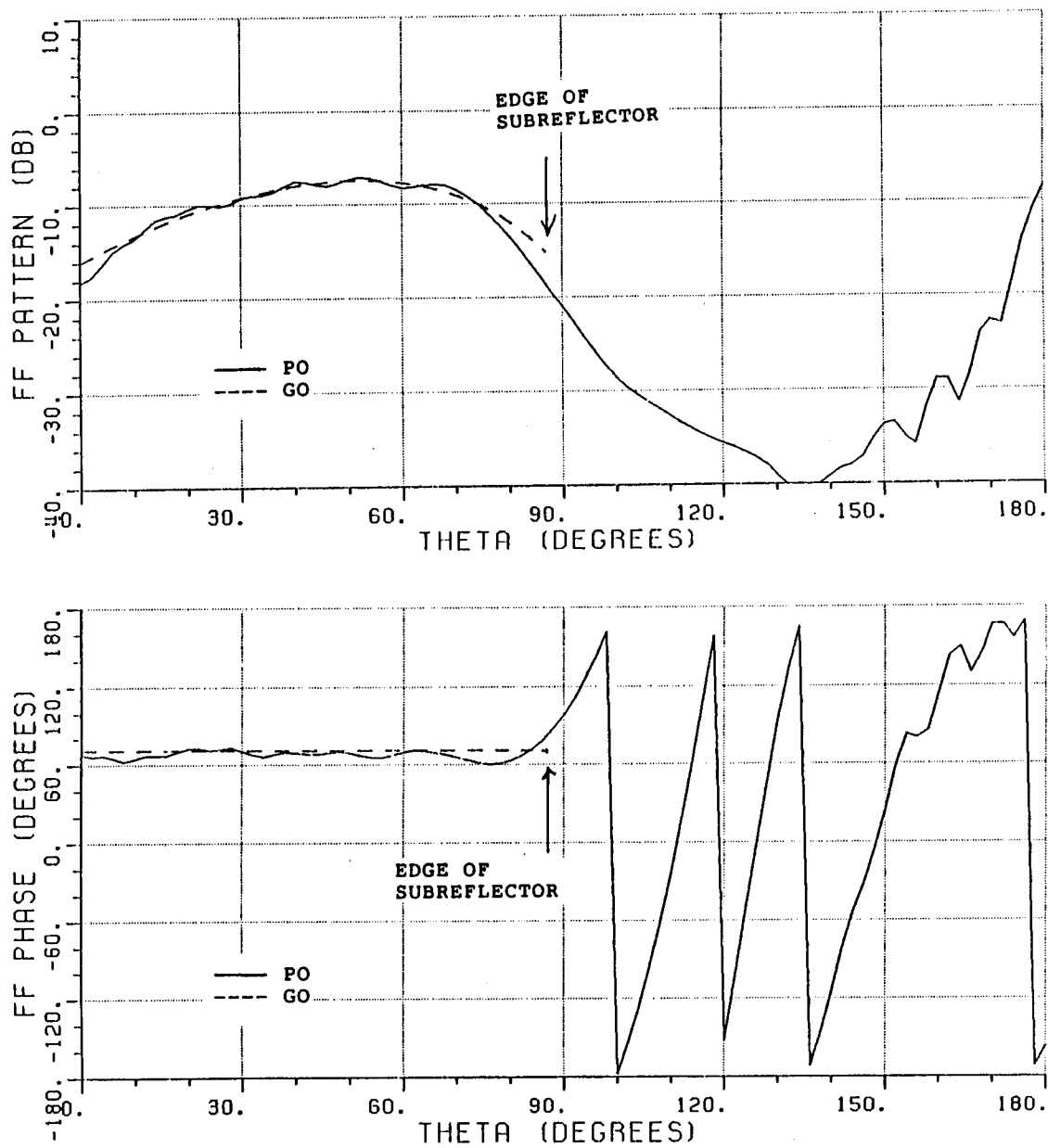


Figure 4.19. Far-zone scattered fields from subreflector of the offset Gregorian reflector with a  $\cos^{200} \phi$  magnetic line source illumination at 3 GHz.

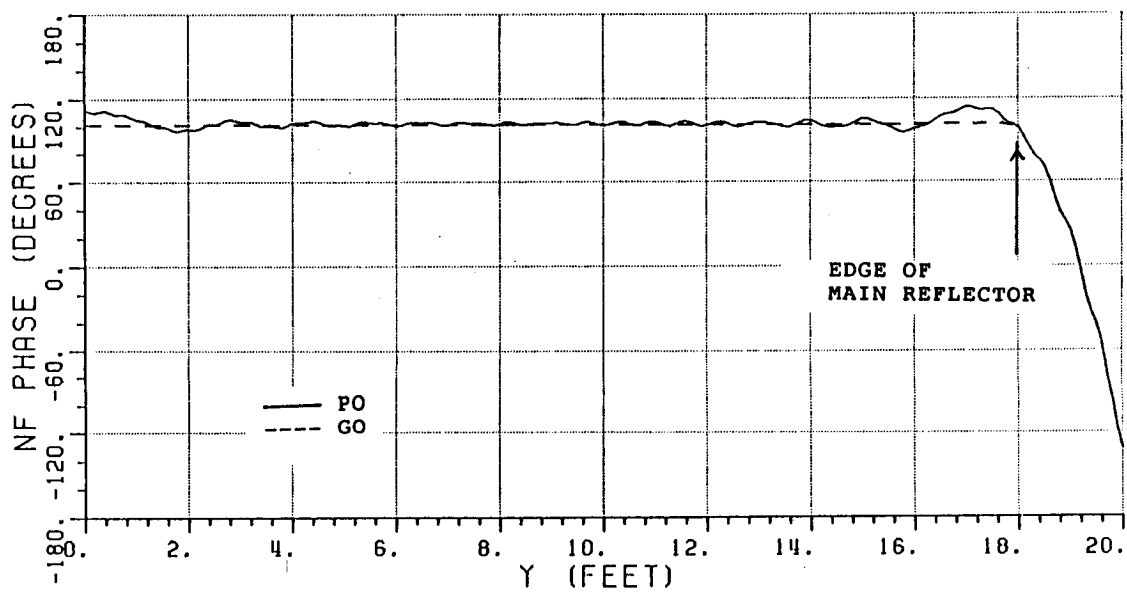
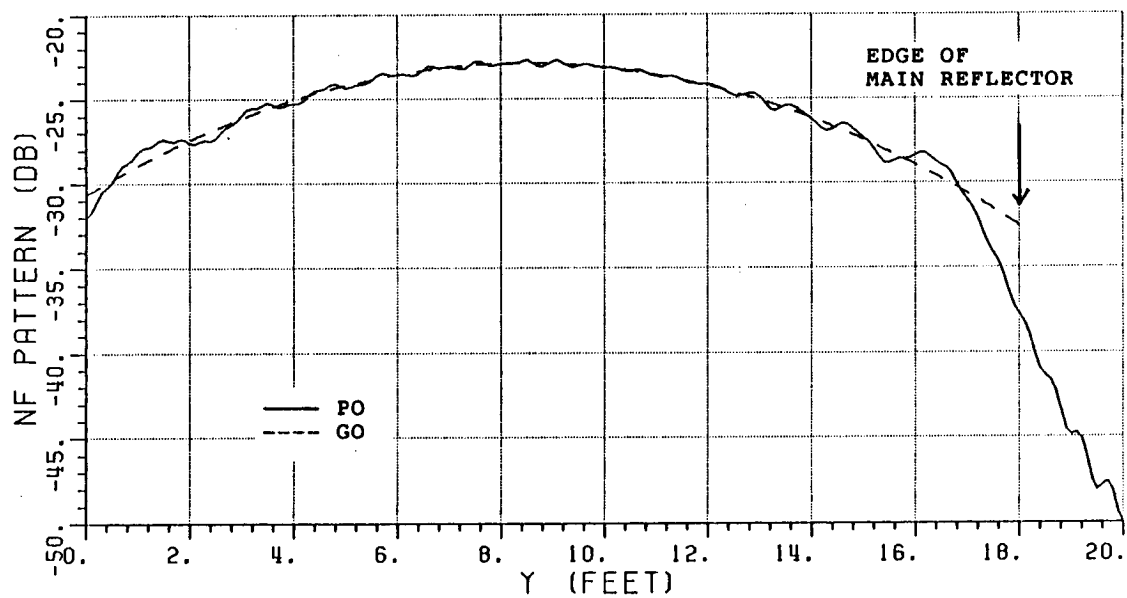


Figure 4.20. Near-zone scattered fields from the main reflector of the offset Gregorian reflector with a  $\cos^{200} \phi$  magnetic line illumination at 3 GHz.

measured from the negative x-axis. The near-zone scattered field of the original main reflector calculated in the  $x=20.0'$  plane and at 3 GHz is shown in Figure 4.20. It can be seen from Figure 4.20 that the original offset Gregorian reflector has an aperture edge taper of about 10 dB.

The initial point on the caustic curve is determined by the ray condition, and the resulting shaped reflectors are given in Figures 4.21 and 4.22. Figure 4.23 shows two rays for the shaped reflectors. The far-zone scattered fields from the shaped subreflector and the near-zone scattered fields from the shaped main reflector calculated at 3 GHz are shown in Figures 4.24 and 4.25, respectively. It is obvious that the requirement of obtaining a uniform aperture distribution is approximately achieved except for the ripple which is caused by the interaction of the edge diffracted field with the reflected field.

#### 4.3. Shaping of a Center-Fed Cassegrain Reflector Antenna for Uniform Aperture Distribution (Example C1)

An example of shaping a center-fed Cassegrain reflector is discussed in this section. The geometry of the original antenna is given in Figure 4.26 with the following parameters:

$$F_m = 0.6667'$$

$$F_c = 0.5667'$$

$$L_v = 0.1'$$

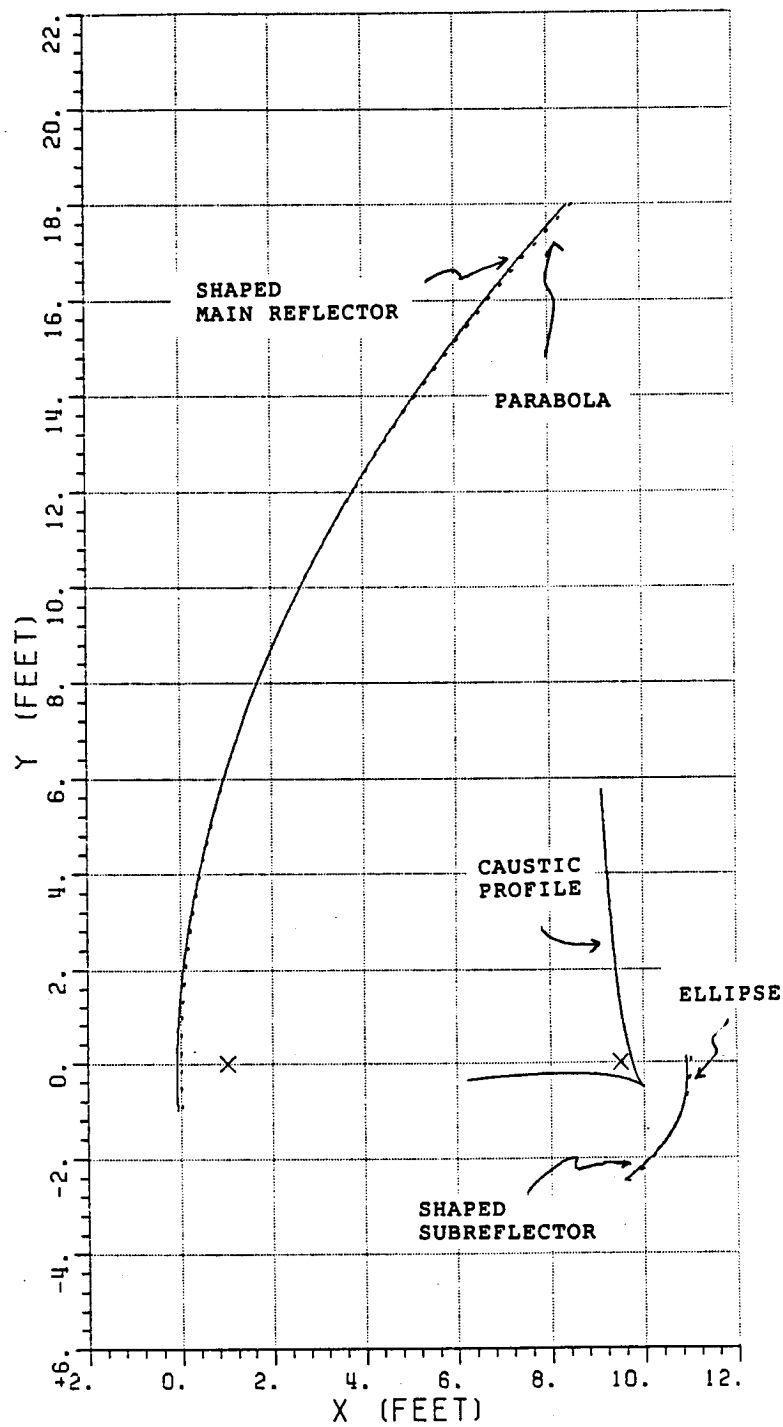


Figure 4.21. Geometry of the shaped offset dual-reflector.

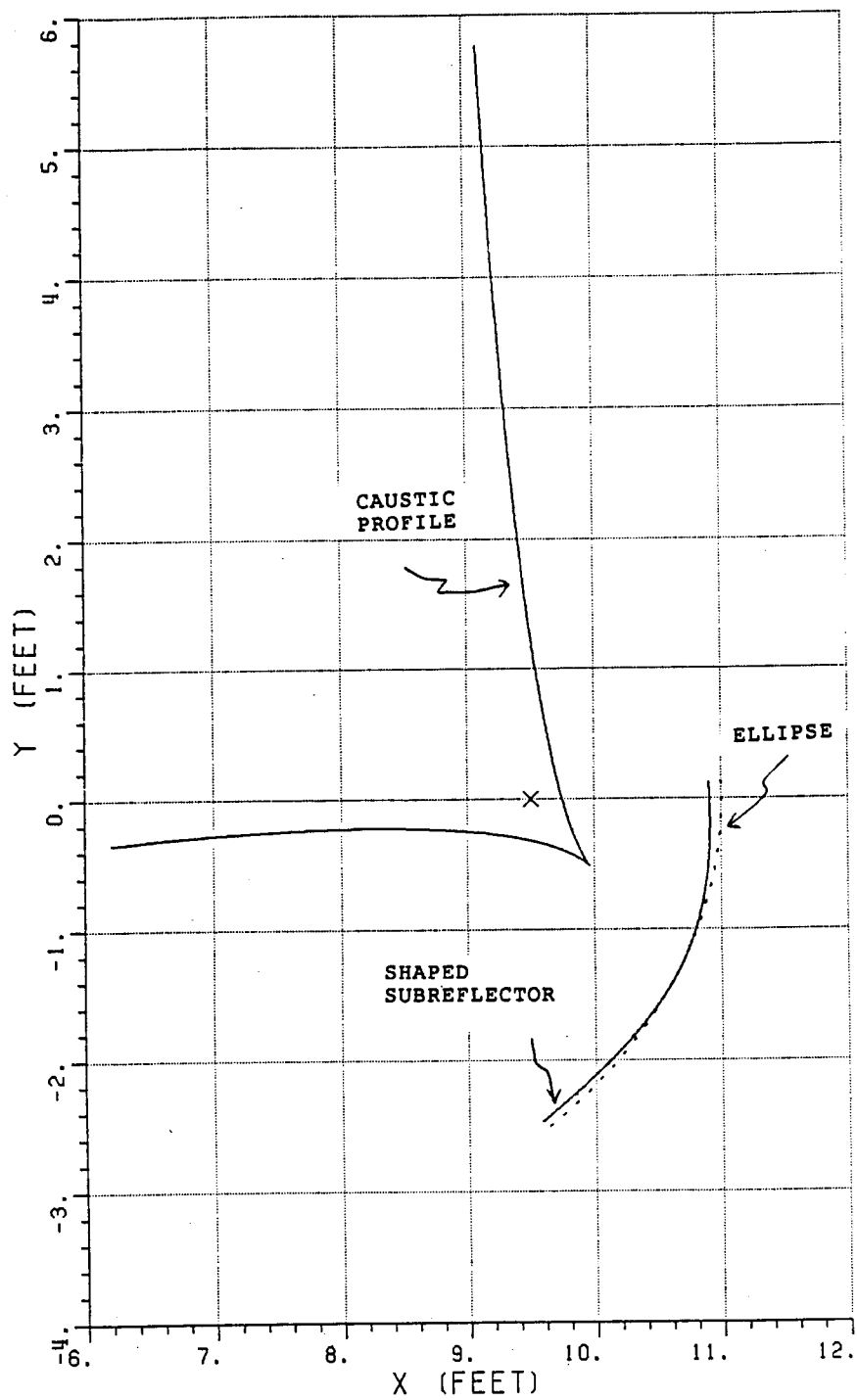


Figure 4.22. Caustics and subreflector of the shaped offset dual-reflector.



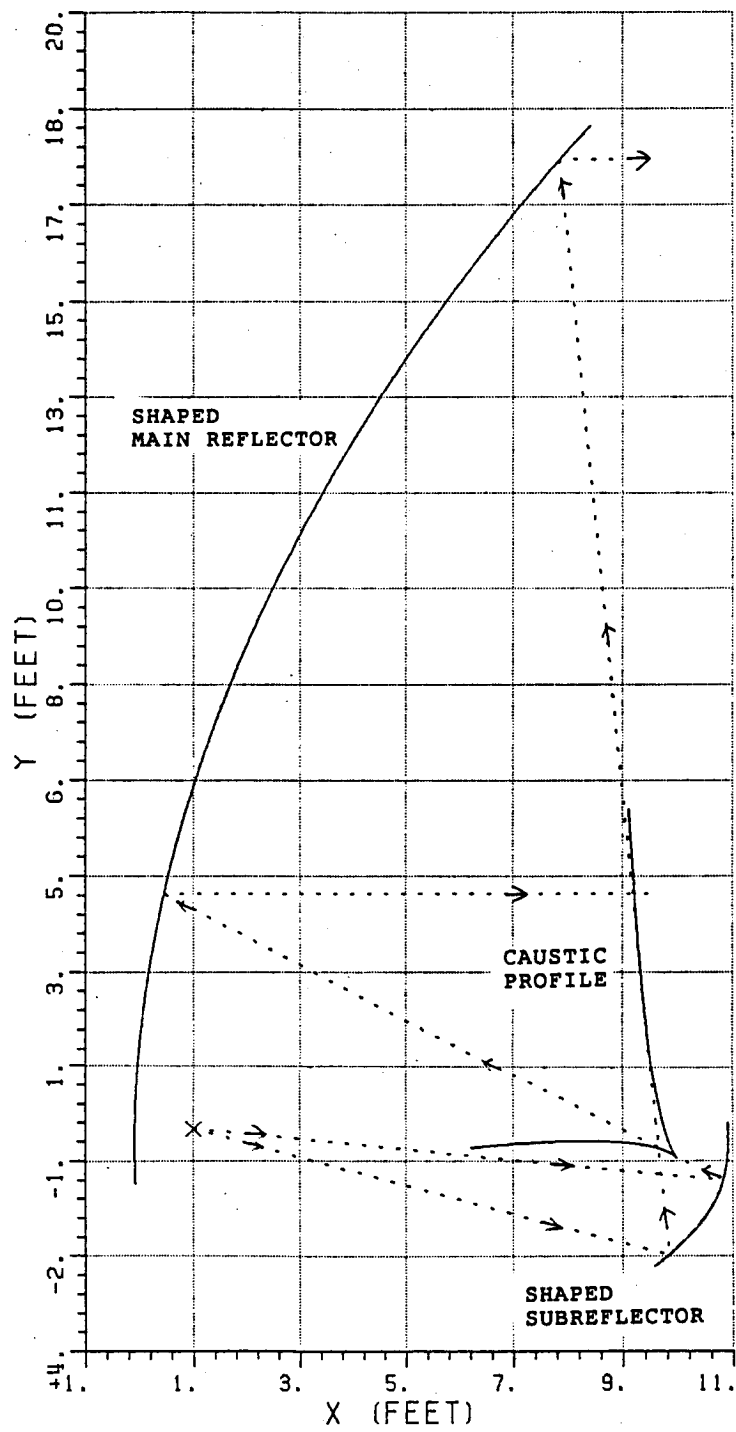


Figure 4.23. Ray geometries for the shaped reflectors of Example G3.

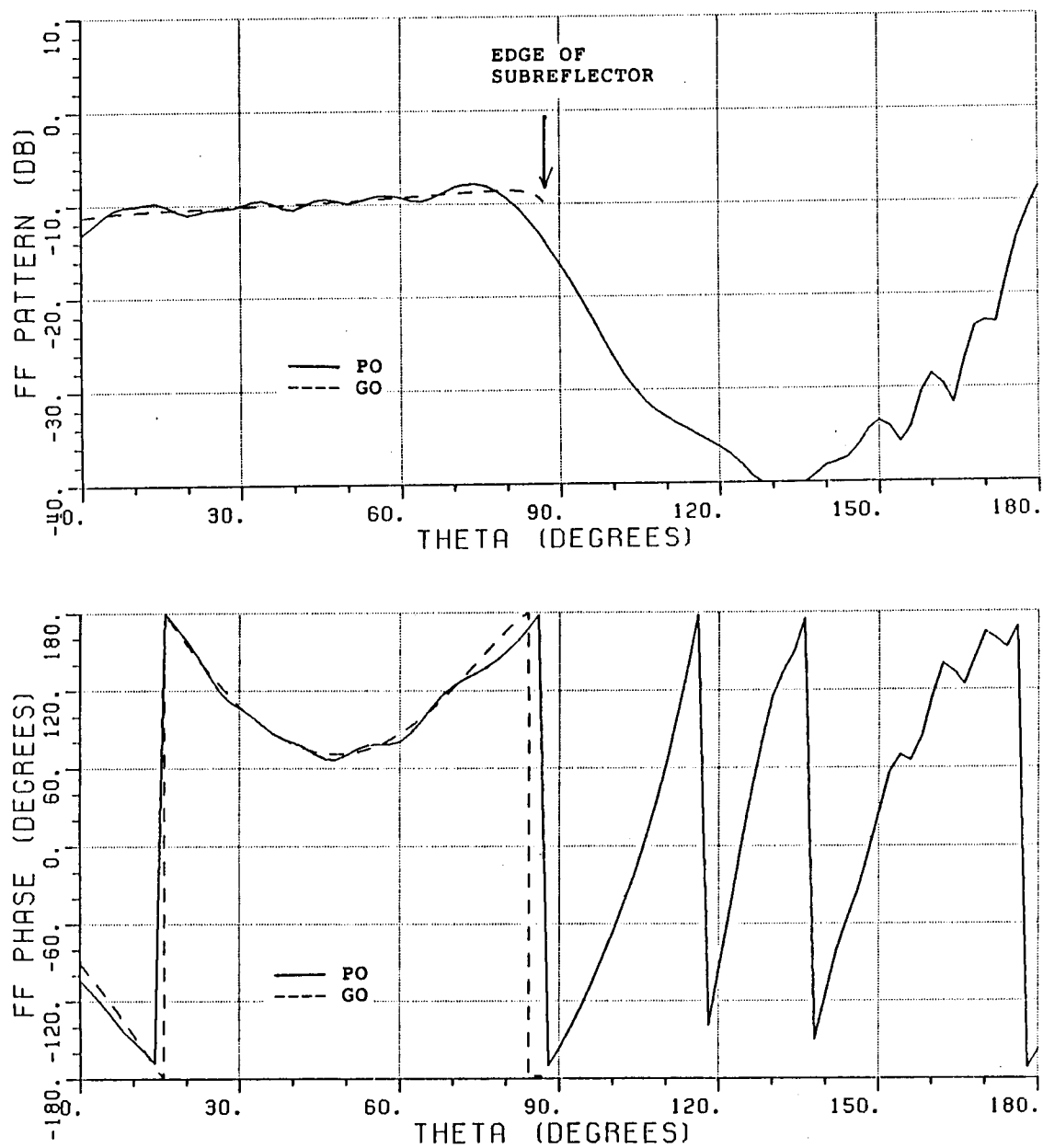


Figure 4.24. Far-zone scattered fields from the subreflector of the shaped offset dual-reflector with a  $\cos^{200} \phi$  magnetic line source illumination at 3 GHz.

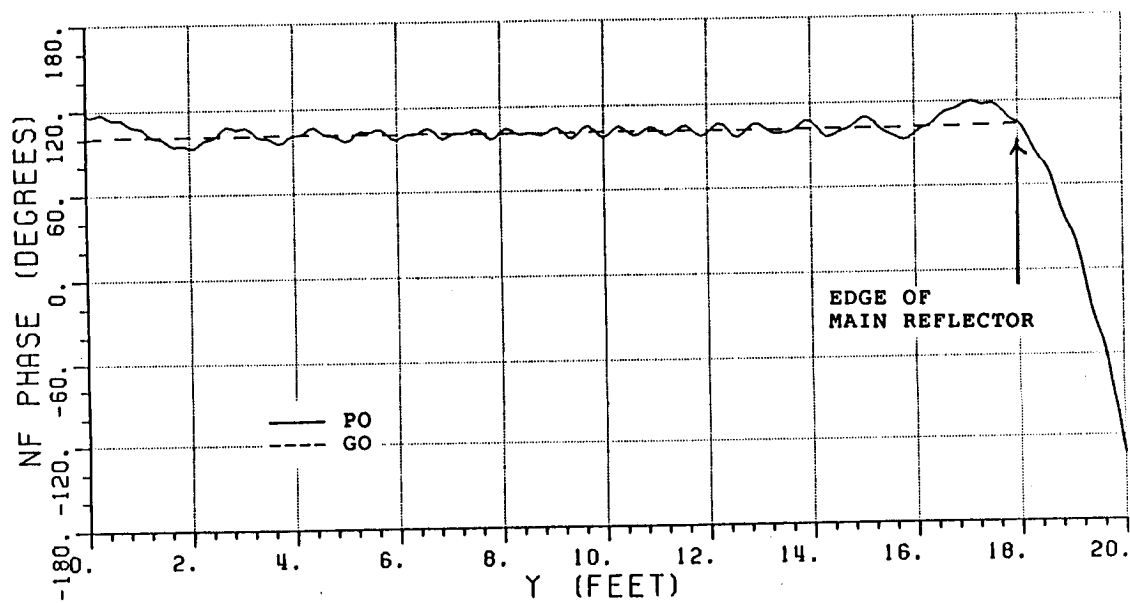
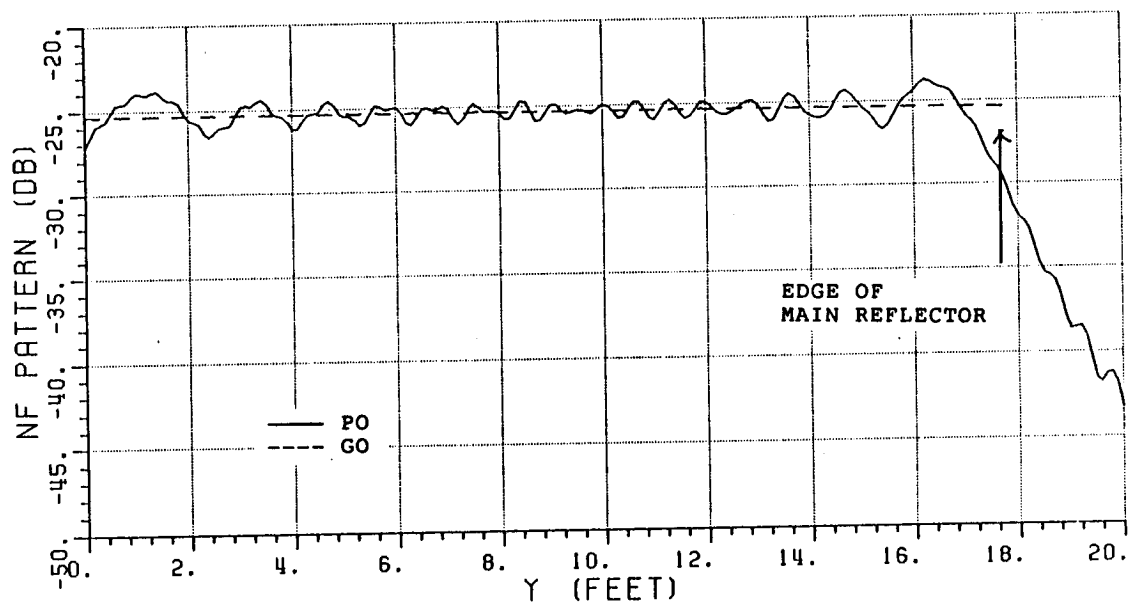


Figure 4.25. Near-zone scattered fields from the main reflector of the shaped offset dual-reflector with a  $\cos^{200} \phi$  magnetic line source illumination at 3 GHz.

C-2

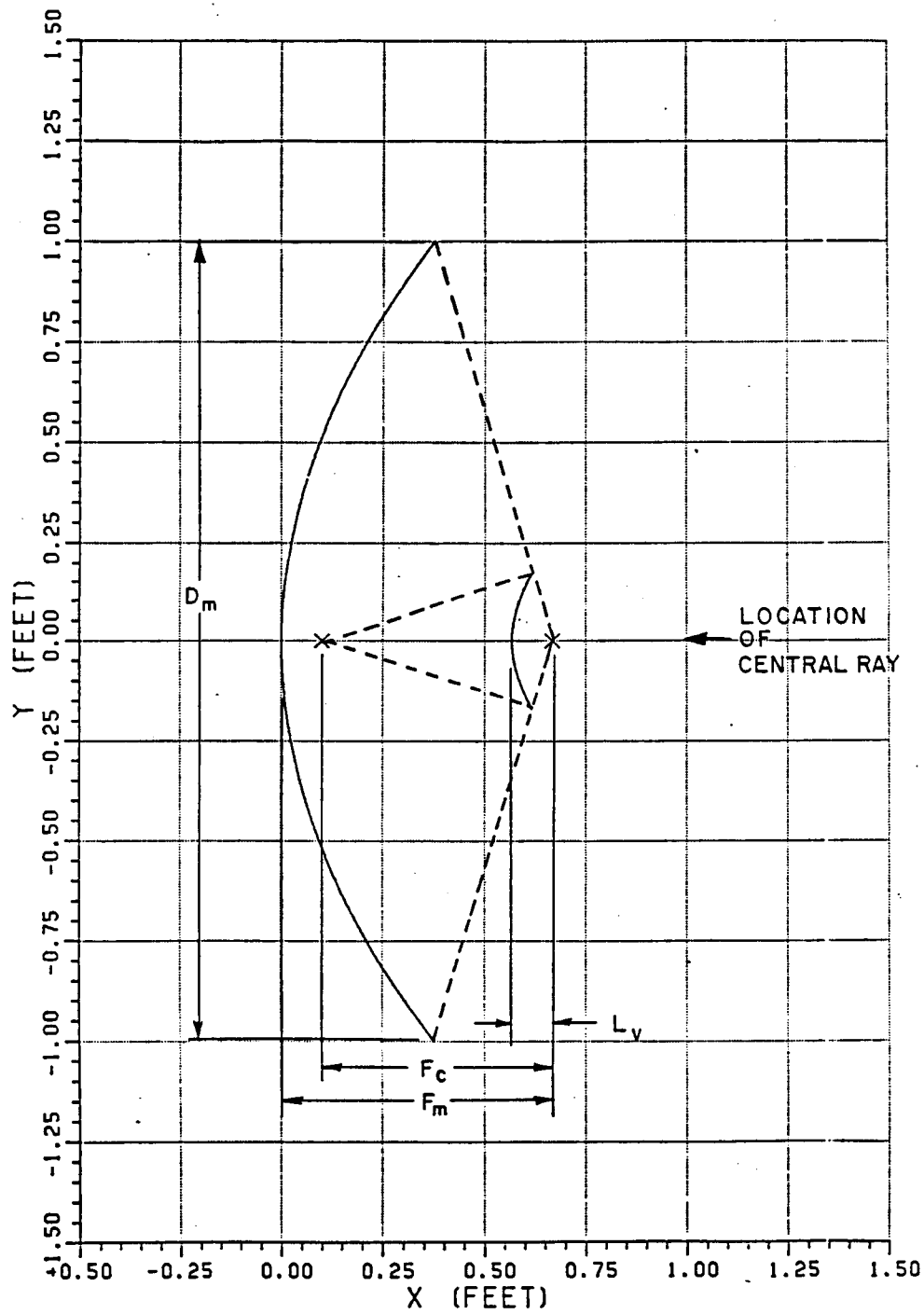


Figure 4.26. A conventional Cassegrain antenna.

$$D_m = 2.0'$$

$$\phi_r = 18.26^\circ$$

A  $\cos^{20} \phi$  power pattern magnetic line source is used as the primary source. The incident field at the edge of the subreflector is 4.5 dB down from the maximum. A uniform plane wave with a uniform amplitude is to be generated between  $y = -1'$  and  $y = 1'$  in which the central ray is defined at  $y = 0$ . The initial points for the shaped reflectors are chosen at the intersection points between the central ray and the original reflectors. The initial point on the caustic curve is thus determined. The resulting shaped reflectors are shown in Figures 4.27 and 4.28 with the original reflectors indicated by dashed lines and the shaped reflectors by solid ones. The upper half of the caustic curve corresponds to the lower half of the subreflector and main reflector; whereas, the lower half of the caustic curve corresponds to the remaining surfaces. The behaviour of the caustic curve can be explained in the same way as for the Gregorian case which is given in Example G1. The caustic curve moves away from the subreflector surface in order to increase the reflected caustic distance  $\rho_c$ , which is given as

$$\sqrt{\frac{\rho_c}{(s_1 + \rho_c)}}$$

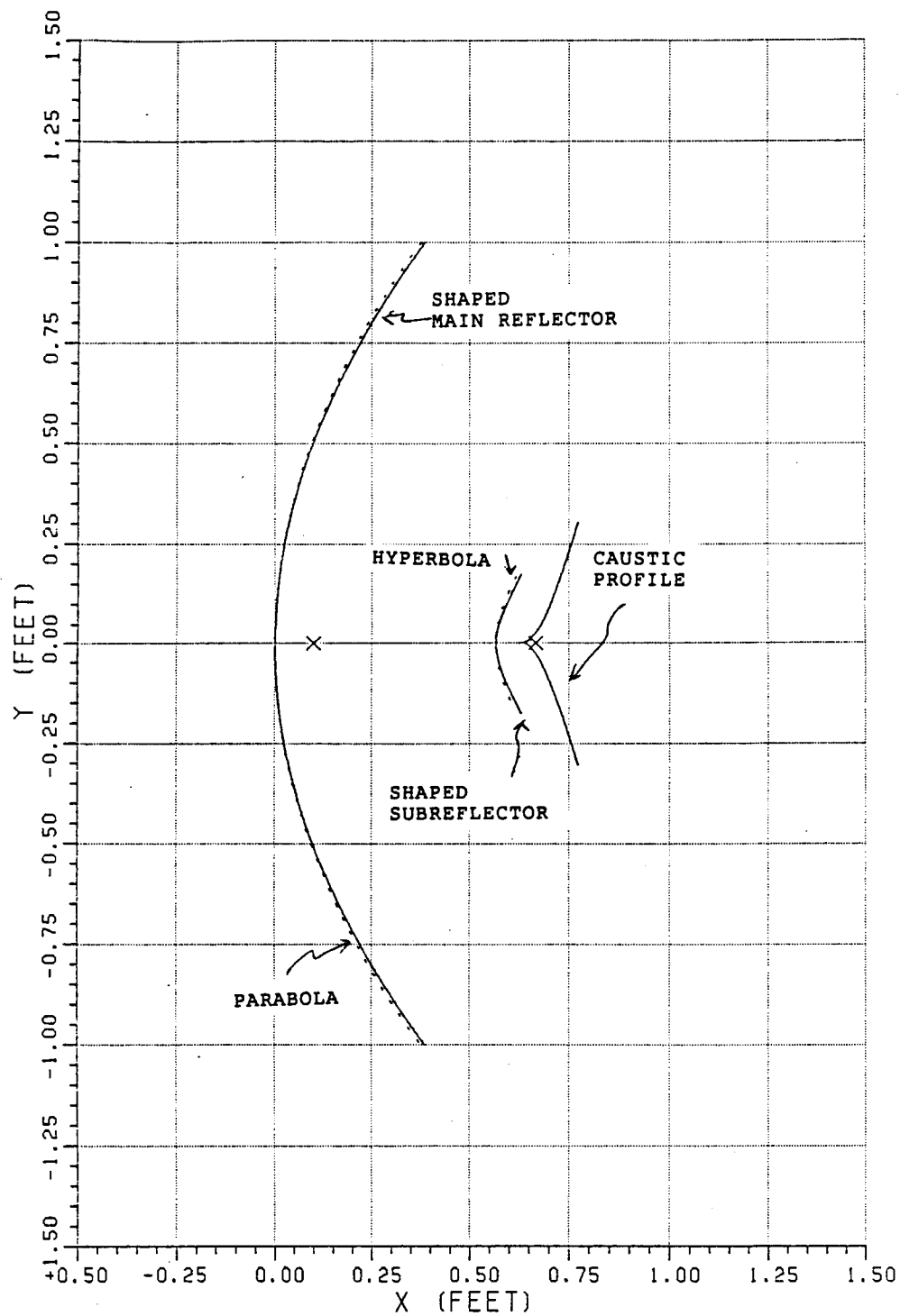


Figure 4.27. Shaped dual-reflector with convex subreflector of Example C1.

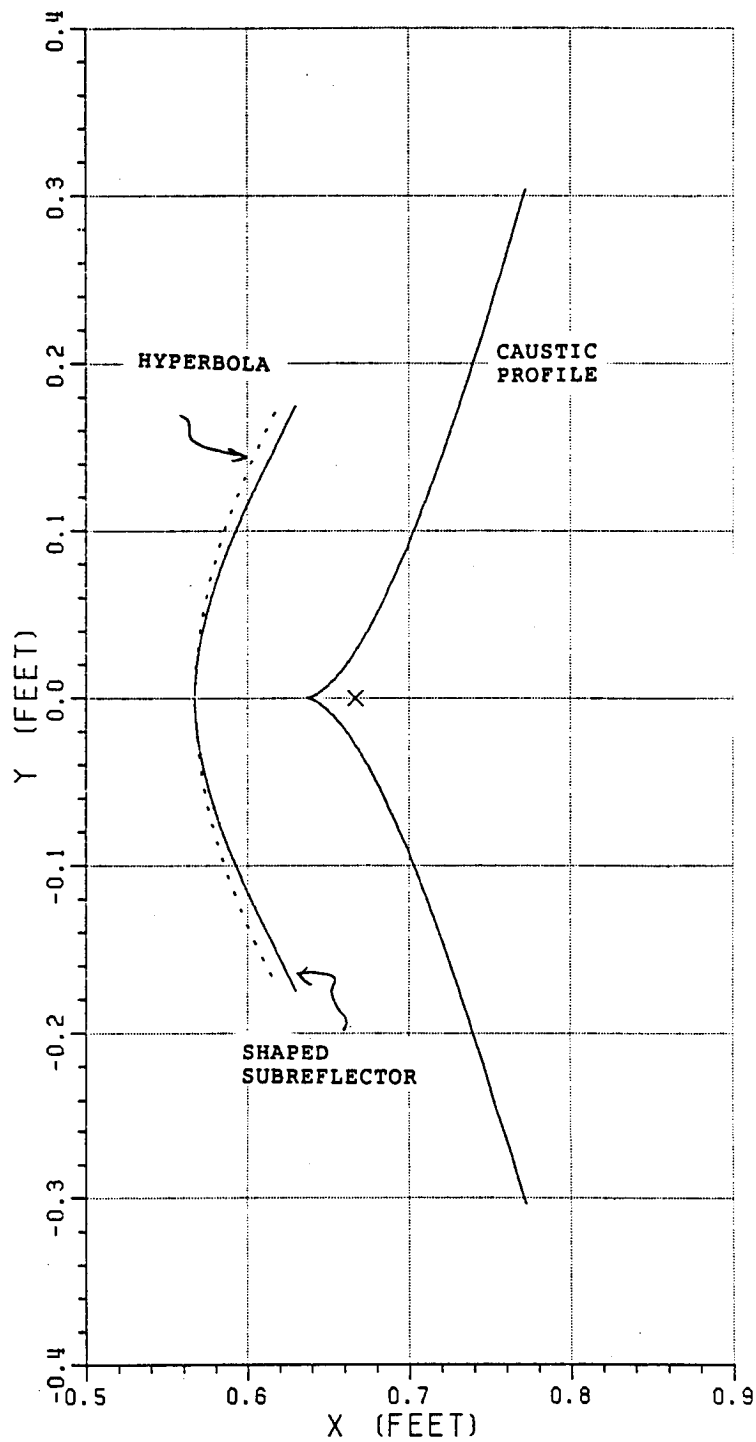


Figure 4.28. Subreflector with the convex surface of shaped dual-reflector Example C1.

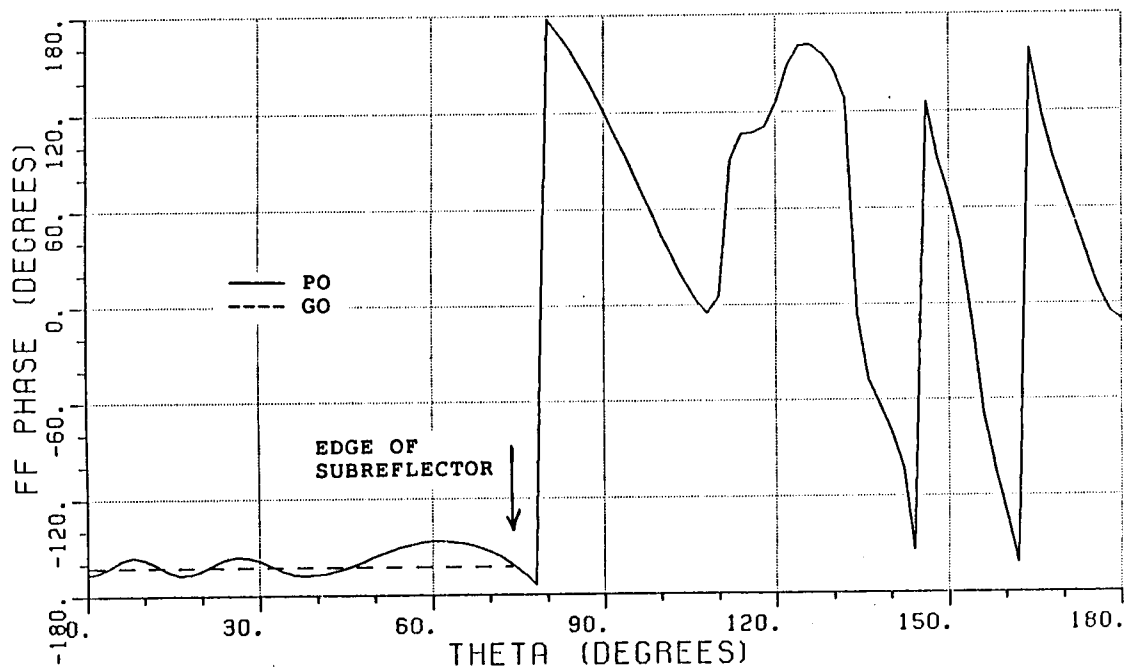
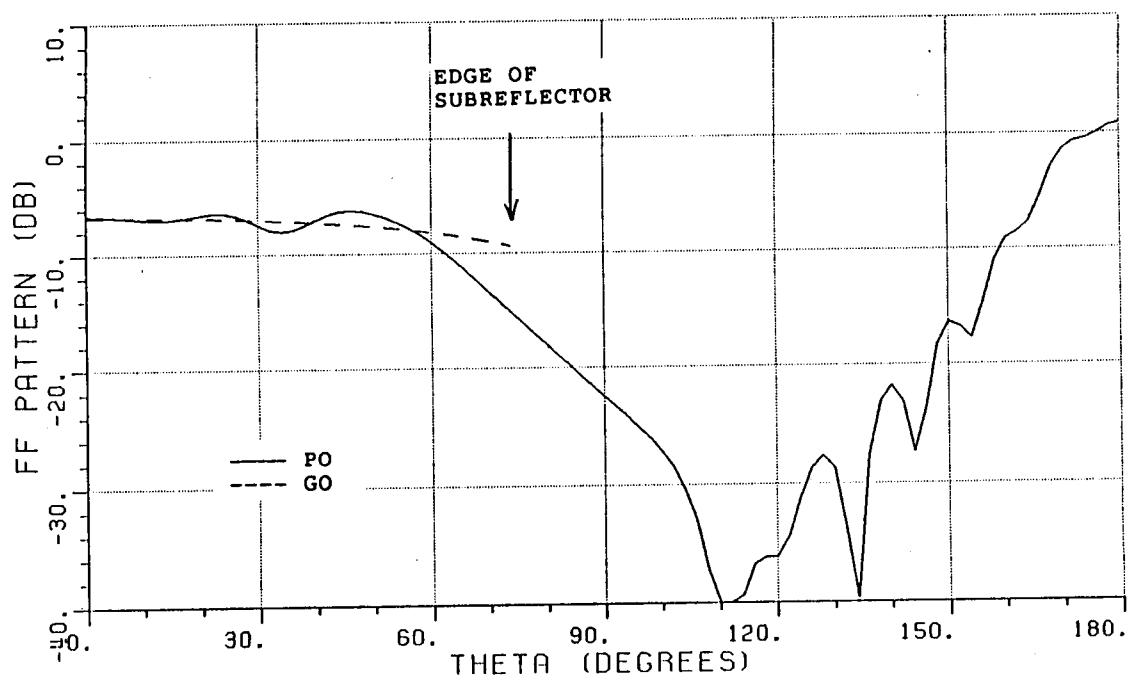


Figure 4.29. Far-zone scattered fields from the subreflector of the conventional Cassegrain antenna at 20 GHz.



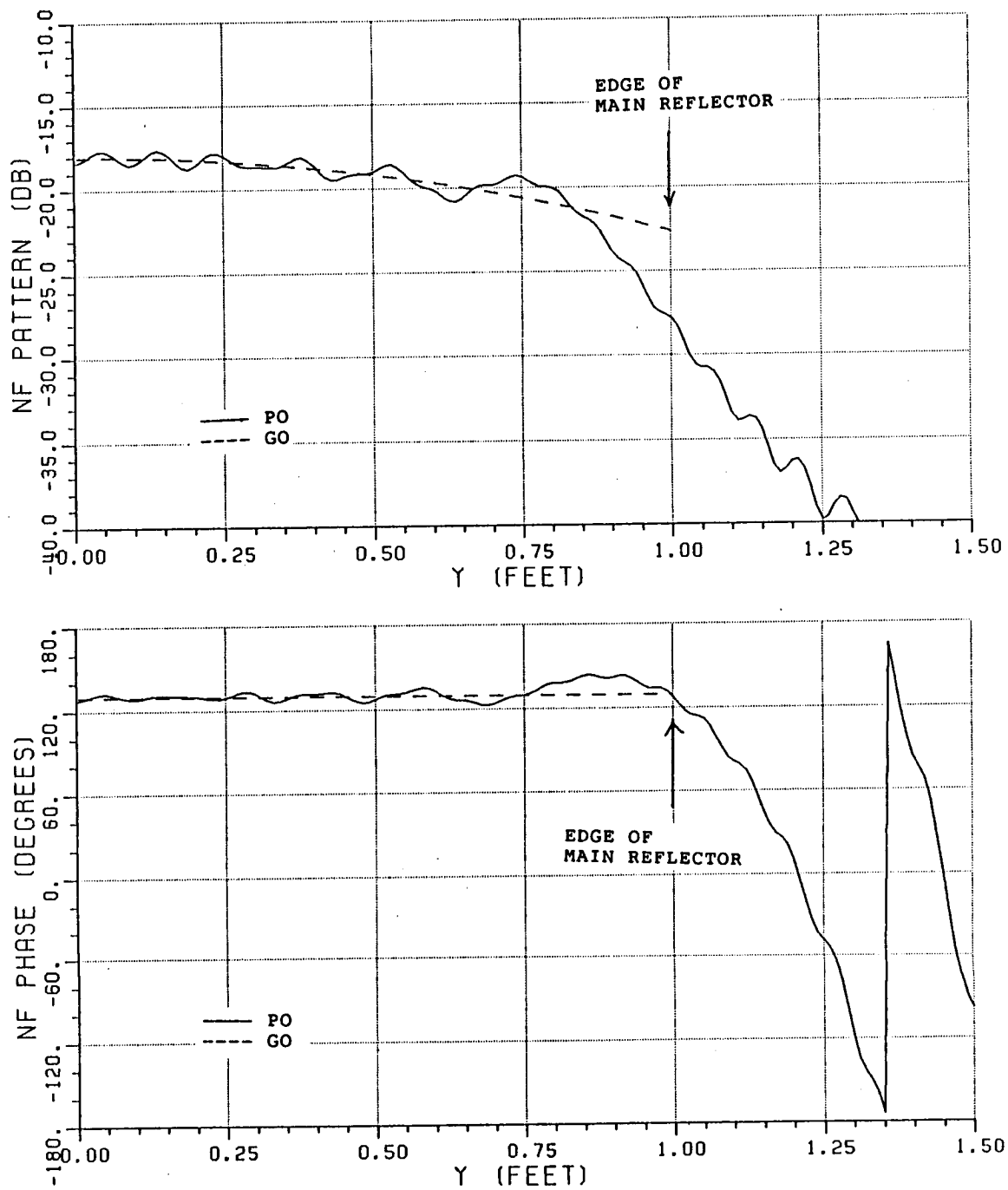


Figure 4.30. Near-zone scattered field from the main reflector of the conventional Cassegrain reflector at 20 GHz.

Note that  $\rho_c$  increases in order to increase the reflected field and thus compensate for the taper of the primary source pattern.

The scattered fields of the original subreflector and main reflector calculated at 20 GHz are shown in Figures 4.29 and 4.30. The scattered fields of the shaped reflectors are shown in Figures 4.31 and 4.32. Two ray geometries for the shaped reflectors are shown in Figure 4.33.

#### 4.4. Shaping of a Center-Fed Gregorian Reflector Antenna for Non-Uniform Aperture Amplitude Distribution (Example G4)

In the previous examples, the purpose of shaping was to generate a uniform amplitude distribution across a given aperture. In this section, an example is used to illustrate that the same shaping process can be used to generate a non-uniform amplitude distribution. The Gregorian reflector antenna of example G1 and a magnetic line source with  $\cos^{20} \phi$  power pattern are used to generate the following aperture distribution:

$$I(y) = \begin{cases} 1 & |y| \leq 0.5' \\ \left[ 386.547 \left( \frac{y-0.5}{0.8} \right)^8 + 1 \right]^{-1}, & 1' \geq |y| \geq 0.5' \end{cases}$$

This aperture distribution which is shown in Figure 4.34 has a -10dB edge taper at the edge of the main reflector; i.e.,  $y=\pm 1.0'$ . The central ray is thus at  $y=0'$ .

The resulting shaped reflectors are given in Figures 4.35 and 4.36. It can be seen from these results that the caustic curve has a discontinuity. The explanation for this behavior is that since the aperture field is a function of

$$\sqrt{\frac{-\rho_c}{(s_1 - \rho_c)}}$$

where  $\rho_c$  is the distance between caustic and the reflection point on the subreflector, the shaping process tried to make  $\rho_c$  smaller in order to generate a rapidly decreasing subreflector reflected field and aperture distribution. Figure 4.37 shows two rays for the shaped reflectors.

The far-zone scattered fields of the shaped subreflector are given in Figure 4.38; while, the near-zone scattered fields calculated in the  $x=2.0'$  plane of the main reflector are given in Figure 4.39. These scattered fields are calculated at 20 GHz. One can see that the amplitude of the ripple on the near-zone scattered fields is smaller than for the uniform aperture distribution case (i.e., Examples G1 and G2) since the incident field at the main reflector edges is smaller, the edge diffraction is not as significant.

#### 4.5 Summary

Several examples are given in this chapter to demonstrate the shaping process discussed in Chapter III. Scattered field results are calculated for each case. These results indicate that the shaped reflector can provide considerable improvement in obtaining the desired

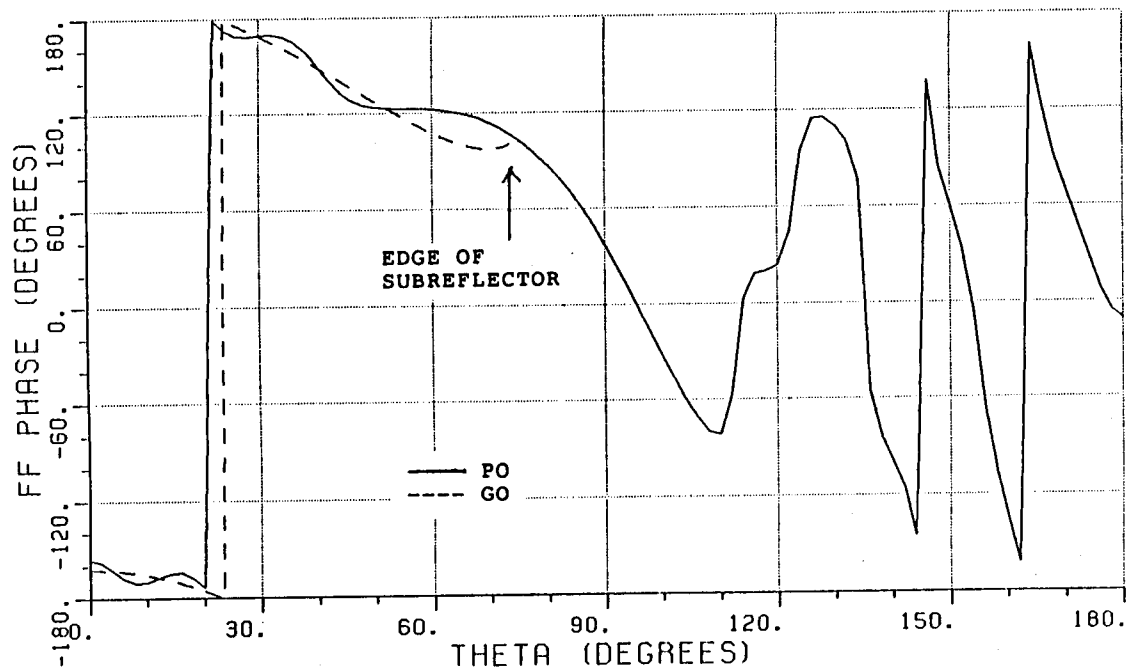
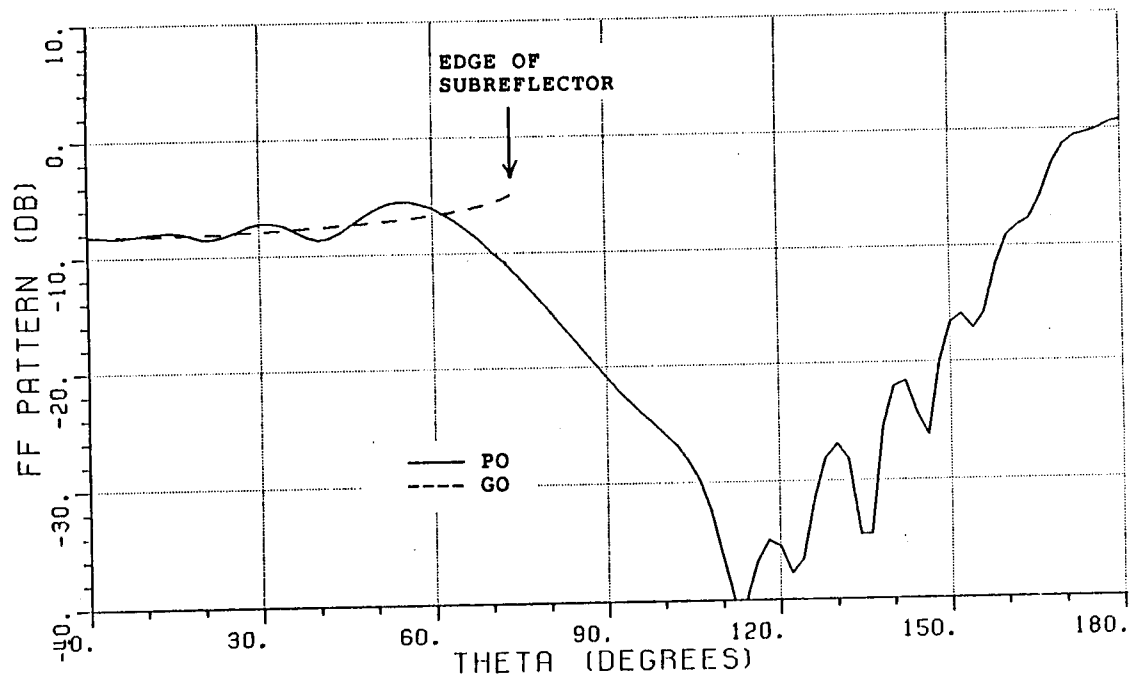


Figure 4.31. Far-zone scattered field from the convex subreflector of the shaped dual-reflector of Example C1 at 20 GHz.

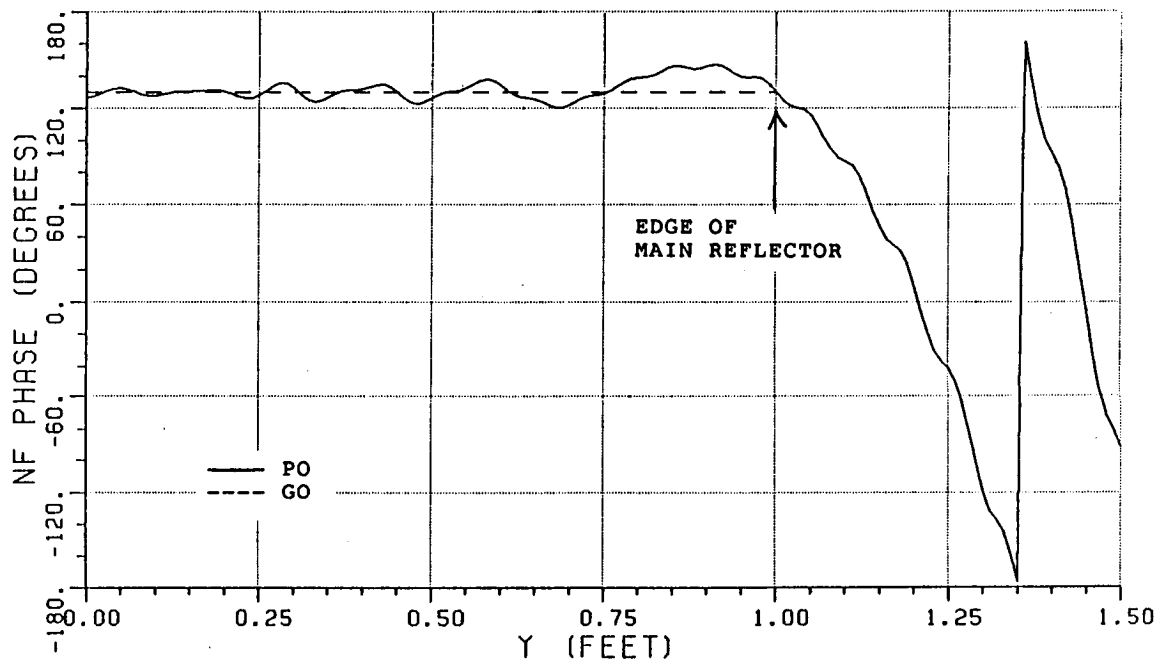
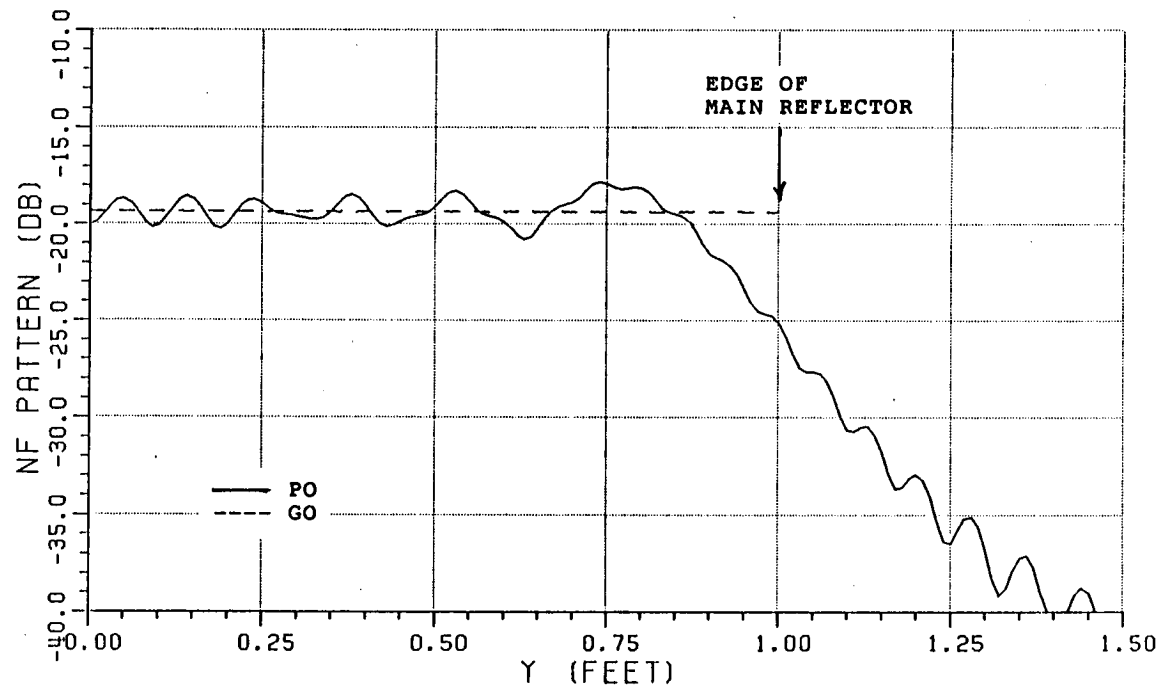


Figure 4.32. Near-zone scattered field from the main reflector of the shaped dual-reflector of Example C1 at 20 GHz.

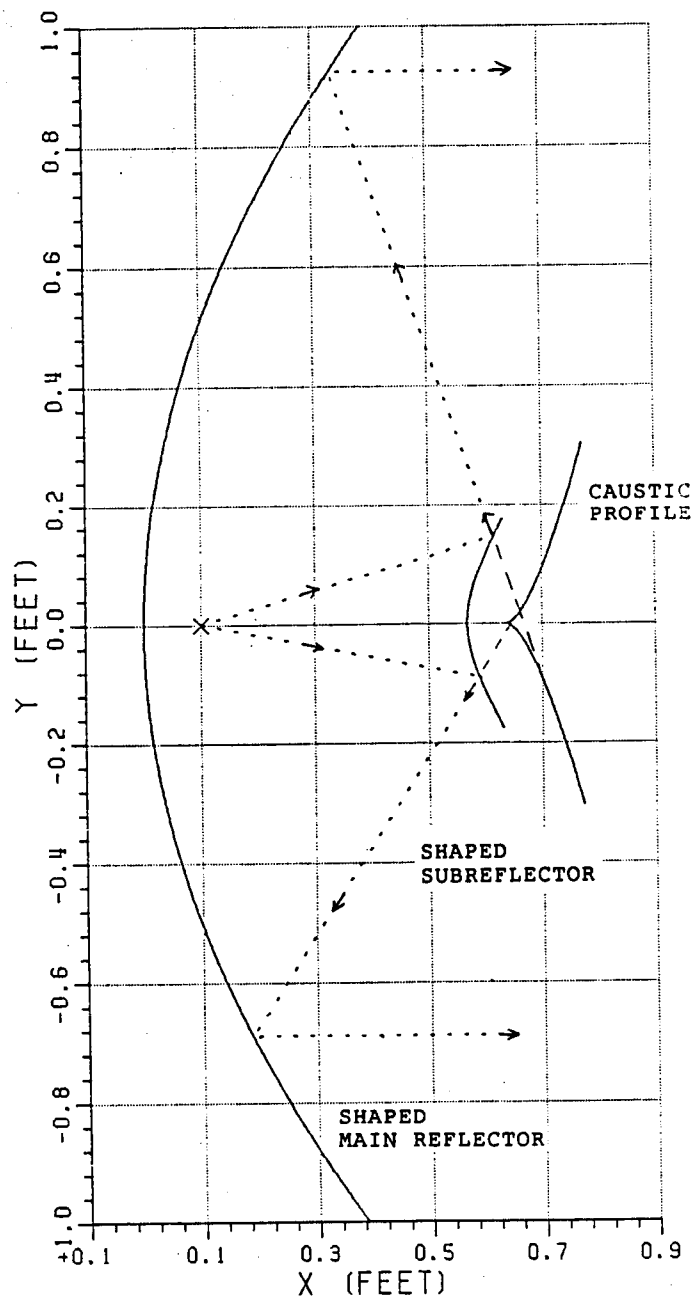


Figure 4.33. Ray geometries for the shaped reflectors of Example C1.

ORIGINAL PAGE IS  
OF POOR QUALITY

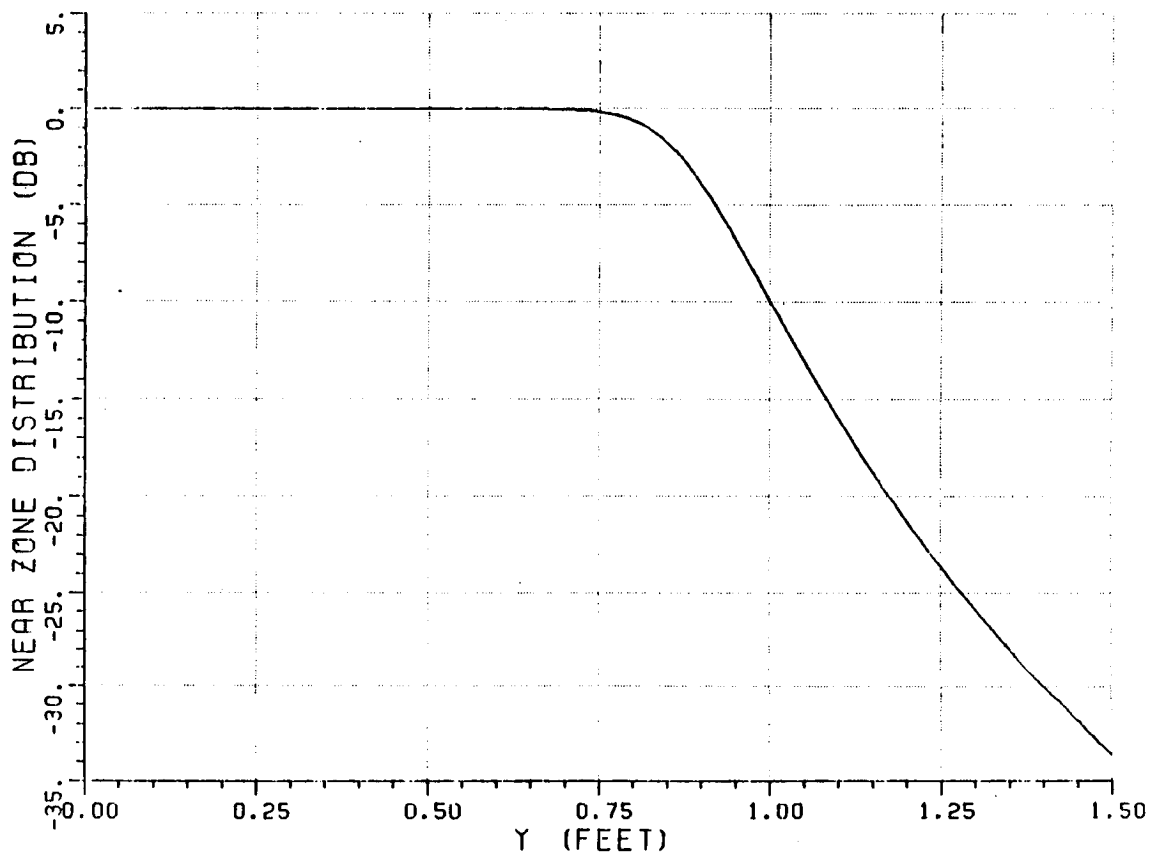


Figure 4.34. Desired near-zone aperture distribution of Example G4.

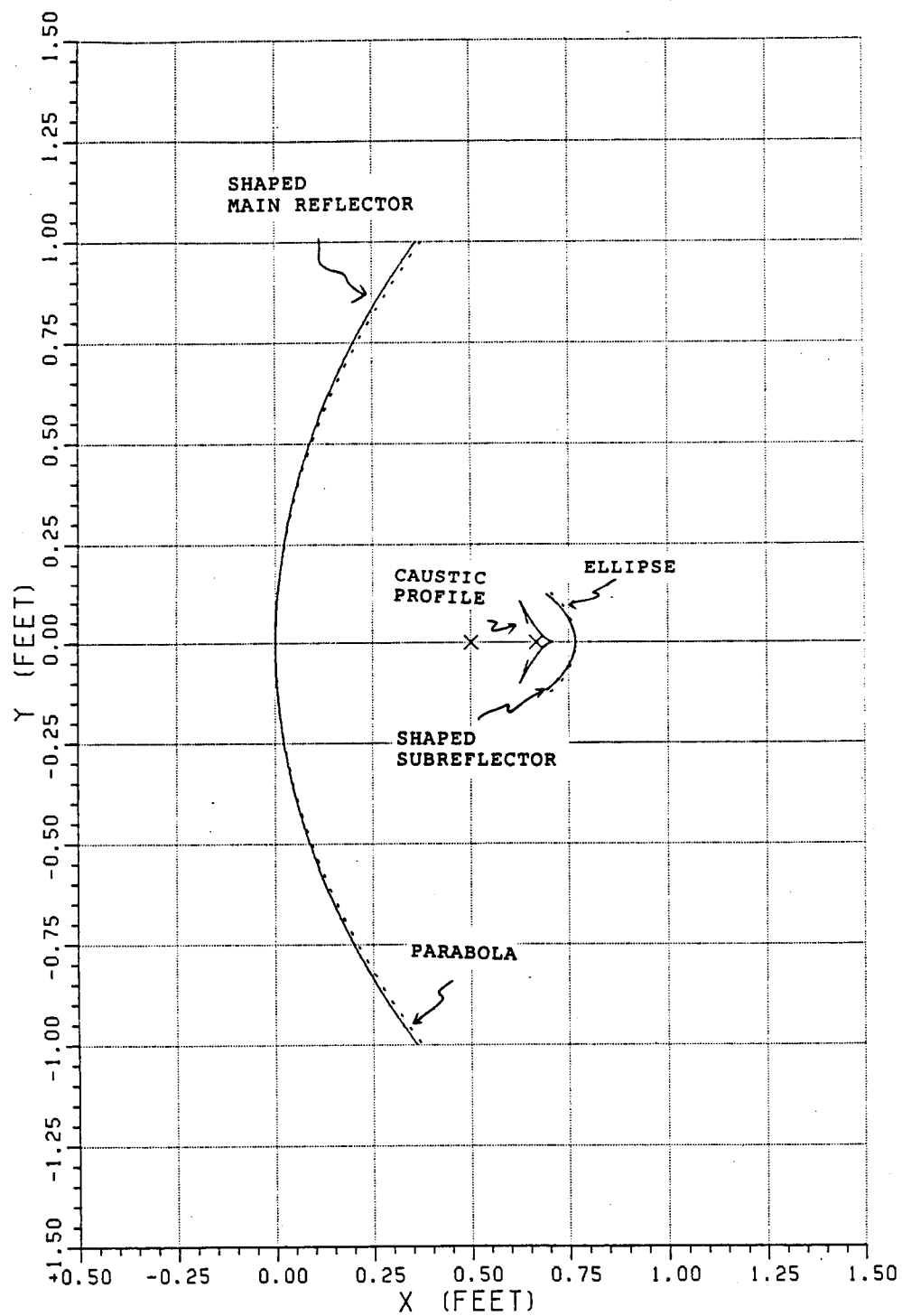


Figure 4.35. Shaped dual-reflector of Example G4.



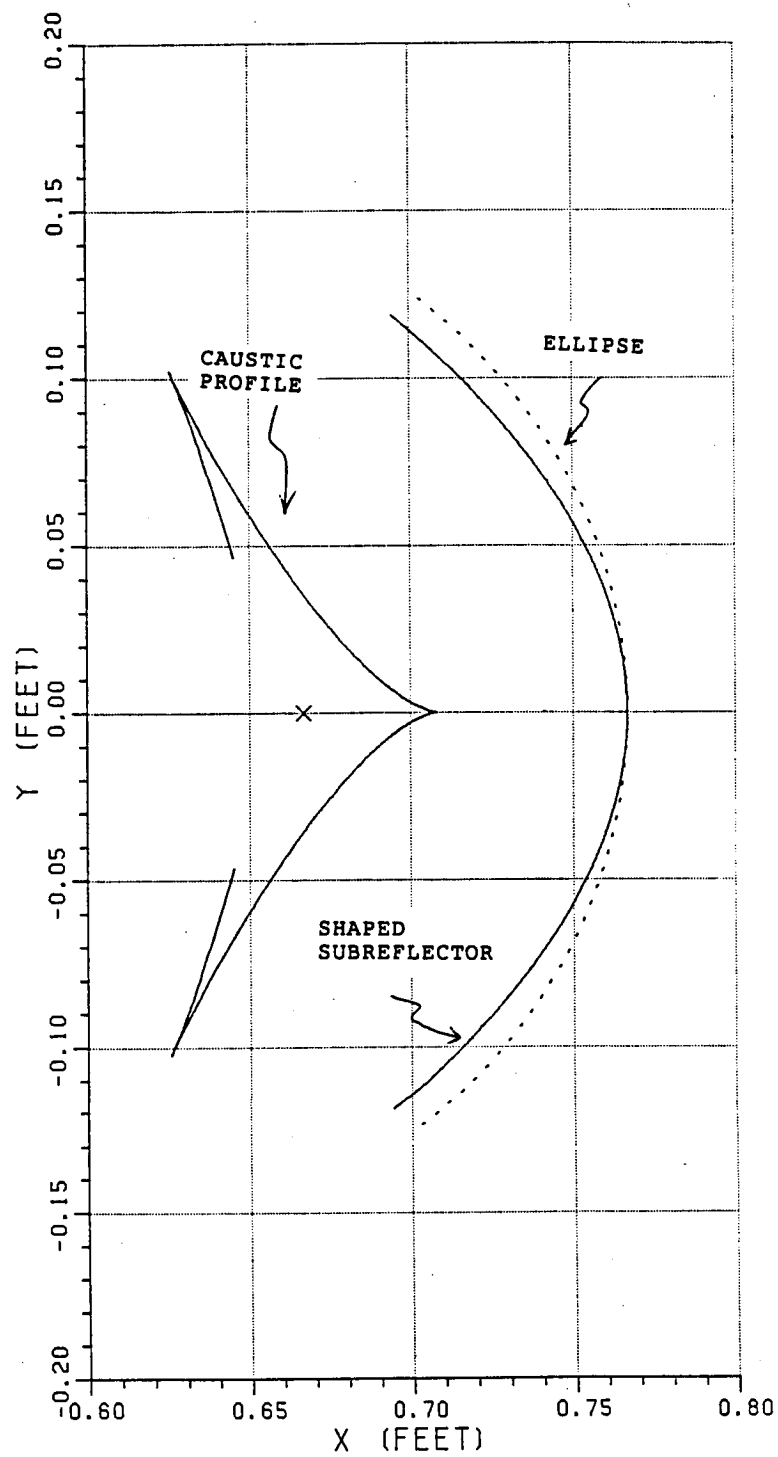


Figure 4.36. Shaped subreflector and caustic of Example G4.

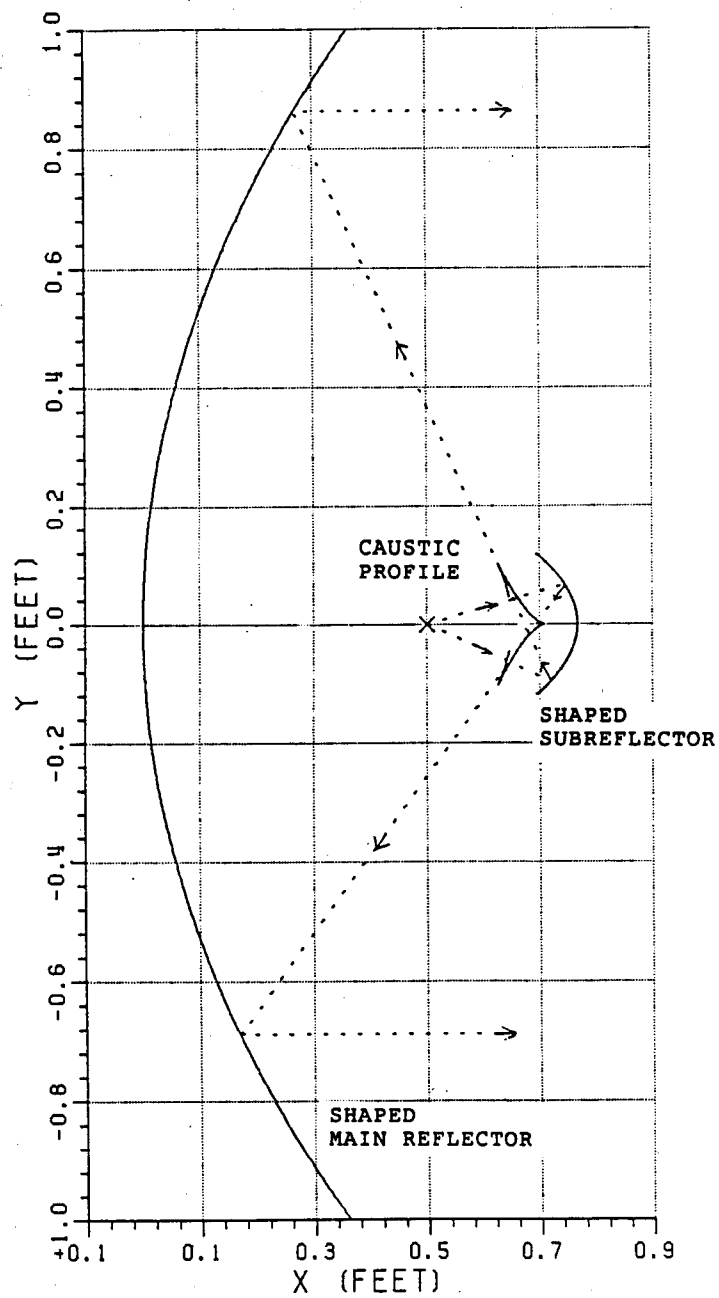


Figure 4.37. Ray geometries for the shaped reflectors of Example G4.

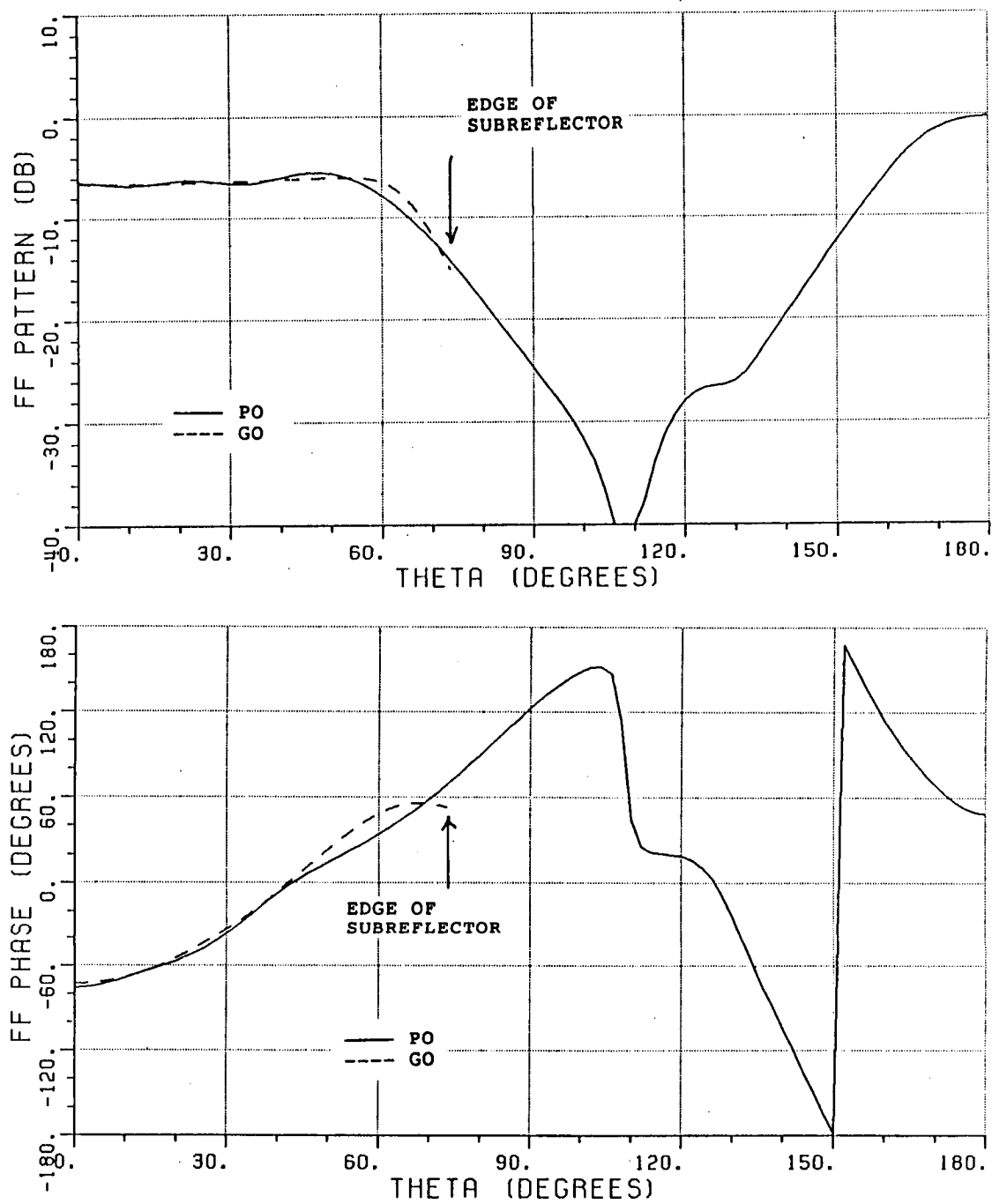


Figure 4.38. Far-zone scattered fields from shaped subreflector of Example G4 at 20 GHz.

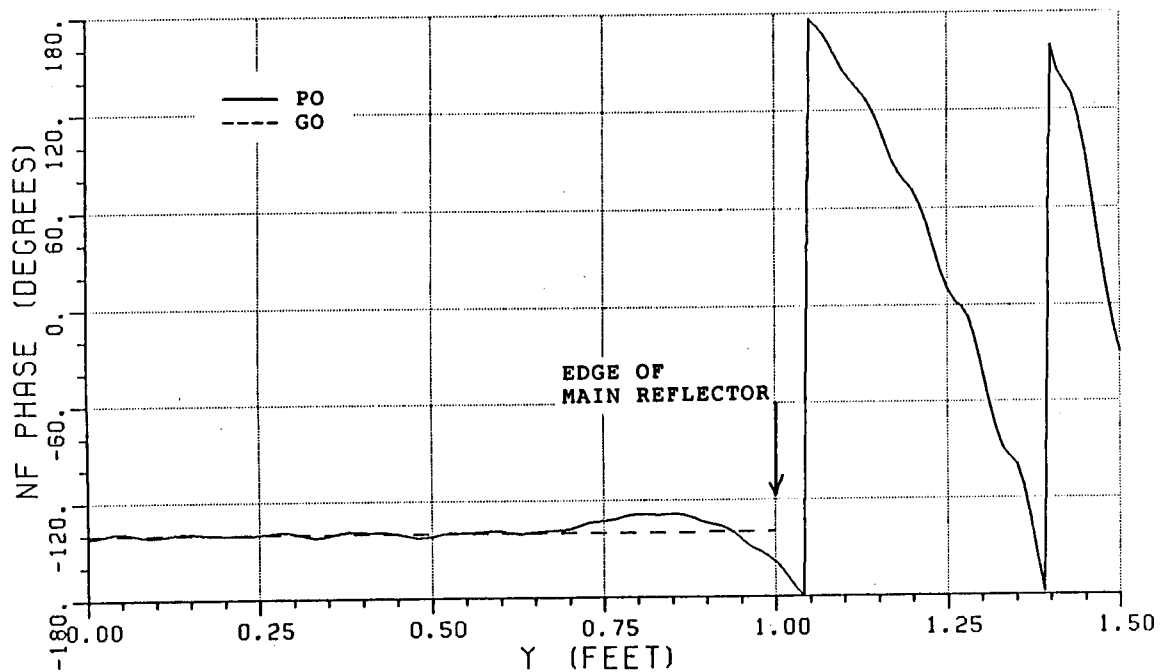
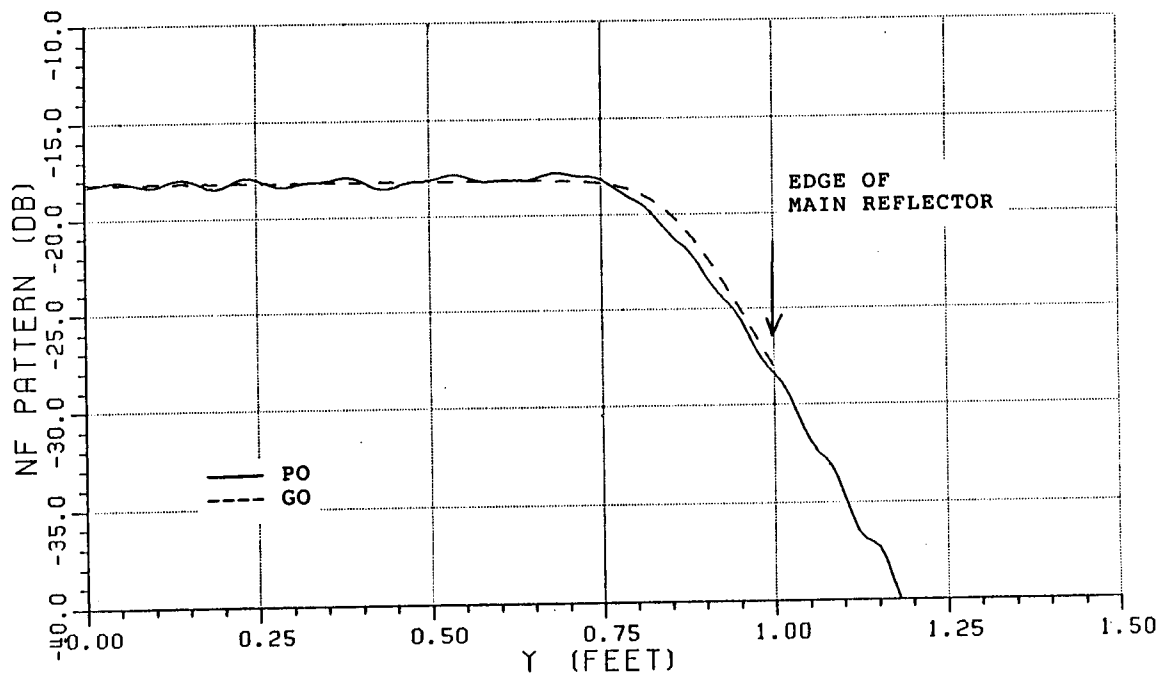


Figure 4.39. Near-zone scattered fields from shaped main reflector of Example G4 at 20 GHz.

aperture distributions, as compared to the conventional Gregorian and Cassegrain reflectors. The geometrical nature of the synthesis method provides more insight into the way that the shaped reflectors work than do the methods which depend on mathematical solutions to a coupled set of differential equations. A major advantage is that one can determine much about the practicality of the resulting reflector surfaces by examining the caustic curve of the shaped subreflector. A good example is the discontinuity in the caustic curve shown in Figure 4.36 for Example G4. The kinks of the caustic curve indicate that the slope of the surface curvature of the shaped subreflector is discontinuous which cannot easily be seen by looking directly at the subreflector.

It should also be noted that the amplitude of the resulting secondary aperture distribution is controlled by the amplitude of the subreflector reflected field at the main reflector surface. The main reflector is used primarily to adjust the phase of the reflected field such that the resulting aperture distribution is uniform in phase.

All the pattern results shown in this chapter include the diffracted fields from the edge of the reflectors. For compact range applications, this will not provide satisfactory performance. In the next chapter, a physical optics analysis is used to determine the performance of the shaped main reflector with a blended rolled edge attachment in order to reduce the edge diffracted fields.

## CHAPTER V

### ROLLED EDGE MODIFICATION FOR THE SHAPED MAIN REFLECTOR

#### 5.1 Introduction

For far-zone scattering and antenna measurements, one is required to have a plane wave with a uniform amplitude illuminate either the scatterer or antenna under test. This is often achieved by using an outdoor far-zone range to simulate the plane wave illumination. There are some serious limitations associated with outdoor measurements, such as weather, interference, etc., which limit the accuracy of measurement. Consequently, indoor measurement facilities are an alternative to outdoor measurements although the uniform plane wave illumination is still a requirement. The creation of a uniform plane wave by a focussed parabolic reflector has been an attractive approach for indoor measurement facilities. Conventional parabolic reflector antennas have been used in so-called compact range measurement facilities [22]. Compact ranges are indoor facilities which provide the capability to measure antenna pattern and scattering by simulating a plane wave illumination on the test antenna or scatterer. There are basically two drawbacks associated with the use of reflectors in compact range applications. The first is that the plane wave reflected from the parabola is not uniform in amplitude, as shown in Figure 5.1, due to the illumination taper of the feed-horn and space-attenuation effects. Consequently, the size of the available measurement volume is limited, thus limiting the size of the test antenna or scatterer. The second

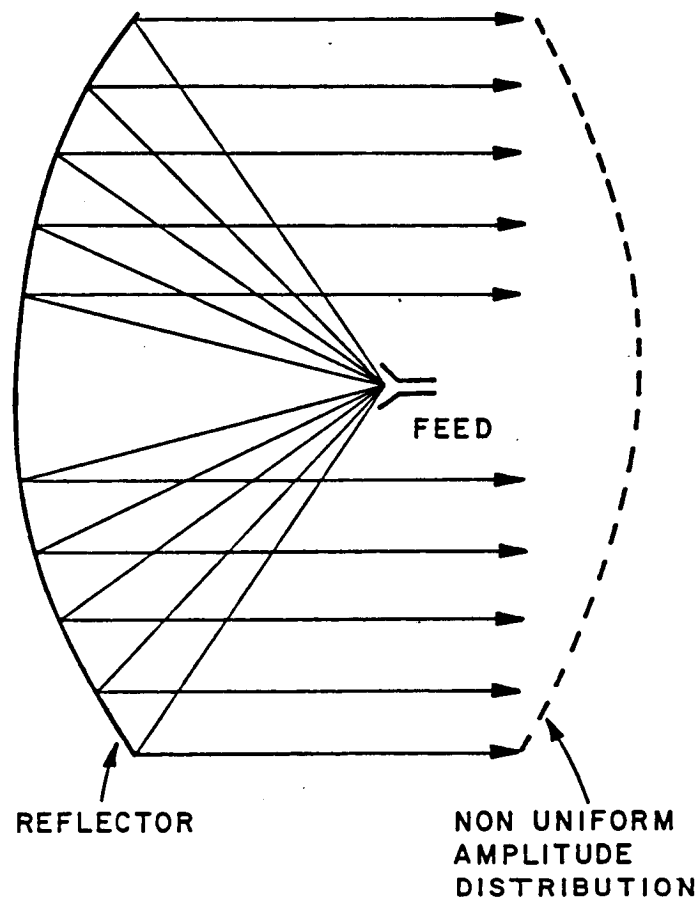


Figure 5.1. Aperture edge taper due to feed-horn pattern and space attenuation.

drawback is that the abrupt termination of the reflector surface which creates a very strong edge diffracted field as shown in Figure 5.2. This diffracted field interferes with the plane wave and results in magnitude and phase variations of the wave illuminating the test antenna or scatterer. The measured results thus may not be accurate.

As pointed out in [2] the nonuniformity of the near-zone distribution can be improved by using an offset reflector system such as a Gregorian antenna with the primary feed tilted properly. It is also conceivable that by properly shaping a dual-reflector antenna, the edge taper problem can also be improved.

To solve the problem of edge diffractions caused by the sharp termination of the reflector surface, one can make the reflector size as large as possible so that the edge diffracted fields are not very strong in the region where the antenna or scatterer under test is located so that the resulting variations in the plane wave are not as significant. However, this approach is very costly because it is not practical to build such a huge reflector. The other way of reducing the edge diffracted fields is to modify the sharp termination of the reflector by adding rolled edges [23], as shown in Figure 5.3. The idea of a rolled edge modification has been extensively studied by Burnside et al. [1,2,3,4]. The addition of rolled edges to the reflector surface introduces reflected fields from both the rolled edges and the reflector. These two reflected fields are not continuous and there are still diffracted fields which emanate from the junction of the rolled edge and the reflector. However, this discontinuity in the reflected



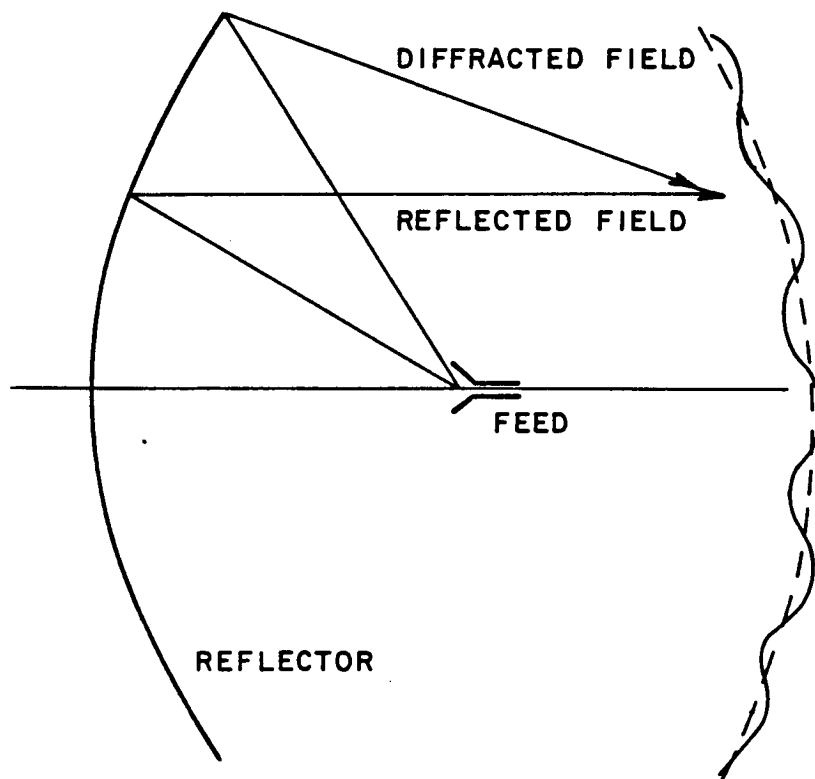


Figure 5.2. Variations of aperture field due to the interference between reflected and diffracted fields.

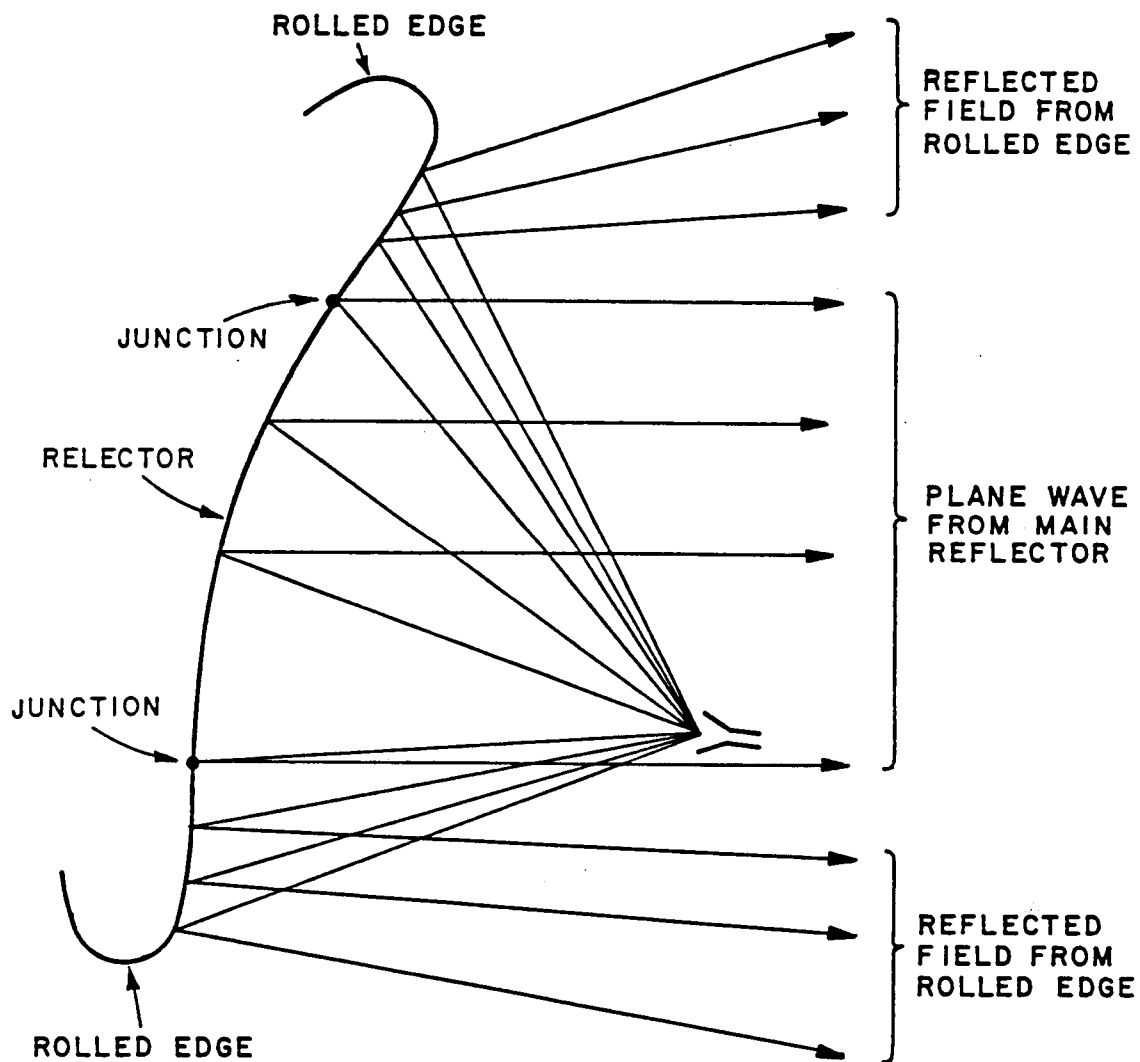


Figure 5.3. Rolled edge modification of main reflector.

fields is much smaller than for the reflector with a sharp termination since in the latter case, the GO reflected field vanishes outside the shadow boundary of the reflector. Consequently, the variations in the aperture fields are not as significant when the reflector is modified with a rolled edge.

In this chapter, the rolled edge idea is implemented in the analyses of the shaped main reflector in order to show the improvement in the performance of the shaped dual-reflector for compact range applications. Some examples are presented to validate this concept. In calculating the scattered fields from the shaped main reflector and the rolled edges, the surface currents are assumed to exist only in the region which is illuminated by the reflected fields from the subreflector and vanish elsewhere, as shown in Figure 5.4. This assumption creates false diffracted fields from the points where the PO currents vanish. The false diffracted fields also interfere with the true scattered fields from the reflector surface. The method for correcting this problem has been studied by Gupta and Burnside [3] and is also discussed and used in this chapter.

## 5.2 Rolled Edge Attachment to Main Reflector

As was discussed earlier, the purpose of adding a rolled edge to the main reflector termination is to create a smooth transition of the geometrical optics reflected fields from the reflector to the rolled edge in such a way that the diffraction from the junction of the reflector and the rolled edge is insignificant. Using this approach, the

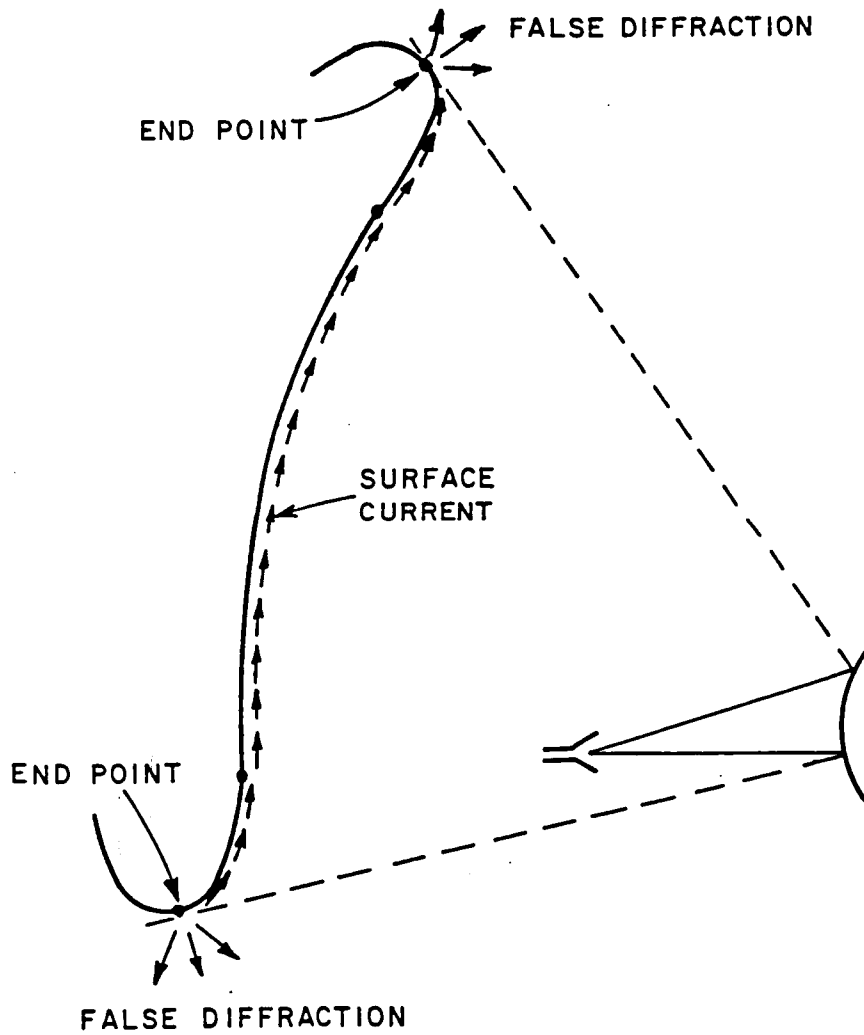


Figure 5.4. Induced currents on main reflector with rolled edge modification.

resulting incident wave in the measurement zone has very small ripple. One other requirement of the rolled edge is that the reflected fields from the rolled edge do not enter the measurement volume to interfere with the reflected fields from the reflector. The detailed analysis of a blended rolled edge attachment to the parabolic reflector can be found in [2]. In this section, the rolled edge is used to modify the edge of the shaped main reflector. The basic concept is still the same as for the parabolic reflector case.

### 5.2.1 Elliptic Rolled Edge

Consider an elliptic rolled edge attachment to the shaped main reflector as shown in Figure 5.5. The shaped main reflector is terminated at point P with surface normal  $\hat{n}$  and the ellipse is attached at P in such a way that the tangents of the main reflector and the ellipse are continuous. The two semi-axes of the ellipse are given by  $a_e$  and  $b_e$ . Consider a local coordinate system for the ellipse in which the coordinate origin is at P, and  $x_e, y_e$  are the two axes such that  $\hat{x}_e = \hat{n}, \hat{y}_e = \hat{t}$ . The parametric equation for the ellipse is given by

$$x_e = a_e(\cos v - 1) \quad (5.1)$$

and

$$y_e = b_e \sin v \quad (5.2)$$

for  $0 \leq v \leq v_m$

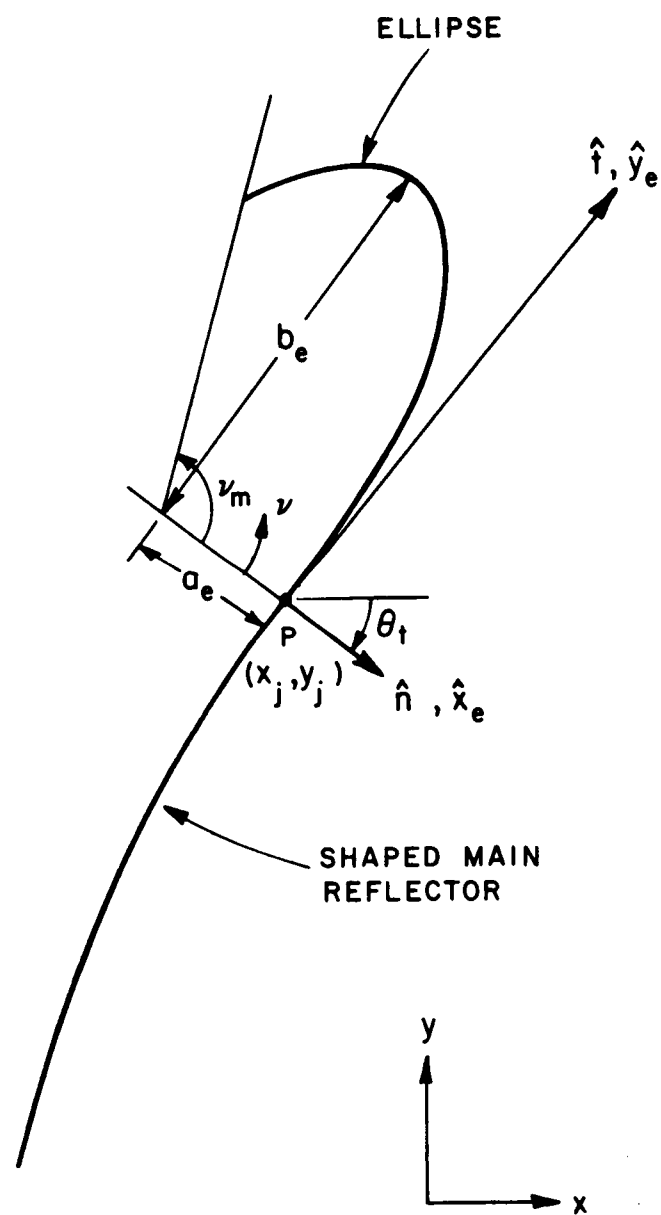


Figure 5.5. An elliptic rolled edge attached to the shaped main reflector.

Note that  $\nu$  is the angle measured from the  $x_e$  axis, and  $\nu_m$  is the angle where the ellipse stops. In terms of the original x-y coordinate system the surface of the ellipse can be expressed by

$$x_{\text{ellipse}} = a_e(\cos\nu-1)\cos\theta_t - b_e\sin\nu\sin\theta_t + x_j \quad (5.3)$$

and

$$y_{\text{ellipse}} = a_e(\cos\nu-1)\sin\theta_t + b_e\sin\nu\cos\theta_t + y_j \quad (5.4)$$

in which  $\theta_t$  is the angle between  $\hat{n}$  and the positive x-axis. This defines the elliptic rolled edge attachment to one edge of the main reflector. A similar definition can be used for the other edge. Since the tangent at the junction of main reflector and ellipse is continuous, the diffracted fields from this junction will be much smaller than for a sharp termination of the main reflector. However, as seen from Figure 5.5, the main reflector is a concave surface; whereas, the ellipse is a convex surface. The radius of curvature at P changes sign between the main reflector and the ellipse and thus is obviously discontinuous. This results in a discontinuity of the G.O. reflected field between the main reflector and ellipse. Consequently, diffracted fields emanate from this junction in order to compensate for the discontinuity in the reflected fields. In order to further reduce this diffracted field, a blended rolled edge which is created by blending the main reflector with the ellipse by some functions is used to improve the performance of the rolled edge. This is discussed in the next section.

### 5.2.2. Blended Rolled Edge

As discussed in the previous section the change of surface from the main reflector to the ellipse creates diffracted fields from the junction. A gradual change of the surface from the main reflector to the ellipse can further reduce the diffracted fields from the junction. This is done by the so-called "blended" rolled edge modification. The elliptic rolled edge discussed in the previous section is transformed into a blended rolled edge by the following relationship:

$$f_{\text{blend}}(v) = f_{\text{ellipse}}(v)b(v) + f_{\text{main}}(v)(1-b(v)) \quad (5.5)$$

in which  $f_{\text{ellipse}}(v)$  is the equation of the ellipse,  $f_{\text{main}}(v)$  is the equation of the main reflector extended beyond the junction and  $b(v)$  is the blending function such that  $0 \leq b(v) \leq 1$  and  $b(0) = 0$ ,  $b(v_m) = 1$ . The idea of blending is shown in Figure 5.6. Note the the blended edge is attached in the same way as the elliptic edge so that the surface at P is smooth and continuous.

The radius of curvature of the surface at the junction is also continuous since the blended edge at the junction is actually the main reflector because  $b(0)=0$ , and  $f_{\text{blend}}(0) = f_{\text{main}}(0)$ . There are many possible blending functions  $b(v)$  such as

$$1) \ b(v) = \frac{v}{v_m} \quad : \text{ linear blending}$$



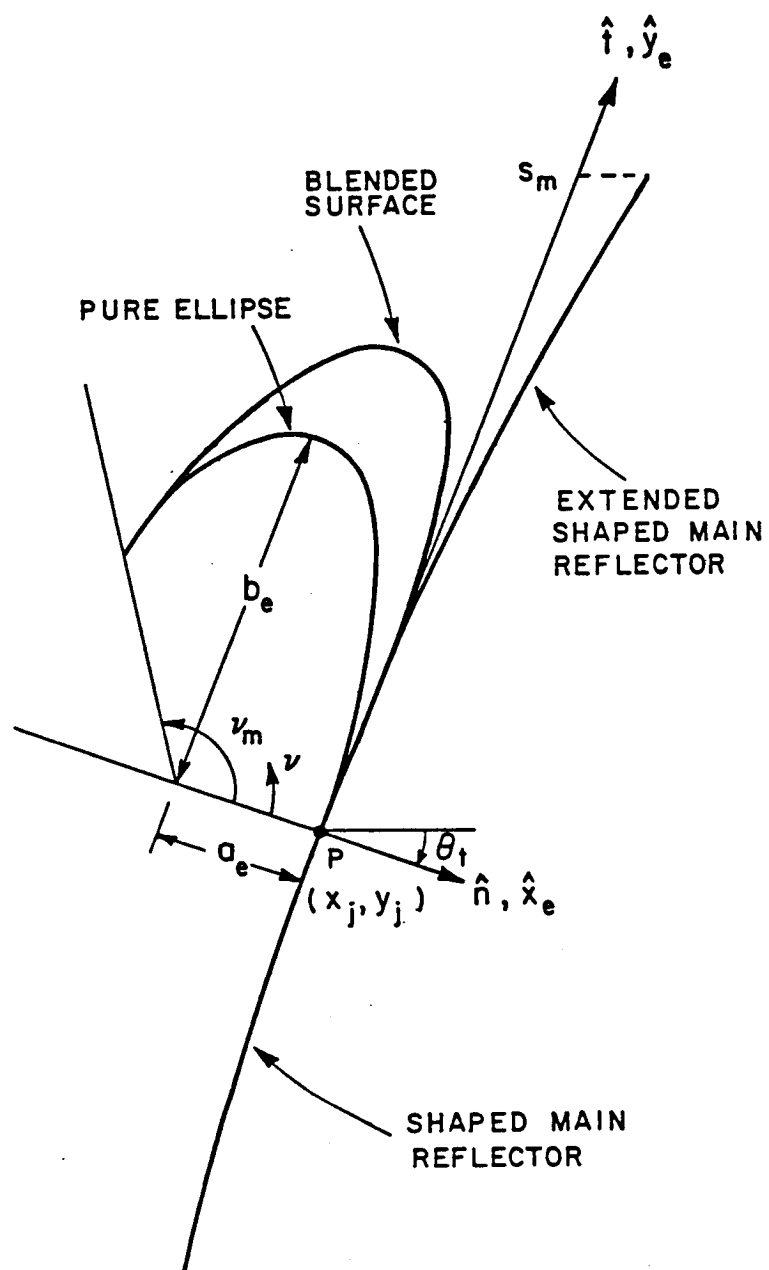


Figure 5.6. A blended rolled edge attached to the shaped main reflector.

- 2)  $b(v) = \left(\frac{v}{v_m}\right)^2$  : square blending
- 3)  $b(v) = \frac{1}{2} \left(1 - \cos \frac{\pi v}{v_m}\right)$  : cosine blending, and
- 4)  $b(v) = \frac{1}{4} \left(1 - \cos \left(\frac{\pi v}{v_m}\right)\right)^2$  : cosine square blending

All of these functions satisfy the condition that  $0 \leq b(v) \leq 1$ ,  $b(0)=0$  and  $b(v_m)=1$ . A detailed analysis of these blending functions can be found in [2].

In order to generate the blended edge, it is necessary to specify the portions of the pure ellipse and the extended main reflector surface to be used. This is done by appropriately choosing the values of the parameters  $a_e$ ,  $b_e$ ,  $v_m$ , and  $s_m$  as shown in Figures 5.6 and 5.7. The portion of the ellipse is defined by the maximum elliptic angle  $v_m$ . The portion of the main reflector is defined by  $s_m$ , the maximum distance along the tangent of the surface at the junction point P. The point on the ellipse which corresponds to a given point  $(x_2, y_2)$  on the extended main reflector is defined as follows. The parameter  $s$  along the tangent  $\hat{t}$  is calculated first by

$$s = |y_2 - y_j| \sqrt{1 + \frac{1}{m_t^2}} \quad (5.6)$$

where  $m_t$  is the slope of  $\hat{t}$ .



Then, the elliptic angle  $v$  which defines a point on the ellipse is related to a point on the extended reflector surface through the parameter  $s$  by

$$v = \frac{s}{s_m} v_m \quad (5.7)$$

From  $v$ , the point on the ellipse corresponding to  $x_2, y_2$  can be calculated by Equations (5.3) and (5.4). Finally, the blended rolled edge is obtained from Equation (5.5) and is given by

$$x_b = [1-b(v)]x_2 + b(v)[a_e(\cos v - 1)\cos\theta_t - b_e \sin v \sin\theta_t + x_j] \quad (5.8)$$

and

$$y_b = [1-b(v)]y_2 + b(v)[a_e(\cos v - 1)\sin\theta_t + b_e \sin v \cos\theta_t + y_j] \quad (5.9)$$

Although the slope and surface radius of curvature at the junction between the main reflector and blended rolled edge are continuous, there are higher order derivatives of the surface which are not continuous at the junction and thus, some diffractions emanate from the junction. The diffraction coefficient for such diffraction is not available so that only the method of Physical Optics can be used to analyze the performance of the reflector surface with a blended rolled edge. However, as mentioned earlier, the induced surface currents in the physical optics integral are assumed zero on the shadow side of the surface although this is not true in reality. A method for correcting

this problem has been investigated in [3] and is discussed in the following section.

### 5.3 End-Point Correction of Physical Optics

The scattered fields calculated by the method of physical optics for a two-dimensional scatterer are given by Equations (2.21) and (2.22). For a magnetic line source illuminating on the scatterer, the scattered magnetic fields are given by

$$H_z^S = - \sqrt{\frac{k_o}{4\pi}} e^{j\pi/4} \int \hat{z} \cdot \left( \vec{J}_{po} \times \hat{\rho} \right) \frac{e^{-jk\rho}}{\sqrt{\rho}} dl \quad (5.10)$$

in which  $\vec{J}_{po}$  is the induced physical optics surface current on the scatterer,  $\hat{\rho}$  is the unit vector in the observation direction from the current and  $\rho$  is the distance between the observation point and the current. The physical optics current,  $\vec{J}_{po}$ , exists over the region directly illuminated by the line source and is assumed to vanish on the shadow side of the scatterer. The integration is thus performed only over the lit side of the scatterer. By applying Equation (5.10) to the shaped main reflector with a blended rolled edge termination on both ends of the main reflector section, one can compute the ordinary PO scattered fields from the entire reflector. The scattered fields calculated this way include the following contributions:

1. The stationary phase or reflection point contribution which is equivalent to the geometrical optics reflected fields,
2. The two end-point contributions which result from the sharp termination of the surface currents at each end shadow boundary, and
3. The diffracted fields from the two junctions between the main reflector and the blended rolled edge.

These contributions are illustrated in Figure 5.8. The end-point contributions are incorrect contributions because surface currents still exist on the shadow side of the rolled edge. It is stated in [3] that these end-point contributions do not give the correct creeping wave of the curved surface. Consequently, the end-point contributions have to be removed from the physical optics integral. This can be accomplished by evaluating the physical optics integral asymptotically.

Consider the integral given by

$$I = \int_a^b F(l) e^{jkf(l)} dl . \quad (5.11)$$

The asymptotic evaluation of this integral [3] results in

$$I \sim \sqrt{\frac{2\pi}{k|f''(l_s)|}} F(l_s) e^{jkf(l_s)} e^{j\pi/4 \operatorname{sgn}[f''(l_s)]} + \sum_{n=0}^{\infty} \frac{(-1)^n F_n}{jkf'} e^{jkf(l)} \Big|_a^b \quad (5.12)$$

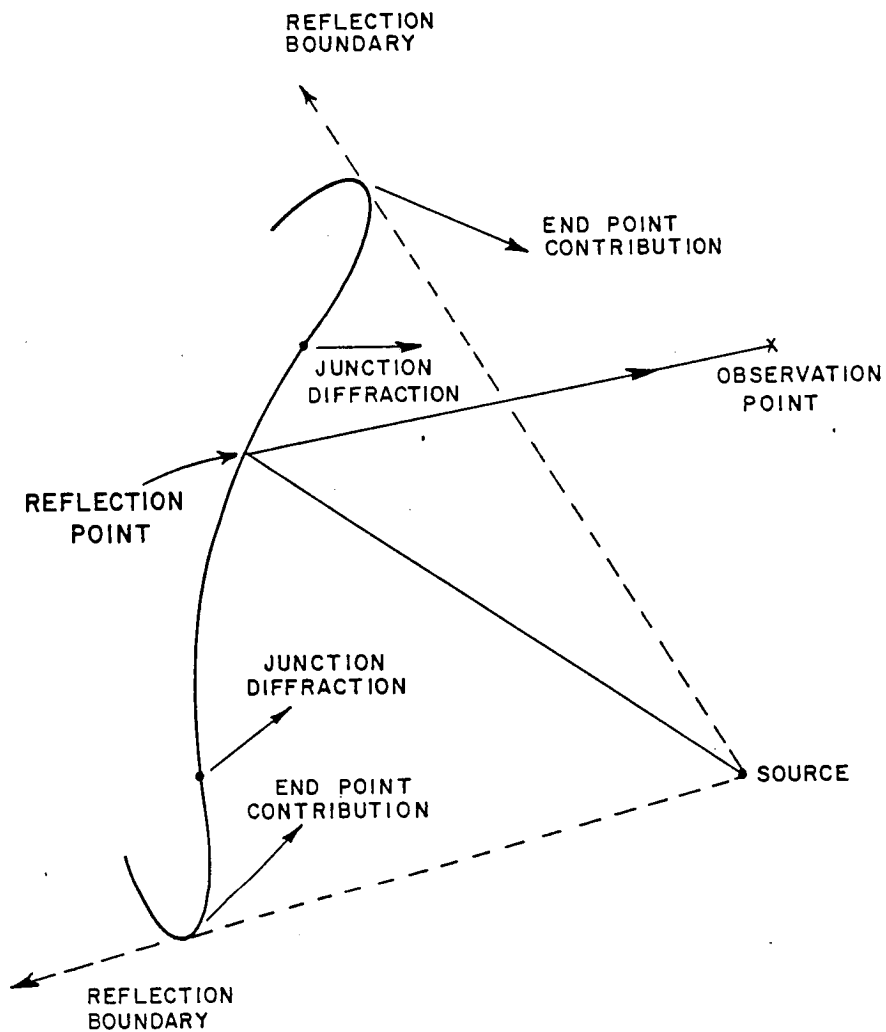


Figure 5.8. Illustration of three contributions from the physical optics integration.

where  $l_s$  is the stationary phase point and is assumed away from the two end-points  $l=a, b$ . Note that  $F_n$  is defined as

$$F_n = \frac{d}{dl} \left[ \frac{F_{n-1}(l)}{jkf'(l)} \right] \quad (5.13)$$

with

$$F_0(l) = F(l) . \quad (5.14)$$

The first term in Equation (5.12) is the specular reflected field and the second term represents the two end-point contributions. Since Equation (5.12) is an asymptotic representation of (5.11), there are some higher order terms which have been neglected. One of these terms is the diffraction from the junction of the main reflector and the blended rolled edge. Consequently, one obtains the desired result by subtracting these end-point contributions from the P0 result such that the scattered field is given by

$$H^S = \int_a^b F(l) e^{jkf(l)} dl - \sum_{n=0}^{\infty} \frac{(-1)^n F_n}{jkf'(l)} e^{jkf(l)} \Big|_a^b \quad (5.15)$$

Thus, by numerically integrating Equation (5.11) and subtracting the end point contributions, one obtains the geometrical optics reflected field plus the diffracted fields from the junction of the main reflector and rolled edge. For surfaces which can be described analytically such as a



parabola, the end-point contributions can be calculated analytically [2]. In this study, the surface is generated numerically, and thus, the end-point contributions are computed numerically. The rest of this section discusses the computation of the physical optics currents on the shaped main reflector by geometrical optics for the cases where the shaped subreflector is either concave or convex.

In formulating the surface equations for the shaped dual-reflector, it is assumed that the surface points  $(x_1, y_1)$  and  $(x_2, y_2)$  are located on either a Cassegrain or Gregorian reflector with the caustic of the subreflector reflected field at  $(x_c, y_c)$ . Thus, the equations for calculating the geometrical optics reflected field of a Cassegrain or Gregorian reflector are used to calculate the reflected field of the shaped reflector. For the case of a shaped dual-reflector with a concave subreflector, as shown in Figure 5.9, the surface points  $(x_1, y_1)$  and  $(x_2, y_2)$  are located on a particular Gregorian antenna with the caustic of the subreflector reflected field located at  $(x_c, y_c)$ . From Equation (C.9), the reflected field at  $(x_2, y_2)$  from the subreflector can be calculated by

$$H_z^i(x_2, y_2) = H_z^r(s_1) = H_z^i(x_1, y_1) \sqrt{\frac{-\rho_c}{-\rho_c + s_1}} e^{-jks_1} \quad (5.16)$$

in which  $H_z^i(x_1, y_1)$  is the incident magnetic field at  $(x_1, y_1)$  and  $\rho_c$  is the distance between  $(x_1, y_1)$  and  $(x_c, y_c)$ , and  $s_1$  is the distance between  $(x_1, y_1)$  and  $(x_2, y_2)$ . The incident magnetic field  $H_z^i(x_1, y_1)$  is given by

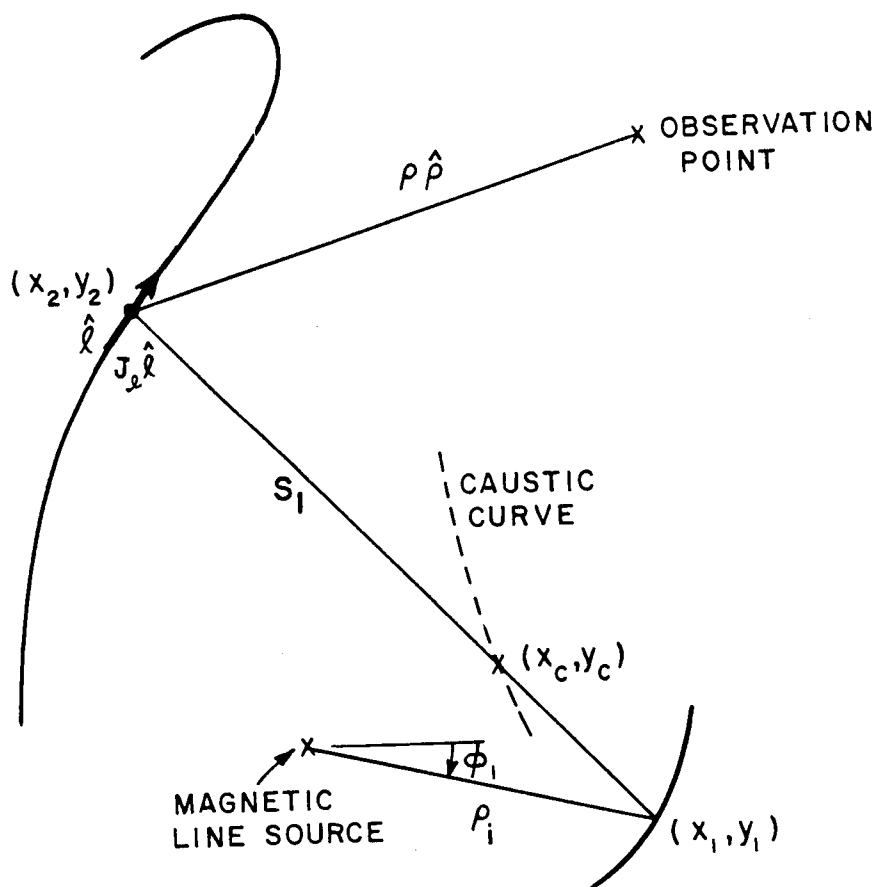


Figure 5.9. Surface current calculation for the case of shaped dual reflector with concave subreflectors.

$$H_z^i(x_1, y_1) = \sqrt{P(\phi_1)} \frac{e^{-jk\rho_i}}{\sqrt{\rho_i}} \quad (5.17)$$

where  $P(\phi_1)$  is the far-zone power pattern of the magnetic line source at angle  $\phi_1$ . The phase of the far-zone field pattern of the line source is assumed constant and suppressed. Thus, the induced physical optics surface current on the main reflector is given by

$$\vec{J}_{po} = 2 \hat{n} \times \vec{H}^i(x_2, y_2) = 2 \hat{n} \times \vec{H}^r(s_1) = -\hat{l} 2 H_z^i(x_2, y_2)$$

or

$$\vec{J}_{po} = \hat{l} J_1 \quad (5.18)$$

where

$$J_1 = -2\sqrt{P(\phi_1)} \frac{e^{-jk\rho_i}}{\sqrt{\rho_i}} \sqrt{\frac{-\rho_c}{-\rho_c + s_1}} e^{-jks_1} \quad (5.19)$$

Consequently, the P0 scattered fields from the main reflector are calculated by

$$H_z^s(x, y) = -\sqrt{\frac{k_0}{4\pi}} e^{j\pi/4} \int_0^{l_m} \hat{z} \cdot (\hat{l} \times \hat{\rho}) J_1 \frac{e^{-jk\rho}}{\sqrt{\rho}} dl$$

or

$$H_z^s(x,y) = - \sqrt{\frac{k_o}{4\pi}} e^{j\pi/4} \int_0^1 \hat{z} \cdot (\hat{l} \times \hat{\rho}) (-2) \sqrt{P(\phi_1)} \frac{e^{-jk\rho_i}}{\sqrt{\rho_i}} \cdot \sqrt{\frac{-\rho_c}{-\rho_c+s_1}} e^{-jks_1} \frac{e^{-jk\rho}}{\sqrt{\rho}} dl . \quad (5.20)$$

For the surface current on the blended edge point  $(x_b, y_b)$ , one has to numerically find the corresponding incident ray from the subreflector; i.e., corresponding to  $(x_1, y_1)$  and  $(x_c, y_c)$ . By comparing Equations (5.20) and (5.11), it is found that

$$F(l) = 2 \sqrt{\frac{k_o}{4\pi}} e^{j\pi/4} (\hat{z} \cdot (\hat{l} \times \hat{\rho})) \sqrt{P(\phi_1)} \frac{1}{\sqrt{\rho_i} \sqrt{\rho}} \sqrt{\frac{-\rho_c}{-\rho_c+s_1}} \quad (5.21)$$

and

$$f(l) = - (\rho_i + s_1 + \rho). \quad (5.22)$$

Similarly, for the case of the convex subreflector, the incident field at the main reflector is given by

$$H_z^i(x_2, y_2) = H_z^r(s_1) = H_z^i(x_1, y_1) \sqrt{\frac{\rho_c}{s_1 + \rho_c}} e^{-jks_1} \quad (5.23)$$

where  $(x_1, y_1)$  and  $(x_2, y_2)$  are the points on the particular Cassegrain reflector with subreflector caustic located at  $(x_c, y_c)$  as shown in Figure 5.10. The surface currents are then given by

$$\vec{J}_{po} = \hat{l} J_1$$

with

$$J_1 = -2 \sqrt{P(\phi_1)} \frac{e^{-jk\rho_i}}{\sqrt{\rho_i}} \sqrt{\frac{\rho_c}{s_1 + \rho_c}} e^{-jks_1} \quad (5.24)$$

Finally, the P0 scattered field from the main reflector is calculated by

$$H_z^S(x,y) = - \sqrt{\frac{k_o}{4\pi}} e^{j\pi/4} \int_0^{lm} \hat{z} \cdot (\hat{l} \times \hat{\rho}) (-2) \sqrt{P(\phi_1)} \frac{e^{-jk\rho_i}}{\sqrt{\rho_i}} \sqrt{\frac{\rho_c}{\rho_c + s_1}} e^{-jks_1} \frac{e^{-jk\rho}}{\sqrt{\rho}} dl \quad (5.25)$$

This gives

$$F(l) = 2 \sqrt{\frac{k_o}{4\pi}} e^{j\pi/4} \hat{z} \cdot (\hat{l} \times \hat{\rho}) \sqrt{P(\phi_1)} \frac{1}{\sqrt{\rho_i}} \frac{1}{\sqrt{\rho}} \sqrt{\frac{\rho_c}{\rho_c + s_1}} \quad (5.26)$$

with  $f(l)$  given in Equation (5.22).

Examples are given in the next section to illustrate the combination of a shaped dual-reflector with blended rolled edge terminations to the main reflector. The scattered fields are calculated for the main reflector with a blended edge. The results of the P0 integration, the P0 integration with the first order end-point

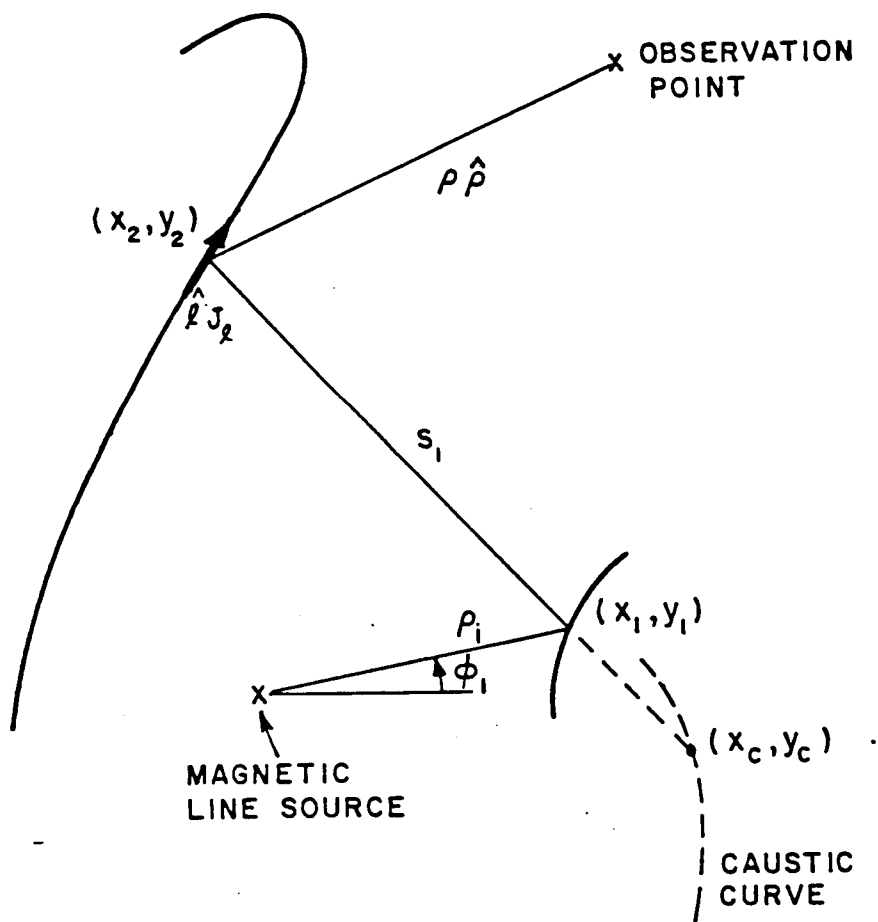


Figure 5.10. Surface current calculation for the case of shaped dual reflector with convex subreflector.

corrections, and the PO integration with the first and second orders end-point corrections are shown to illustrate the effects of the false end-point contributions of the ordinary physical optics integral. Normally, the rest of the higher order end-point contributions are very small and thus are neglected in the following examples.

#### 5.4. Examples of Shaped Dual-Reflectors with Blended Rolled Edge Terminations on the Main Reflector

##### 5.4.1. Example BL1

In this example, the Gregorian reflector antenna given in Examples G1 and G2 of Chapter IV is used as the starting point for the shaping, and the cosine-squared blending function is used to generate the blended rolled edges which are attached to the main reflector at  $y=0.5'$  and  $y=-0.5'$ . The parameters for the blended edges are given by  $a_e=0.2'$ ,  $b_e=0.5'$ ,  $s_m=1.2'$  and  $\nu_m = 90^\circ$ . Since the blended rolled edges require an extension of the shaped main reflector, the shaping of the main reflector is extended to  $y=1.3'$  and  $y=-1.3'$ . The aperture field within this region is assumed to be uniform. A magnetic line source with a power pattern of  $\cos^{20} \phi$  is used as the primary source. The tilt angle of the feed axis is  $0^\circ$  and the power between  $\phi=-40^\circ$  and  $\phi=40^\circ$  is redistributed uniformly over the region between  $y=-1.3'$  and  $y=1.3'$ .

The resulting shaped reflectors are shown in Figure 5.11. Note that these surfaces are different from those of Example G2 which are shown in Figure 4.12. This is due to the difference in the designated aperture size and the amount of the feed power which is redistributed. As seen

from Figure 5.11, the caustic curve intersects the subreflector surface so that one might think that some of the reflected field from the subreflector will be blocked by the subreflector itself. However, it is found by tracing the rays that only the reflected fields from the central part of the subreflector illuminate the blended main reflector. This is shown in Figure 5.12. Therefore, the scattered fields from the blended main reflector can still be calculated to validate the performance of the blended rolled edges. The near-zone scattered fields calculated by the method of PO at 20 GHz are shown in Figure 5.13. The scattered fields with the first order end-point corrections are shown in Figure 5.14, and the scattered fields with both first and second order end-point corrections are shown in Figure 5.15. One can see the effects of the false end-point contributions by comparing these results. By taking out these false contributions, the scattered fields within the unblended section of the whole main reflector, i.e.,  $y=0'$  to  $y=0.5'$  in Figure 5.15, are very smooth and uniform. This is a significant improvement in the ripple of the scattered fields for compact range applications compared to the one without blended edges. The slight ripple shown in Figure 5.15 is caused mainly by the diffraction from the junction of the unblended and blended sections of the main reflector. Also note that if the "true" scattered fields from the subreflector (i.e., not just the reflected fields from the subreflector) are used to calculate the surface currents on the main reflector, there will be slowly varying ripple in addition to the scattered fields from the main reflector.



ORIGINAL PAGE IS  
OF POOR QUALITY

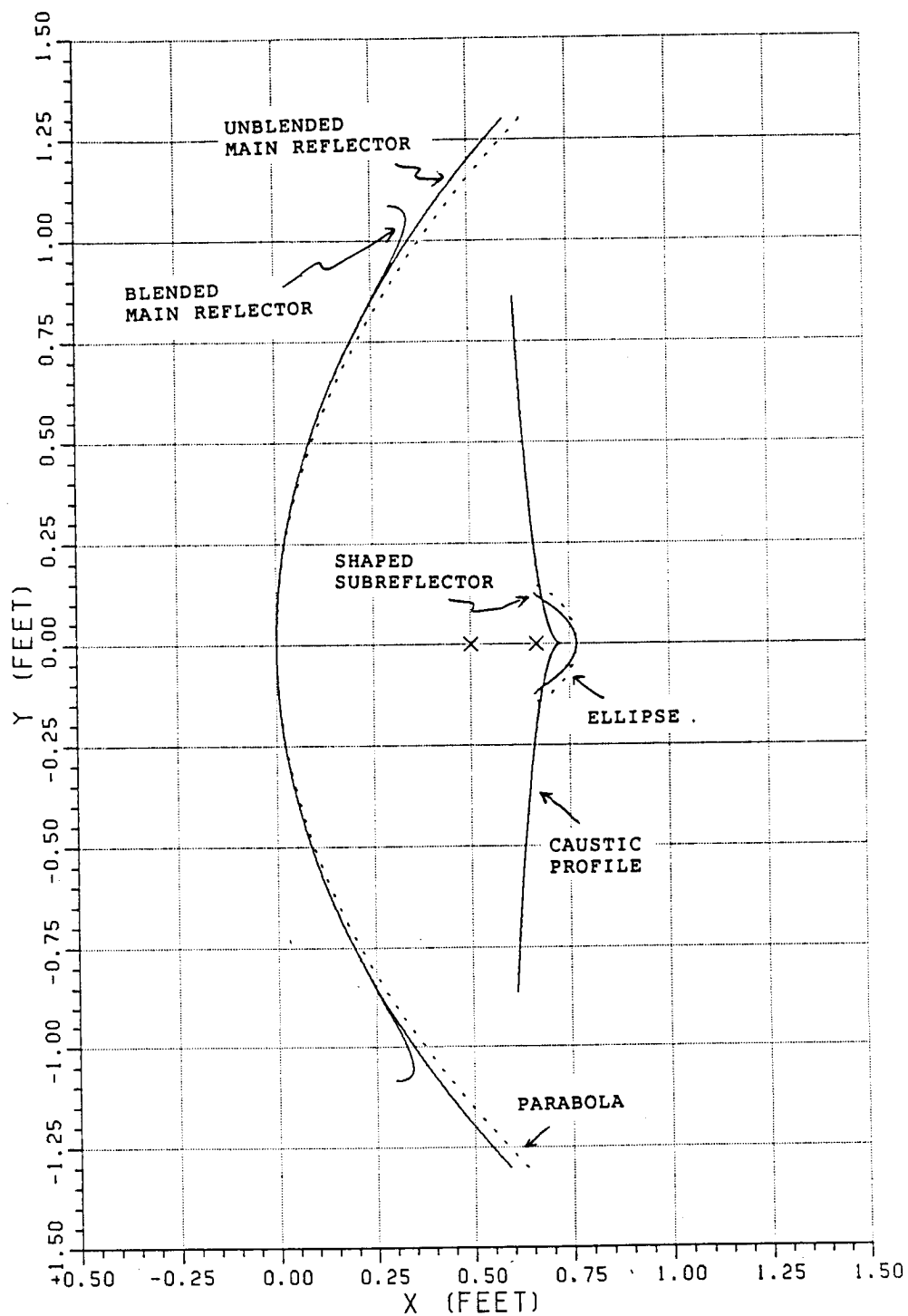


Figure 5.11. Shaped dual reflectors with blended rolled edge terminations for Example BL-1.

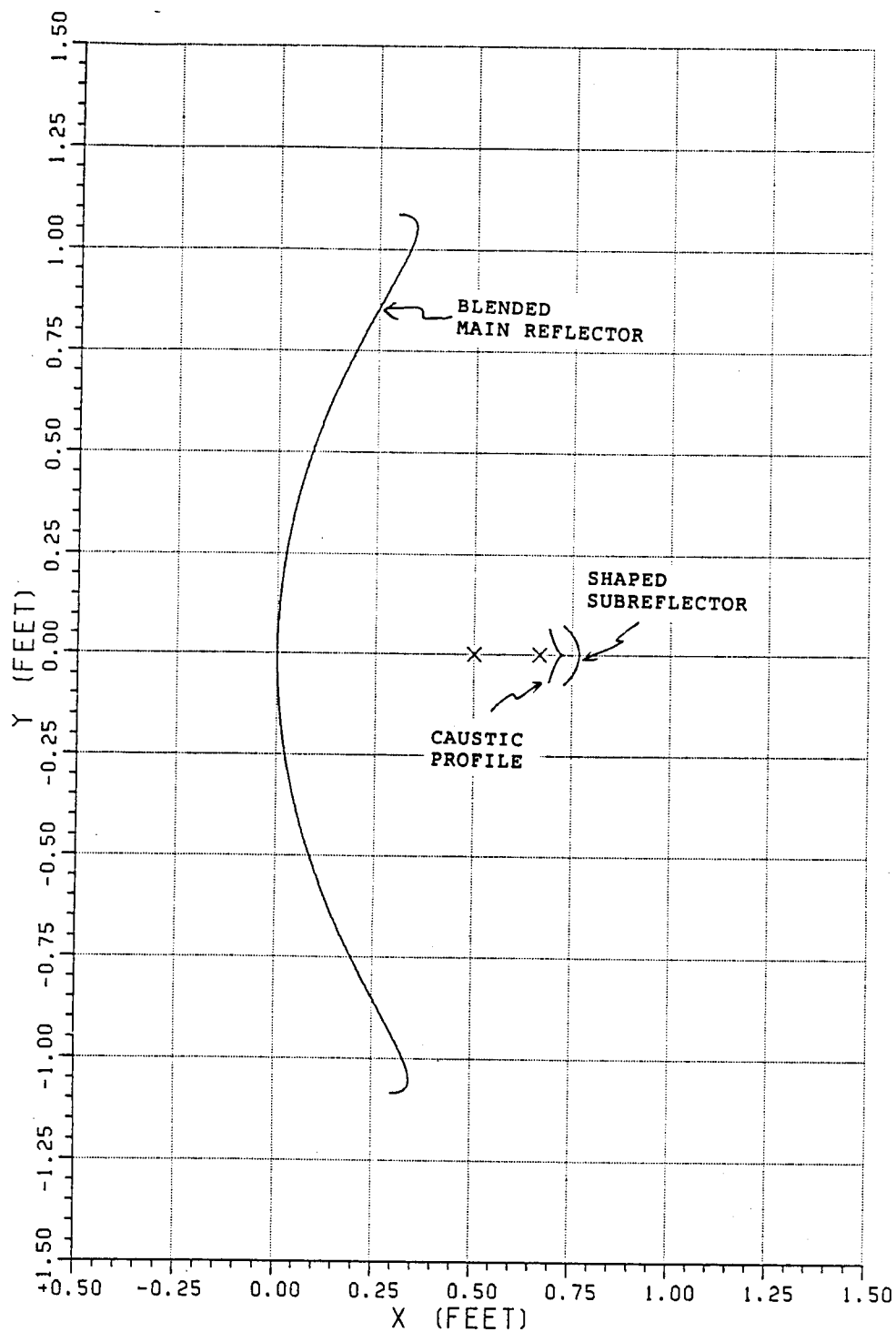


Figure 5.12. Section of subreflector from which the reflected fields illuminate the blended main reflector in example BL-1.

#### 5.4.2. Example BL2

The same Gregorian reflector antenna used in the previous example is also used here as the starting point for shaping. However, instead of a uniform aperture distribution, the distribution given in Figure 4.34 of Chapter IV is used and the blended rolled edges are attached to the main reflector at  $y=\pm 0.5'$ . The parameters associated with blended rolled edges, feed pattern, and feed power to be redistributed over the designated aperture, are all the same as in the previous example.

The resulting shaped reflectors with blended rolled edge terminations to the main reflector are shown in Figure 5.16. Again, the section of the subreflector from which the reflected fields illuminate the blended main reflector is replotted in Figure 5.17.

The near-zone scattered fields calculated at 20 GHz from the blended main reflector are given in Figures 5.18 through 5.20 for the PO, the PO with first order end-point corrections, and the PO with first and second order end-point corrections, respectively. A very smooth result is obtained between  $y=0'$  and  $y=0.5'$  when the first and second order end-point corrections are used. However, if one compares the pattern shown in Figures 5.15 and 5.20 where the first one is obtained by shaping reflectors to generate a uniform aperture distribution while the second one is obtained by shaping the reflectors to generate a non-uniform aperture distribution, the ripple in Figure 5.20 between  $y=0.5'$  and  $y=0.7'$  is higher than for the one in Figure 5.15. This shows that a potential problem can occur if one tries to shape the reflectors to generate an aperture distribution which is constant over one region and

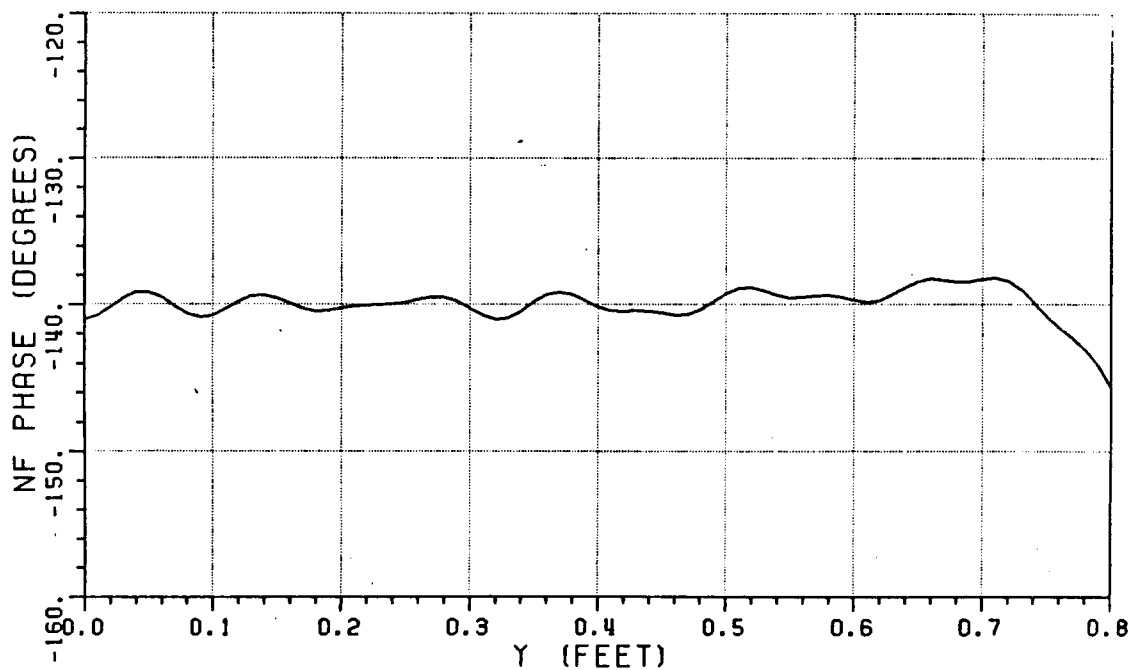
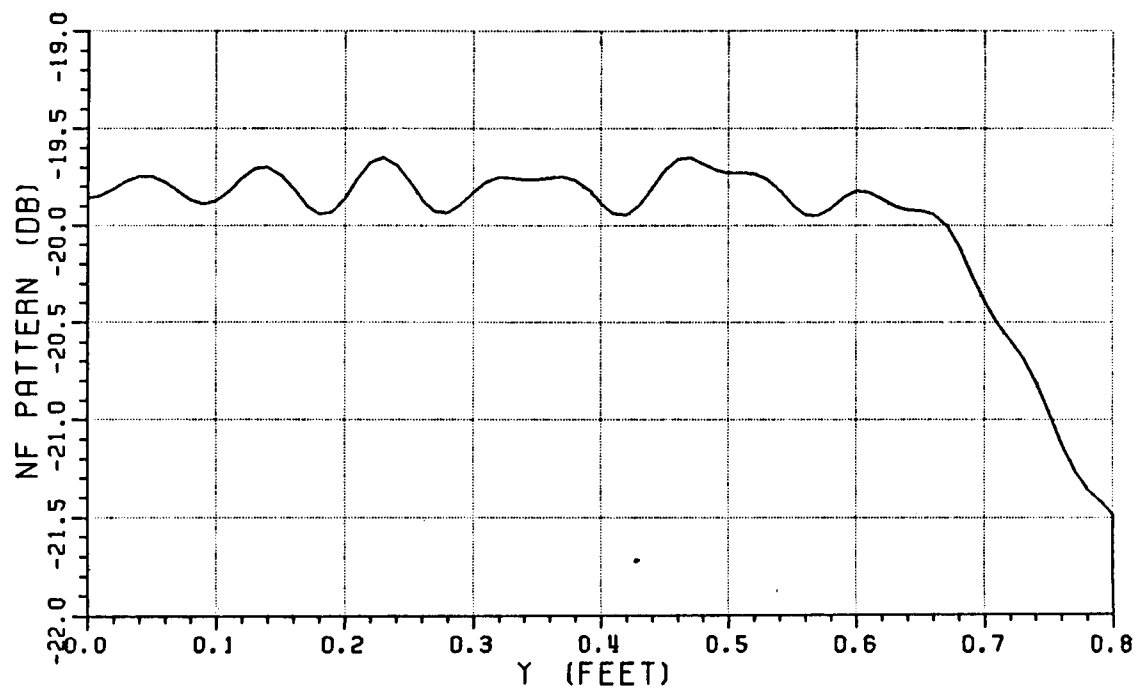


Figure 5.13. Near-zone scattered fields from the blended main reflector of Example BL-1 at 20 GHz using P0 alone.

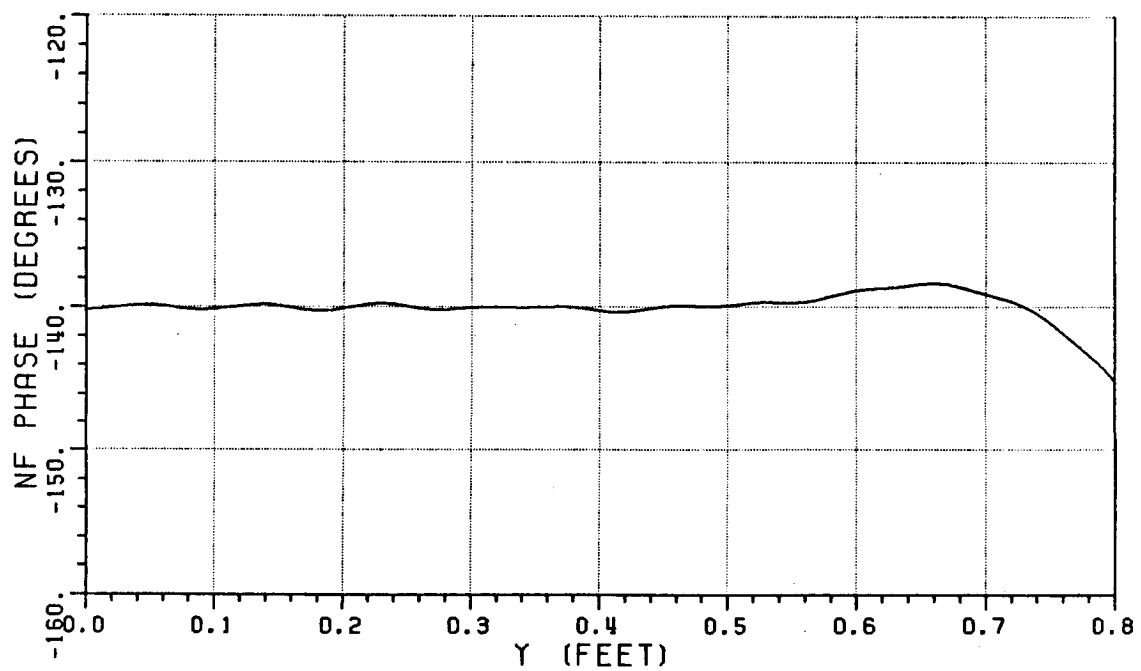
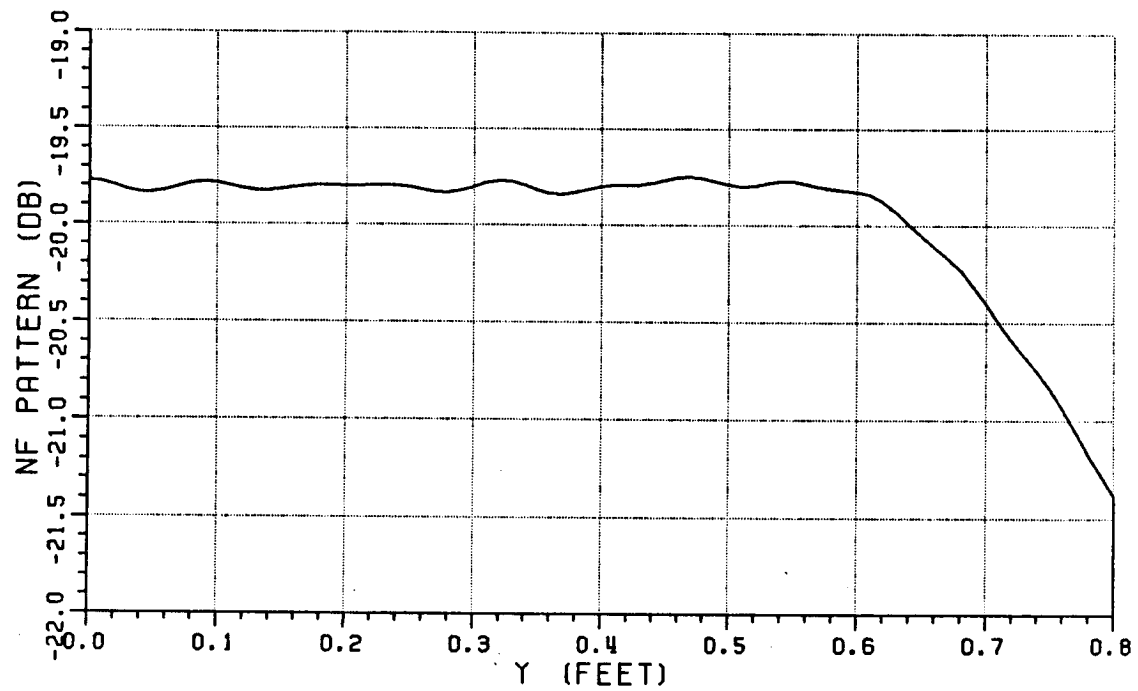


Figure 5.14. Near-zone scattered fields from the blended main reflector of example BL-1 using PO with first order end-point corrections at 20 GHz.

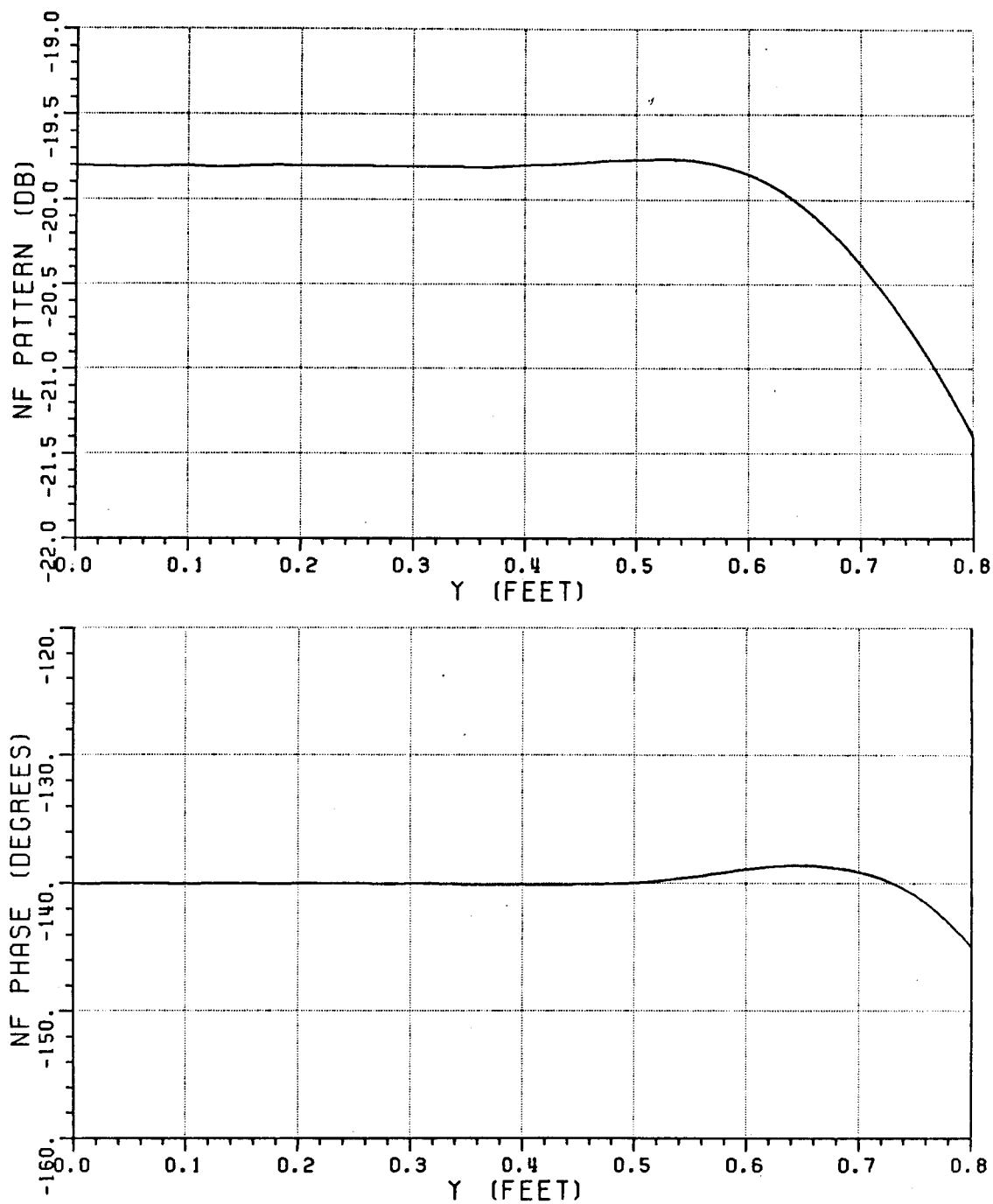


Figure 5.15. Near-zone scattered fields from blended main reflector of example BL-1 using P0 with first and second order end-point corrections at 20 GHz.

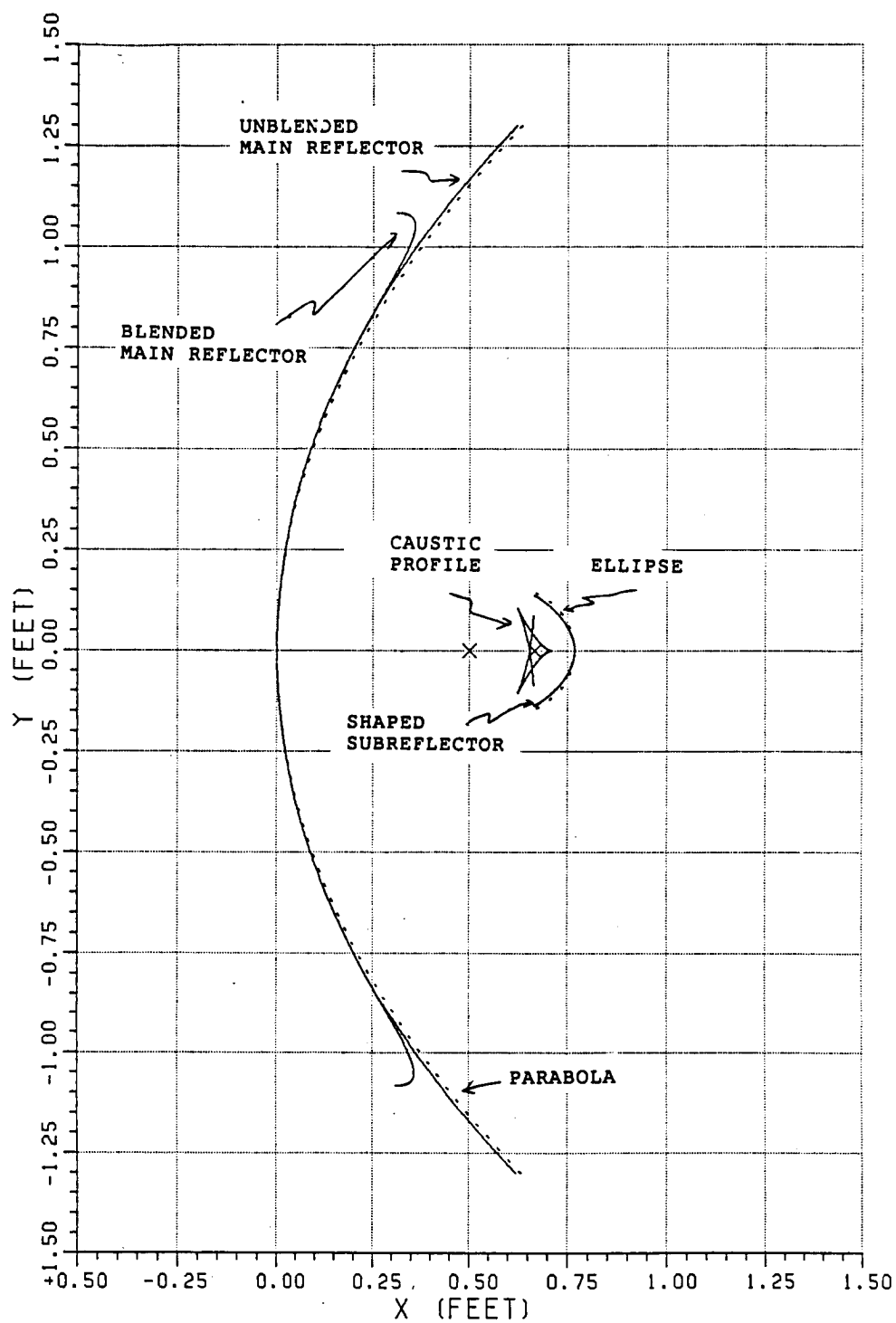


Figure 5.16. Shaped dual reflectors with blended rolled edge terminations for example BL-2.

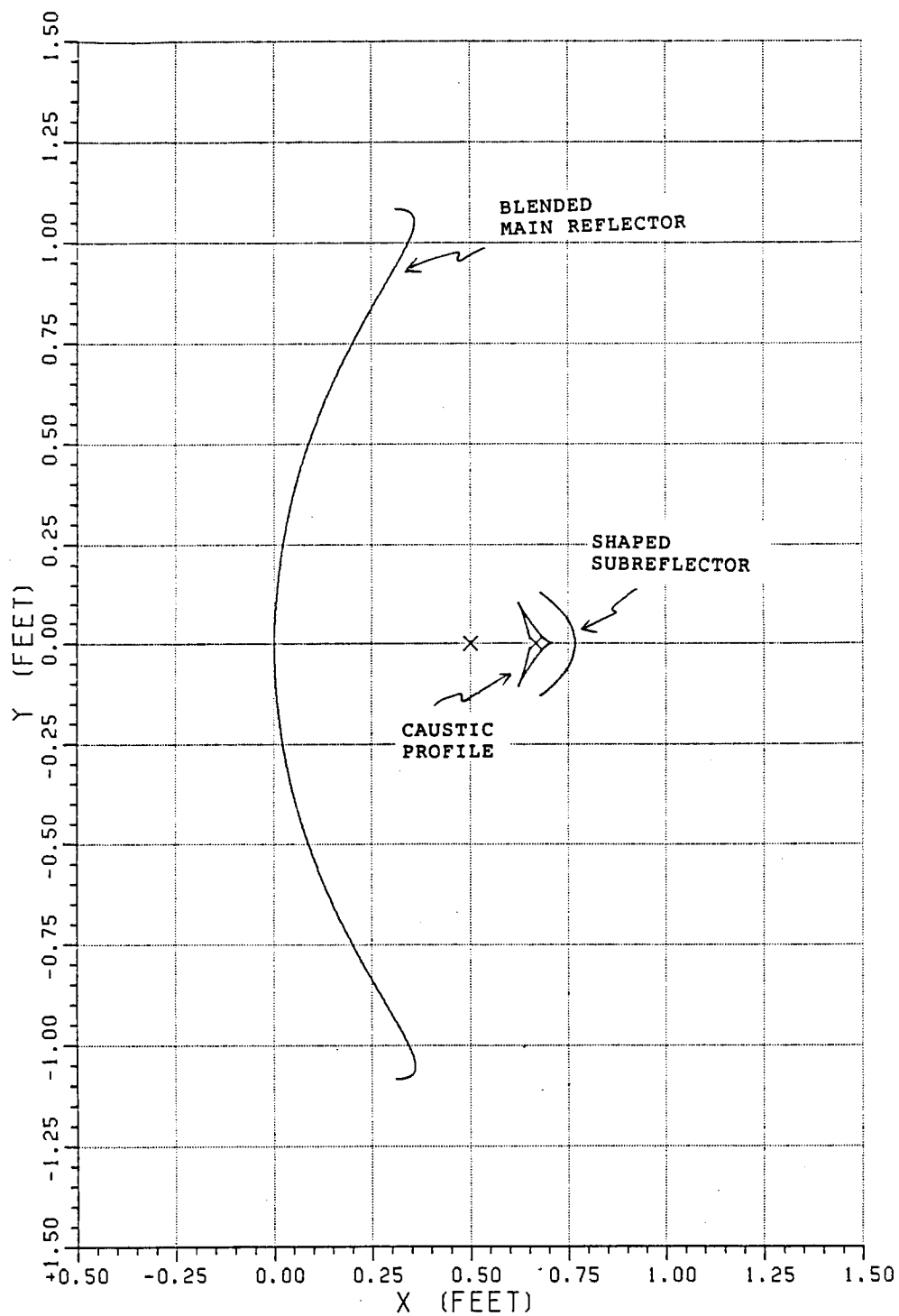


Figure 5.17. Section of subreflector from which the reflected fields illuminate the blended main reflector in example BL-2.



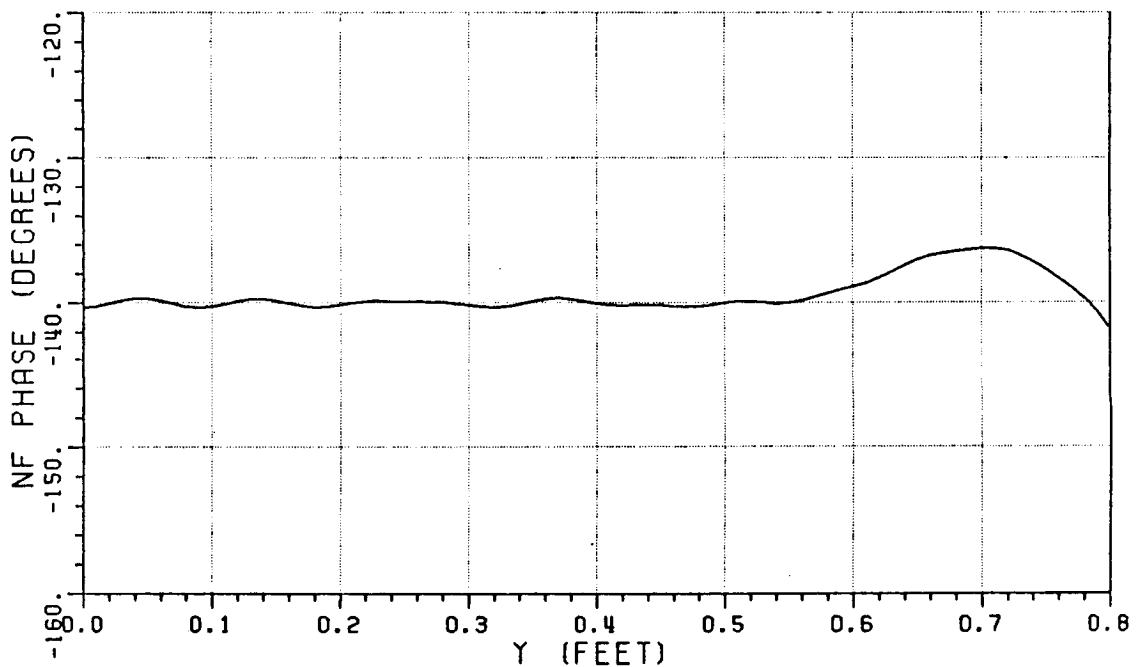
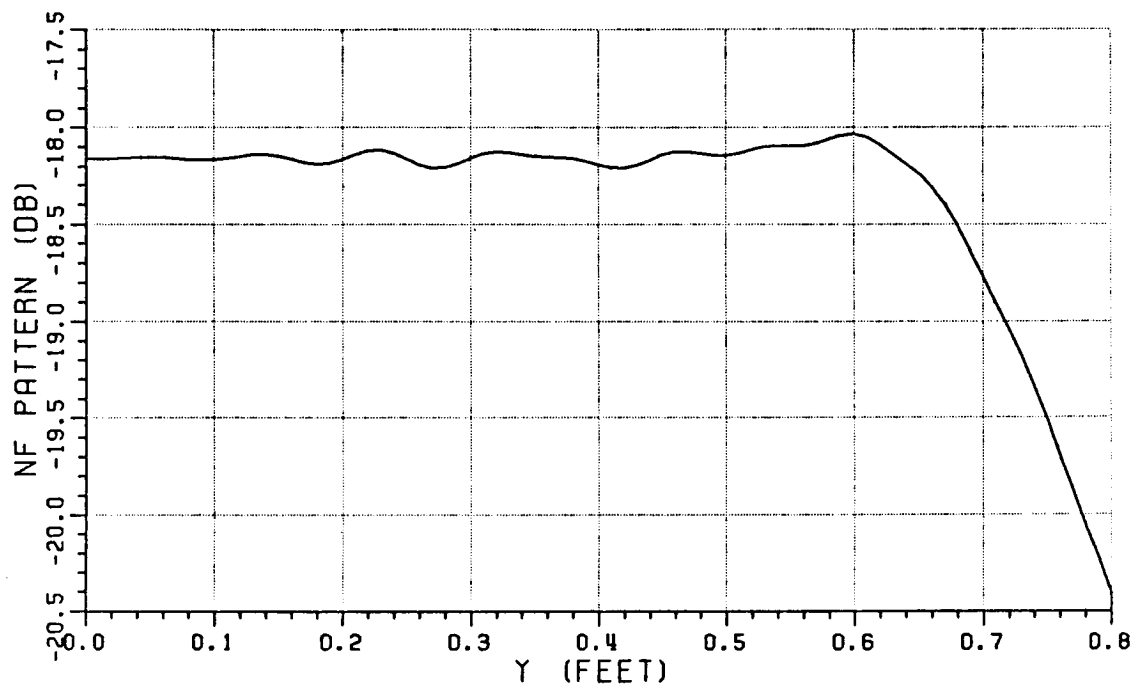


Figure 5.18. Near-zone scattered fields from blended main reflector of example BL-2 using P0 at 20 GHz.

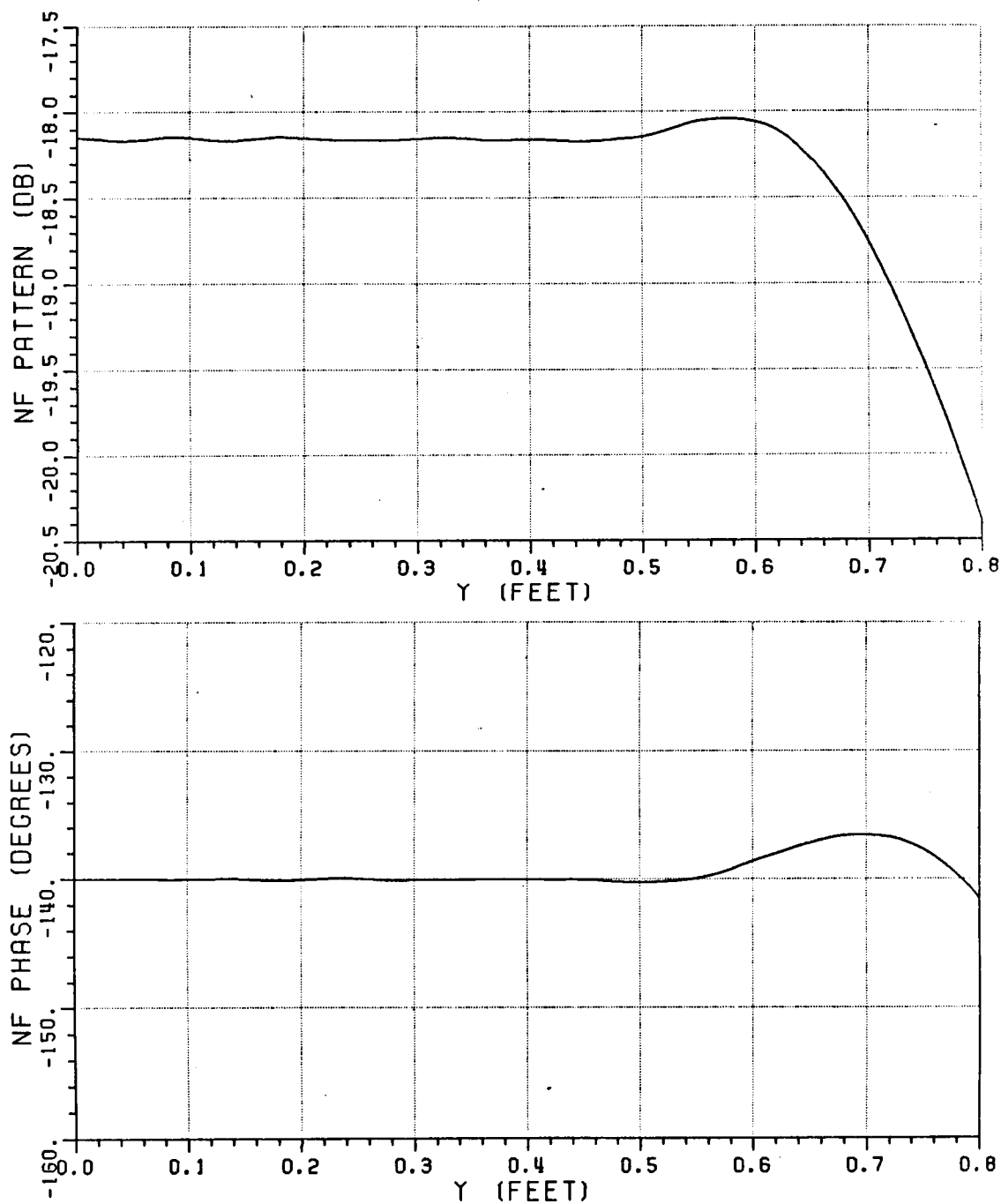


Figure 5.19. Near-zone scattered fields from the blended main reflector of example BL-2 using P0 with first order end-point corrections at 20 GHz.

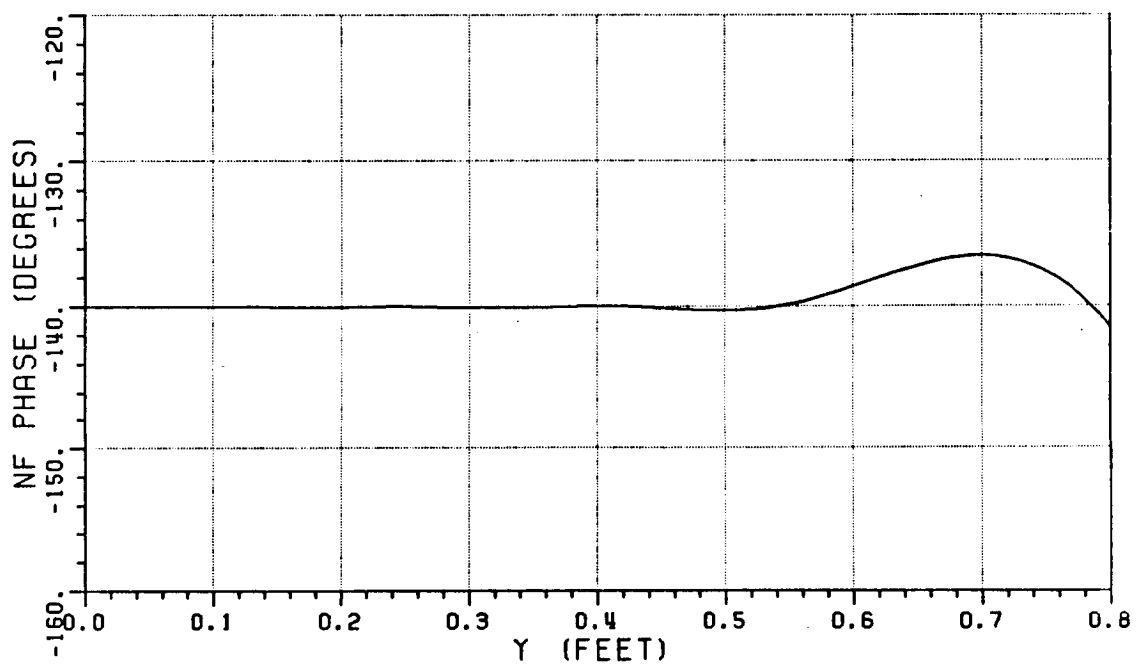
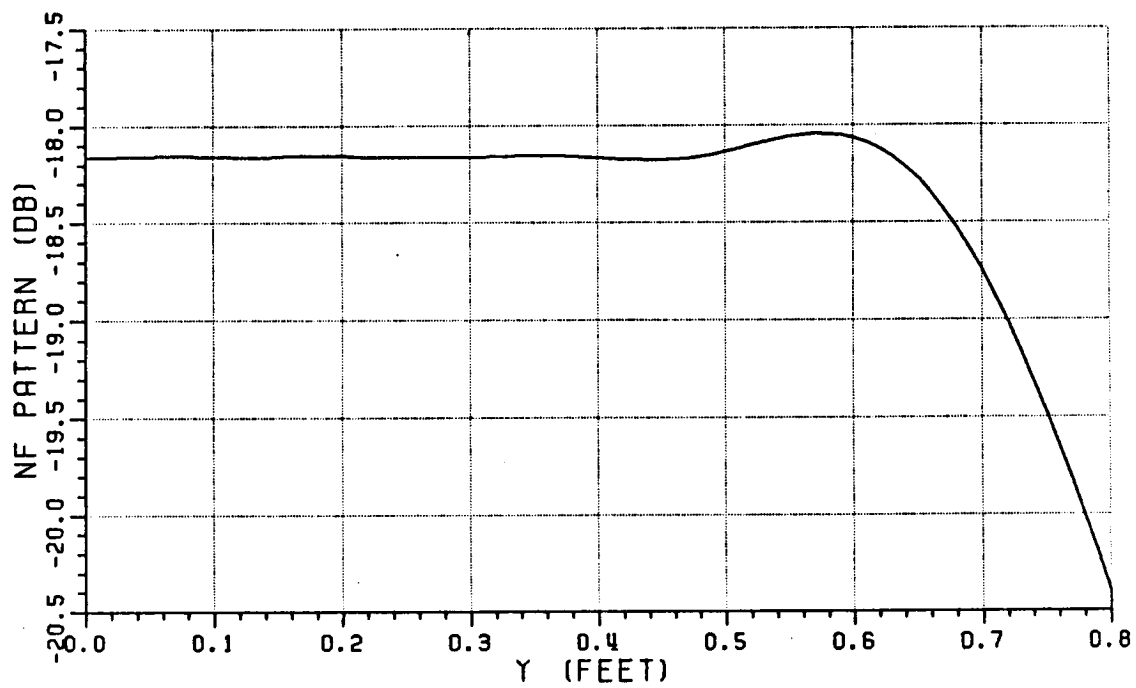


Figure 5.20. Near-zone scattered fields from the blended main reflector of example BL-2 using P0 with first and second order end-point corrections at 20 GHz.

drops off rapidly over the other region. This can cause some diffractions which will create significant ripple in the desired aperture distribution.

#### 5.4.3. Example BL3

The offset Gregorian reflector used in Example G3 of Chapter IV is used as the starting point for shaping in this example. A uniform aperture distribution over the region between  $y=-2.6'$  and  $y=18.8'$  is used to generate the shaped dual reflector. The blended rolled edge begins at  $y=5.5'$  for the lower edge and at  $y=11.5'$  for the upper one. A magnetic line source with a power pattern of  $\cos^{200} \phi$  is used as the primary source. The tilt angle of the feed axis is  $-7.7^\circ$  so that the central ray is located at  $y=8.5'$ . The power between  $-9^\circ$  and  $10^\circ$  with respect to the tilted feed axis is redistributed uniformly over  $y=-2.6'$  to  $y=18.8'$ . The parameters for the blended rolled edges are as follows:

$$a_e=0.78', b_e=4.5', s_m=8.5', \text{ and } \nu_m = 90^\circ$$

and the cosine-squared blending function is used. The resulting reflector surfaces are shown in Figure 5.21.

The near-zone scattered fields calculated at 3 GHz for this new reflector system are shown in Figures 5.22 through 5.24 for the P0, the P0 with first order end-point corrections, and the P0 with both the first and second order end-point corrections, respectively. Similar results calculated at 10 GHz are shown in Figures 5.25 through 5.27.

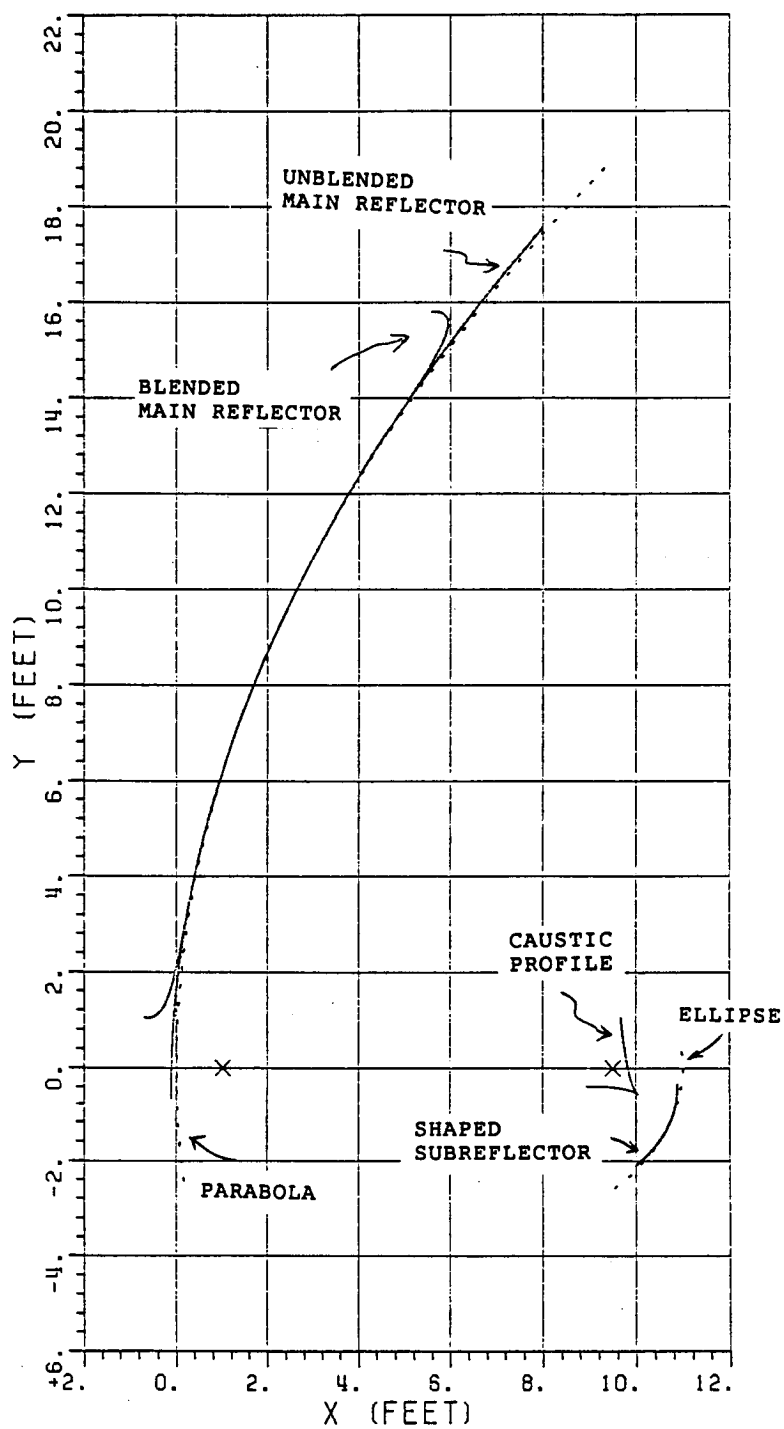


Figure 5.21. Shaped offset dual reflectors with blended rolled edges of example BL-3.

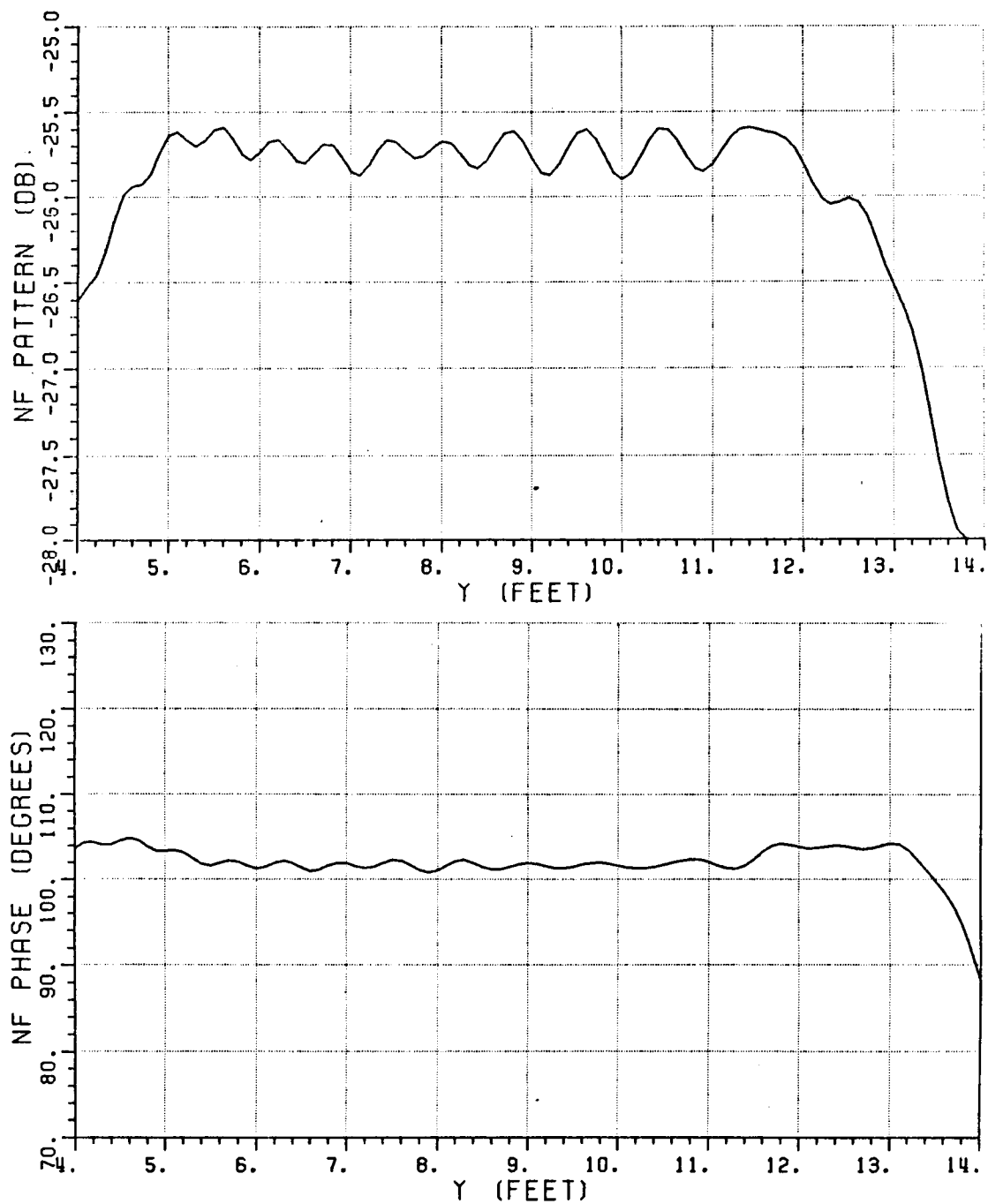


Figure 5.22. Near-zone scattered fields from the blended main reflector of example BL-3 at 3 GHz using P0.

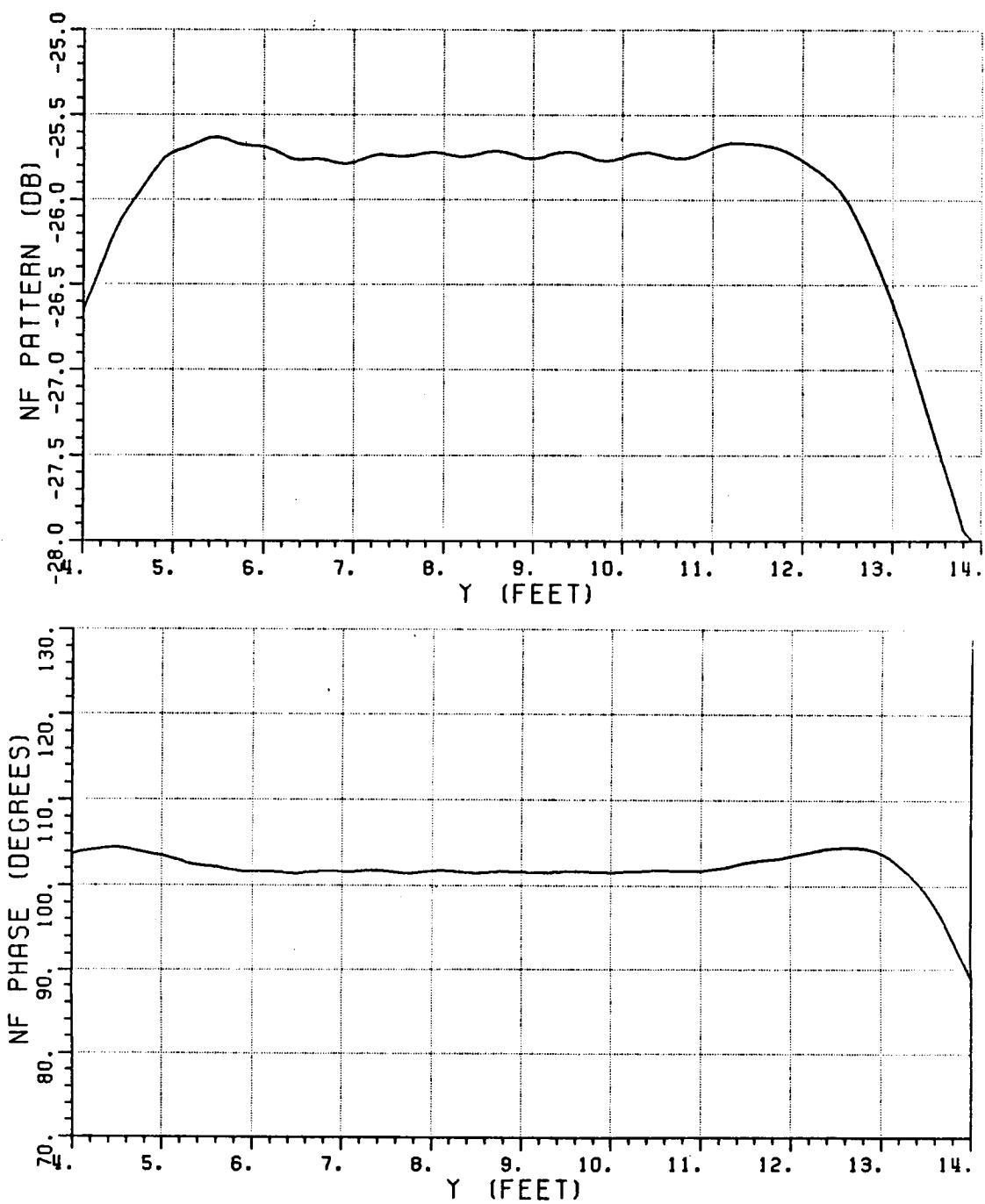


Figure 5.23. Near-zone scattered fields from the blended main reflector of example BL-3 at 3 GHz using PO with first order end-point corrections.

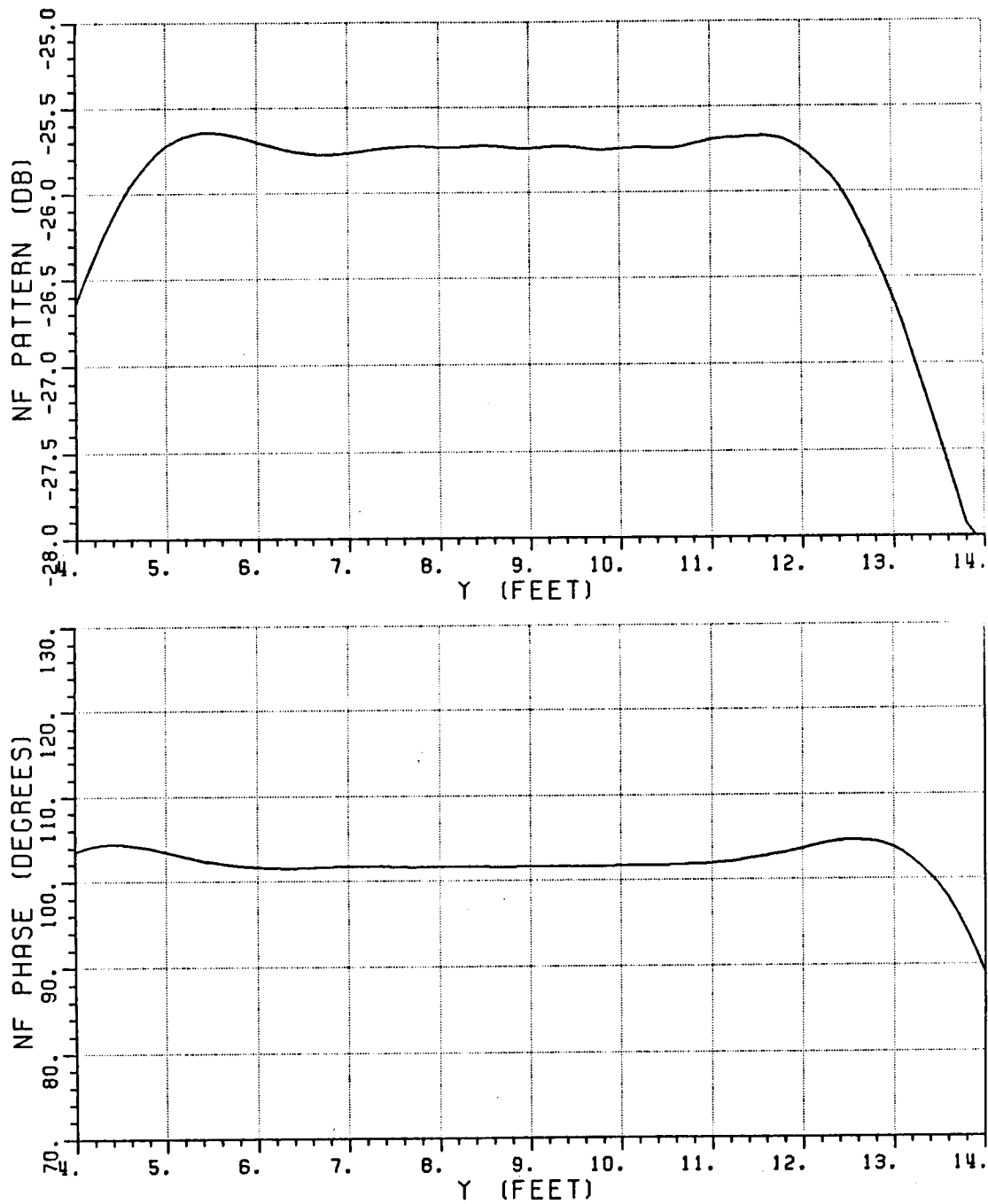


Figure 5.24. Near-zone scattered fields from the blended main reflector of example BL-3 at 3 GHz using P0 with first and second order end-point corrections.



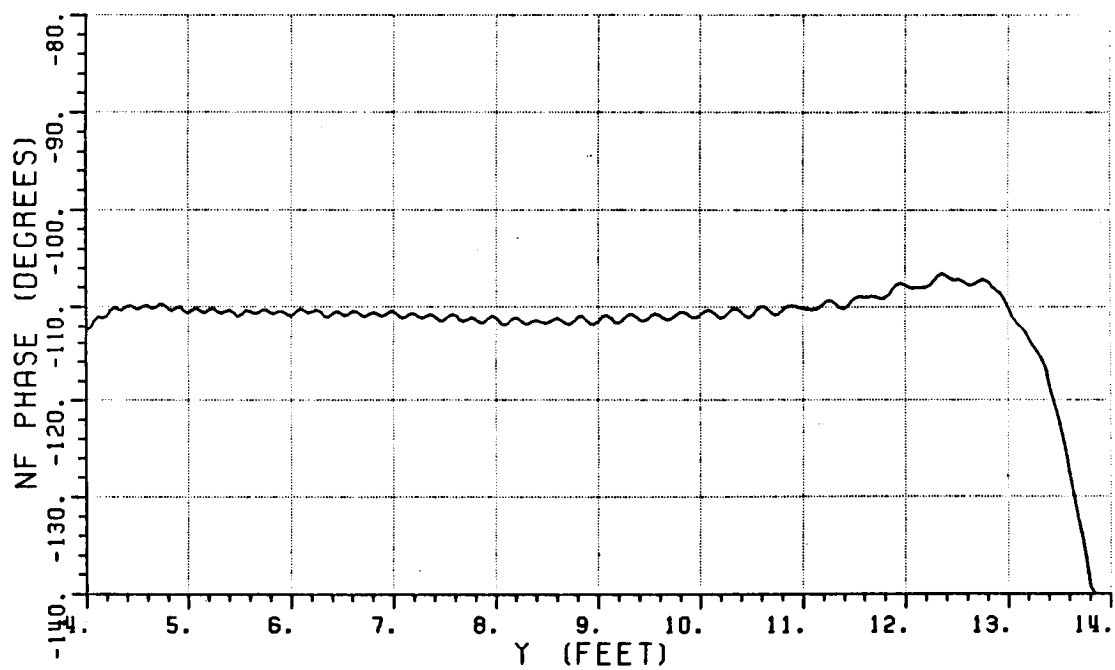
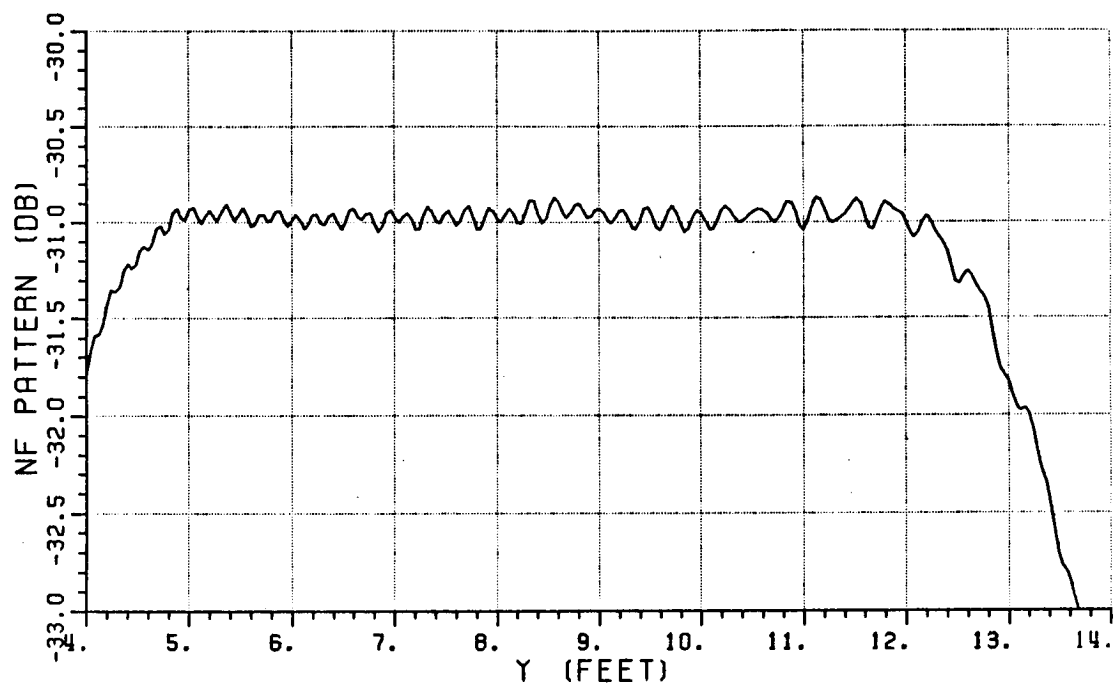


Figure 5.25. Near-zone scattered fields from blended main reflector of example BL-3 at 10 GHz using P0.

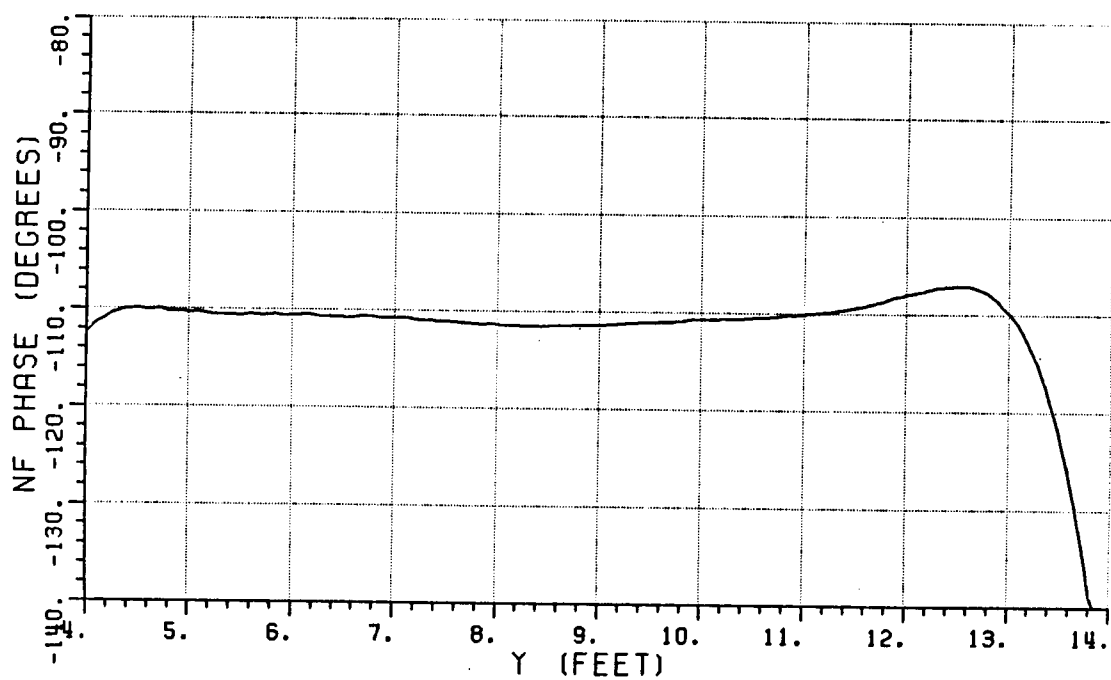
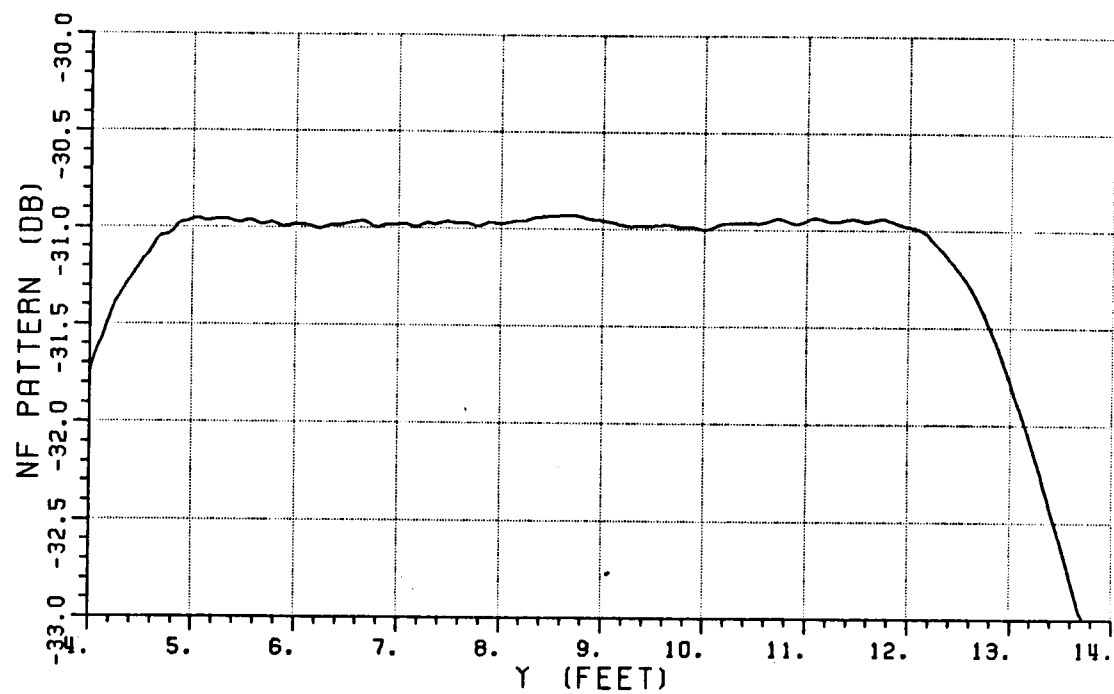


Figure 5.26. Near-zone scattered fields from blended main reflector of example BL-3 at 10 GHz using P0 with first order end-point corrections.

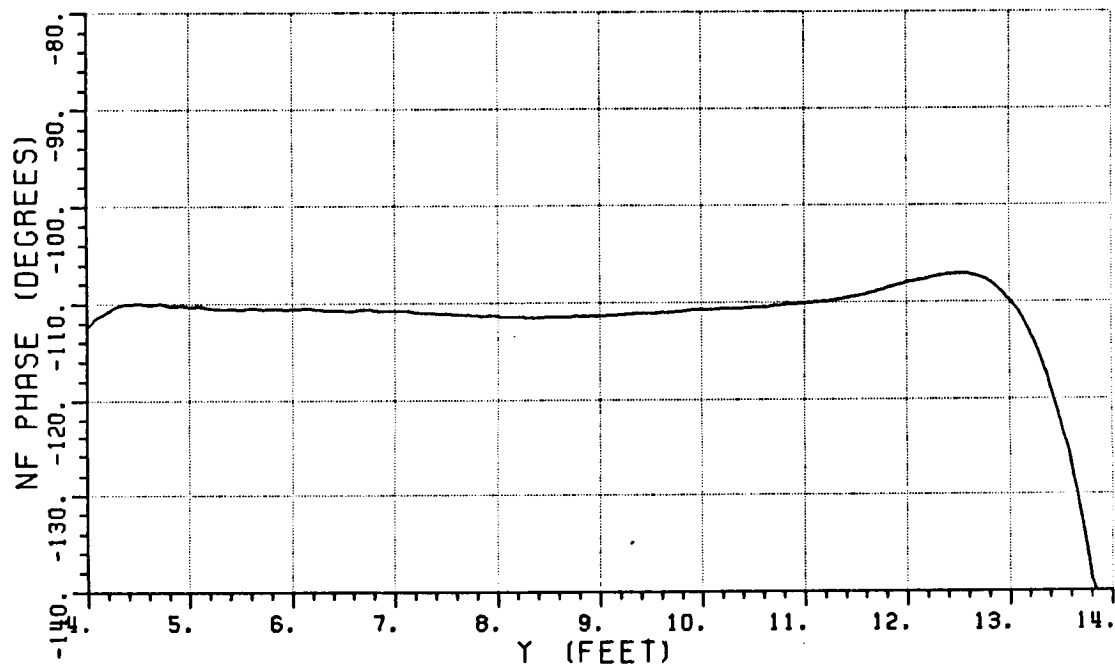
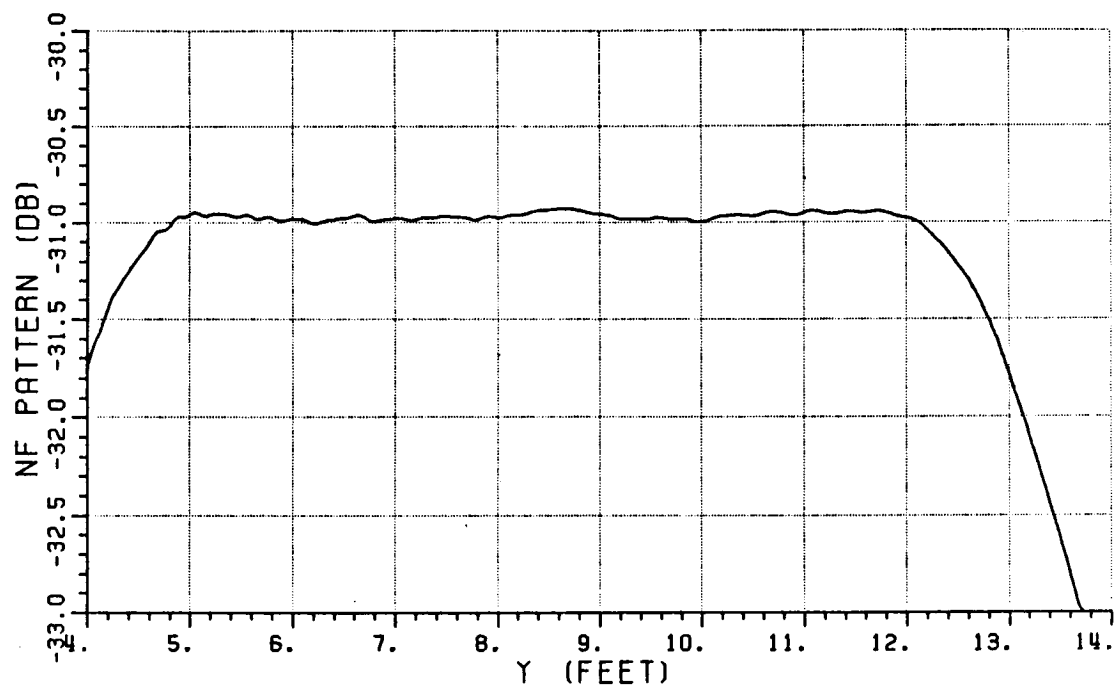


Figure 5.27. Near-zone scattered fields from the blended main reflector of example BL-3 at 10 GHz using P0 with first and second order end-point corrections.

The very small difference between Figure 5.26 and Figure 5.27 reveals that the second order end-point corrections are insignificant in this case. The ripple shown in Figure 5.27 results from the numerical integration errors associated with the P0 solution.

### 5.5. Summary

The addition of rolled edges to the main reflector reduces the edge diffracted fields and consequently, reduces the ripple in the near-zone scattered fields, as compared to the reflector with a sharp termination. This is very helpful in improving the performance of the compact range reflector. Several examples are used to verify this concept. The physical optics method is used to calculate the scattered field from the main reflector with blended rolled edges. Corrections are made for the false end-point contributions which result from the physical optics approximation. The resulting scattered fields of these examples show that very good performance of the reflectors are achieved.

## CHAPTER VI

### SHAPING OF THREE-DIMENSIONAL CIRCULARLY SYMMETRIC DUAL-REFLECTOR ANTENNAS

Discussions in the previous chapters have concentrated on the shaping of two-dimensional dual-reflector antennas. However, as was mentioned in Chapter III, the same approach can be applied to three-dimensional dual-reflector antennas with circular symmetry and circularly symmetric feed pattern illuminations. The approach for circularly symmetric shaped reflectors is discussed briefly in this chapter.

#### 6.1. Method of Shaping

A three-dimensional circularly symmetric surface is a body of revolution which is generated by rotating a generating curve about its axis of symmetry. For example, a three-dimensional circularly symmetric Cassegrain antenna can be generated by rotating the curves shown in Figure 2.6 about the x-axis, the axis of symmetry. By using the conventional cylindrical coordinates  $(\rho, \phi, z)$ , one can replace the x and y axes in Figure 2.6 by z and  $\rho$  axes, respectively. Similarly, if one defines the generating curves for a shaped dual-reflector for  $0 \leq \rho \leq \rho_{\max}$ , as shown in Figure 6.1, a three-dimensional circularly symmetric shaped dual-reflector can be found by rotating these curves about the z-axis,

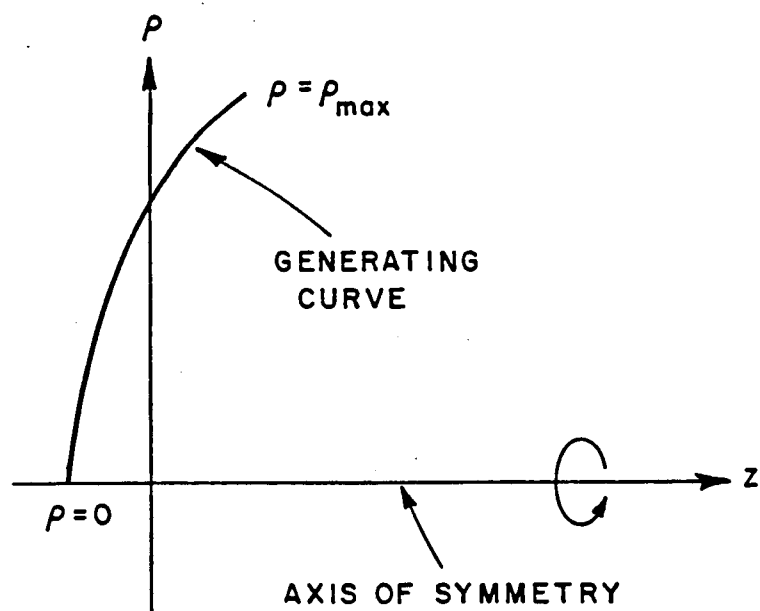


Figure 6.1. Generating curve and axis of symmetry for surface of revolution.

provided that the given primary source has a circularly symmetric pattern, and the desired aperture distribution is also circularly symmetric.

One major difference between the two-dimensional case and the three-dimensional one is that the formula for calculating the geometrical optics field is different. As discussed in Chapter II the geometrical optics field is proportional to a spread factor which involves the radius of curvature of the geometrical optics wavefront. For the two-dimensional case, the ray tube is two-dimensional, and the wavefront has only one radius of curvature. For the three-dimensional case, the ray tube is three-dimensional, and the wavefront has two radii of curvature. Consequently, one has to integrate the power pattern of the geometrical optics field over a surface in order to calculate the power contained in a three-dimensional ray tube.

Consider the shaping of a three-dimensional dual-reflector antenna to generate a symmetric near field aperture distribution  $CI(\rho)$  when a primary source with a symmetric radiation pattern  $F(\theta)$  is given. Conservation of power states that

$$\int_0^{2\pi} \int_0^{\theta_{\max}} F(\theta) \sin\theta \, d\theta d\phi = \int_0^{2\pi} \int_0^{\rho_{\max}} CI(\rho) \rho d\rho d\phi \quad (6.1)$$

in which  $\theta_{\max}$  is the maximum illumination angle at the subreflector edge, and  $\rho_{\max}$  is the maximum radius of the secondary aperture as defined in Figure 6.2. From Equation (6.1), the constant  $C$  is found as

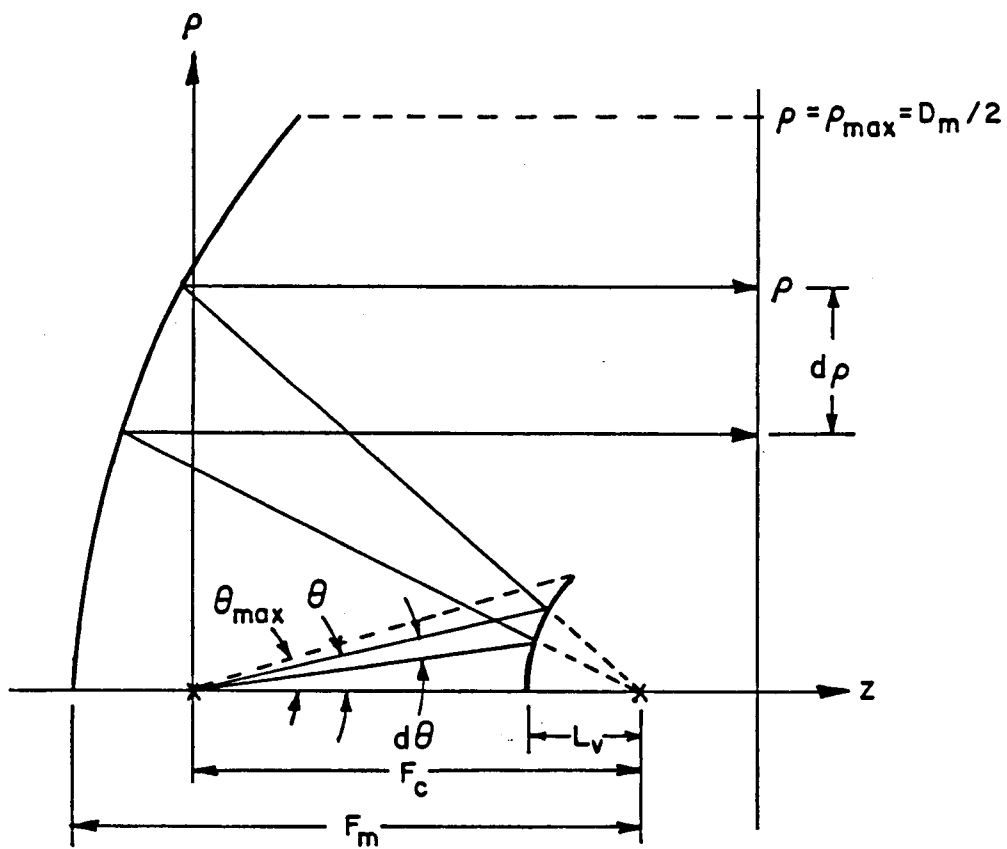


Figure 6.2. Geometry for defining parameters associated with a three-dimensional circular dual-reflector.



$$C = \frac{\int_0^{\theta_{\max}} F(\theta) \sin \theta d\theta}{\int_0^{\rho_{\max}} I(\rho) \rho d\rho} \quad (6.2)$$

Therefore, the relationship between  $\theta$  and  $\rho$  is given by

$$\int_0^{\theta} F(\theta) \sin \theta d\theta = \frac{\int_0^{\theta_{\max}} F(\theta) \sin \theta d\theta}{\int_0^{\rho_{\max}} I(\rho) \rho d\rho} \int_0^{\rho} I(\rho) \rho d\rho \quad (6.3)$$

It is obvious that the tilt angle of the feed axis is  $0^\circ$  in the circularly symmetric case. Equation (6.3) shows that one can use the identical shaping process given in Chapter III to create generating curves for three-dimensional circularly symmetric dual-reflector antennas by using this equation as the appropriate equation for conservation for power. The coordinates  $x$  and  $y$  used for the two-dimensional case are changed to  $z$  and  $\rho$  for the three-dimensional case.

The initial points for the shaping process have to be chosen as in the two-dimensional case. The condition which these initial points have to satisfy is given in Appendix C. Normally, these initial points are located on the axis of symmetry. Also the caustic curve in the two-dimensional case becomes a caustic surface in the three-dimensional case.

Three examples are given in the next sections to illustrate the shaping of three-dimensional circularly symmetric dual-reflector antennas. The results of the first two examples are compared with ones obtained via a different approach proposed by Narasimhan [24] and Ekelman [25]. The third example is the same example used by Williams [16]. Narasimhan modified the partial differential equation derived for an offset dual-reflector by Lee [19] to a ordinary differential equation which has to be solved numerically.

## 6.2. Examples of Shaping of Three-Dimensional Dual-Reflector Antennas

### 6.2.1. Example 3D1

In this example, a shaped dual-reflector with a concave subreflector is to be generated so that a uniform aperture distribution is obtained at the aperture of the main reflector. The primary source has a  $\cos^{20} \theta$  symmetric power pattern and is located 0.5' from the vertex of the shaped main reflector. The diameter of the main reflector is 2.0'. The vertex of the shaped subreflector is located 0.2667' from the primary source. The maximum illumination angle of the primary source on the subreflector is  $\theta_{\max} = 31.42^\circ$ . The initial points for the shaping are thus given by

$$(z_{10}, \rho_{10}) = (0.7667', 0.)$$

$$(z_{20}, \rho_{20}) = (0.0, 0.0)$$

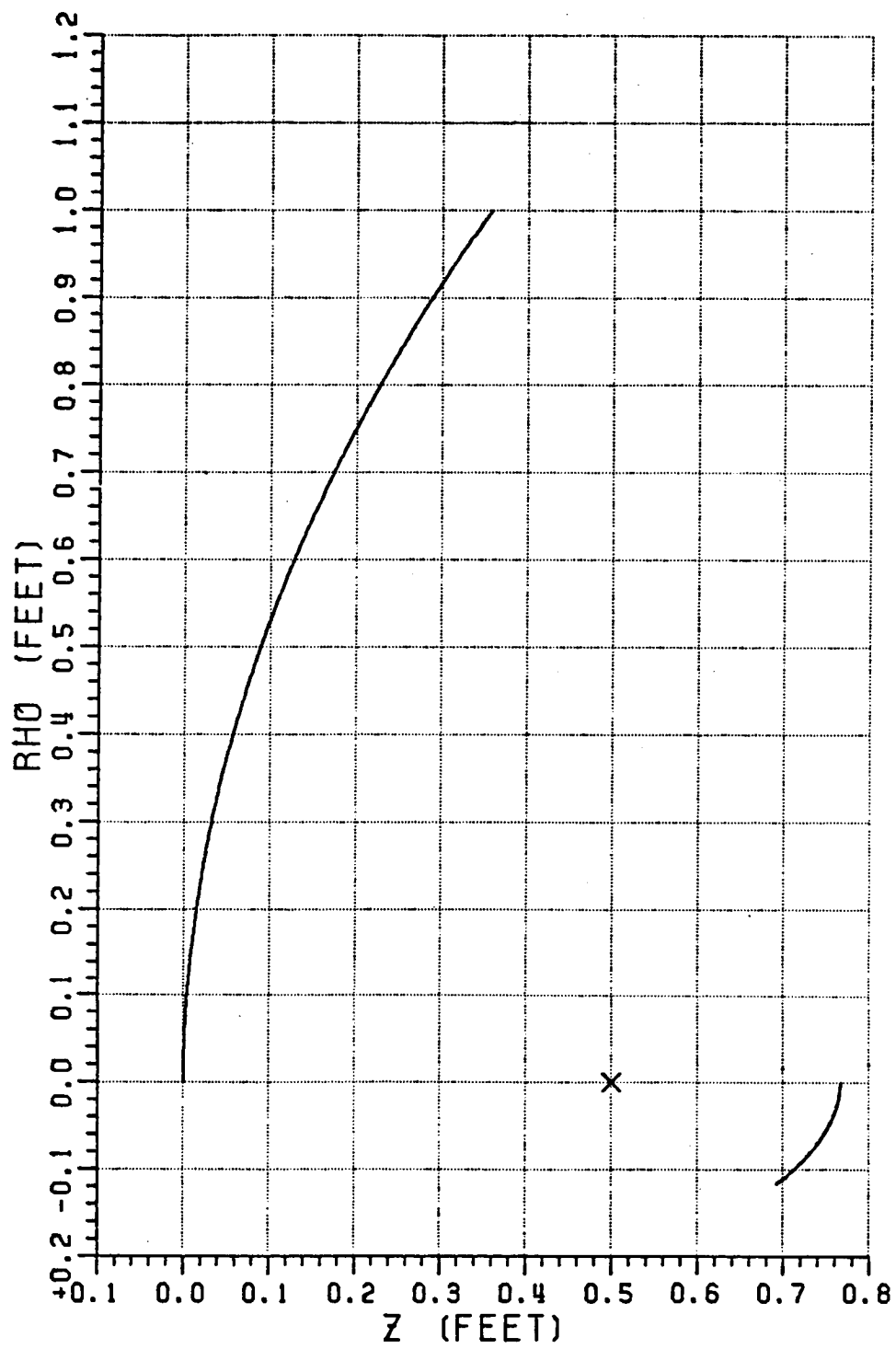


Figure 6.3. Shaped dual-reflector of example 3D1.

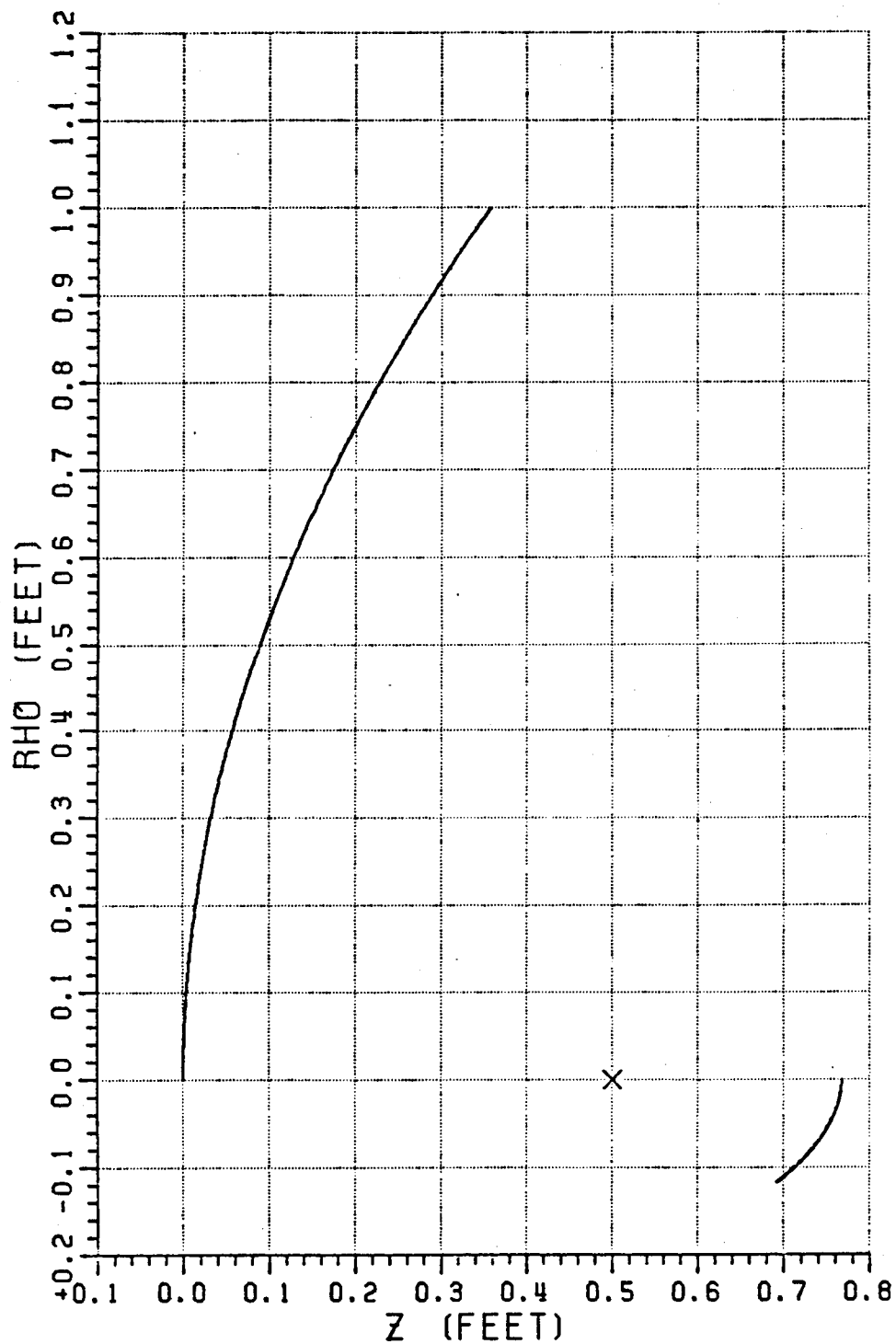


Figure 6.4. Shaped dual-reflector of example 3D1 obtained by the method of Narasimhan [24] and Ekelman [25].

and  $(z_{co}, \rho_{co})$  is determined from the ray condition given in Appendix C. The resulting shaped dual-reflector is shown in Figure 6.3. The surfaces obtained by using the method proposed by Narasimhan [24] and Ekelman [25] are shown in Figure 6.4. The results are in very good agreement as can be seen by comparing Figures 6.3 and 6.4.

#### 6.2.2. Example 3D2

This example is similar to Example 3D1 except that the subreflector is a convex surface and the primary source is located 0.1' from the vertex of the main reflector. The maximum illumination angle  $\theta_{max}$  is  $18.26^\circ$ , and the vertex of the subreflector is 0.4667' from the primary source. The initial points on the reflectors are

$$(z_{10}, \rho_{10}) = (0.5667', 0.0)$$

$$(z_{20}, \rho_{20}) = (0.0, 0.0)$$

and  $(z_{co}, \rho_{co})$  is thus determined. The resulting shaped dual-reflector is shown in Figure 6.5 and is again in very good agreement with the one obtained by using the method of Narasimhan [24] and Ekelman [25] which is shown in Figure 6.6.

#### 6.2.3. Example 3D3

In this example, the conventional Cassegrain reflector used by Williams [16] is used as the starting point of shaping. The parameters

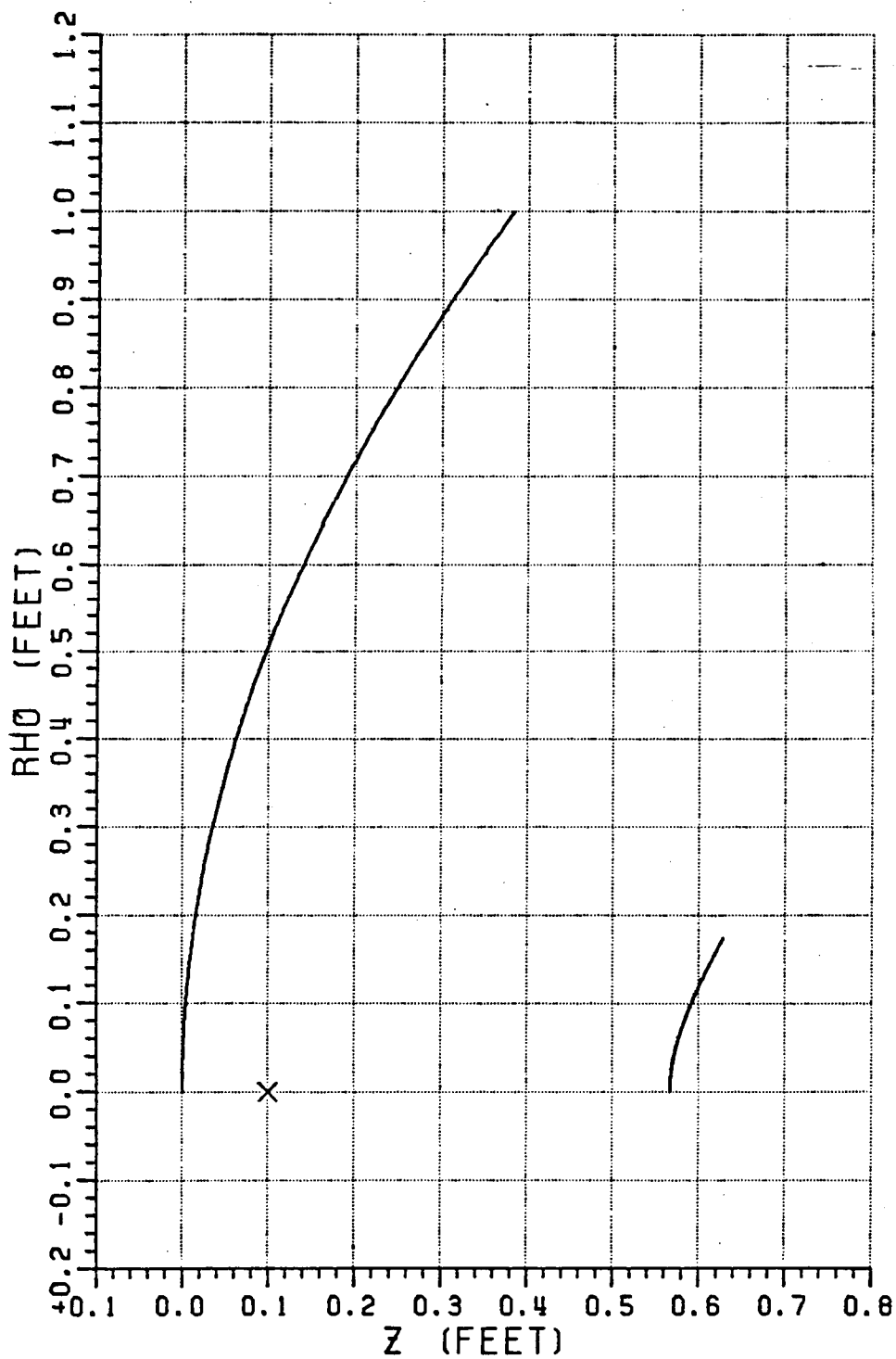


Figure 6.5. Shaped dual-reflector of example 3D2.

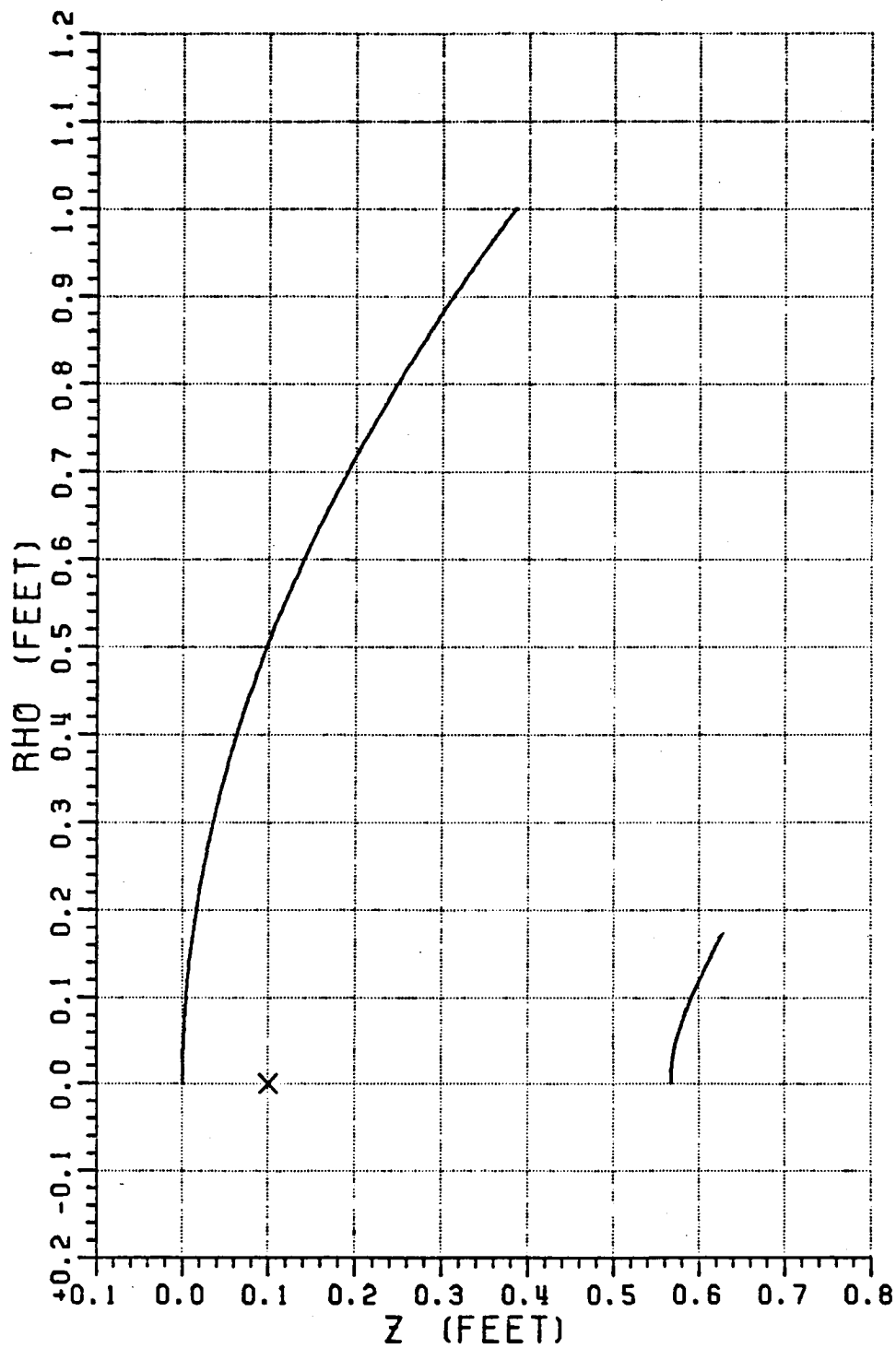


Figure 6.6. Shaped dual-reflector of example 3D2 obtained by the method of Narasinhham [24] and Ekelman [25].

associated with this Cassegrain antenna are

$$F_m = 2.5'$$

$$F_c = 1.5'$$

$$L_v = 0.20943'$$

$$D_m = 10.0'$$

and a point source with  $\cos^{84.5} \theta$  power pattern is used as the primary feed. The secondary aperture is required to have uniform amplitude and phase distributions. The shaped surface obtained by Williams are shown in Figure 6.7. This is an enlarged version of Figure 3 of [16]. These surfaces are obtained by shaping the subreflector first and the main reflector is designed to create the desired uniform phase distribution. Figures 6.8 and 6.9 show the shaped reflectors calculated by the method of Narasimhan [24] and Ekelman [25].

In order to use the approach of shaping discussed in this chapter, the initial points for the shaping are chosen as

$$(z_{10}, \rho_{10}) = (2.18357', 0')$$

$$(z_{20}, \rho_{20}) = (-0.107', 0.0')$$



for the subreflector and main reflector, respectively. These points are actually obtained from Figure 6.7 which are the intersection points of the axis of symmetry and the shaped reflectors designed by Williams. The initial point of the caustic surface is thus determined. The resulting shaped surfaces are shown in Figures 6.10 and 6.11. These results show that very good agreement has been obtained among the three methods.

### 6.3. Summary

In this chapter, the shaping process for the two-dimensional dual-reflector was modified slightly for shaping of the three-dimensional dual-reflector with circular symmetry. Examples were used to verify the process. Comparisons were shown between different approaches. Although the method of synthesis discussed in this chapter is not much simpler than Narasimhan's approach, one can still examine the caustic surface of the subreflector reflected field as in the two-dimensional case. The behavior of the shaped reflectors can be explained physically.

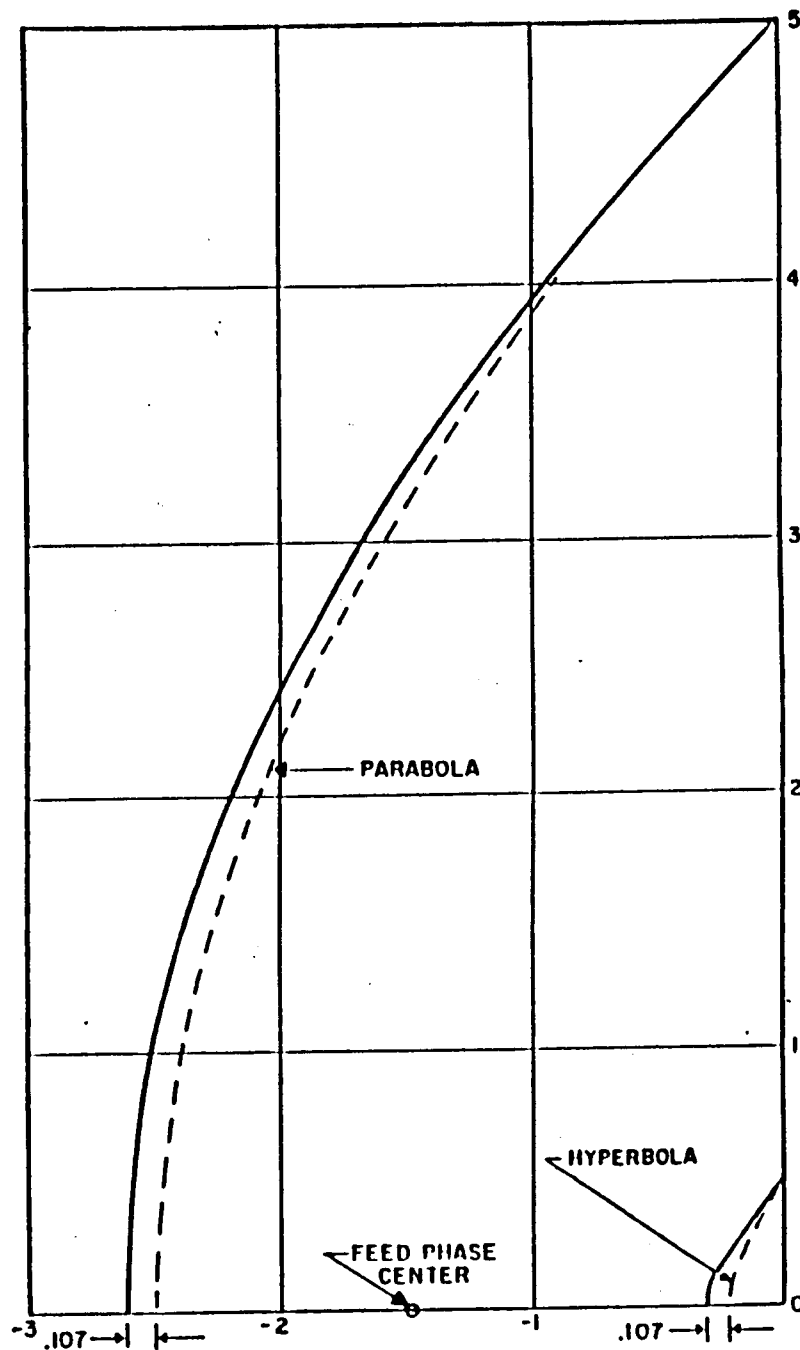


Figure 6.7. Shaped 3-dimensional circular symmetric dual-reflector from [16].

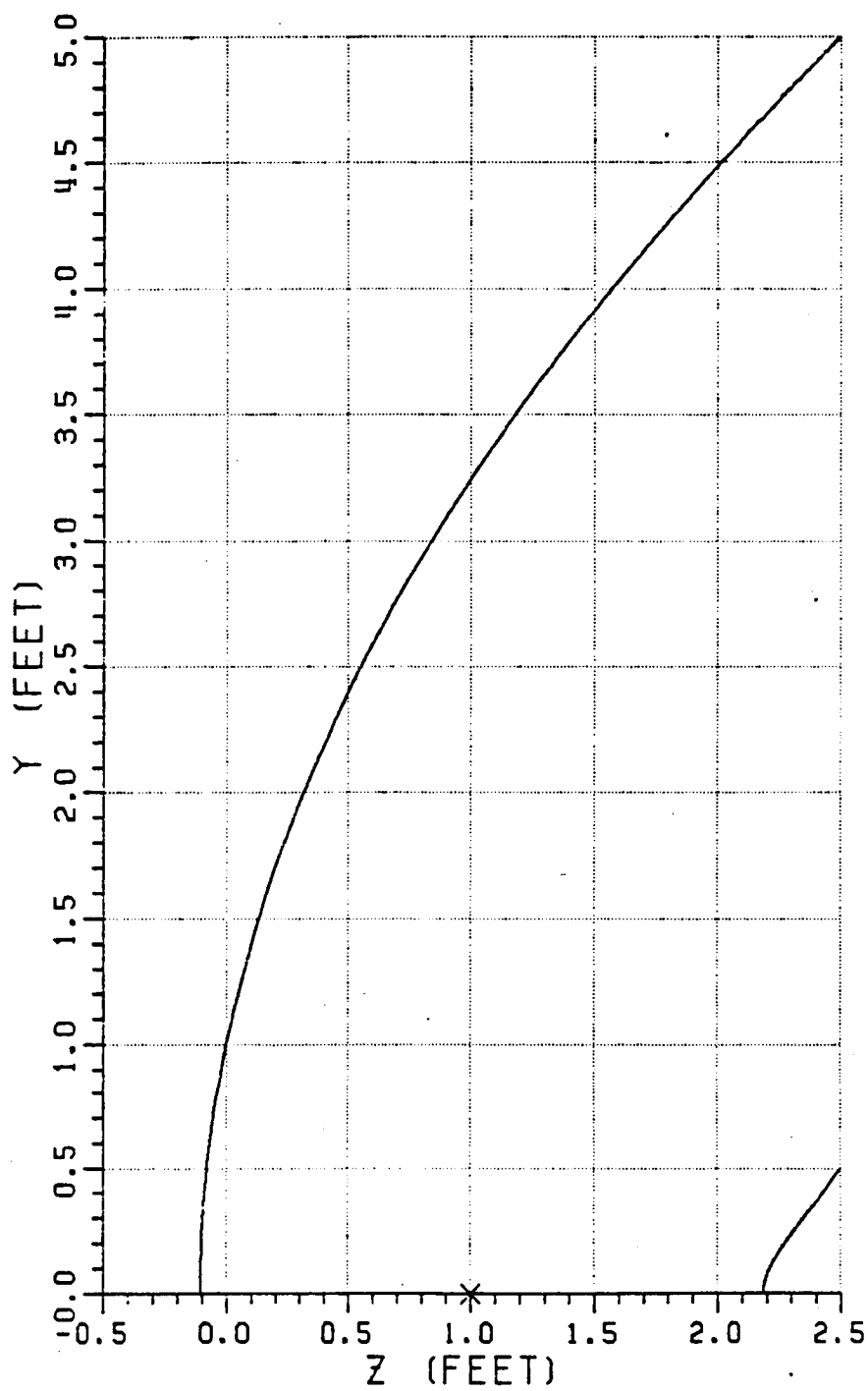


Figure 6.8. Shaped dual-reflector of example 3D3 obtained by the method of Narasimhan [24] and Ekelman [25].

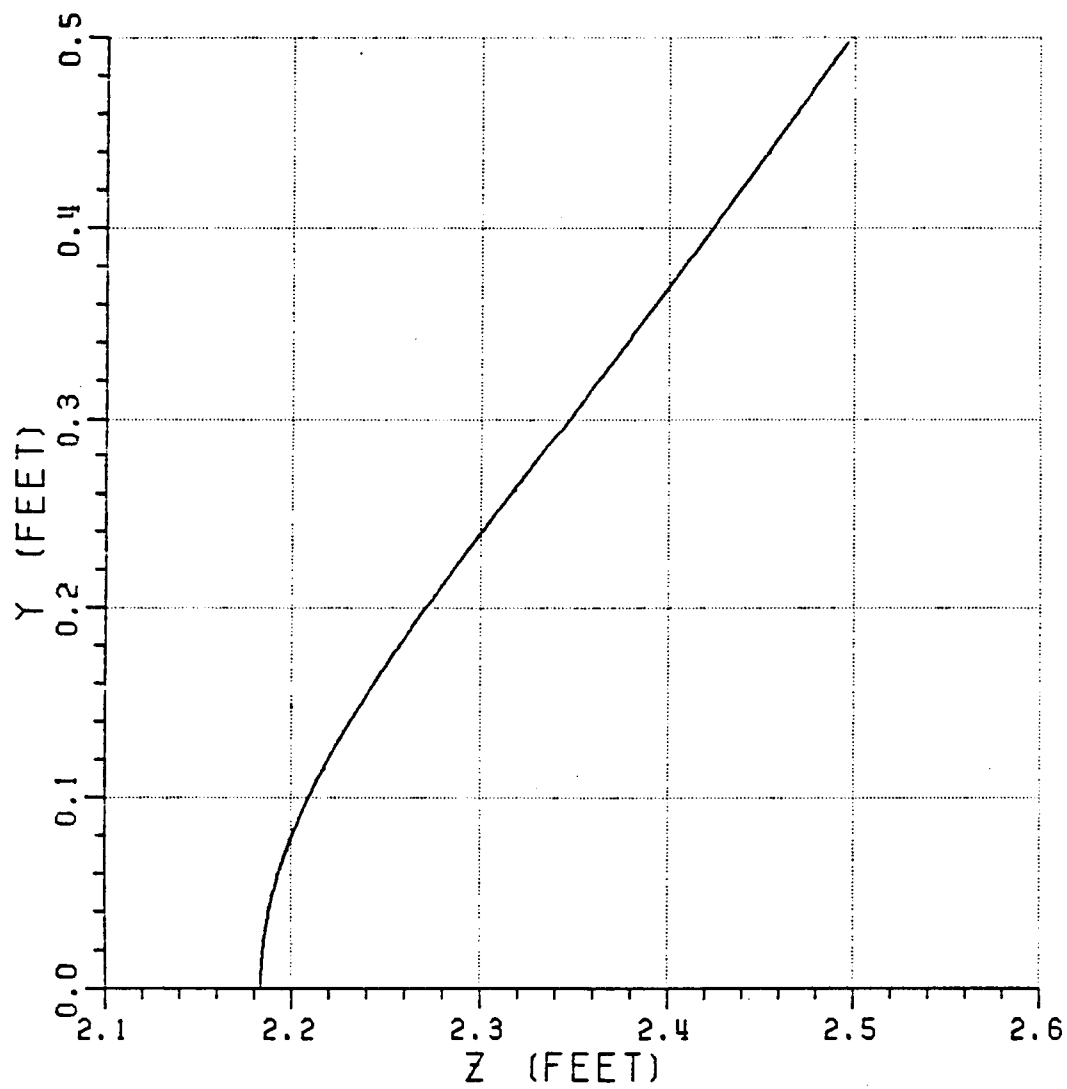


Figure 6.9. Shaped subreflector of example 3D3 obtained by the method of Narasimhan [24] and Ekelman [25].

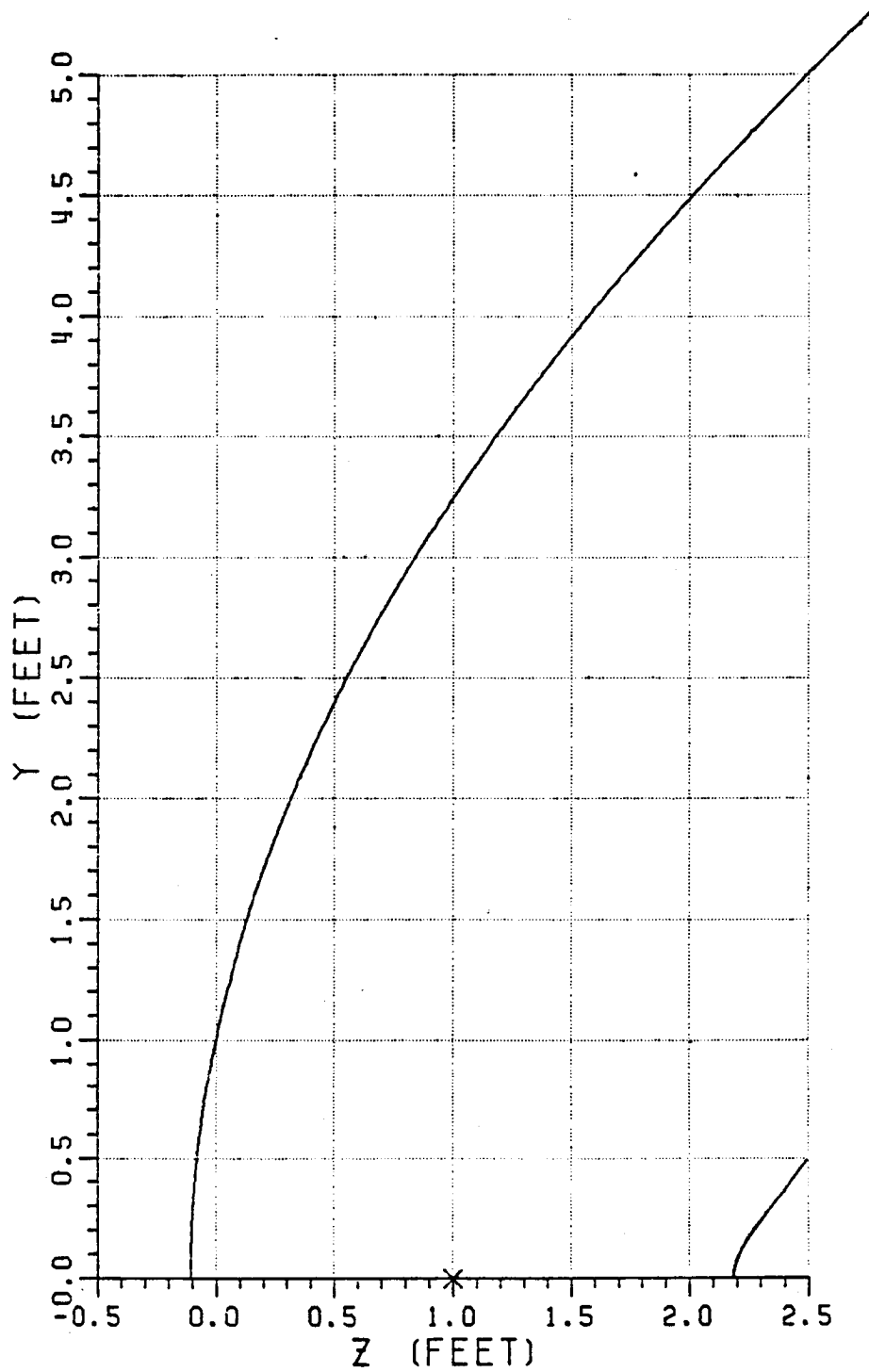


Figure 6.10. Shaped dual-reflector of example 3D3 obtained by the new approach.

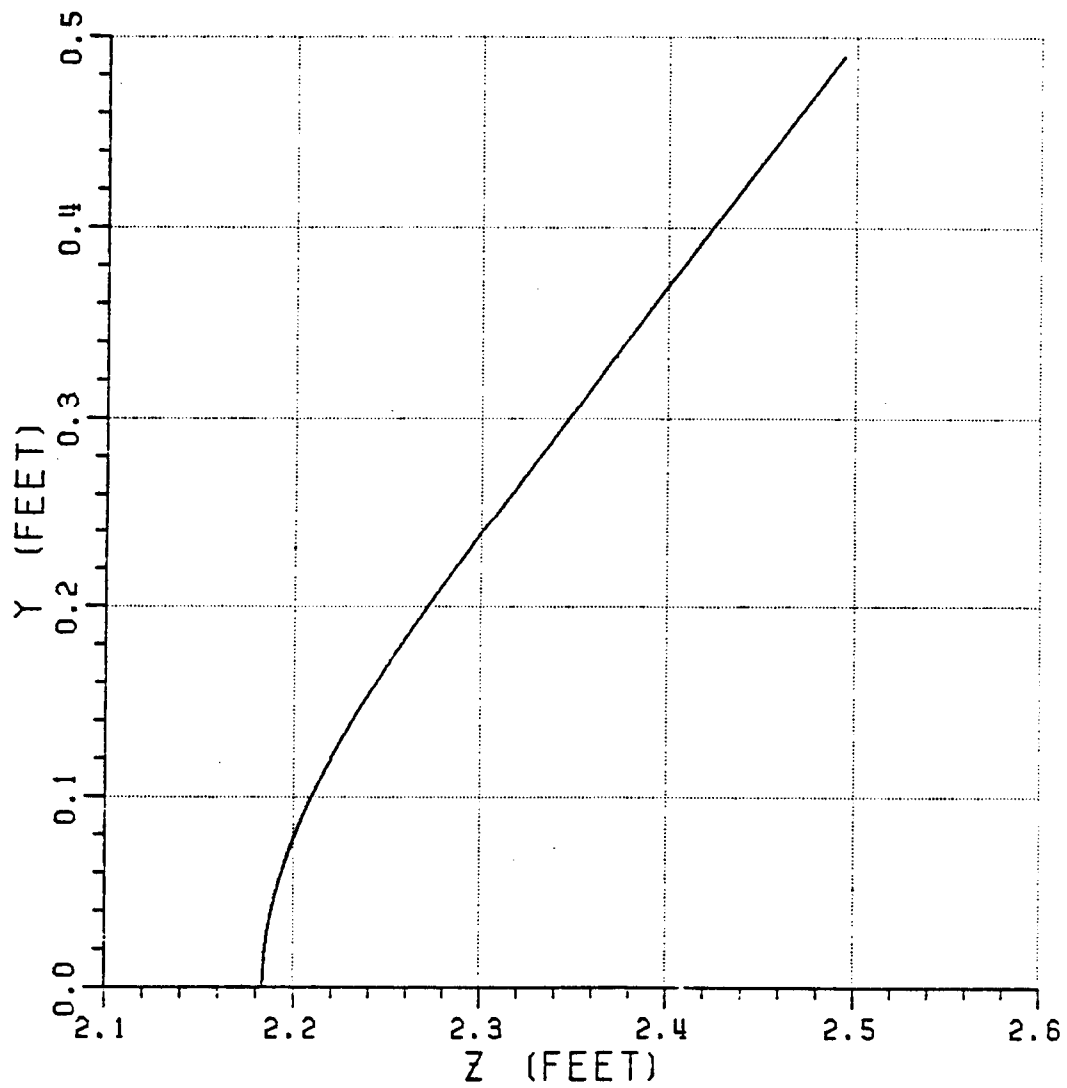


Figure 6.11. Shaped subreflector of example 3D3 obtained by the new approach.

## CHAPTER VII

### SUMMARY AND CONCLUSIONS

A new approach for the shaping of dual-reflector antenna systems to generate a prescribed aperture distribution is proposed and studied in this research. The approach is based on the geometrical optics properties of conventional Cassegrain and Gregorian reflector antennas. A set of algebraic equations has been obtained and solved by a numerical method. This approach also explains how the shaped dual-reflector works for generating a prescribed aperture distribution by examining the behavior of the caustic curve of the shaped subreflector reflected fields. Several two-dimensional examples are presented to validate the formulation and solution of this new approach for shaping dual-reflector antennas. A conventional Cassegrain or Gregorian reflector antenna is provided as the starting point of shaping when a primary source power pattern is given. The method of physical optics is used to calculate the far-zone scattered fields from the subreflector and the near-zone scattered fields from the main reflector. The results are compared between the conventional and shaped reflectors. As expected, the shaped reflector system provides the aperture field prescribed.

Rolled edge treatment to the shaped dual-reflector is also studied. The addition of the rolled edges to the shaped main reflector can reduce the edge diffracted fields and consequently, the ripple in the near-zone scattered fields. This improvement is especially important in the

application of compact range reflectors because creating a uniform plane wave illumination is a strict requirement. Corrections are made for the false end-point contributions of the rolled edges which are caused by the sharp termination of physical optics currents. By removing the false end-point contributions from the physical optics integration results, a more accurate representation of the scattered fields from reflector surfaces is obtained. Examples are also presented to show the improvement of adding blended rolled edges to the shaped main reflector.

The shaping of three-dimensional circularly symmetric dual-reflectors is achieved by a simple modification of the two-dimensional case. The reflectors are illuminated by primary sources with circularly symmetric power patterns and the secondary aperture distributions also have the property of circular symmetry. Examples are presented and compared with the results obtained by other approaches.

Throughout this study, a numerical method is used to approximately solve for the surface equations. Different numerical methods could be used to solve these equations.

Although some research has been done in the past for the shaping of dual-reflector antennas, only the shapes of the reflector surfaces were examined by most people. By using the method of shaping proposed in this study, one can clearly understand the detail of how the shaped reflector works to transform a given primary feed pattern into a prescribed aperture distribution. This is accomplished by examining the behavior of the caustic curve for the fields reflected from the shaped subreflector. Consequently, some potential problems associated with the



shaped reflectors can be disclosed through unusual properties of the caustic curve, such as a discontinuity in its slope. These possible problems affect the performance of the shaped reflectors especially in the compact range applications.

Further study is recommended for applying the shaping approach proposed in this research to three-dimensional offset dual-reflectors. Unlike the circularly symmetric case for which the shaping can be done on a two-dimensional basis, the offset dual-reflector has to be shaped on a three-dimensional basis. It is pointed out in [14] and [26] that the exact solution to the dual-reflector synthesis does not exist in general. Consequently, an approximate solution must be sought when an exact solution cannot be found. Further investigation will have to be done on this topic.

## APPENDIX A

### DIRECT APPLICATION OF PRINCIPLES OF GEOMETRICAL OPTICS TO DUAL-REFLECTOR ANTENNA SHAPING

In this appendix, the principles of geometrical optics mentioned in Chapter III are used directly to generate a two-reflector antenna system from which a prescribed secondary aperture distribution is obtained.

#### A.1. Formulation

Consider the geometry shown in Figure A.1 where a given primary source is located at the coordinate origin. Assume that the points  $(x_{10}, y_{10})$  on the subreflector and  $(x_{20}, y_{20})$  on the main reflector are also known. For a given ray  $y=m_0x$  which emanates from the primary source, the corresponding reflected ray from the main reflector,  $y=Y_2$ , is to be generated and is parallel to the  $x$ -axis. The unknown point  $(X_1, Y_1)$  on the subreflector is assumed to be located on a line which passes through  $(x_{10}, y_{10})$  and has the slope  $m_1$ . Similarly, the unknown point  $(X_2, Y_2)$  on the main reflector is located on a line which passes through  $(x_{20}, y_{20})$  and has slope  $m_2$ . These assumptions are valid when the surface points are very close to each other. From the application of the principles of geometrical optics and the above assumptions, a set of algebraic equations is generated and solved to obtain the surfaces.

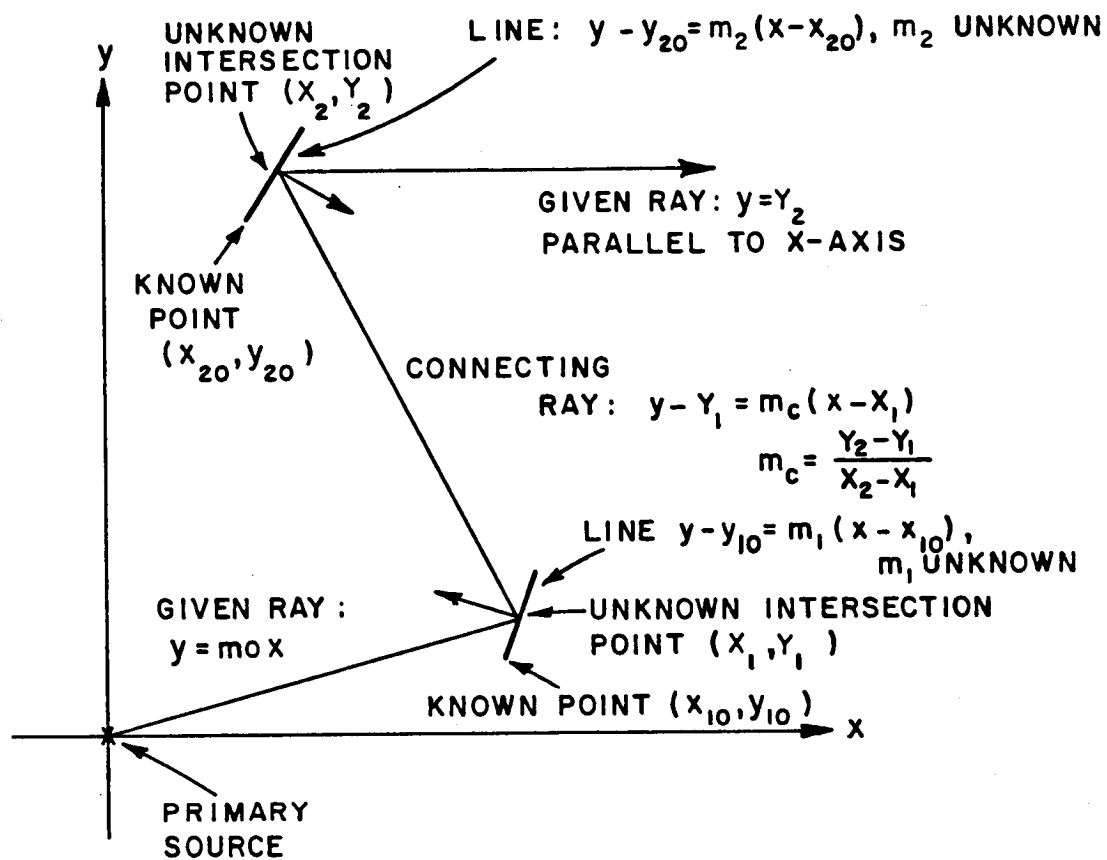


Figure A.1. Geometry for direct application of principles of geometrical optics to dual-reflector shaping.

At the first reflector (i.e. the subreflector), which is given in Figure A.2, the incident ray, reflected ray, and surface normal  $\hat{n}_1$  satisfy Snell's law of reflection, in other words,

$$\theta_o - \theta_1 = \theta_1 - \theta_c \quad (A.1)$$

or

$$2\theta_1 = \theta_o + \theta_c \quad (A.2)$$

By taking tangent on both sides of Equation (A.2), one finds that

$$\tan(2\theta_1) = \tan(\theta_o + \theta_c) . \quad (A.3)$$

From the identity

$$\tan(\alpha + \beta) = \frac{\tan\alpha + \tan\beta}{1 - \tan\alpha\tan\beta}$$

Equation (A.3) results in

$$\frac{2\tan\theta_1}{1 - \tan^2\theta_1} = \frac{\tan\theta_o + \tan\theta_c}{1 - \tan\theta_o\tan\theta_c} \quad (A.4)$$

but,

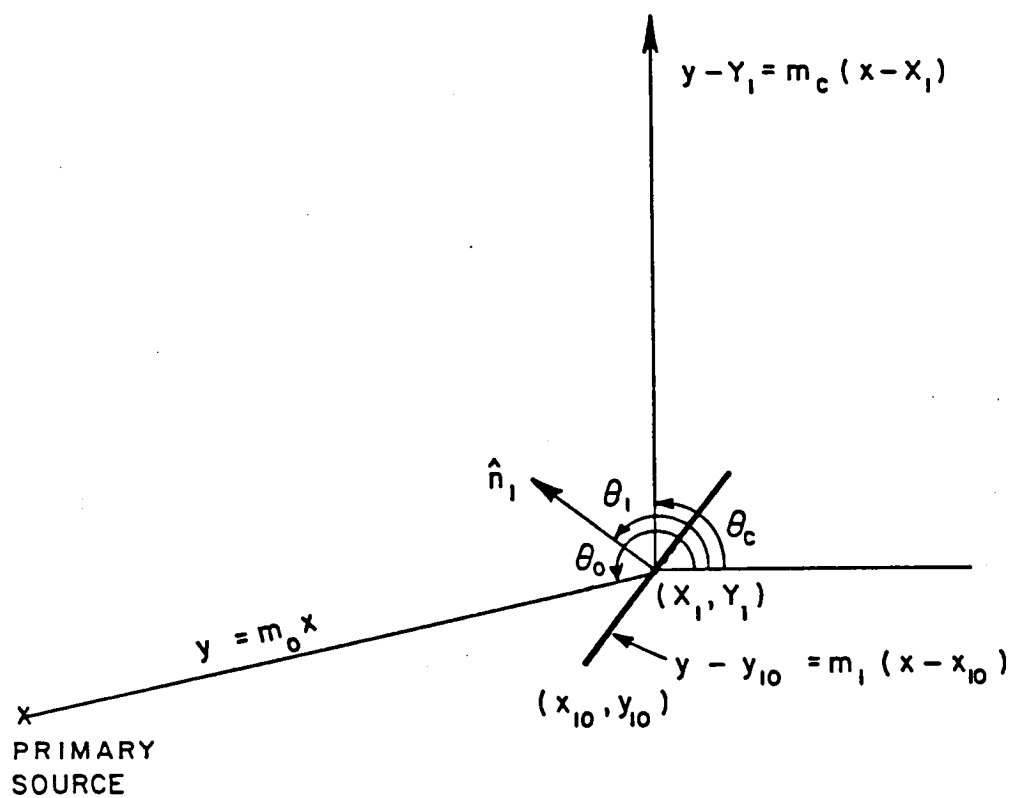


Figure A.2. Snell's law on the subreflector.

$$\tan\theta_o = m_o$$

$$\tan\theta_c = m_c$$

$$\tan\theta_1 = -\frac{1}{m_1}$$

Consequently, Equation (A.4) becomes

$$\frac{-2m_1}{m_1^2 - 1} = \frac{m_o + m_c}{1 - m_o m_c} \quad (\text{A.5})$$

For the main reflector, as shown in Figure A.3, Snell's law states that

$$\theta'_c = 2\theta_2 \quad (\text{A.6})$$

in which

$$\theta'_c = 180^\circ - \theta_c \quad (\text{A.7})$$

Substituting (A.7) into (A.6) and taking the tangent on both sides of the equation, the following equation is obtained:

$$m_c = \frac{-2m_2}{m_2^2 - 1} \quad (\text{A.8})$$

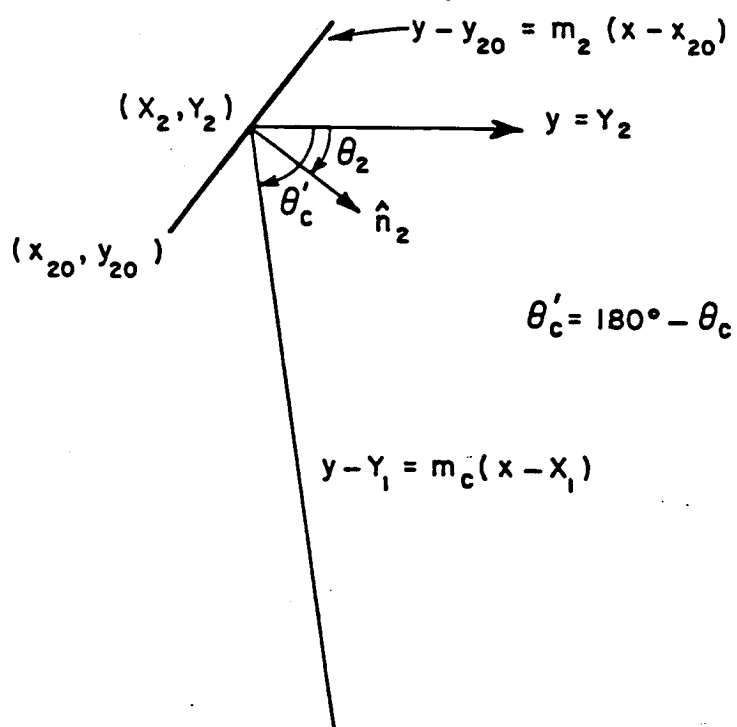


Figure A.3. Snell's law on the main reflector.

Also notice that  $X_1, Y_1$  have to satisfy

$$Y_1 = m_o X_1 \quad (A.9)$$

$$Y_1 - y_{10} = m_1 (X_1 - x_{10}) \quad (A.10)$$

and  $X_2$  has to satisfy

$$Y_2 - y_{20} = m_2 (X_2 - x_{20}) \quad (A.11)$$

In the above formulations,  $m_o$  and  $Y_2$  are assumed known so there are six unknowns  $X_1, Y_1, X_2, m_1, m_2, m_c$ , with six equations which are summarized as follows:

$$\frac{-2m_1}{m_1^2 - 1} = \frac{m_o + m_c}{1 - m_o m_c} \quad (A.12)$$

$$m_c = \frac{-2m_2}{m_2^2 - 1} \quad (A.13)$$

$$m_c = \frac{Y_2 - Y_1}{X_2 - X_1} \quad (A.14)$$

$$Y_1 = m_o X_1 \quad (A.15)$$

$$Y_1 - y_{10} = m_1 (X_1 - x_{10}) \quad (A.16)$$



$$Y_2 - y_{20} = m_2(X_2 - x_{20}) \quad (\text{A.17})$$

It is apparent that the above equations have to be solved numerically in order to obtain the surface of the reflectors. In the next section, a perturbation method is presented to solve the above equations.

## A.2. Method of Solution

From Equations (A.15) and (A.16), it is found that

$$X_1 = \frac{y_{10} - m_1 x_{10}}{m_o - m_1} \quad (\text{A.18})$$

$$Y_1 = \frac{m_o}{m_o - m_1} (y_{10} - m_1 x_{10}) \quad (\text{A.19})$$

From Equation (A.17),

$$X_2 = \frac{1}{m_2} (Y_2 - y_{20} + m_2 x_{20}) \quad (\text{A.20})$$

Substituting (A.18), (A.19), and (A.20) into (A.14), the following equation is obtained,

$$\begin{aligned} m_c [(m_o - m_1)(Y_2 - y_{20} + m_2 x_{20}) - m_2(y_{10} - m_1 x_{10})] \\ = m_2(m_o - m_1)Y_2 - m_o m_2(y_{10} - m_1 x_{10}) \end{aligned} \quad (\text{A.21})$$

Equations (A.12), (A.13), and (A.21) involve the unknowns  $m_1, m_2$ , and  $m_c$  and are very difficult to solve exactly. Consequently, a perturbation method which assumes that

$$m_c = m_{c0} + \Delta m_c \quad (A.22)$$

$$m_1 = m_{10} + \Delta m_1 \quad (A.23)$$

$$m_2 = m_{20} + \Delta m_2 \quad (A.24)$$

is used to solve  $m_1, m_2$ , and  $m_c$  numerically. In Equations (A.22) through (A.24),  $m_{c0}, m_{10}$ , and  $m_{20}$  are the corresponding slopes  $m_c, m_1$  and  $m_2$  for the previous ray and surfaces;  $\Delta m_c, \Delta m_1$ , and  $\Delta m_2$  are small perturbation of  $m_c, m_1$ , and  $m_2$ . By substituting these three equations into Equations (A.12), (A.13), and (A.21) and neglecting the higher order terms such as  $\Delta m_c \Delta m_1, \Delta m_c \Delta m_2, \Delta m_1 \Delta m_2$ , etc., the following three linear equations in  $\Delta m_c, \Delta m_1$ , and  $\Delta m_2$  are obtained.

$$A_{11} \Delta m_c + A_{12} \Delta m_1 + A_{13} \Delta m_2 = B_1 \quad (A.25)$$

$$A_{21} \Delta m_c + A_{22} \Delta m_1 + A_{23} \Delta m_2 = B_2 \quad (A.26)$$

$$A_{31} \Delta m_c + A_{32} \Delta m_1 + A_{33} \Delta m_2 = B_3 \quad (A.27)$$

where

$$A_{11} = 1 + 2m_o m_{10} - m_{10}^2$$

$$A_{12} = 2(m_o m_{co} - m_o m_{10} - m_{10} m_{co} - 1)$$

$$A_{13} = 0$$

$$B_1 = 2m_{10}(1 - m_o m_{co}) + (m_o + m_{co})(m_{10}^2 - 1)$$

$$A_{21} = m_{20}^2 - 1$$

$$A_{22} = 0$$

$$A_{23} = 2(m_{co} m_{20} + 1)$$

$$B_2 = m_{co}(1 - m_{20}^2) - 2m_{20}$$

$$A_{31} = (m_o - m_{10})(Y_2 - y_{20} + m_{20}x_{20}) - m_{20}(y_{10} - m_{10}x_{10})$$

$$A_{32} = m_{co}[m_{20}x_{10} - (Y_2 - y_{20} + m_{20}x_{20})] + m_{20}(Y_2 - m_o x_{10})$$

$$A_{33} = m_{co}[x_{20}(m_o - m_{10}) - (y_{10} - m_{10}x_{10})] - [(m_o - m_{10})Y_2 - m_o(y_{10} - m_{10}x_{10})]$$

$$B_3 = [m_{20}(m_o - m_{10})Y_2 - m_o m_{20}(y_{10} - m_{10}x_{10})]$$

$$- m_{co}[(m_o - m_{10})(Y_2 - y_{20} + m_{20}x_{20}) - m_{20}(y_{10} - m_{10}x_{10})]$$

The above equations are solved for  $\Delta m_c$ ,  $\Delta m_1$ , and  $\Delta m_2$  as

$$\Delta m_c = \frac{A_{12}A_{23}B_3 - A_{23}A_{32}B_1 - A_{12}A_{33}B_2}{A_{31}A_{12}A_{23} - A_{11}A_{23}A_{32} - A_{12}A_{21}A_{33}} \quad (A.28)$$

$$\Delta m_1 = \frac{1}{A_{12}} (B_1 - A_{11} \Delta m_c) \quad (A.29)$$

$$\Delta m_2 = \frac{1}{A_{23}} (B_2 - A_{21} \Delta m_c) \quad (A.30)$$

and the unknowns  $X_1, Y_1, X_2, m_1, m_2, m_c$  are obtained.

It is noted that the above method is valid provided that  $m_{10}, m_{20}, m_{c0}$  are known and  $\Delta m_1, \Delta m_2, \Delta m_3$  are very small. There is a difficulty associated with this approach. When the initial slopes are very large, the changes of the slopes  $\Delta m_1, \Delta m_2$ , or  $\Delta m_c$  are not small and the solutions are not accurate. Another method for solving the surface equations might have to be used.

## APPENDIX B

### NUMERICAL METHOD FOR SOLVING THE SURFACE EQUATIONS

As discussed in Chapter III the equations related to the shaped reflector, i.e., Equations (3.1) through (3.6) in that chapter, can be reduced to

$$\begin{aligned}
 & \left[ \left( x_c + m_o y_c \right)^2 - 4a^2 \left( 1 + m_o^2 \right) \right] \left\{ 4F x_c y_c - y_c \left[ \left( Y_2 - y_c \right)^2 + 4F x_c - 4F^2 \right] \right\}^2 \\
 & - \left( x_c + m_o y_c \right) \left( F_c^2 - 4a^2 \right) \left\{ 4F x_c Y_2 - y_c \left[ \left( Y_2 - y_c \right)^2 + 4F x_c - 4F^2 \right] \right\} \cdot \\
 & \left\{ 4F \left( Y_2 - y_c + m_o x_c \right) - m_o \left[ \left( Y_2 - y_c \right)^2 + 4F x_c - 4F^2 \right] \right\} \\
 & = - \frac{1}{4} \left( F_c^2 - 4a^2 \right)^2 \left\{ 4F \left( Y_2 - y_c + m_o x_c \right) - m_o \left[ \left( Y_2 - y_c \right)^2 + 4F x_c - 4F^2 \right] \right\}^2
 \end{aligned} \tag{B.1}$$

where all the variables have been defined in Chapter III. In Equation (B.1),  $m_o$  and  $Y_2$  are known and,  $F$  and  $F_c$  are functions of  $x_c$  and  $y_c$  only. In addition,  $x_c$  and  $y_c$  are related to  $x_{co}$  and  $y_{co}$  by

$$\begin{aligned}
 x_c &= x_{co} + \cos \alpha_o \Delta \rho \\
 y_c &= y_{co} + \sin \alpha_o \Delta \rho
 \end{aligned} \tag{B.2}$$

where  $\Delta\rho$  is the unknown distance between  $(x_{co}, y_{co})$  and  $(x_c, y_c)$  and  $\alpha_o$  is the angle of the old ray with respect to the positive x-axis which is defined in Chapter III.

By substituting Equation (B.2) into (B.1), an 8<sup>th</sup> order polynomial equation in  $\Delta\rho$  has to be solved numerically. Although one can try to solve  $\Delta\rho$  numerically directly from the polynomial equation, it is still very tedious. A method which assumes  $\Delta\rho$  is small is used in this study to solve  $\Delta\rho$ . This assumption is an appropriate one since that the incremental ray tube formed by the old and new rays is very small so that one will expect that variation of  $\Delta\rho$  is very small. Consequently, the higher order terms such as  $(\Delta\rho)^2, (\Delta\rho)^3, \dots, \text{etc.}$ , in the polynomial equation are neglected so that a linear equation in  $\Delta\rho$  is obtained and solved. In the following, different terms in Equation (B.1) are discussed separately by substituting Equation (B.2) for  $x_c$  and  $y_c$  into Equation (B.1). Also notice that

$$F = \frac{1}{2} (1 - \sec \alpha_o) (x_c - x_{20})$$

or

$$F = -\frac{1}{2} \tan \frac{\alpha_o}{2} (y_c - y_{20})$$

$$F_c^2 = x_c^2 + y_c^2$$

The first expression of  $F$  is used in the following analyses.

$$\begin{aligned}
(1) \quad & (Y_2 - y_c)^2 + 4F x_c - 4F^2 \\
&= (y_{co} + \sin \alpha_o \Delta \rho - Y_2)^2 + 2(1 - \sec \alpha_o)(x_{co} + \cos \alpha_o \Delta \rho - x_{20}) \\
&\quad (x_{co} + \cos \alpha_o \Delta \rho) - (1 - \sec \alpha_o)^2 (x_{co} + \cos \alpha_o \Delta \rho - x_{20})^2 \\
&= (y_{co} - Y_2)^2 + 2 \sin \alpha_o (y_{co} - Y_2) \Delta \rho + \sin^2 \alpha_o (\Delta \rho)^2 + 2(1 - \sec \alpha_o) \cdot \\
&\quad [x_{co}(x_{co} - x_{20}) + (x_{co} - x_{20}) \cos \alpha_o \Delta \rho + x_{co} \cos \alpha_o \Delta \rho + \cos^2 \alpha_o (\Delta \rho)^2] \\
&\quad - (1 - \sec \alpha_o)^2 [(x_{co} - x_{20})^2 + 2 \cos \alpha_o (x_{co} - x_{20}) \Delta \rho + \cos^2 \alpha_o (\Delta \rho)^2] \\
&= \{(y_{co} - Y_2)^2 + 2(1 - \sec \alpha_o) x_{co} (x_{co} - x_{20}) - (1 - \sec \alpha_o)^2 (x_{co} - x_{20})^2\} \\
&\quad + 2\{\sin \alpha_o (y_{co} - Y_2) + (1 - \sec \alpha_o)(2x_{co} - x_{20}) \cos \alpha_o - \cos \alpha_o (1 - \sec \alpha_o)^2 \cdot \\
&\quad (x_{co} - x_{20})\} \Delta \rho + \{\sin^2 \alpha_o + 2 \cos^2 \alpha_o (1 - \sec \alpha_o) - \cos^2 \alpha_o (1 - \sec \alpha_o)^2\} (\Delta \rho)^2
\end{aligned}$$

It can be shown that the coefficient of  $(\Delta \rho)^2$  is zero. Thus,

$$(Y_2 - y_c)^2 + 4F x_c - 4F^2 = Z_1 + Z_2 \Delta \rho \quad (B.3)$$

in which

$$Z_1 = (y_{co} - Y_2)^2 + 2(1 - \sec \alpha_o) x_{co} (x_{co} - x_{20}) - (1 - \sec \alpha_o)^2 (x_{co} - x_{20})^2$$

$$Z_2 = 2 \left( \sin \alpha_o (y_{co} - Y_2) + (\cos \alpha_o - 1) \left( (1 + \sec \alpha_o) x_{co} - x_{20} \sec \alpha_o \right) \right)$$

$$(2) \quad 4a^2 = \left\{ (x_{10}^2 + y_{10}^2)^{1/2} \pm \left[ (x_{10} - x_c)^2 + (y_{10} - y_c)^2 \right]^{1/2} \right\}^2 \quad \begin{array}{l} +: \text{ ellipse} \\ -: \text{ hyperbola} \end{array}$$

$$= \left\{ (x_{10}^2 + y_{10}^2)^{1/2} \pm |x_{10} - x_c| \cdot \left[ 1 + \left( \frac{y_{10} - y_c}{x_{10} - x_c} \right)^2 \right]^{1/2} \right\}^2$$

but

$$\frac{y_{10} - y_c}{x_{10} - x_c} = \tan \alpha_o$$

Thus,

$$4a^2 = \left\{ (x_{10}^2 + y_{10}^2)^{1/2} \pm |x_{10} - x_c| \left| \sec \alpha_o \right| \right\}^2$$

when  $\sec \alpha_o < 0$ ,

$$x_{10} - x_c < 0 \quad \text{for hyperbola}$$

$$x_{10} - x_c > 0 \quad \text{for ellipse}$$

when  $\sec \alpha_o > 0$ ,



$$x_{10} - x_c > 0 \quad \text{for hyperbola}$$

$$x_{10} - x_c < 0 \quad \text{for ellipse}$$

Consequently,

$$4a^2 = \left\{ (x_{10}^2 + y_{10}^2)^{1/2} + (x_c - x_{10}) \sec \alpha_o \right\}^2$$

The geometry for the above analysis is shown in Figure B.1.

$$(3) \quad F_c^2 - 4a^2$$

$$\begin{aligned} &= (x_c^2 + y_c^2) - \left\{ (x_{10}^2 + y_{10}^2)^{1/2} + (x_c - x_{10}) \sec \alpha_o \right\}^2 \\ &= \left[ (x_{co} + \cos \alpha_o \Delta \rho)^2 + (y_{co} + \sin \alpha_o \Delta \rho)^2 \right] \\ &\quad - \left\{ \left[ (x_{10}^2 + y_{10}^2)^{1/2} + (x_{co} - x_{10}) \sec \alpha_o \right] + \cos \alpha_o \sec \alpha_o \Delta \rho \right\}^2 \\ &= x_{co}^2 + 2 x_{co} \cos \alpha_o \Delta \rho + \cos^2 \alpha_o (\Delta \rho)^2 + y_{co}^2 + 2 y_{co} \sin \alpha_o \Delta \rho \\ &\quad + \sin^2 \alpha_o (\Delta \rho)^2 - \left[ (x_{10}^2 + y_{10}^2)^{1/2} + (x_{co} - x_{10}) \sec \alpha_o \right]^2 \\ &\quad - 2 \left[ (x_{10}^2 + y_{10}^2)^{1/2} + (x_{co} - x_{10}) \sec \alpha_o \right] \Delta \rho - (\Delta \rho)^2 \end{aligned}$$

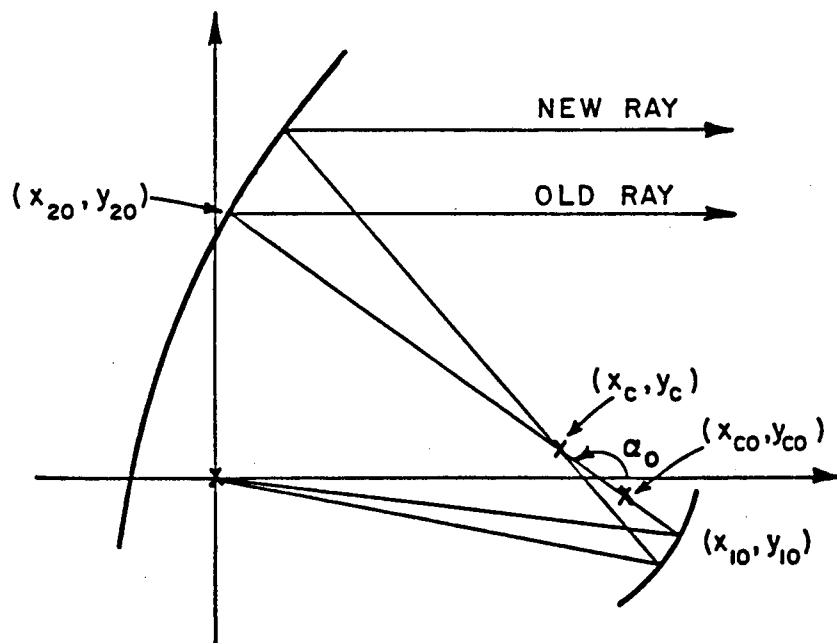
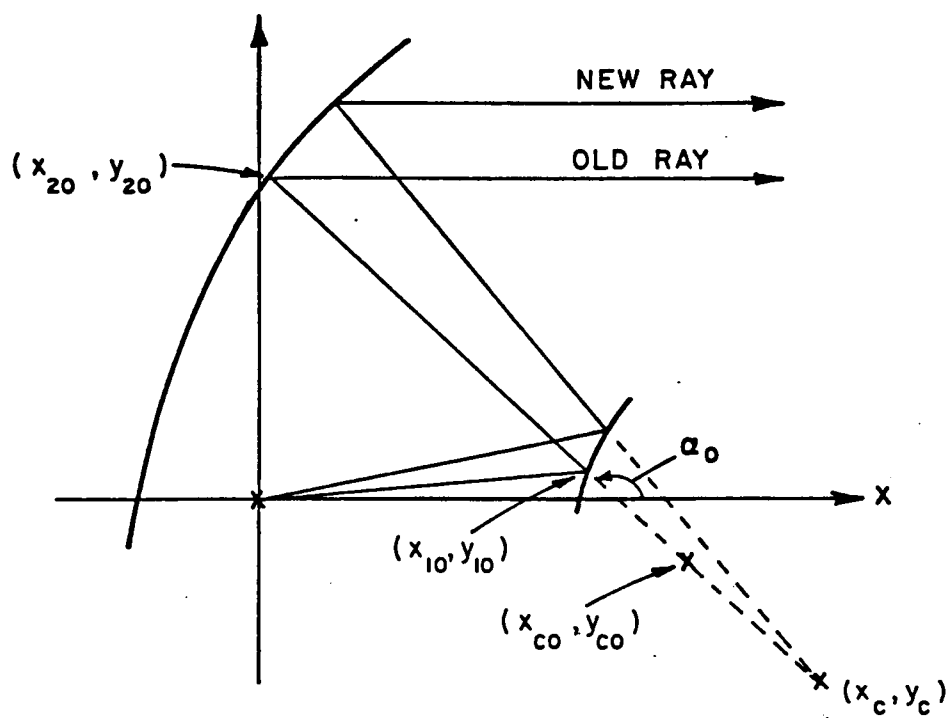


Figure B.1. Geometry for analysis of  $4a^2$ .

$$= Z_3 + Z_4 \Delta \rho$$

in which

$$Z_3 = x_{co}^2 + y_{co}^2 - \left[ (x_{10}^2 + y_{10}^2)^{1/2} + (x_{co} - x_{10}) \sec \alpha_o \right]^2$$

$$Z_4 = 2 \left\{ x_{co} \cos \alpha_o + y_{co} \sin \alpha_o - \left[ (x_{10}^2 + y_{10}^2)^{1/2} + (x_{co} - x_{10}) \sec \alpha_o \right] \right\}$$

$$(4) \quad x_c + m_o y_c = (x_{co} + \cos \alpha_o \Delta \rho) + m_o (y_{co} + \sin \alpha_o \Delta \rho)$$

$$= Z_5 + Z_6 \Delta \rho$$

$$\text{where } Z_5 = x_{co} + m_o y_{co}$$

$$Z_6 = \cos \alpha_o + m_o \sin \alpha_o$$

$$(5) \quad \text{From (2), } 4a^2 = \left\{ (x_{10}^2 + y_{10}^2)^{1/2} + (x_c - x_{10}) \sec \alpha_o \right\}^2$$

$$= \left\{ \left[ (x_{10}^2 + y_{10}^2)^{1/2} + (x_{co} - x_{10}) \sec \alpha_o \right] + \Delta \rho \right\}^2$$

$$= \left[ (x_{10}^2 + y_{10}^2)^{1/2} + (x_{co} - x_{10}) \sec \alpha_o \right]^2$$

$$+ 2 \left[ (x_{10}^2 + y_{10}^2)^{1/2} + (x_{co} - x_{10}) \sec \alpha_o \right] \Delta \rho + (\Delta \rho)^2$$

$$\sim Z_7 + Z_8 \Delta \rho$$

where

$$Z_7 = \left[ (x_{10}^2 + y_{10}^2)^{1/2} + (x_{co} - x_{10}) \sec \alpha_o \right]^2$$

$$Z_8 = 2 \left[ (x_{10}^2 + y_{10}^2)^{1/2} + (x_{co} - x_{10}) \sec \alpha_o \right]$$

$$(6) \quad 4F x_c Y_2 = 2 (1 - \sec \alpha_o) (x_c - x_{20}) x_c Y_2$$

$$= 2 (1 - \sec \alpha_o) Y_2 (x_{co} + \cos \alpha_o \Delta \rho - x_{20}) (x_{co} + \cos \alpha_o \Delta \rho)$$

$$= 2 (1 - \sec \alpha_o) Y_2 \left\{ x_{co} (x_{co} - x_{20}) + (2x_{co} - x_{20}) \cos \alpha_o \Delta \rho + \cos^2 \alpha_o (\Delta \rho)^2 \right\}$$

$$\sim Z_9 + Z_{10} \Delta \rho$$

where

$$Z_9 = 2 (1 - \sec \alpha_o) Y_2 x_{co} (x_{co} - x_{20})$$

$$Z_{10} = 2(1 - \sec \alpha_o) Y_2 (2x_{co} - x_{20}) \cos \alpha_o$$

$$(7) \quad 4F(Y_2 - y_c + m_o x_c)$$

$$= 2(1 - \sec \alpha_o)(x_c - x_{20})[Y_2 - y_c + m_o x_c]$$

$$= 2(1 - \sec \alpha_o) [(x_{co} - x_{20}) + \cos \alpha_o \Delta \rho] (Y_2 + m_o x_{co} - y_{co})$$

$$+ (m_o \cos \alpha_o - \sin \alpha_o) \Delta \rho]$$

$$= 2(1 - \sec \alpha_o) \{ (x_{co} - x_{20}) (Y_2 + m_o x_{co} - y_{co})$$

$$+ [(x_{co} - x_{20}) (m_o \cos \alpha_o - \sin \alpha_o) + \cos \alpha_o (Y_2 + m_o x_{co} - y_{co})] \Delta \rho$$

$$+ \cos \alpha_o (m_o \cos \alpha_o - \sin \alpha_o) (\Delta \rho)^2 \}$$

$$= Z_{11} + Z_{12} \Delta \rho$$

where

$$Z_{11} = 2(1 - \sec \alpha_o)(x_{co} - x_{20})(Y_2 + m_o x_{co} - y_{co})$$

$$Z_{12} = 2(1 - \sec \alpha_o) [(x_{co} - x_{20}) (m_o \cos \alpha_o - \sin \alpha_o) + \cos \alpha_o (Y_2 + m_o x_{co} - y_{co})]$$

$$\begin{aligned}
(8) \quad & (x_c + m_o y_c)^2 - 4a^2 (1 + m_o^2) \\
&= (z_5 + z_6 \Delta \rho)^2 - (z_7 + z_8 \Delta \rho) (1 + m_o^2) \\
&\sim [z_5^2 - z_7 (1 + m_o^2)] + [2z_5 z_6 - (1 + m_o^2) z_8] \Delta \rho \\
&= W_1 + W_2 \Delta \rho
\end{aligned}$$

where

$$\begin{aligned}
W_1 &= z_5^2 - z_7 (1 + m_o^2) \\
W_2 &= 2z_5 z_6 - (1 + m_o^2) z_8
\end{aligned}$$

$$\begin{aligned}
(9) \quad & 4Fx_c Y_2 - y_c [(Y_2 - y_c)^2 + 4Fx_c - 4F^2] \\
&= z_9 + z_{10} \Delta \rho - (y_{co} + \sin \alpha_o \Delta \rho) [z_1 + z_2 \Delta \rho] \\
&= z_9 + z_{10} \Delta \rho - [y_{co} z_1 + (y_{co} z_2 + \sin \alpha_o z_1) \Delta \rho + \sin \alpha_o z_2 (\Delta \rho)^2] \\
&\sim [z_9 - y_{co} z_1] + (z_{10} - (y_{co} z_2 + \sin \alpha_o z_1)) \Delta \rho \\
&= W_3 + W_4 \Delta \rho
\end{aligned}$$

in which

$$W_3 = Z_9 - y_{co} Z_1$$

$$W_4 = Z_{10} - y_{co} Z_2 - \sin \alpha_o Z_1$$

$$(10) \quad 4F(Y_2 - y_c + m_o x_c) - m_o \left[ (Y_2 - y_c)^2 + 4Fx_c - 4F^2 \right]$$

$$= Z_{11} + Z_{12} \Delta \rho - m_o (Z_1 + Z_2 \Delta \rho)$$

$$= (Z_{11} - m_o Z_1) + (Z_{12} - m_o Z_2) \Delta \rho$$

$$= W_5 + W_6 \Delta \rho$$

in which

$$W_5 = Z_{11} - m_o Z_1$$

$$W_6 = Z_{12} - m_o Z_2$$

By substituting (1) - (10) into Equation (B.1):

1<sup>st</sup> term of lefthand side of (B.1):

$$\begin{aligned}
&= (w_1 + w_2 \Delta \rho) (w_3 + w_4 \Delta \rho)^2 \\
&= (w_1 + w_2 \Delta \rho) (w_3^2 + 2w_3 w_4 \Delta \rho + w_4^2 (\Delta \rho)^2) \\
&\sim v_1 + v_2 \Delta \rho
\end{aligned}$$

where

$$\begin{aligned}
v_1 &= w_1 w_3^2 \\
v_2 &= 2w_1 w_3 w_4 + w_2 w_3^2
\end{aligned}$$

2<sup>nd</sup> term of lefthand side of (B.1):

$$\begin{aligned}
&= (z_5 + z_6 \Delta \rho) (z_3 + z_4 \Delta \rho) (w_3 + w_4 \Delta \rho) (w_5 + w_6 \Delta \rho) \\
&\sim v_3 + v_4 \Delta \rho
\end{aligned}$$

where

$$\begin{aligned}
v_3 &= z_3 z_5 w_3 w_5 \\
v_4 &= z_3 z_5 (w_3 w_6 + w_4 w_5) + w_3 w_5 (z_3 z_6 + z_4 z_5)
\end{aligned}$$



Righthand side of (B.1):

$$= -\frac{1}{4} (Z_3 + Z_4 \Delta \rho)^2 (W_5 + W_6 \Delta \rho)^2$$

$$\sim V_5 + V_6 \Delta \rho$$

where

$$V_5 = -\frac{1}{4} Z_3^2 W_5^2$$

$$V_6 = -\frac{1}{2} (Z_3 Z_4 W_5^2 + Z_3^2 W_5 W_6)$$

Finally, from Equation (B.1)

$$(V_1 + V_2 \Delta \rho) - (V_3 + V_4 \Delta \rho) \sim V_5 + V_6 \Delta \rho$$

thus

$$\Delta \rho = \frac{-(V_1 - V_3 - V_5)}{V_2 - V_4 - V_6}$$

From  $\Delta \rho$ , the surfaces of the reflector and the caustic curve are solved.

## APPENDIX C

### GEOMETRICAL OPTICS REFLECTED FIELDS FOR CASSEGRAIN AND GREGORIAN REFLECTOR ANTENNAS

In this appendix, the geometrical optics reflected fields for the Cassegrain and Gregorian reflector antennas are calculated. In addition, the conditions which the initial points on the subreflector, main reflector, and caustics curve for the shaped dual-reflector must satisfy are derived in this appendix.

#### C.1. Reflected Fields for the Two-Dimensional Cassegrain Reflector Antenna

The geometry of a Cassegrain reflector antenna is given in Figure 2.6 of Chapter II. As discussed in Chapter II, for a source located at the real focus of the subreflector, the reflected field from the subreflector appears to emanate from the virtual focus. In other words, the virtual focus is the caustic of the subreflector reflected fields. Assuming that the primary source is a magnetic line source, the reflected magnetic field is calculated as

$$H^z(s_1) = H_i^z(Q_1) \sqrt{\frac{\rho_1^r}{\rho_1^r + s_1}} e^{-jks_1} \quad (C.1)$$

in which  $H_1^Z(Q_1)$  is the incident magnetic field at the point of reflection on the subreflector,  $\rho_1^r$  is the reflected field caustic distance and  $s_1$  is the distance from the point of reflection to the field point. In this case,  $\rho_1^r$  is the distance between the virtual focus and the point of reflection, i.e.,  $\rho_1^r = \rho_c$  as shown in Figure C.1. The far-zone reflected field is calculated by letting  $s_1 \rightarrow \infty$  and is given as

$$H_s^Z(s \rightarrow \infty) = H_1^Z(Q_1) \sqrt{\rho_c} \frac{e^{-jks_1}}{\sqrt{s_1}} \quad (C.2)$$

The reflected field from the parabolic main reflector is calculated by

$$H_m^Z(s_2) = H_1^Z(Q_2) \sqrt{\frac{\rho_2^r}{\rho_2^r + s_2}} e^{-jks_2} \quad (C.3)$$

in which  $H_1^Z(Q_2)$  is the incident magnetic field at the reflection point  $Q_2$ ,  $\rho_2^r$  is the reflected field caustic distance, and  $s_2$  is the distance from the point of reflection  $Q_2$  to the point of observation. For a focussed parabola, the reflected field caustic distance  $\rho_2^r$  is infinite and the reflected ray is parallel to the axis of symmetry. Consequently,

$$H_m^Z(s_2) = H_1^Z(Q_2) e^{-jks_2} \quad (C.4)$$

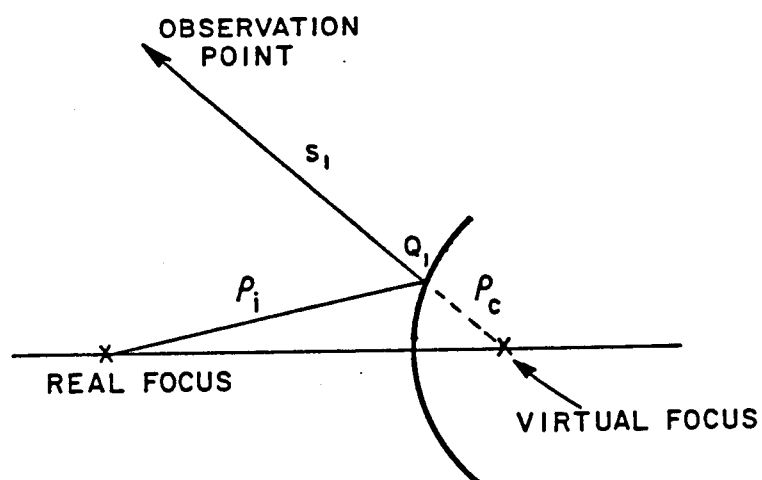


Figure C.1. Geometrical optics reflected field from a hyperbolic subreflector.

For the Cassegrain reflector, the incident field  $H_i^z(Q_2)$  is the reflected field of the subreflector and is given by

$$H_i^z(Q_2) = H_i^z(Q_1) \sqrt{\frac{\rho_c}{\rho_c + s_1}} e^{-jks_1} \quad (C.5)$$

where  $s_1$  is the distance between  $Q_1$  and  $Q_2$  as shown in Figure C.2.

Thus, the reflected field of the parabolic reflector is given by

$$H_m^z(s_2) = H_i^z(Q_1) \sqrt{\frac{\rho_c}{\rho_c + s_1}} e^{-jk(s_1 + s_2)} \quad (C.6)$$

If the magnetic line source has a far-zone pattern of  $F(\phi)$ ,

$$H_i^z(Q_1) = \sqrt{F(\phi_1)} \frac{e^{-jk\rho_i}}{\sqrt{\rho_i}} \quad (C.7)$$

Thus,

$$H_m^z(s_2) = \sqrt{F(\phi_1)} \frac{e^{-jk\rho_i}}{\sqrt{\rho_i}} \sqrt{\frac{\rho_c}{\rho_c + s_1}} e^{-jk(s_1 + s_2)} \quad (C.8)$$

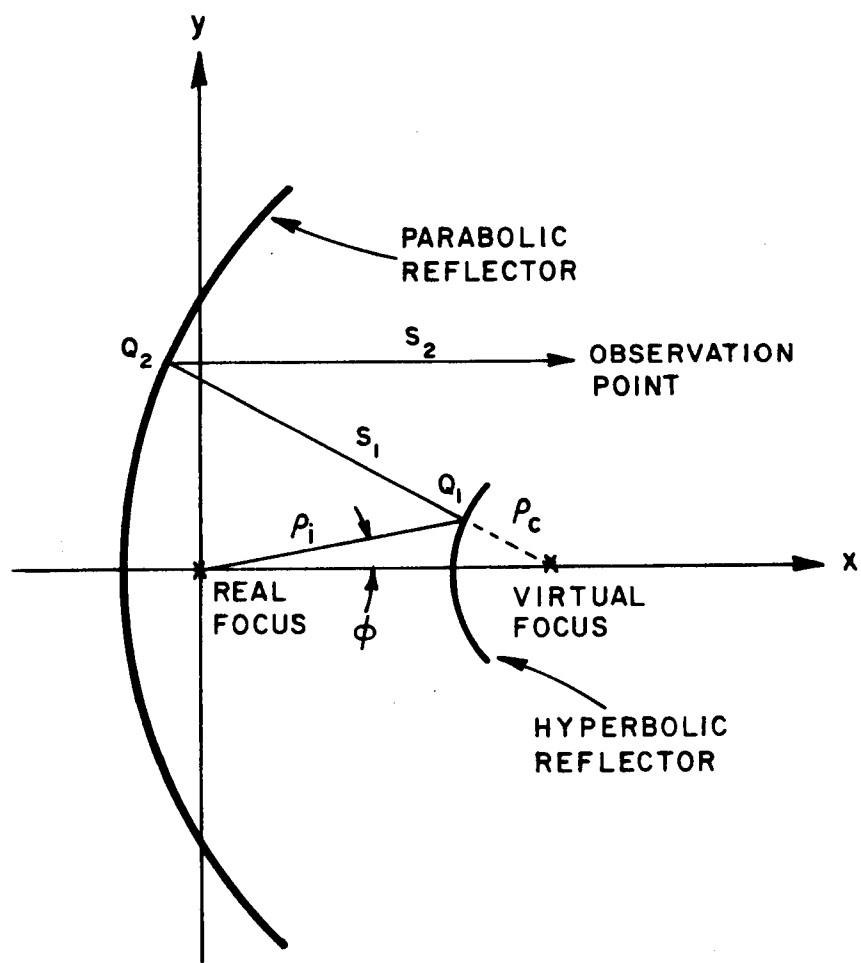


Figure C.2. Ray geometry of a Cassegrain reflector for calculation of reflected fields.

## C.2. Reflected Fields for the Two-Dimensional Gregorian Reflector

### Antenna

The geometry of a Gregorian reflector antenna is given in Figure 2.8 of Chapter II. For a line source located at the first focus of the elliptic subreflector, the reflected field from the subreflector appears to emanate from the second focus. Thus, the second focus is the caustic of the subreflector reflected field. The reflected field from the subreflector is calculated by Equation (C.1), except that the reflected field caustic distance is negative since the caustic is located in between the points of reflection and observation as shown in Figure C.3. Thus,

$$H_s^z(s_1) = H_i^z(Q_1) \sqrt{\frac{-\rho_c}{-\rho_c + s_1}} e^{-jks_1} \quad (C.9)$$

where  $\rho_c$  is the distance between  $Q_1$  and the caustic and is positive. The far-zone reflected field is given as

$$H_s^z(s_1 \rightarrow \infty) = H_i^z(Q_1) \sqrt{-\rho_c} \frac{e^{-jks_1}}{\sqrt{s_1}} \quad (C.10)$$

Similar to the Cassegrain case, the reflected field from the parabolic reflector is given by

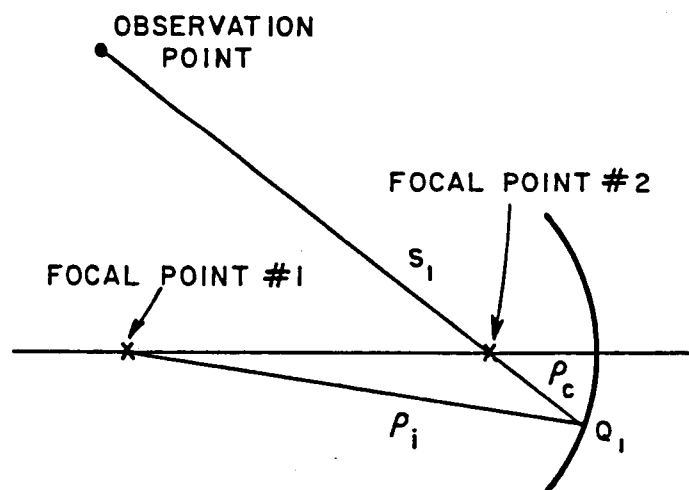


Figure C.3. Geometrical optics reflected field from an elliptic subreflector.



$$H_m^z(s_2) = \sqrt{F(\phi_1)} \frac{e^{-jk\rho_i}}{\sqrt{\rho_i}} \sqrt{\frac{-\rho_c}{-\rho_c + s_1}} e^{-jk(s_1+s_2)} \quad (C.11)$$

The ray geometry of this Gregorian antenna is shown in Figure C.4 where  $s_1$  is the distance between  $Q_1$  and  $Q_2$  and  $\rho_c$  is the distance between  $Q_1$  and the second focus.

### C.3. Relationship of Initial Points For Shaping of Two-Dimensional Dual-Reflector Antenna

It is mentioned in Chapters III and IV that in order to solve the surface equations, a set of initial points on the subreflector, main reflector, and caustic curve must be provided a priori. For given primary source and secondary aperture distributions, these initial points have to satisfy a ray condition. This condition is derived in this section for a dual-reflector with either a convex or concave subreflector.

#### C.3.1. Dual-Reflector with Convex Subreflector

The basic assumption in this research for dual-reflector shaping is that the corresponding points on the subreflector, main reflector and caustic curve are points on a Cassegrain or Gregorian antenna. Connecting these points forms a ray such that the reflected field at the corresponding aperture point is given by

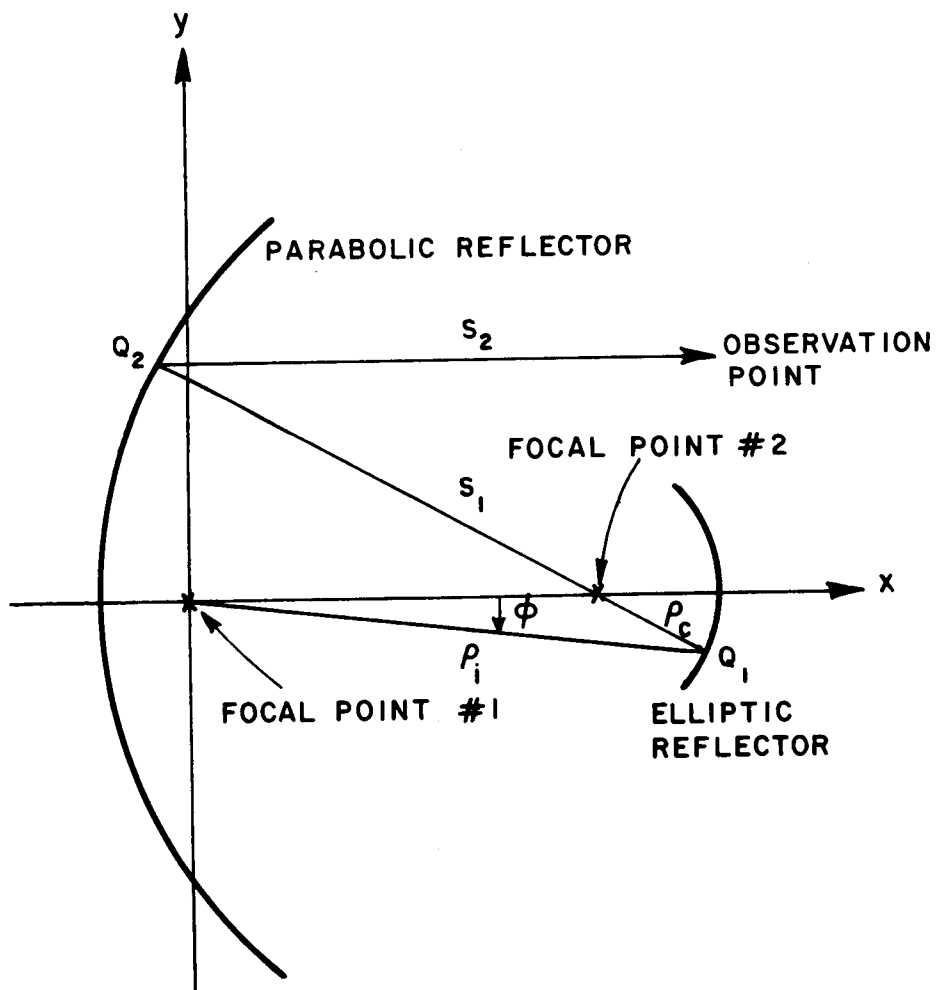


Figure C.4. Ray geometry of Gregorian reflector for calculation of reflected fields.

$$H_m^z = \sqrt{F(\phi)} \frac{e^{-jk\rho_i}}{\sqrt{\rho_i}} \sqrt{\frac{\rho_c}{s_1+\rho_c}} e^{-jk(s_1+s_2)} \quad (C.12)$$

when the subreflector is a convex surface. Assuming that the aperture distribution corresponding to this ray is known as  $U_o$ , then

$$\left| \sqrt{F(\phi)} \frac{e^{-jk\rho_i}}{\sqrt{\rho_i}} \sqrt{\frac{\rho_c}{s_1+\rho_c}} e^{-jk(s_1+s_2)} \right|^2 = U_o \quad (C.13)$$

which simplifies to

$$\left| F(\phi) \right| \frac{1}{\rho_i} \frac{\rho_c}{\rho_c+s_1} = U_o \quad (C.14)$$

This is the condition that each ray has to follow. In Equation (C.14),  $\rho_i$ ,  $\rho_c$  and  $s_1$  are functions of  $(x_1, y_1)$ ,  $(x_2, y_2)$  and  $(x_c, y_c)$  and  $U_o$  is a function of  $y_2$ . The initial points  $(x_{10}, y_{10})$ ,  $(x_{20}, y_{20})$  and  $(x_{co}, y_{co})$  have to follow Equation (C.14) also. In this study, it is assumed that the shaping process starts along the primary feed axis which is tilted by  $\phi_o$ . Consequently, one can assume that  $|F(\phi_o)| = 1$  and we obtain

$$\frac{1}{\rho_i} \frac{\rho_c}{\rho_c+s_1} = U_o(y_{20}) \quad (C.15)$$

Although there are many ways to determine the initial points from (C.15), it is noted that  $y_{20}$  has to be known in order to determine  $U_o$  and also  $(x_{10}, y_{10})$  has to be on the primary source axis. Thus,  $(x_{10}, y_{10})$  and  $(x_{20}, y_{20})$  are assumed and  $(x_{co}, y_{co})$  is solved from (C.15), as shown below.

Since  $(x_{10}, y_{10})$  and  $(x_{20}, y_{20})$  are known,  $\rho_i$  and  $s_1$  are known for the initial ray. From Equation (C.15) one finds that

$$\frac{\rho_c}{s_1} = \frac{\rho_i U_o}{1 - \rho_i U_o} \quad (C.16)$$

From the geometry shown in Figure C.5, it is found that

$$\frac{x_{co} - x_{10}}{x_{10} - x_{20}} = \frac{y_{co} - y_{10}}{y_{10} - y_{20}} = \frac{\rho_c}{s_1} \quad (C.17)$$

Consequently,  $x_{co}$  and  $y_{co}$  can be calculated from

$$x_{co} = \frac{\rho_i U_o}{1 - \rho_i U_o} (x_{10} - x_{20}) + x_{10} \quad (C.18)$$

$$y_{co} = \frac{\rho_i U_o}{1 - \rho_i U_o} (y_{10} - y_{20}) + y_{10} \quad (C.19)$$

From these initial points, one can start shaping the reflector above and below the ray which is formed by connecting these initial points.

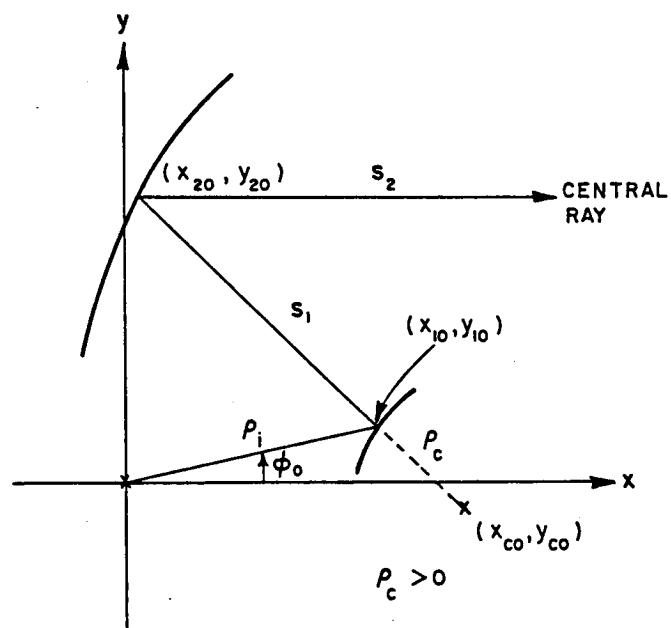


Figure C.5. Relation of initial points for a shaped dual reflector with a convex subreflector.

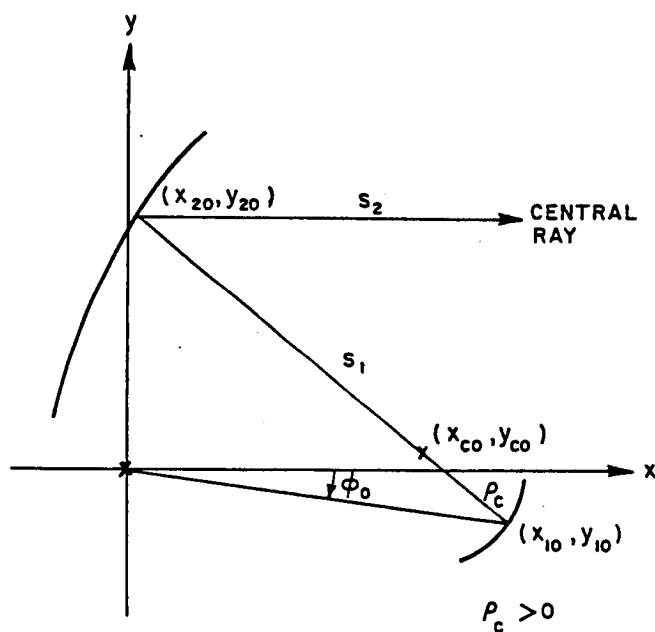


Figure C.6. Relation of initial points for a shaped dual reflector with a concave subreflector.

### C.3.2. Dual-Reflector with Concave Subreflector

Similar to the convex subreflector case, the corresponding points on the subreflector, main reflector and caustic curve for this case are on a Gregorian reflector. The reflected field at the corresponding aperture point is given by

$$H_m^z = \sqrt{F(\phi)} \frac{e^{-jk\rho_i}}{\sqrt{\rho_i}} \sqrt{\frac{-\rho_c}{s_1-\rho_c}} e^{-jk(s_1+s_2)} \quad (C.20)$$

where  $\rho_c > 0$ . Thus, one finds that

$$\left| \sqrt{F(\phi)} \frac{1}{\sqrt{\rho_i}} \sqrt{\frac{-\rho_c}{s_1-\rho_c}} e^{-jk\rho_i} e^{-jk(s_1+s_2)} \right|^2 = U_o \quad (C.21)$$

or

$$|F(\phi)| \frac{1}{\rho_i} \frac{\rho_c}{s_1-\rho_c} = U_o \quad (C.22)$$

Again, by assuming that the shaping starts along the feed axis with a tilt angle  $\phi_o$  and  $|F(\phi_o)|=1$ , the following relationship is obtained:

$$\frac{1}{\rho_i} \frac{\rho_c}{s_1-\rho_c} = U_o \quad (C.23)$$

From the same assumption that  $(x_{10}, y_{10})$  and  $(x_{20}, y_{20})$  are fixed so that  $\rho_i$  and  $s_i$  are known, then

$$\frac{\rho_c}{s_1} = \frac{\rho_i U_o}{1 + \rho_i U_o} \quad (C.24)$$

and

$$\frac{x_{co} - x_{10}}{x_{20} - x_{10}} = \frac{y_{co} - y_{10}}{y_{20} - y_{10}} = \frac{\rho_c}{s_1} \quad (C.25)$$

Thus,

$$x_{co} = - \frac{\rho_i U_o}{1 + \rho_i U_o} (x_{10} - x_{20}) + x_{10} \quad (C.26)$$

$$y_{co} = - \frac{\rho_i U_o}{1 + \rho_i U_o} (y_{10} - y_{20}) + y_{10} \quad (C.27)$$

#### C.4. Relationship of Initial Points for the Shaping of A Three-Dimensional Circularly Symmetric Dual-Reflector

The major difference between the two-dimensional and three-dimensional case is that the spread factor of the reflected field in the three-dimensional case is dependent on the two radii of curvature since the ray tube is three-dimensional. By simple modification of the two-dimensional case, the condition which the initial points have to satisfy for the three-dimensional case can be obtained.

#### C.4.1. Dual-Reflector with Convex Surface

For a point source with radiation power density  $F(\theta, \phi)$  illuminating the subreflector of the dual-reflector, the reflected field at the aperture of the main reflector is calculated by

$$u^r = \sqrt{F(\theta, \phi)} \frac{e^{-jk\rho_i}}{\rho_i} \sqrt{\frac{\rho_1 \rho_2}{(\rho_1 + s_1)(\rho_2 + s_1)}} e^{-jk(s_1 + s_2)} \quad (C.28)$$

in which  $\rho_i$  is the distance between the primary source and the point of reflection on the subreflector,  $\rho_1$  and  $\rho_2$  are the subreflector reflected field caustic distances,  $s_1$  is the distance between the point of reflection of the subreflector and main reflector, and  $s_2$  is the distance from the point of reflection on the main reflector to the aperture.

For the shaped dual-reflector with a convex subreflector, the corresponding points on the subreflector and main reflector are assumed to be located on a particular Cassegrain reflector; consequently, the two radii of curvature  $\rho_1$  and  $\rho_2$  are the same and are equal to the distance  $\rho_c$  between the caustic and point of reflection on the subreflector, thus, Equation (C.28) becomes:

$$u^r = \sqrt{F(\theta, \phi)} \frac{e^{-jk\rho_i}}{\rho_i} \left( \frac{\rho_c}{\rho_c + s_1} \right) e^{-jk(s_1 + s_2)} \quad (C.29)$$



It is assumed that the power density at the aperture point is given by  $U_o$ , and is related to  $u_r$  as

$$\left| \frac{1}{\sqrt{F(\theta, \phi)}} \frac{e^{-jk\rho_i}}{\rho_i} \left( \frac{\rho_c}{\rho_c + s_1} \right) e^{-jk(s_1 + s_2)} \right|^2 = U_o \quad (C.30)$$

Assume that the shaping begins from the axis of symmetry, thus, let  $F(\theta, \phi) = F(0, 0) = 1$ , one finds that

$$\frac{1}{\rho_i} \frac{\rho_c}{\rho_c + s_1} = \sqrt{U_o} \quad (C.31)$$

Comparing Equation (C.31) with (C.15), the condition that the initial caustic point has to satisfy is given by

$$\rho_{co} = \frac{\rho_i \sqrt{U_o}}{1 - \rho_i \sqrt{U_o}} (\rho_{10} - \rho_{20}) + \rho_{10} \quad (C.32)$$

$$z_{co} = \frac{\rho_i \sqrt{U_o}}{1 - \rho_i \sqrt{U_o}} (z_{10} - z_{20}) + z_{10} \quad (C.33)$$

provided that  $(z_{10}, \rho_{10})$  and  $(z_{20}, \rho_{20})$ , the initial points on the subreflector and main reflector are known. Note that the coordinates in the three-dimensional case are  $(z, \rho)$ .

#### C.4.2. Dual-Reflector with Concave Subreflector

The difference between this case and the convex subreflector case is that the subreflector reflected field caustic distance is negative, i.e.,

$$\rho_1 = \rho_2 = -\rho_c \quad (C.34)$$

in which  $\rho_c$  is the distance between the caustic and the point of reflection on the concave subreflector. Thus, from Equation (C.28), it is found that

$$u^r = \sqrt{F(\theta, \phi)} \frac{e^{-jk\rho_i}}{\rho_i} \frac{-\rho_c}{(-\rho_c + s_1)} e^{-jk(s_1 + s_2)} \quad (C.35)$$

Consequently,

$$\left| \sqrt{F(\theta, \phi)} \frac{e^{-jk\rho_i}}{\rho_i} \frac{-\rho_c}{-\rho_c + s_1} e^{-jk(s_1 + s_2)} \right|^2 = U_o \quad (C.36)$$

or, by letting  $F(\theta, \phi) = F(0,0)=1$ ,

$$\frac{1}{\rho_i} \frac{\rho_c}{s_1 - \rho_c} = \sqrt{U_o} \quad (C.37)$$

Thus,

$$\rho_{co} = - \frac{\rho_i \sqrt{U_o}}{1 + \rho_i \sqrt{U_o}} (\rho_{10} - \rho_{20}) + \rho_{10} \quad (C.38)$$

$$z_{co} = - \frac{\rho_i \sqrt{U_o}}{1 + \rho_i \sqrt{U_o}} (z_{10} - z_{20}) + z_{10} \quad (C.39)$$

## REFERENCES

- [1] M.D. Rader, "A Cassegrain Reflector System for Compact Range Reflector," M.Sc. thesis, The Ohio State University, Department of Electrical Engineering, Columbus, Ohio, 1985.
- [2] C.W. Pistorius, "New Main Reflector, Subreflector and Dual Chamber Concepts for Compact Range Applications," Ph.D. dissertation, The Ohio State University, Department of Electrical Engineering, Columbus, Ohio, 1986.
- [3] I.J. Gupta and W.D. Burnside, "A Physical Optics Correction for Backscattering from Curved Surfaces," accepted for publication in IEEE Trans. on Antennas and Propagation.
- [4] I.J. Gupta and W.D. Burnside, "Electromagnetic Performance Study of a New Compact Range Reflector," The Ohio State University ElectroScience Laboratory, Technical Report 718331-1, June, 1986.
- [5] M. Born and E. Wolf, Principles of Optics, Chapter 3, Pergamon Press, New York, 1959.
- [6] R.G. Kouyoumjian and P. Pathak, "A Uniform Geometrical Theory of Diffraction for an Edge of a Perfectly Conducting Surface," Proc. IEEE, Vol. 62, No. 11, pp. 1448-1461, November 1974.
- [7] J.A. Stratton, Electromagnetic Theory, McGraw-Hill Book Company, New York, 1941.
- [8] P.W. Hannan, "Microwave Antennas Derived from the Cassegrain Telescope," IRE Trans. on Antennas and Propagation, Vol. AP-9, pp. 140-153, March 1961.
- [9] T.H. Lee, "Geometrical Optics and GTD Analysis of Subreflectors in Cassegrain and Gregorian Reflector Antennas," M.Sc. thesis, The Ohio State University, Department of Electrical Engineering, Columbus, Ohio, 1984.
- [10] S. Silver (ed.), Microwave Antenna Theory and Design, McGraw-Hill Book Company, New York, Section 4.8, 1949.
- [11] Ibid., sec. 4.4.
- [12] Ibid., sec. 4.9.
- [13] V. Galindo, "Design of Dual-Reflector Antennas with Arbitrary Phase and Amplitude Distribution," IEEE Trans. on Antennas and Propagation, Vol. AP-12, pp. 403-408, July 1964.

- [14] B. Ye. Kinber, "On Two-Reflector Antennas," Radio Eng. Electron. Phys., Vol. 6, pp. 914-921, June 1962.
- [15] K.A. Green, "Modified Cassegrain Antenna for Arbitrary Aperture Illumination," IEEE Trans. on Antennas and Propagation, Vol. AP-11, pp. 589-590, September 1963.
- [16] W.F. Williams, "High Efficiency Antenna Reflector," Microwave Journal, Vol. 8, pp. 79-82, July 1965.
- [17] R.L. Barger, personal note.
- [18] V. Galindo-Israel, R. Mittra and A.G. Cha, "Aperture Amplitude and Phase Control of Offset Dual Reflectors," IEEE Trans. on Antennas and Propagation, Vol. AP-27, No. 2, pp. 154-164, March 1979.
- [19] J.J. Lee, L.I. Parad, and R.S. Chu, "A Shaped Offset-Fed Dual-Reflector Antenna," IEEE Trans. on Antennas and Propagation, Vol. AP-27, No. 2, pp. 165-171, March 1979.
- [20] R. Mittra, F. Hyjazie and V. Galindo-Israel, "Synthesis of Offset Dual-Reflector Antenna Transforming a Given Feed Illumination Pattern into a Specified Aperture Distribution," IEEE Trans. on Antennas and Propagation, Vol. AP-30, No. 2, pp. 251-259, March 1982.
- [21] B.S. Westcott, Shaped Reflector Antenna Design, Research Studies Press, Ltd., Letchworth, Hertfordshire, England, 1983.
- [22] R.C. Johnson, H.A. Ecker, and R.A. Moore, "Compact Range Techniques and Measurements," IEEE Trans. on Antennas and Propagation, Vol. AP-17, No. 5, pp. 568-576, September 1969.
- [23] W.D. Burnside, "Reflector Edge, Target Support and Feed Antenna Design for Compact Range," Internal notes of The Ohio State University ElectroScience Laboratory.
- [24] M.S. Narasimhan, V. Anantharam and K.M. Prasad, "A Note on the Shaping of Dual Reflector Antenna," IEEE Trans. on Antennas and Propagation, Vol. AP-29, No. 3, pp. 551-552, May 1981.
- [25] E.P. Ekelman and S.W. Gilmore, "Comments on A Note on the Shaping of Dual-Reflector Antenna," IEEE Trans. on Antennas and Propagation, Vol. AP-34, No. 1, pp. 123-125, January 1986.
- [26] R. Mittra and F. Hyjazie, "A Method for Synthesizing Offset, Dual Reflector Antennas," Proc. IEEE/AP and USNC/URSI Symposium, p. 243, 1978.